

Influence of Morphology, Climate Change and Landuse Change on Water Partitioning in Olifants River Basin

Zur Erlangung des akademischen Grades eines

DOKTOR-INGENIEURS

von der KIT-Fakultät für

Bauingenieur-, Geo- und Umweltwissenschaften

des Karlsruher Instituts für Technologie (KIT)

genehmigte

DISSERTATION

von

MSc. Phoebe Pauline Ingado Onjira

aus Kisumu, Kenya

Tag der Mündlichen Prüfung : 14.05.2020

Hauptreferent: Prof. Dr.-Ing. Dr. h.c. mult. Franz Nestmann
(Karlsruher Institut für Technologie)

Korreferent: Assoc. Prof. Dr. -Eng. Takahiro Sayama
(Kyoto University)

Karlsruhe, 2020

“We grow when we wade through murky waters”

Kurzfassung

Das Einzugsgebiet des Olifants River befindet sich derzeit in einer umfassenden Entwicklung der landwirtschaftlichen Landnutzungsaktivität. Trotz verschiedener Schutzpraktiken und Schutzmaßnahmen führt die Veränderung der Landnutzung immer noch zu einer Verschiebung im hydrologischen Regime. Als Treiber dieser rasanten Entwicklung in der Landnutzungsänderung durch landwirtschaftliche Nutzung sind der stetig steigende Nahrungsmittelbedarf und günstige klimatische Bedingung für die Landwirtschaft zu nennen. Ein stetiges Bevölkerungswachstum in Südafrika von etwa 1,4% pro Jahr weist auf eine kontinuierliche Nachfrage nach Nahrungsmitteln hin, die zu weiteren landwirtschaftlichen Expansionen und anschließend zu weiteren Veränderungen in der Hydrologie führen werden. Diese Situation könnte durch den Klimawandel und dadurch bedingte zunehmende Schwere extremer Phänomene wie Dürren und Überschwemmungen weiter verschärft werden. Diese Studie quantifiziert die Veränderungen des Klimas und der Landnutzung in den Teileinzugsgebieten Blyde River und Steelpoort River des Olifants Rivers, analysiert deren Einfluss auf die Hydrologie und schlägt eine Methode für die Landnutzungsplanung vor, mit der Änderungen im hydrologischen Regime abgemindert werden können.

Historische Abflüsse, Temperatur und Niederschläge wurden mit statistischen Methoden ausgewertet, um das Vorhandensein von Veränderungen in den Zeitreihen für 37 Jahre ab dem Jahr 1980 festzustellen. 1996 und 2012 wurden zwei abrupte Veränderungen im Abflussgeschehen festgestellt. Diese Veränderungen wurden auf die hohe Häufigkeit extremer Niederschläge (> 40 mm / Tag) zwischen 1996 und 2012 zurückgeführt. Es wurde auch ein allmählicher Anstieg des Abflusses nachgewiesen, der jedoch nicht auf klimatische Faktoren zurückzuführen war. Darüber hinaus wurde ein allmählicher Temperaturanstieg festgestellt, der jedoch keinen nachweisbaren Einfluss auf die Evapotranspiration und andere hydrologische Faktoren hatte.

Fernerkundliche Daten wurden zur Erkennung von Landnutzungsänderungen verwendet; vier Karten für 1992, 1998, 2002 und 2014 aus LANDSAT-Bildern. Die festgestellten signifikanten Veränderungen waren hauptsächlich auf die Urbanisierung und die landwirtschaftliche Entwicklung von etwa 169 km² und 514 km² zurückzuführen. Das SWAT-Modell wurde basierend auf dem LULC von 1992 kalibriert und zur Bewertung der Auswirkungen von Landnutzungsänderungen auf die Hydrologie verwendet. Basierend auf den LULC-Szenarien von 1992 und 2002 zeigten die Modellergebnisse eine Verringerung der Evapotranspiration um 6 mm, insbesondere in Gebieten, in denen Wälder durch Landwirtschaft ersetzt wurden, und eine allgemeine Erhöhung des Oberflächenabflusses um 3 mm, was auf die Verringerung der Oberflächenbedeckung zurückzuführen ist. Die weitere Ausdehnung des urbanen Bereichs und der Landwirtschaft zwischen 2002 und 2014 führte zu einer weiteren Erhöhung des Oberflächenabflusses um ca. 3 mm.

Diese Studie schlägt einen Ansatz für die landwirtschaftliche Landnutzungsplanung vor, bei dem die Wechselwirkungen von Morphologie und Klima genutzt werden, um Gebiete zu identifizieren, die zu

minimalen Auswirkungen auf die Landwirtschaft führen werden. Grünland wurde als Landnutzung identifiziert, die engere hydrologische Eigenschaften als die Landwirtschaft aufwies. Das Grünland wurde als LULC-Klasse ausgewählt, die durch Landwirtschaft ersetzt werden kann. Morphologische Analysen zeigten, dass eine geringe Hangneigung, eine höhere Bodenschüttdichte und eine geringe Robustheit des Geländes die besten physikalischen Bedingungen für die landwirtschaftliche Praxis sind.

Dies würde jedoch zu einem Verlust der Vegetationsvielfalt bei anhaltender landwirtschaftlicher Expansion führen. Daher sollte das Ausmaß der Umwidmung von Grünland auf Landwirtschaft begrenzt werden und es sollten zusätzliche Studien zu den Auswirkungen dieser Methode auf die biologische Vielfalt durchgeführt werden.

Abstract

The Olifants River Basin is currently experiencing extensive evolution of agricultural landuse activities. Despite various conservation practices put in place, landuse development is still causing a shift in hydrological regimes. The drivers of this rapid evolution of agriculture in the river basin are a constant increase in food demand and conducive climatic conditions for agriculture. Steady population growth in South Africa of about 1.4% annum is indicative of continuous demand for food production, which would lead to further agricultural expansions and subsequently, further changes in hydrology; this situation could be further exacerbated by climate change through increased severity of extreme phenomena like droughts and floods. This research quantifies the changes in climate and landuse in Olifants' sub-basins of Blyde and Steelpoort, analyzes their influence on hydrology, and proposes a method for landuse planning that would improve mitigating changes in hydrology.

Historical river discharge, temperature, and rainfall were evaluated using statistical methods to detect the presence of changes in their time series for 37 years beginning 1980. Two abrupt change points were detected in the river discharge in 1996 and 2012; these changes were attributed to a high frequency of extreme rainfall, above 40 mm/day between 1996 and 2012. A gradual increase of discharge was also detected, but this change had no attributions to any climatic factors. A gradual increase in temperature was also detected, but this had no detectable influence on evapotranspiration and other hydrological factors.

Remotely sensed images were used for landuse change detection; four maps for 1992, 1998, 2002, and 2014 from LANDSAT images. Significant changes detected were human-driven mainly by urbanization and agricultural development of about 169 km² and 514 km², respectively. SWAT Model was calibrated based on 1992 LULC and used to evaluate the impacts of landuse change on hydrology. Based on 1992 and 2002 LULC scenarios, the model outputs revealed a reduction in evapotranspiration by 6mm, especially in areas where forests were replaced with agriculture and a general increase in surface runoff by 3 mm, which is attributed to the reduction in surface cover. Further expansion of urban area and agriculture between 2002 and 2014 led to a further increase in surface runoff by about 3 mm.

This research proposes an approach for agricultural landuse planning that utilizes the interactions of morphology and climate to identify areas that would result in minimal impacts under agriculture. Grassland was identified as landuse that exhibited closer hydrological characteristics to agriculture and was selected as the LULC class that can be replaced by agriculture. Morphological analysis indicated that low slope, higher soil bulk density, and low terrain ruggedness are the best physical conditions for the establishment of agriculture.

However, the shortcomings of this would be loss of vegetation diversity in case of sustained agricultural expansion. Therefore, there should be a limitation on the extent of grassland conversion to agriculture, and additional studies on the impacts of this method on biodiversity.

Acknowledgment

Many people have earned my gratitude for their contribution to my time in graduate school. More specifically, I would like to thank five groups of people, without whom this thesis would not have been possible: my advisors and supervisory team, my colleagues, funding agencies, and my family.

First, I am indebted to my thesis advisors, Prof. Dr.-Ing. Dr.hc mult. Franz Nestmann (Karlsruhe Institute for Technology), Prof. Dr. rer. nat. Harro Stolpe (Ruhr-University Bochum) and Assoc. Prof. Dr. Eng. Takahiro Sayama (Kyoto University) for believing in me and for their unreserved supervision and support throughout my graduate studies.

Besides my supervisor, I would like to thank other members of my dissertation committee from Karlsruhe Institute for Technology, Prof. Dr. Stefan Norra, and Prof. Dr.-Ing Erwin Zehe for their invaluable advice. Secondly, I would like to express my gratitude to Dr. Peter Oberle, Dr. Mark Musall, and Dr. Christian Jolk (Ruhr-University-Bochum) for their invaluable guidance and mentorship that enabled me to develop and grow skills necessary in a research career.

I would like to thank Mr. Leonard Sweta of Regional Center for Mapping of Resources for Development (RCMRD), Ms. Rose Waswa (RCMRD), and Mr. Degalo Sendabo (RCMRD) for training, supervision, and provision of software/research material. I acknowledge the efforts the iWaGSS project partners for their support in the acquisition of data for my research, especially Anneliza Collett (DAFF), Dr. Eddie Riddell (SANPARKS) Celiwe Ntuli (DAFF), Justin Wiggett (Ruhr-University-Bochum) Ingo Nienhaus (Gewässer Experten) and especially Thabo Mohlala (SAEON) who accompanied and guided me during the data collection exercise.

I am grateful to Dr. Andreas Kron and Dr. Andreas Schenk (both of Karlsruhe Institute for Technology) for providing me with information, directing me through various procedures, and informing me of opportunities within the research community at the institute.

Thanks are also due to Hector Fellow Academy for the financial support they provided me and various capacity-building exercises to enable me effectively undertake my research work.

This dissertation would not have been possible without the warm love, continued patience, and endless support of my parents Harris Daudi Onjira and Rose M'mbone Onjira, my sister Dellah Onjira, my brothers Justin, Robert, Michael, Joseph, and Antony Onjira to whom am very grateful.

Table of Contents

Kurzfassung	i
Abstract.....	iii
Acknowledgment	v
Table of Contents.....	vi
List of Figures	ix
List of Tables	xiii
Nomenclature	xv
1 INTRODUCTION.....	19
1.1 Background.....	19
1.2 Overview of water resources in South Africa	21
1.3 Problem Description.....	24
1.4 Research Questions and Objectives	28
1.5 State of Art	29
1.6 Description of the study area	31
2 CLIMATE CHANGE AND ITS IMPACTS ON HYDROLOGY.....	34
2.1 Background.....	34
2.2 Data acquisition and pre-processing	35
2.3 Hydro-climatic change: detection and attributions	37
2.3.1 Homogeneity Test	37
2.3.2 Trend	45
2.3.3 Seasonality shift detection.....	48
2.4 Discussions.....	49
3 QUANTIFICATION OF LULC CHANGE AND ITS IMPACTS ON HYDROLOGY.....	51
3.1 Background.....	51

3.2	LULC change mapping using remote sensing images.....	52
3.2.1	Overview of satellite remote sensing techniques.....	52
3.2.2	Data source selection.....	53
3.2.3	Image acquisition.....	55
3.2.4	LULC classification.....	56
3.2.5	Accuracy assessment of LULC Maps.....	62
3.3	Hydrological Modelling.....	63
3.3.1	Model Selection.....	64
3.3.2	Description of SWAT Model Processes.....	65
3.3.3	Model setup.....	71
3.3.4	Model Calibration and sensitivity analysis.....	76
3.3.5	Results: Model calibration and validation.....	78
3.3.6	Results: Hydrological impacts of LULC change.....	80
3.4	Discussions.....	84
4	ADAPTATION OF AGRICULTURAL LANDUSE PLANNING TO IMPROVE MITIGATION OF IMPACTS ON HYDROLOGY.....	85
4.1	Background.....	85
4.2	Identification of LULC classes that exhibit similar hydrological responses to agriculture....	86
4.2.1	Methods.....	90
4.2.2	Results.....	91
4.3	Identification of “hydrologically suitable” morphological features for agricultural use.....	93
4.3.1	Methods.....	95
4.3.2	Results.....	103
4.4	LULC scenario development.....	109
4.4.1	Results.....	109
4.5	Evaluation of the proposed LULC planning approach.....	112
4.5.1	Results.....	112
4.6	Discussions.....	114
5	TRANSFER OF FINDINGS TO MAPPING SUITABLE AREA FOR FUTURE AGRICULTURAL USE AND PROJECTION OF ITS CORRESPONDING HYDROLOGICAL SCENARIOS UNDER CLIMATE CHANGE.....	116

5.1	Background.....	116
5.2	Climate change and global warming scenarios	117
5.2.1	Data acquisition and pre-processing.....	118
5.2.2	Results: Bias correction of rainfall and temperature	119
5.2.3	GCM selection	121
5.2.4	Analysis of projected climate data	125
5.3	Future LULC scenario.....	131
5.4	Simulations of hydrological scenarios future scenarios	133
5.4.1	Results: Simulations of hydrological scenarios future scenarios	134
5.5	Discussions.....	136
6	RESEARCH CONCLUSIONS	138
7	REFERENCES.....	140
8	APPENDICES.....	153

List of Figures

Figure 1-1: Schematic illustration of water partitioning (Source: www.virginiaplaces.org)	19
Figure 1-2: Location map of Olifants River Basin (Hijmans, Guarino and Mathur, 2012; Tadono et al., 2014; Takaku, Tadono, and Tsutsui, 2016; Takaku, Tadono, Tsutsui, et al., 2016, Processed and modified in ArcGIS)	21
Figure 1-3: Rainfall distribution in South Africa ((Schulze et al., 2011)	22
Figure 1-4: Location of Western Cape Province (www.123rf.com) and constantly decreasing dam levels (source: www.economist.com).....	22
Figure 1-5:Gap between existing water supply and projected demand by 2030 (Boccaletti et al., 2010)	24
Figure 1-6: LULC map showing the spatial distribution of agriculture in the Olifants River Basin (GeoterrageImage, 2015).....	25
Figure 1-7: Rainfall distribution in the Olifants River basin	26
Figure 1-8: Changes in discharge patter at station B7H015 (data source: DWS)	26
Figure 1-9: Monthly trends of dissolved SO_4^{-2} and volume of flow at KNP Station (de Villiers and Mkwelo, 2009)	27
Figure 1-10: Seasonal distribution of rainfall in the Olifants River Basin	28
Figure 1-11: (Left) Trenches and ridges on a farm and (right) farms are perpendicular to river flow in Olifants River basin (Source: Photograph taken during field survey)	30
Figure 1-12: Distribution of rainfall, minimum and maximum temperatures for the study area (Date source: CRU TS 4.0)	31
Figure 1-13: Geological map of Steelpoort and Blyde River Basins (Du Tiot and Sonnekus, 2014; Du Tiot et al., 2014; Toit and Sonnekus, 2014)	33
Figure 2-1: Global temperature trends due to natural and human influences	34
Figure 2-2: Data point locations from CRU TS	36
Figure 2-3: correlation between CRU 4.0 TS rainfall and observed rainfall from SAWS	36
Figure 2-4: Illustration of changepoint detection using a binary segmentation algorithm	38
Figure 2-5: Average annual discharge in Blyde and Steelpoort.....	39

Figure 2-6: Abrupt changes in discharge in Blyde and Steelpoort Rivers; (black line shows the mean values for each segment).....	40
Figure 2-7: Frequency distribution of rainfall in Blyde and Steelpoort River Basins based on segments of abrupt changes	41
Figure 2-8: Abrupt shift in temperature and evapotranspiration.....	42
Figure 2-9: Trend of rainfall, discharge, and temperature in Blyde and Steelpoort River Basins	47
Figure 2-10: Distribution of seasonality Index over three sub-series (1980-1995, 1996-2002, 2003-2016) of rainfall.....	49
Figure 3-1: Illustration of active and passive remote sensing (Source: analytik.co.uk).....	52
Figure 3-2: illustration of the electromagnetic spectrum (Source: Kiran, 2015)	53
Figure 3-3: Illustration of a data collection plan of LANDSAT sensors (source: USGS, 2017).....	55
Figure 3-4: Location of Blyde and Steelpoort River Basins in the LANDSAT WRS	55
Figure 3-5: Flowchart for LULC Classification process	57
Figure 3-6: Illustration of LULC class identification process	58
Figure 3-7: LULC map series for Steelpoort and Blyde River Basins	61
Figure 3-8: Soil textural triangle used for soil texture classification and.....	67
Figure 3-9: Schematic illustration of Model setup.....	71
Figure 3-10: Elevation and river network map(Source: ALOS DEM).....	72
Figure 3-11: soil distribution map for Steelpoort and Blyde River Basins (Source: FAO).....	73
Figure 3-12: Slope classes derived from DEM.....	75
Figure 3-13: Location map of River gauging stations used for model calibration	77
Figure 3-14: Changes in hydrological parameters due to LULC changes.....	81
Figure 3-15: Shift in mean monthly discharge curves in the basins due to 1992-2014 LULC change ..	82
Figure 3-16: Spatial anomalies of various hydrological components due to LULC changes.....	83
Figure 4-1: Evapotranspiration rates for various landuse categories in different regions	87
Figure 4-2: Conceptual illustration of canopy storage relationship with leaf area Index, and rainfall partitioning by vegetation canopy.....	88
Figure 4-3: conceptual illustration of water uptake relationship with root depth.....	89
Figure 4-4: Illustration of soil cover relationship with surface runoff (Marongiu and Cenceti, 2015) .	89
Figure 4-5: Landuse Scenarios prepared with 100% coverage of Agriculture, Forest, Grassland and Shrubland.....	90

Figure 4-6: Process flow for selection of landuse class that exhibit similar hydrological response to agriculture; output shows grassland exhibits minimal anomalies.....	92
Figure 4-7: Illustration of increasing complexity in hydrological prediction with an increase in controlling morphological features	94
Figure 4-8: Sub-basins used in correlation analysis for identifying dominant morphological parameters.....	95
Figure 4-9: Hypothetical square grids DEMs and their corresponding TRIs, where a) is peak type topography that is highly rugged, b) is pit type topography that is highly rugged, and c) is a gently undulating topography.	96
Figure 4-10: Terrain Ruggedness Index of Steelpoort and Blyde River Basins	97
Figure 4-11: Hypothetical illustration of the varied aspects for each grid cell, with their corresponding TCI s (source: Kiss, 2004)	98
Figure 4-12: Terrain Convergences Index of Steelpoort and Blyde River Basins.....	98
Figure 4-13: Illustration of slope classes for Steelpoort and Blyde River Basins	99
Figure 4-14: Map of the Bulk density of Steelpoort and Blyde River Basins	100
Figure 4-15: illustration of Soil Available Water and Field Capacity (Utah State University, no date)	101
Figure 4-16: Graphs show relationship between morphological parameters and hydrological anomalies from grassland and agriculture LULC based simulations	106
Figure 4-17: Maps showing the spatial distribution of TRI that meet hydrological conservation thresholds	107
Figure 4-18: map of grassland under 1992 LUL (a)C and protected areas (b) in Blyde and Steelpoort River Basins.	108
Figure 4-19: Map of suitable areas for agricultural use.....	109
Figure 4-20: Development of hypothetical 2014 LULC scenario and the difference maps of the 1992 LULC baseline scenario (b), 2014 LULC real scenario and 2014 LULC scenario developed using the new approach	111
Figure 4-21: comparison of various hydrological components under the 1992 LULC, the actual 2014 LULC, and the hypothetical 2014 LULC scenarios.....	112
Figure 4-22: Illustration of the shift in discharge curves under the 1992 LULC, the actual 2014 LULC and the hypothetical 2014 LULC.....	113
Figure 5-1: Rainfall distribution in South Africa.....	116
Figure 5-2: Illustration of RCPs (Intergovernmental Panel for Climate Change (IPCC), 2013)	118
Figure 5-3: comparison of monthly distribution of raw historical rainfall from four GCM with observed rainfall and bias-corrected	120

Figure 5-4: comparison of monthly distribution of raw historical average daily rainfall from four GCM with observed and bias-corrected temperatures (average daily)	121
Figure 5-5: GCM performance evaluation of the seasonal distribution of bias-corrected rainfall over the study area.	123
Figure 5-6: GCM performance evaluation of the seasonal distribution of bias-corrected temperature over the study area.	124
Figure 5-7: comparison of long-term seasonal distribution of projected rainfall (RCP 2.6, 4.5 & 8.5) with observed rainfall data	126
Figure 5-8: Box plots of long-term seasonal distribution of projected rainfall under RCP 2.6, 4.5 and 8.5 (2015-2035; in blue) and observed historical (1979-2005; in red). (x) represents monthly mean and (-) monthly median rainfall values	127
Figure 5-9: Box plots of 31 years (2015-2035) mean monthly rainfall under RCP 2.6, 4.5, and 8.5;(x) represents monthly mean and (-) monthly rainfall values for each year	128
Figure 5-10: Box plots of long-term seasonal distribution of projected temperature under RCP 2.6, 4.5 and 8.5 (2015-2035; in grey) and observed historical (1979-2005; in red). (x) represents mean and (-) represents median temperature	129
Figure 5-11: Box plots of 31 years (2015-2035) mean monthly rainfall under RCP 2.6, 4.5, and 8.5;(x) represents monthly mean and (-) monthly rainfall values for each year	130
Figure 5-12: Map of Agricultural areas under 2014 LULC and the recommended areas for future agricultural use	131
Figure 5-13: The actual 2014 LULC map	132
Figure 5-14: LULC map showing combined current (2014 LULC) and recommended future agricultural development.....	133
Figure 5-15: Flow process for hydrological modelling.....	134
Figure 5-16: Monthly distributions of observed and bias-corrected projected (RCP 2.6, 4.5 & 8.5) discharge at four gauging stations in Blyde and Steelpoort River Basins.....	135
Figure 5-17: Spatial distribution of evapotranspiration, surface runoff, rainfall, and groundwater recharge	136

List of Tables

Table 1-1: Reconciliation of water availability and requirements for 2020 (million m^3/a) (source:DWS, 2006)	23
Table 2-1: Summary of changepoints in rainfall and discharge Blyde and Steelpoort.....	41
Table 2-2: Rainfall changepoint locations in relation to the number of wet days	43
Table 2-3: Changepoint locations in relation to the percentage of extreme rainfall events (> 40mm/day)	44
Table 2-4: Summary of trend parameters for rainfall, discharge, and temperature in Blyde and Steelpoort	48
Table 2-5: Seasonality index (SI) classes and the associated rainfall regimes	48
Table 3-1: Categories of Remote Sensing sensors, EMS ranges, and typical applications	53
Table 3-2: Major satellites used in remote sensing and their properties.....	54
Table 3-3: Properties of LANDSAT Images and their applications	54
Table 3-4: Summary of LANDSAT images acquired for LULC mapping	56
Table 3-5: LULC change statistics, where (+) means increase and (-) means a decrease in respective LULC classes	60
Table 3-6: Summary of accuracy assessment of land use land cover classification of Blyde and Steelpoort River Basins	63
Table 3-7: Model screening against selection criteria	65
Table 3-8: The USDA-NRCS Hydrologic Soil Group Classification	67
Table 3-9: Soil classes in Steelpoort and Blyde River Basins with their corresponding texture classes and hydrologic group	73
Table 3-10:Summary of Hydrologic Soil Groups and their corresponding original and slope-adjusted $CN2$	76
Table 3-11: Discharge calibration and validation model performance statistics	78
Table 3-12: Average calibrated parameters' values	79
Table 4-1: Correlation of various morphological parameters and hydrological components.....	104

Table 4-2: Summary of hydrological components from grassland and agriculture LULC and the anomalies of their ratios.....	105
Table 4-3: Summary of morphological parameters, hydrological parameters and anomalies and equations used in the identification of limits morphological parameters	106
Table 5-1: Sources and resolutions of databases provided by WWEE	118
Table 5-2: Ranking of criteria used for selection of GCM source for rainfall data	124
Table 5-3: Ranking of criteria used for selection of GCM source for temperature data	125

Nomenclature

Organizations and Projects

IPCC	Intergovernmental Panel for Climate Change
BMBF	Bundesministerium für Bildungs und Forschung
DWS	Department of Water and Sanitation
DEA	Department of Environmental Affairs
SADC	Southern African Development Community
CGIAR	Science for Humanity's Greatest Challenges
DAFF	Department of Agriculture, Forestry and Fisheries
UNFCCC	United Nation Framework Convention for Climate Change
UN	United Nations
EPA	Environmental Protection Agency
UN CC Learn	United Nations Climate Change Learning platform
CRU	Climatic Research Unit
FAO	Food and Agriculture Organization
SAWS	South Africa Weather Services
JAXA	Japan Aerospace Exploration Agency
WWF	World Wildlife Fund
NASA	National Aeronautics and Space Administration
ESA	European Space Agency
USGS	United States Geological Survey
UNESCO	United Nations Educational, Scientific and Cultural Organization
NASA	National Aeronautics and Space Administration
USDA-ARS	United States Department for Agriculture Research Service
NOAA	National Oceanic and Atmospheric Administration
AORI	Atmosphere and Ocean Research Institute, the University of Tokyo

JAMSTEC:	Japan Agency for Marine-Earth Science and Technology
NIES:	National Institute for Environmental Studies
GFDL-ESM2M:	Geophysical Fluid Dynamics Laboratory Earth System Model
HadGEM2-ES:	Hadley Centre Global Environment Model version 2 Earth System Model
IPSL-CM5A-L:	Institut Pierre Simon Laplace Climate Model 5A
MIROC:	Model for Interdisciplinary Research on Climate
iWaGSS:	Integrated Water Governance Support System

Application software

MODAWEC:	Monthly to Daily Weather Converter
SWAT :	Soil and Water Analysis Tool
SUFI-2:	Sequential Uncertainties Fitting Algorithm, Ver-2
CCT:	Climate Change Toolkit

Scientific abbreviations

IWRM:	Integrated Water Resource Management
IDW:	Inverse Distance Weighting
ALOS:	Advanced Land Observing Satellite
MAR :	Mean Annual Rainfall
masl :	Meters above sea level
EIA:	Environmental Impact Assessment
SI:	Seasonality Index
EM:	Electromagnetic
EMS:	Electromagnetic Spectrum
ITCZ:	Inter-Tropical Convergence Zone
LULC:	Landuse/Landcover
WRS:	Worldwide Reference System
SID:	Spectral Information Divergence
SAM:	Spectral Angle Mapper
PET:	Potential Evapotranspiration
TM:	Thematic Mapper
ETM:	Enhanced Thematic Mapper

DN:	Digital Number
TOA:	Top-of-atmospheric
SCS-CN:	Soil Conservation Service Curve Number
HSG:	Hydrologic soil Group
AMC:	Antecedent Soil Moisture Condition
DEM :	Digital Elevation Model
GHG:	Greenhouse Gas
CN_1, CN_2, CN_3 :	Curve Number for soil moisture conditions 1, 2 and 3
SAW:	Soil Available Water (mm/m)
SOL_Z:	Active soil depth (mm)
ALPHA_BF:	Baseflow factor
GWQMN:	Water depth threshold in shallow aquifer required for return flow to occur (mm)
ESCO:	Soil evaporation compensation factor
EPCO:	Plant uptake compensation factor
SOL_K:	Saturated hydraulic conductivity (mm/hr)
CH_N2:	Manning's roughness for channel flow
OV_N:	Manning's roughness for overland flow
GWHT:	Initial groundwater height (mm)
HRU_SLP:	HRU slope (%)
GW_SPYLD:	Specific yield from shallow aquifer
SURLAG:	Lag time of surface runoff (days)
GW_DELAY:	Groundwater delay (days)
REVAPMN:	Water depth threshold in shallow aquifer required for "revap" to occur (mm)
GW_REVAP:	Factor of water movement from shallow aquifer to top soil layer
CH_K2:	Channel's effective hydraulic conductivity (mm/hr)
SLSUBBSN:	Average slope length for flow saturation (mm)
WRSM :	Water Resources Simulation Model
NSE :	Nash-Sutcliffe Efficiency
95PPU:	95% prediction uncertainty
LAI:	Leaf Area Index
TRI:	Terrain Ruggedness Index

TCI:	Terrain Convergence Index
LFI:	Lateral Flow Index
GWRI:	Groundwater Recharge Index
SR_c :	Surface Runoff Coefficient
PI:	Percolation Index
ET:	Evapotranspiration
HRU:	Hydrological Response Unit
RCP:	Representative Concentration Pathway
WWEE:	Water, Weather Energy, and Ecosystem
GCM	: Global Circulation Model
ISI-MIP5:	Inter-Sectoral Impact Model Intercomparison Project
KGE:	Kling Gupta Efficiency
RMSE:	Root Mean Square Error
IA:	Index of Agreement
R^2 :	Pearson's correlation coefficient
PBIAS:	Percentage Bias
NSE:	Nash-Sutcliffe Efficiency
NetCDF:	Network Common Data Form
Others	
GDP:	Gross Domestic Product

1 INTRODUCTION

1.1 Background

Water or hydrological partitioning refers to the separation of precipitation into various hydrological components and their pathways, as shown in Figure 1-1. It is mainly controlled by climatic factors, landuse/landcover (LULC), and physical (morphology) characteristics of the land; hence, LULC change and climate change/variability subsequently lead to shifting in water partitioning (Voepel et al., 2011). Observed patterns of change in climatic indices include the rise in global average temperature by about 0.85° C between 1880 and 2012, a general reduction in precipitation around the tropics, increased precipitation in higher latitude regions, increased droughts in semi-arid areas, and intensified hydrological events (IPCC, 2014).

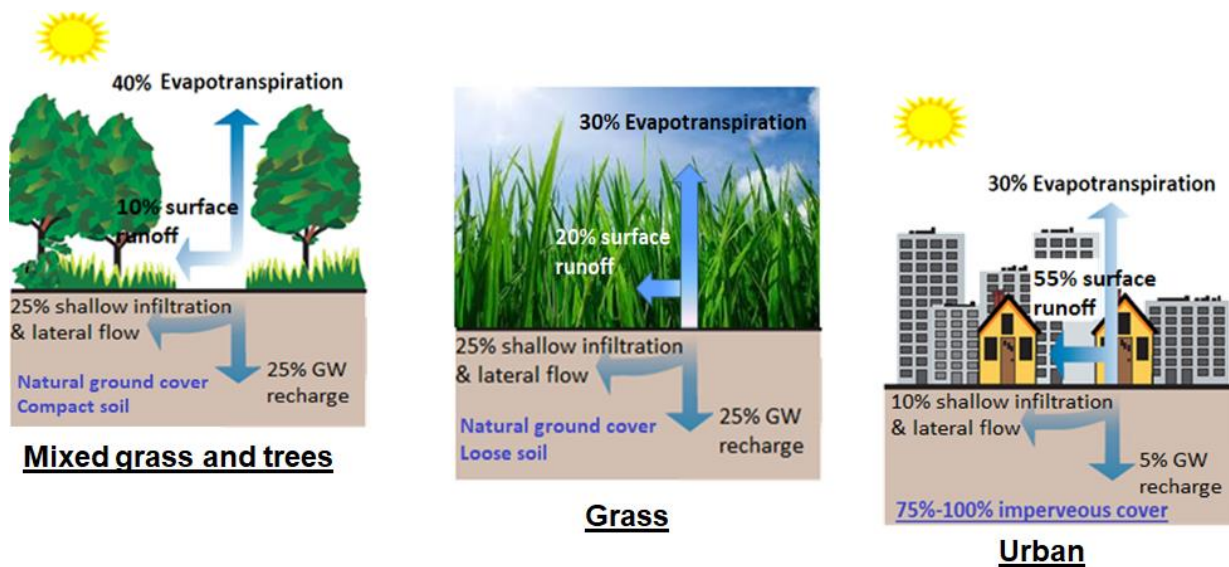


Figure 1-1: Schematic illustration of water partitioning (Source: www.virginiaplaces.org)

LULC changes cause alterations in hydraulic conditions of watersheds and subsequently change water partitioning (Bosch, J.M. and Hewlett, 1982). Studies carried out by various researchers like Guzha et al. (2018), Zhang et al. (2016), Nugroho et al. (2013), Gyamfi, Ndambuki and Salim (2016), Shao et al. (2018), and Zhu and Li (2014) demonstrate that urbanization and agricultural activities have generally led to changes in surface runoff, baseflow, evapotranspiration and groundwater recharge with increase in surface runoff being a common observation (Guzha et al., 2018). According to Bruijnzeel (2004), Guzha et al. (2018), and Blanton (2014), the expansion of the agricultural area, loss of forests, and urbanization in most cases limits infiltration, subsequently

leading to reduced baseflow in dry seasons. Urbanization and agricultural development therefore pose detrimental hydrological impacts in semi-arid river basins where baseflow dominate streamflow regimes.

Tropical semi-arid river basins experience extensive landuse activities, which eventually alter their hydrology; limited arable land in these regions has seen vast forested water towers rapidly converted to agricultural land (Rudel, 2013). The coupling effect of climate change and sustained human activities poses uncertainty in the future of our hydrological systems, thus necessitating the development of mitigation measures for sustainability. Morphology is a key factor that also controls hydrological regimes; according to Wang et al. (2018) and Price (2011), soil texture, geology, and topography largely influence the timing of streamflow generation, baseflow processes, evapotranspiration, and subsurface storage. Price (2011) also indicates that influences of land use on hydrological regimes can be mitigated or amplified by watershed's physical conditions. Based on the analyses of these studies, it can, therefore, be concluded that the exploration of hydrological responses of different landuse classes under various morphological conditions could, therefore, inform the planning of landuse activities for the mitigation of hydrological variability.

The objective of this research is to quantify hydrological impacts of climate change and landuse change in Blyde and Steelpoort River Basins, South Africa, and analyze the role of morphology in water partitioning under agricultural area LULC. The outcome of this research will serve as a base for developing an adapted landuse planning approach for mitigating changes in the hydrological regime. The research is undertaken within the context of the Integrated Water Governance (iWaGSS) Project.

iWaGSS Project: The German Ministry of Education and Research (Bundesministerium für Bildung und Forschung (BMBF)) has funded a research project, Integrated Water Governance support system (iWaGSS), to develop and test tools and techniques for relieving water-related stresses. The pilot project area is located in the Olifants River Basin in the North-Eastern region of South Africa, shown in Figure 1-2.

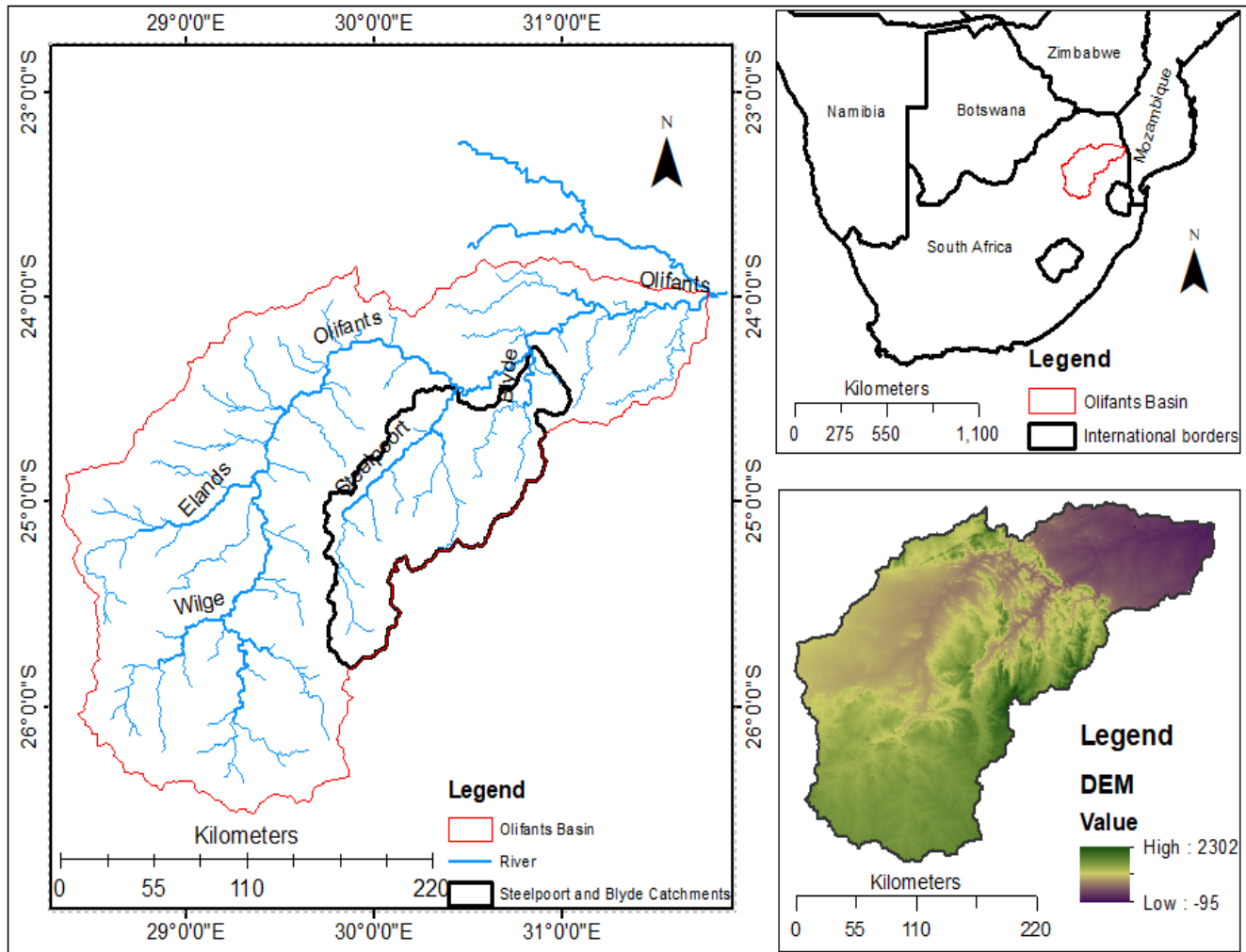


Figure 1-2: Location map of Olifants River Basin (Hijmans, Guarino and Mathur, 2012; Tadono et al., 2014; Takaku, Tadono, and Tsutsui, 2016; Takaku, Tadono, Tsutsui, et al., 2016, Processed and modified in ArcGIS)

1.2 Overview of water resources in South Africa

According to Hoffman and Todd (1999), South Africa is predominantly under arid and semi-arid conditions, as shown in Figure 1-3. It receives a mean annual rainfall of about 450 mm (Botai, Botai, and Adeola, 2018) and a mean annual Potential Evapotranspiration (PET) of 2164 mm (Jovanovic et al., 2015). As a result, water scarcity in South Africa is a prevalent and widespread problem Schulze and Lynch (2011). Inter-seasonal variability, intra-seasonal variability, and occasional extreme rainfall events are observed in most parts of the county. As a result, river discharge is dominated by low flow, highly variable, with sporadic high flows (Basson and Rossouw, 2003).

CLIMATE CHANGE AND ITS IMPACTS ON HYDROLOGY

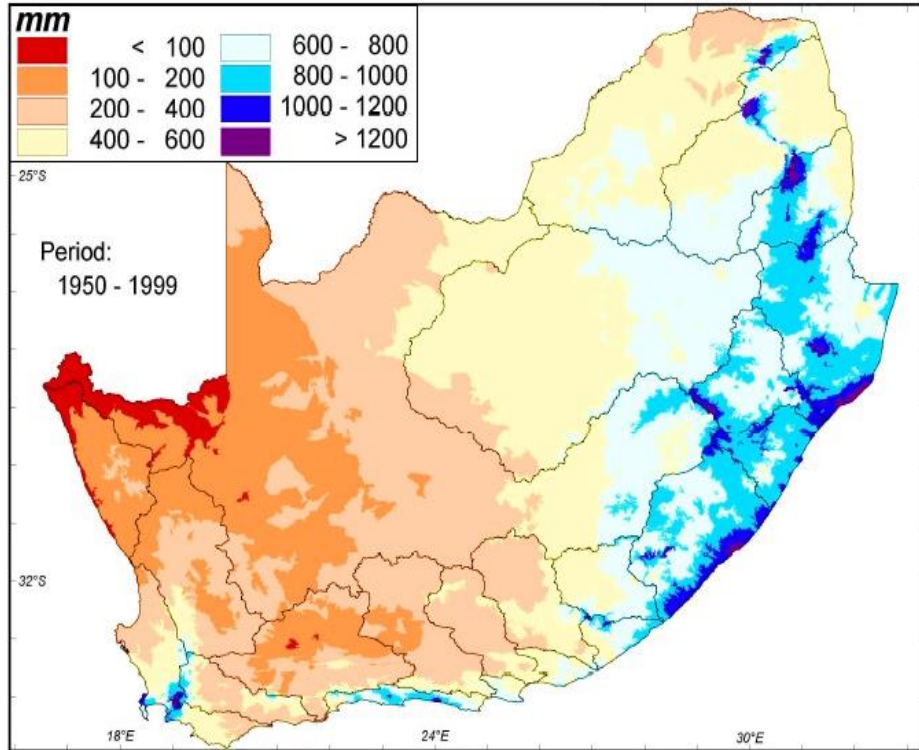


Figure 1-3: Rainfall distribution in South Africa ((Schulze et al., 2011)

To tackle the water scarcity issue, South Africa has developed extensive infrastructure for water harvesting with drought emergency plans. However, drought events have been exacerbated by climate change leading to extreme water shortages. For example, variability in climate in the recent past has seen a continued reduction in water level in the Western Cape region, as shown in Figure 1-4, which created a prolonged drought crisis that nearly led to a shut-down of operations of the whole town (Alexander, 2019).

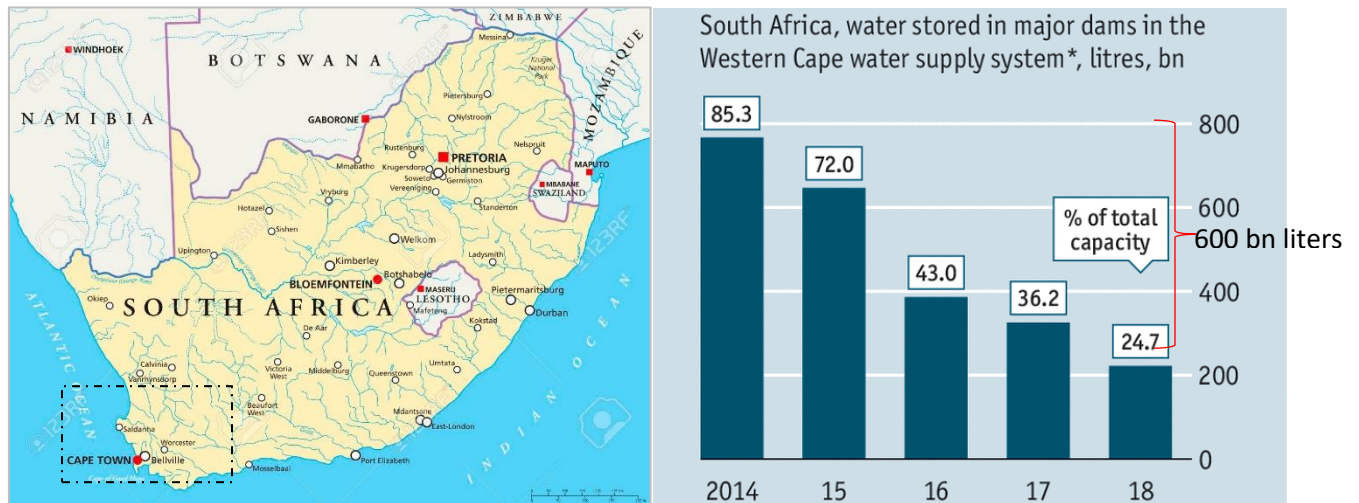


Figure 1-4: Location of Western Cape Province (www.123rf.com) and constantly decreasing dam levels (source: www.economist.com)

CLIMATE CHANGE AND ITS IMPACTS ON HYDROLOGY

Table 1-1: Reconciliation of water availability and requirements for 2020 (million m³/a) (source:DWS, 2006)

	Water Management Area	Reliable Local Yield	Transfers in	Local Requirement	Transfers Out	Balance
1	Limpopo	282	19	325	0	-24
2	Luvuvhu/Letaba	310	0	334	13	-37
3	Crocodile West & marico	693	656	1328	10	11
4	Olifants	611	172	971	8	-196
5	Inkomati	943	0	1048	148	-253
6	Usuti to Mhlatuze	1010	32	693	114	235
7	Thuleka	738	0	338	497	-97
8	Upper Vaal	1723	1443	1204	1481	481
9	Middle Vaal	201	791	389	605	-2
10	Lower Vaal	50	651	653	0	48
11	Mvoti to Unzikhulu	527	34	828	0	-267
12	Mzimvubu to Keiskamma	855	0	375	0	480
13	Upper Orange	4557	2	968	3105	486
14	Lower Orange	-1007	1886	834	54	-9
15	Fish to Tsistikamma	437	571	902	0	106
16	Goutitz	277	0	342	1	-66
17	Olifants/Doring	335	3	373	0	-35
18	Breede	868	1	637	203	29
19	Berg	501	203	738	0	-34
	National Figure	13911	0	13280	124	540

Water supply for domestic use in urban centres and industrial use is reliant on surface water with predominant reliance on groundwater in rural areas. Water requirements in many parts of South Africa generally exceed availability, as shown in Table 1-1 (Department of Water and Sanitation, 2006). Due to population growth and climate change impacts, the gap between existing water supply and availability is projected to widen by 2030, as shown in Figure 1-5 (Department of Water and Sanitation, 2006; Boccaletti, Stuchtey, and van Olst, 2010).

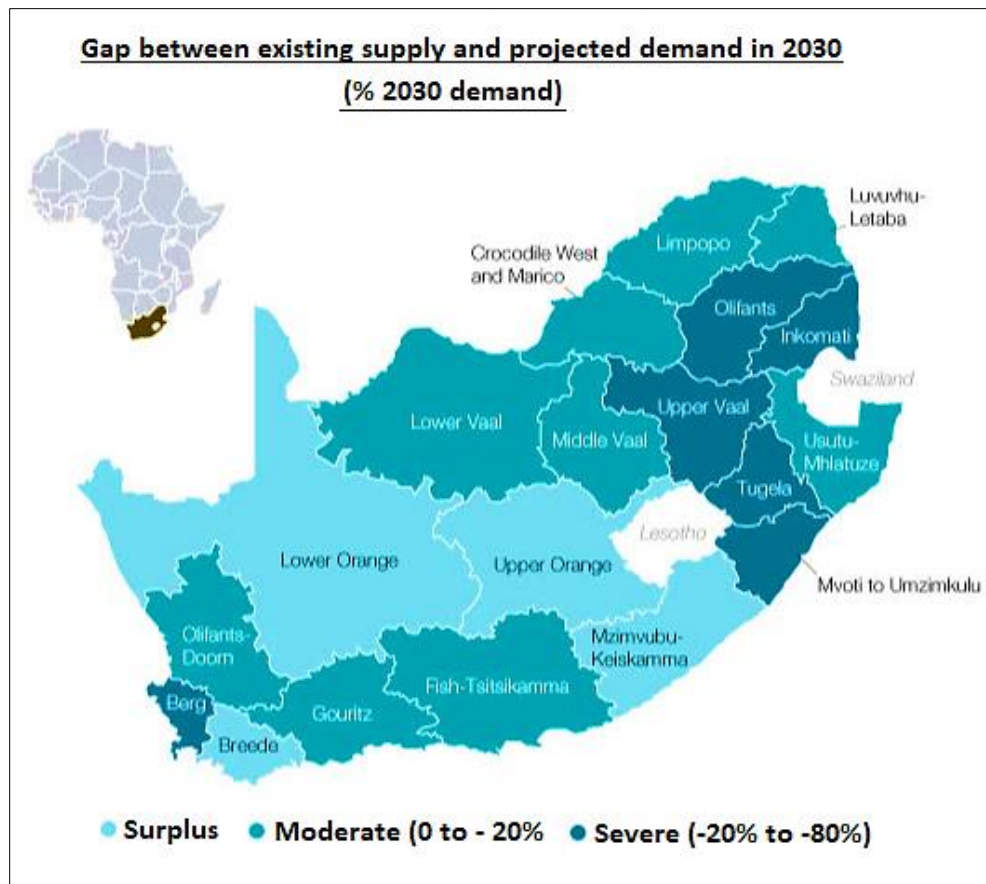


Figure 1-5: Gap between existing water supply and projected demand by 2030 (Boccaletti et al., 2010)

Apart from water scarcity, South Africa experiences water contamination due to the presence of industries, expanse agriculture, and human settlement. As a result, traces of various solutes generated from these activities and partially treated wastewater are often detected in the watercourses. Water scarcity aggravates water contamination problems since, in low flows, the rivers have a low hydraulic capacity for mass transport leading to high concentrations of pollutants in water (Kings, 2017).

1.3 Problem Description

South Africa has a steadily growing population that drives up food demand and subsequently increased the need for agricultural land. The current population of the country stands at 57 million, with an annual growth rate of about 1.4% (The World Bank, 2019); these statistics mean that the demand for food and agricultural land will continuously increase in the future. Because of an extensive spread of arid and semi-arid conditions, agricultural activities are predominant in areas with slightly higher rainfall and available water for irrigation like the Olifants River Basin.

Olifants River Basin is one of the areas in the country that receives higher rainfall relative to many parts of the country, where that annual average rainfall is 660 mm relative to the national annual average of 450 mm. This presents relatively conducive conditions for farming activities. Hence, the extensive development of agriculture is a dominant economic activity in the river basin. Figure 1-6 shows the LULC map developed by GeoterrageImage (2015) and provided by the South African Department of Environmental Affairs (DEA), where the expanse of

CLIMATE CHANGE AND ITS IMPACTS ON HYDROLOGY

agricultural activities covers about a fifth of the total area of the basin. Extensive agriculture is also conducted in the headwaters areas that receive relatively high rainfall, as indicated in Figure 1-7.

The World Bank projects South Africa's Population growth to be 67 million by 2035; this would translate to further demand for agricultural expansion and subsequently leading to further alteration of the basin's hydrology. Research conducted by Gyamfi et al. (2016) reveals that the expansion of agriculture in the Olifants River Basin has significant impacts on the hydrological regime, especially an increase in surface runoff, which in turn limits infiltration.

Analysis of the work conducted by Gyamfi indicate that agricultural development between the year 2002 and 2013 agricultural expansion was approximately $19,000 \text{ km}^2$. Corresponding to this period, a distinctive reduction of discharge between 2012 and 2018 relative to 2001 and 2011 period, as shown in Figure 1-8.

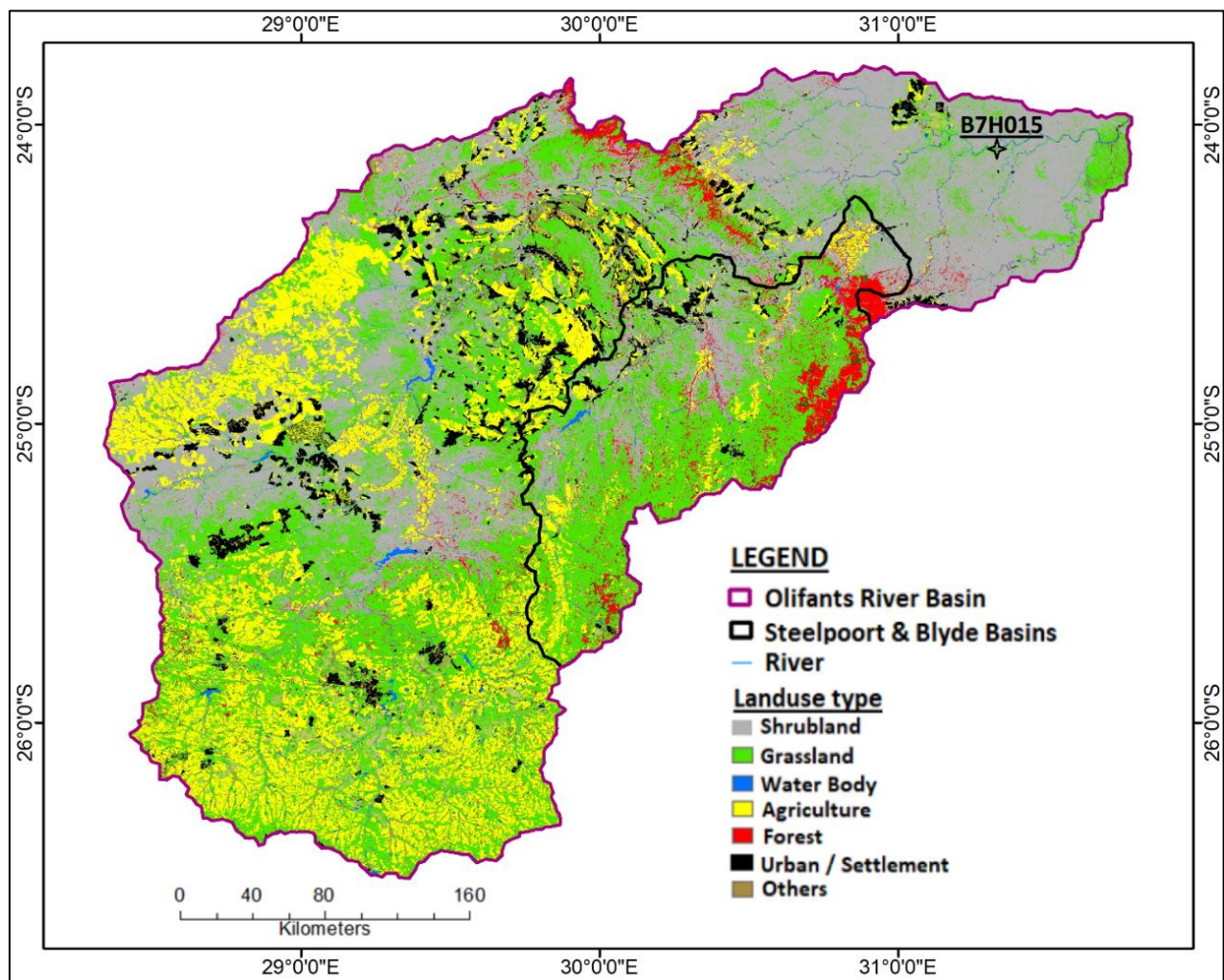


Figure 1-6: LULC map showing the spatial distribution of agriculture in the Olifants River Basin (Geoterragelimage, 2015)

CLIMATE CHANGE AND ITS IMPACTS ON HYDROLOGY

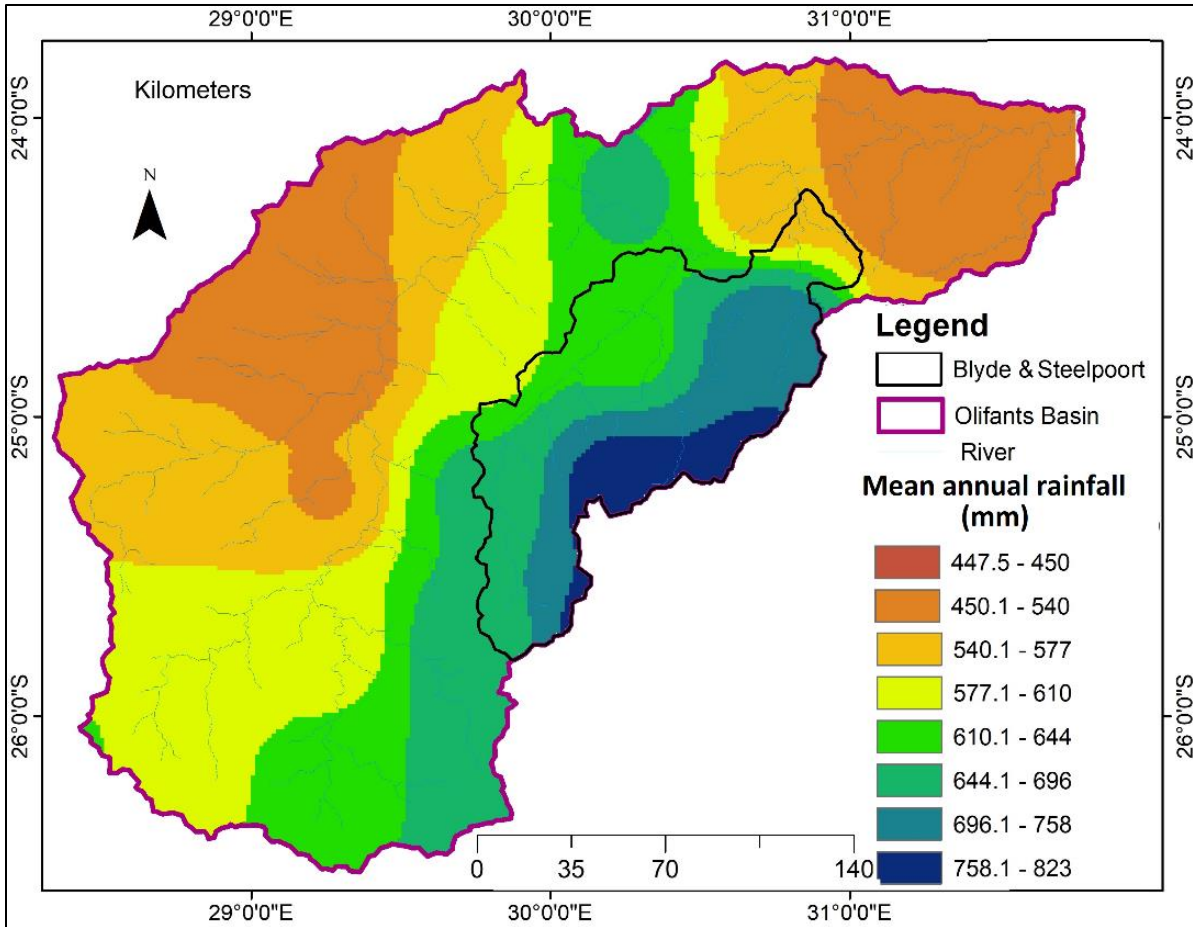


Figure 1-7: Rainfall distribution in the Olifants River basin

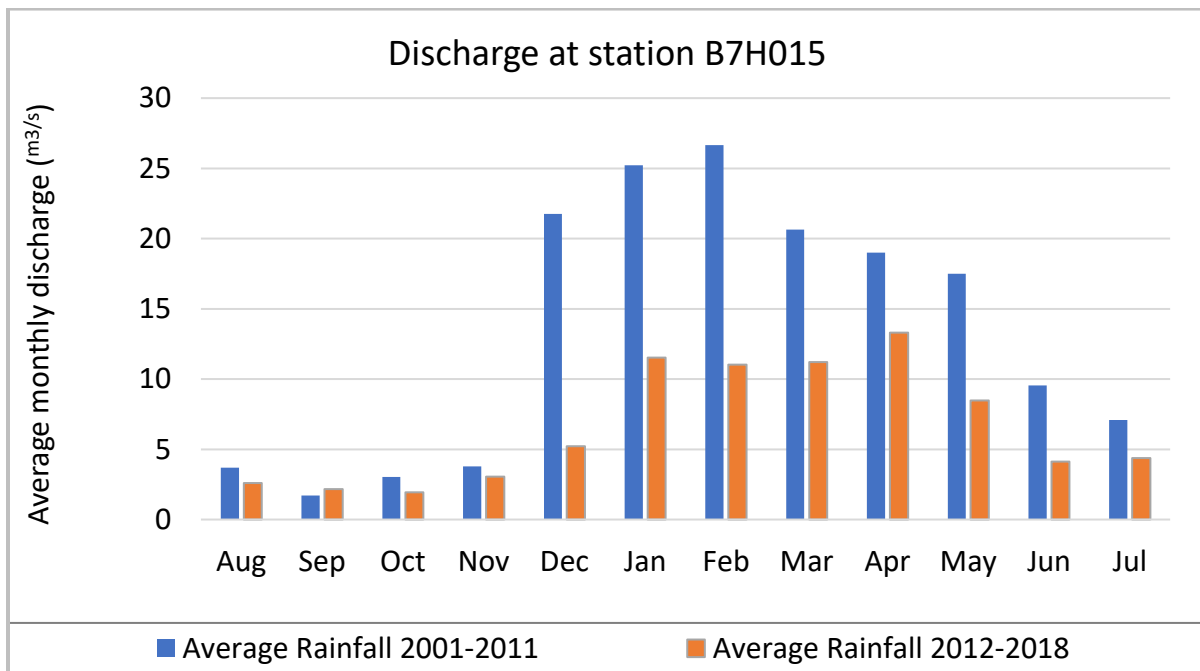


Figure 1-8: Changes in discharge patten at station B7H015 (data source: DWS)

Changes in streamflow like reduced streamflow, as seen in Figure 1-8 and limited infiltration due to LULC change as reported by Gyamfi *et al.* (2016), can be very detrimental to the ecosystem and water users in general. In low flow seasons, the concentration levels of chemicals and pollutants in the Olifants River increases due to insufficient water for dilution of wastewater effluent and other non-point sources of pollution. Figure 1-8 shows the concentration of sulfates at a downstream station of the Olifants River relative to seasonal flow, where the concentration increases with a decrease in flow volume. Siyabona Africa (2017) has also reported the mass death of fish due to extremely low flows in the Olifants River.

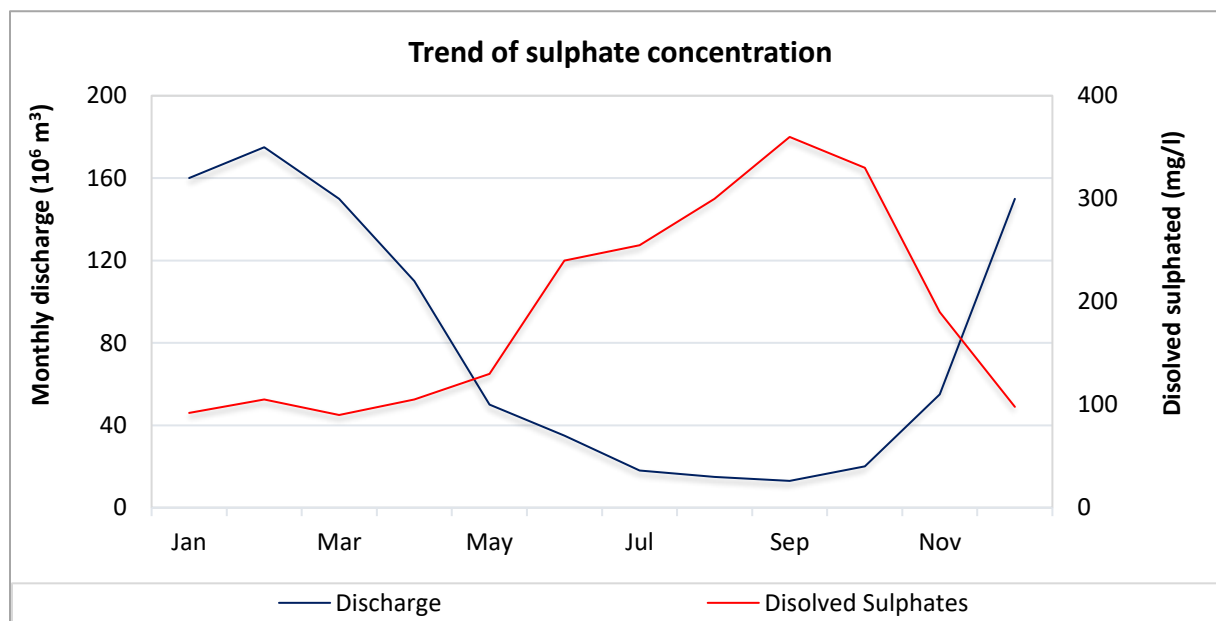


Figure 1-9: Monthly trends of dissolved SO_4^{2-} and volume of flow at KNP Station (de Villiers and Mkwelo, 2009)

As reported by Gyamfi *et al.* (2016), expansion of agriculture increases surface runoff and limits infiltration, which in turn reduces the volume of baseflow generated. With anticipated further development of agriculture in the Olifants River Basin, changes in hydrological regimes are inevitable; the risk for pollution and water scarcity may be exacerbated since there may occur a reduction in baseflow, which dominates the flow regime throughout the winter season (from May-September).

Climate change and variability also play a crucial role in water availability and distribution (Urama and Ozor, 2010; Sun *et al.*, 2013; Vactor *et al.*, 2014). Water stresses in South Africa are projected to worsen under climate change influence (Hoerling *et al.*, 2006; Boccaletti *et al.*, 2010; Urama *et al.*, 2010). The pressure on water resources is exacerbated by the coupled effect of climate change and human activities like landuse changes (Menzel *et al.*, 2007; Bates *et al.*, 2008). The Olifants River basin is already experiencing variability in climatic patterns; Figure 1-10 shows the seasonal distribution of rainfall for three different periods (2001-2005, 2006-2011, and 2012-2017). It can be seen that the statistical properties of rainfall for each change throughout the season, especially in the rainy seasons beginning October until April.

According to SADC *et al.* (2013), Science for Humanity's Greatest Challenges (CGIAR) classifies the Olifants region under arid to semi-arid, where water resources are under immense pressure from the environmental system alone, even before human development demands are factored in. Therefore, water is seen as a limiting factor in

development in the region. Water resources are under pressure to sustain ecosystem demands as well as our human needs. Therefore, it is necessary to adapt the management and planning of water resources so as to sustainably meet the ecosystem’s demand as well as demands for economic development. Therefore, to ensure that the agricultural demands are met without compromising the hydrology of the river basin, it is necessary to evaluate the impacts of climate change and landuse change on the hydrologic regime in this river and develop adapted approaches for water resources management.

Studies by Price (2011), Voepel *et al.* (2011), Kelleher, Wagener, and McGlynn (2015), and Wang *et al.* (2018) indicate that variation in morphology and landuse type are bound to produce a totally varied hydrologic condition in areas with similar climatic conditions. Based on their findings, it can be hypothesized that morphology can mitigate or augment the influence of landuse changes on hydrology. This research characterizes the hydrologic response of agricultural landuse under various morphological conditions in order to determine areas within the Blyde and Steelpoort River Basins that produce minimal reactions to landuse changes.

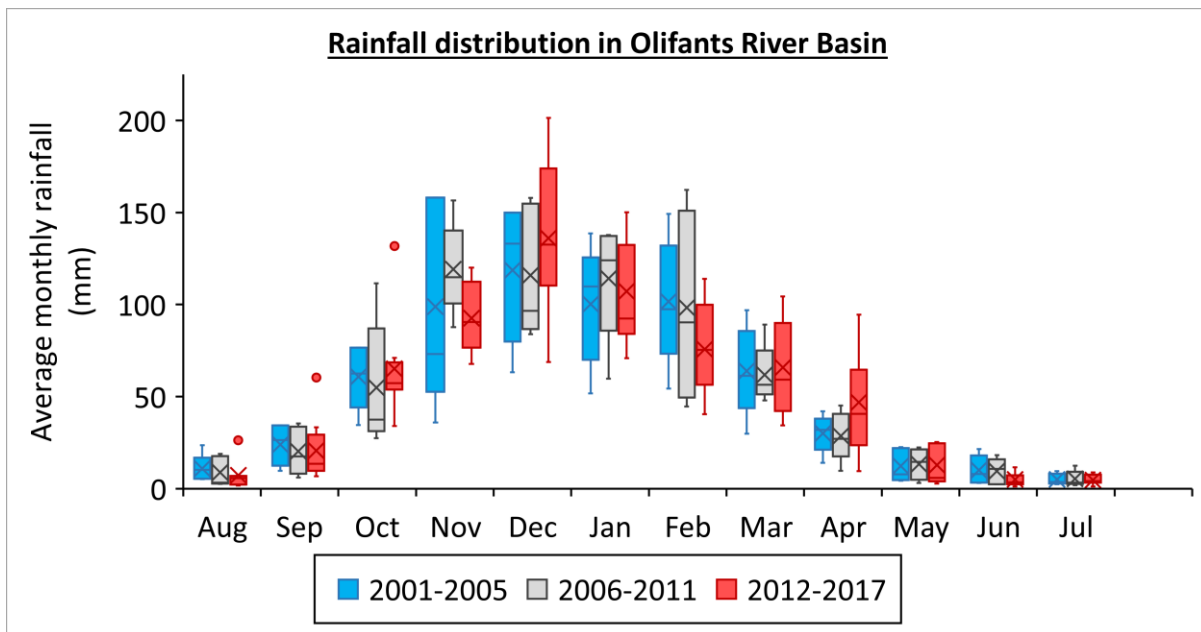


Figure 1-10: Seasonal distribution of rainfall in the Olifants River Basin

1.4 Research Questions and Objectives

Based on the water resources state in Blyde and Steelpoort rivers highlighted herein, this research seeks to answer the following questions:

- i. How are climate and LULC changing in Blyde and Steelpoort River Basins?
- ii. What are the impacts of climate change/variability and LULC change on hydrological partitioning?
- iii. Which morphological conditions are “hydrologically suitable” for agricultural area use?

Following the research questions identified, the objectives of this research are outlined as follows:

- i. To quantify LULC change and climate change patterns in Blyde and Steelpoort River Basins and analyze their impacts on hydrology?

- ii. Adapt the LULC planning approach to enhance mitigation of changes in hydrological regimes based on morphology-landuse-hydrology interactions
- iii. Identification of morphological parameters to consider in Environmental Impact Assessments (EIA) in Agricultural landuse planning projects.
- iv. Based on the findings of objective (i) and (ii) develop/map potential agricultural landuse expansion scenarios and its corresponding future hydrological scenarios

1.5 State of Art

Most water-related problems originate from landuse activities; hence water resources planning can only be holistic once integrated with landuse planning (Mitchell, 2005). The agricultural sector is considered a key player in Integrated Water Resource Management (IWRM) since it is one of the major consumers of water and influences water availability through the modification of physical characteristics of land (African Development Bank, 2000; Lange *et al.*, 2003; Food and Agriculture Organization, 2004; Mitchell, 2005).

Implementation of IWRM is gradually gaining momentum in South Africa (Claassen, 2013) through still faced with many challenges. Lange *et al.*, 2003, Claassen, 2013, and Jonker, 2014 highlight the status and advances of implementation of IRWM in South Africa based on legislation, institutional arrangements, and practices; in view of these collections of literature, discussions of IWRM in South Africa focus appears to be on water use and distribution with very little focus on land management practices. The agricultural sector is acknowledged in these studies as a key stakeholder with a focus on its water consumption with little or no mention of the impacts of agriculture on hydrology.

Reconciliation of landuse activities and water resources is addressed by the Department of Environmental Affairs through the Environmental Act of 1998 and its successive amendments, which clearly stipulates that natural resources should be harnessed/developed in an environmentally sustainable manner (Department of Environmental Affairs, 1998). Through this act introduces the use of Environmental Impact Assessment (EIA) as a tool for evaluating the impacts of projects on various aspects of the environment, social and economic systems, both negative and positive impacts have to be evaluated and mitigation measures for anticipated impacts proposed. The guidelines developed by the Department of Environmental Affairs, 2010 for conducting EIA enlists various stakeholders who are to provide their technical expertise in their areas of jurisdiction, including actors in the agricultural sector and water resources like the Department of Agriculture, Forests, and Fisheries (DAFF) and Department of Water and sanitation.

During discussions with senior DAFF staff as part data collection, an exercise in May 2019, it emerged that some farms established did not conduct EIA prior to their establishment, especially farms practicing subsistence agriculture; this situation translates to modification of land with little or no mitigation of adverse impacts on environmental aspects like hydrology. During this meeting, DAFF outlined the aspects that it evaluates in an EIA study assessing the impacts of agricultural development as follows:

- All agricultural land should be established on slopes under 20%
- Various methods are adopted to reduce surface runoff speed, like contour farming, ridges, mulching, and planting crops in rows that are perpendicular to the flow direction of surface runoff, as shown in Figure 1-11.

- Soil productivity and climate are also evaluated to assess the viability of the project



Figure 1-11: (Left) Trenches and ridges on a farm and (right) farms are perpendicular to river flow in Olifants River basin (Source: Photograph taken during field survey)

Other aspects of the EIA forbids the development of agriculture in protected areas like forests, game reserves, and wetlands. The meeting at DAFF reveals that the only morphological aspect of the river basin in consideration is the slope and soil. However, there are other important morphological factors that are responsible for water partitioning, like surface roughness, terrain characteristics, groundwater-surface water interactions that are not considered in these assessments. As highlighted by Price, 2011, morphology can amplify or mitigate the impacts of landuse change on hydrology.

According to Price (2011), Voepel *et al.* (2011), Kelleher *et al.* (2015), and Wang *et al.* (2018), the morphology of the river basin can mitigate or amplify the impacts of landuse changes on hydrology. Therefore, more morphological factors in EIA studies may help improve the analysis of hydrological impacts resulting from agriculture and subsequently aide in better site identification.

Despite these measures put across, research carried out by Gyamfi *et al.*, 2016 indicates that agricultural development still produces significant shifts in hydrological flows. Based on the background given herein, these changes may be attributed to the haphazard agricultural development that has no mitigation measures or insufficient mitigation measures in place. Allocation of “hydrologically suitable” agricultural land prior to development could provide a solution for mitigating changes in hydrological regimes that are fueled by unauthorized developments; this can be achieved by conducting a basin-wide evaluating various agricultural.

This research quantifies hydrological characteristics of agricultural areas under various morphologies at a basin-wide scale in the river basin in order to identify conditions that limit changes in hydrological regimes. The initial output of the work is then utilized in adapting the landuse planning approach to mitigate changes in hydrological regimes. The outcome of this research will provide a basin-wide scenario that can be referenced in EIAs, therefore, providing an overview of a long-term plan and limiting the need for recurrent assessments in long-term reference. The outputs also include quantifiable hydrological components that can also be directly referenced in the EIAs.

This research proposes an innovative idea for landuse planning for enhanced conservation of hydrological regimes in Blyde and Steelpoort; this will be achieved by evaluating morphology-landuse-hydrology interactions in order

to identify landuse classes that can be replaced by agriculture and morphological conditions under which agricultural land can be established with minimal hydrological impacts.

Assumptions made in this study are that all crops in the river basin exhibit similar hydrological characteristics and have the same growing and maturity seasons; water uptake, evapotranspiration, and surface cover. In the establishment/expansion of farms in South Africa, several aspects like productivity potential, climate, water availability, and soil conditions are also considered. However, the scope of the current research is hydrological aspects, especially mitigation of hydrological changes resulting from agricultural activities.

1.6 Description of the study area

The Blyde and Steelpoort River Basins are located in the mid-southern section of the Olifants River Basin, as shown in Figure 1-2. The rivers rise from northern areas of Mpumalanga Province at an elevation of about 2,300 masl and flow into the Main Olifants River in Limpopo Province. Terrain analysis of the ALOS Digital Elevation Model (DEM) indicates that both rivers drain an area of approximately 10,000 km²; Blyde River Basin spans over 2,800 km² with a drainage length of 125km, whereas Steelpoort spans over 7,200 km² having a drainage length of 230 km.

The study area has an elevation ranging between 370 and 2,300 masl. Mean annual rainfall in the study area ranges from 640 mm at lower elevations to 850 mm at higher elevations. Precipitation is seasonal and mainly occurs in Spring (September – November), Summer (December – February), and Fall (March – May). The highest rainfall occurs in Summer months, as indicated in Figure 1-9. Precipitation is controlled by air mass fluxes associated with the Iter-Tropical Convergence Zone (ITCZ), where high land temperature induces low pressure causing an inflow of moist, maritime air from the Indian Ocean. In winter, the sun moves north towards Tropic of Cancer, creating high-pressure zones in the southern hemisphere and causing hence reducing the inflow of moist air masses (McCartney, 2003). The approximate mean annual runoff of Blyde River is 9 m³/s, while that of Steelpoort is seven m³/s.

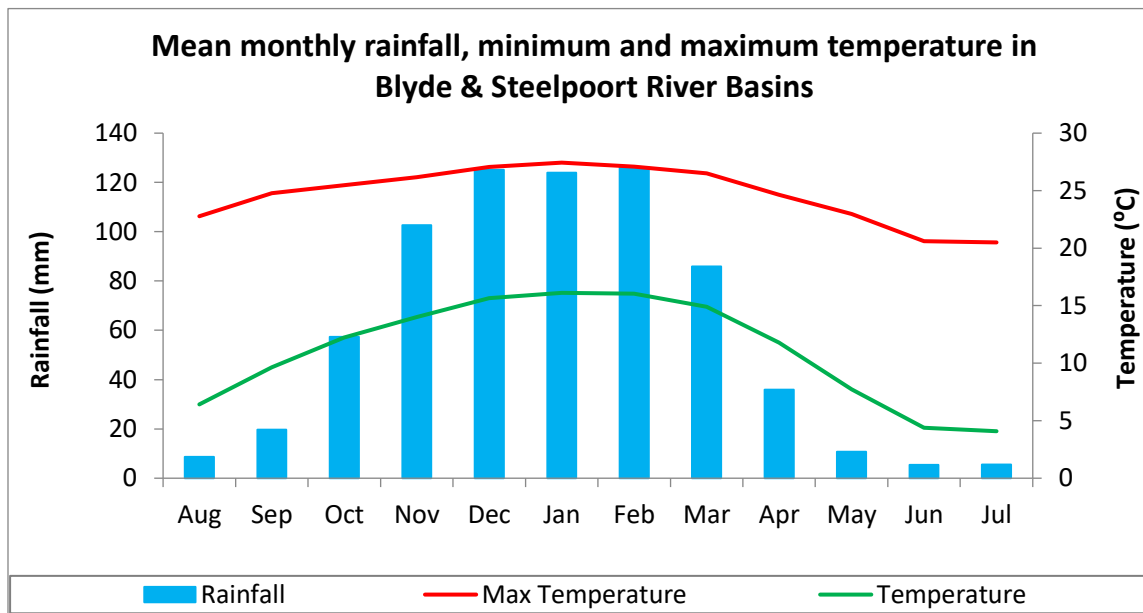


Figure 1-12: Distribution of rainfall, minimum and maximum temperatures for the study area (Date source: CRU TS 4.0)

Though the river basin receives relatively high rainfall in comparison to many basins in the country, water scarcity is still a persistent problem; According to Turton, 2015, annual water demand in Olifants River was estimated by the National Water Strategy of 2004 to be 1,075 million m³ which exceeded annual availability of 840 million m³. According to McCartney and Arranz (2007), power generation, Irrigation, Forestry, domestic/industrial, and mining sectors are the major water users in the two basins.

The Steelpoort and Blyde River Basins have complex groundwater system are defined by varied geological conditions. The geology is composed of various forms of sedimentary rocks, intrusive rocks, effusive rocks, and alluvium, as shown in Figure 1-12. The geological structure and composition of these sub-basins form different types of aquifers; fractured aquifers, intra-granular aquifer, karst aquifers, and a combination of fractured and inter-granular aquifers.

The Olifants river contributes 5% of the national Gross Domestic Product (GDP) through a vast range of economic activities like mining, agriculture, hydropower generation, tourism, and manufacturing (Basson *et al.*, 2003). Within the Steelpoort and Blyde River Basins, there are over 90 mines and 19,000 km² of land under agriculture. The river basins have an approximate population of about 3 million persons, with the urban centres having a higher population in comparison to the population in rural areas (Crafford *et al.*, 2011)

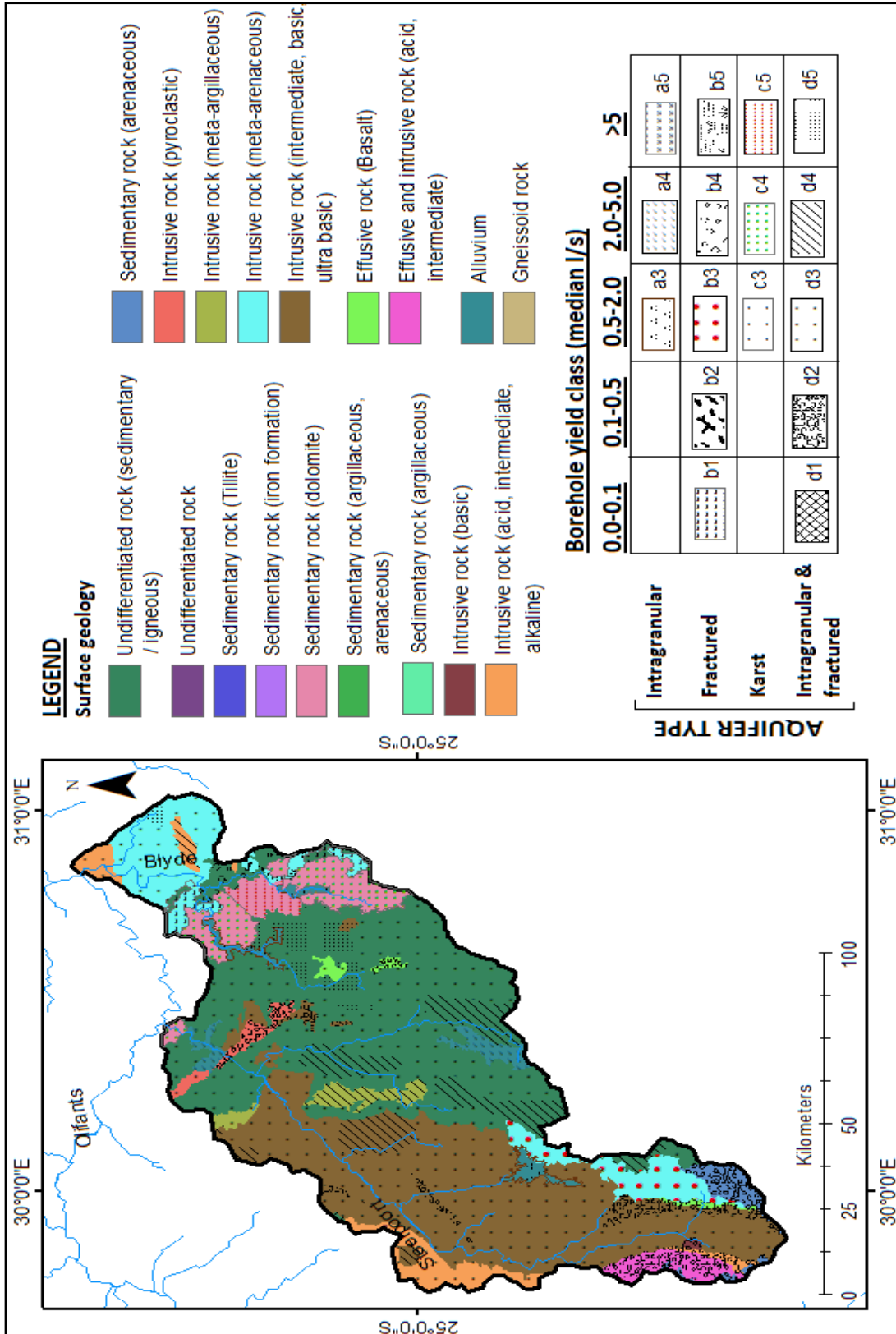


Figure 1-13: Geological map of Steelpoort and Blyde River Basins (Du Tioit and Sommekus, 2014; Du Tioit et al., 2014; Toit and Sommekus, 2014)

2 CLIMATE CHANGE AND ITS IMPACTS ON HYDROLOGY

2.1 Background

Climate change refers to an alteration in the normal weather conditions at a particular place over an extended period of time; these changes can be detected in the variability of mean values of climate parameters (UNFCCC, 2011). According to Department for Business Energy & Industrial Strategy, 2014, EPA, 2016, IPCC, 2014, climate change results from changes in global energy balance resulting from both natural and human **influences** (UN CC: Learn, 2015). The global energy balance is influenced by variations in the sun's energy reaching earth, changes in the reflectivity of earth's atmosphere and surface and changes in the greenhouse (GHG) effect, which affects the amount of heat retained by earth's atmosphere (EPA, 2016). Climate changes prior to the Industrial Revolution in the 1700s can be explained by natural causes, whereas human factors in the post-industrialization are attributed to the recent climate changes, as shown in Figure 2-1.

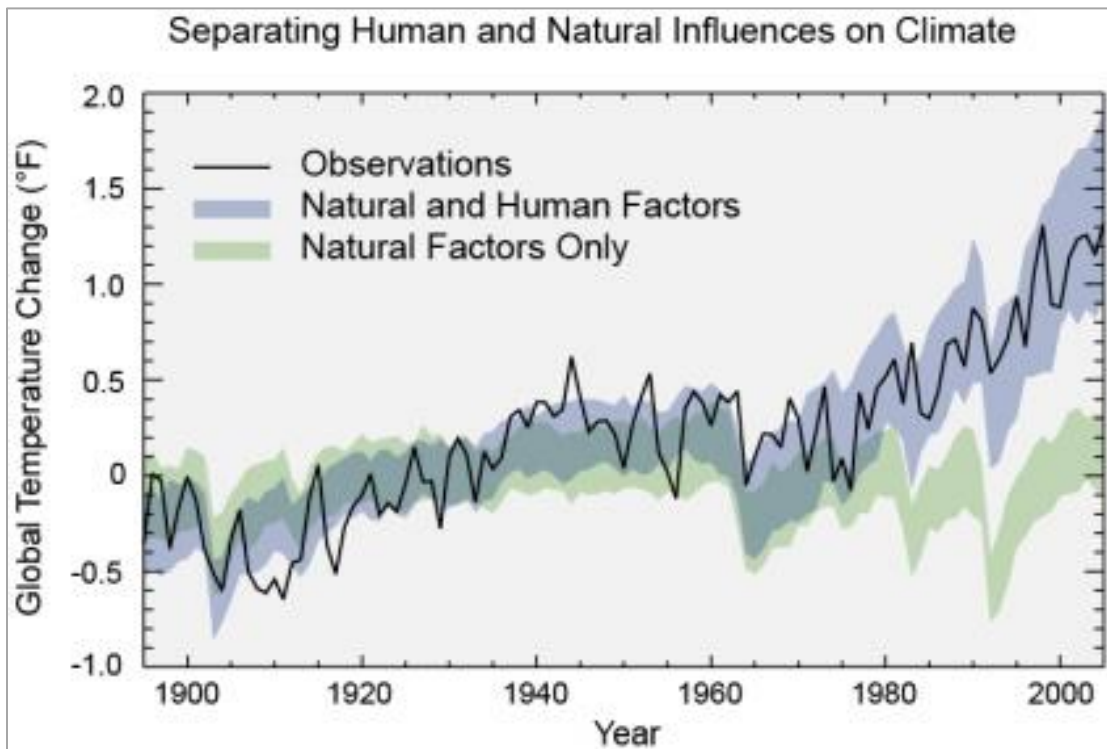


Figure 2-1: Global temperature trends due to natural and human influences

Climate change has devastating consequences on various sectors, including water resources (UN, 2018). Therefore, analysis of both spatial and temporal trends can provide information on the magnitudes of these impacts and how best to manage them. The objective of this chapter is to analyze climatic (temperature and precipitation) time series and assess its contributions to hydrological patterns and variability.

In this research, three categories of statistical tests were carried out on temperature, rainfall, and streamflow for a period of 37 years from 1980 to 2016, as described in the following section. Streamflow was tested for a period of only 30 years based on data availability of naturalized flow.

2.2 Data acquisition and pre-processing

Temperature and precipitation: Precipitation, daily average minimum temperature, and daily average maximum temperature data were acquired from the University of East Anglia Climate Research Unit (CRU TS version 4.0) under the following link; https://crudata.uea.ac.uk/cru/data/hrg/cru_ts_4.00/. The CRU TS v4.0 data was preferred since observed data from South African Weather Services (SAWS) is considered insufficient for the analysis; observed data has large data gaps at most stations, and only two stations at the headwaters are located within the basin. CRU TS v4.0 data is in gridded format and is constructed from monthly observations from various meteorological stations around the world at a spatial resolution of 0.5° latitude/longitude grid cells (Harris et al., 2014).

CRU data has successfully been applied in hydrological analysis and simulations in different regions in the world with a good outcome. Examples of these studies include Vasel *et al.* (2015) and Eini, Javadi and Delavar, (2018), who successfully modelled basins in Iran and demonstrated that the data performed comparatively well to measured data. Abbaspour *et al.* (2015) uses CRU in hydrological simulations of 29 river basins and indicates minimal biases in the data.

Time series of these data were then extracted from mid-locations (demoted by CRU met stations) of each CRU TS v4.0 grid cell, as shown in Figure 2-2. Daily precipitation data, daily maximum temperature, and daily minimum temperature are generated from monthly precipitation, number of wet days, and maximum and minimum temperature data from the Climatic Research Unit (CRU) using Monthly to Daily Weather Converter (MODAWEC) developed by Liu *et al.* (2008).

Figure 2-3 shows the performance of CRU data in relation to the observed data from South Africa Weather Services (SAWS) at two different stations; the performance is above average at Belfast Met station, and very good at Hoedspruit Met Station. The location of Belfast and Hoedspruit Met Stations are indicated in Figure 2-2.

CLIMATE CHANGE AND ITS IMPACTS ON HYDROLOGY

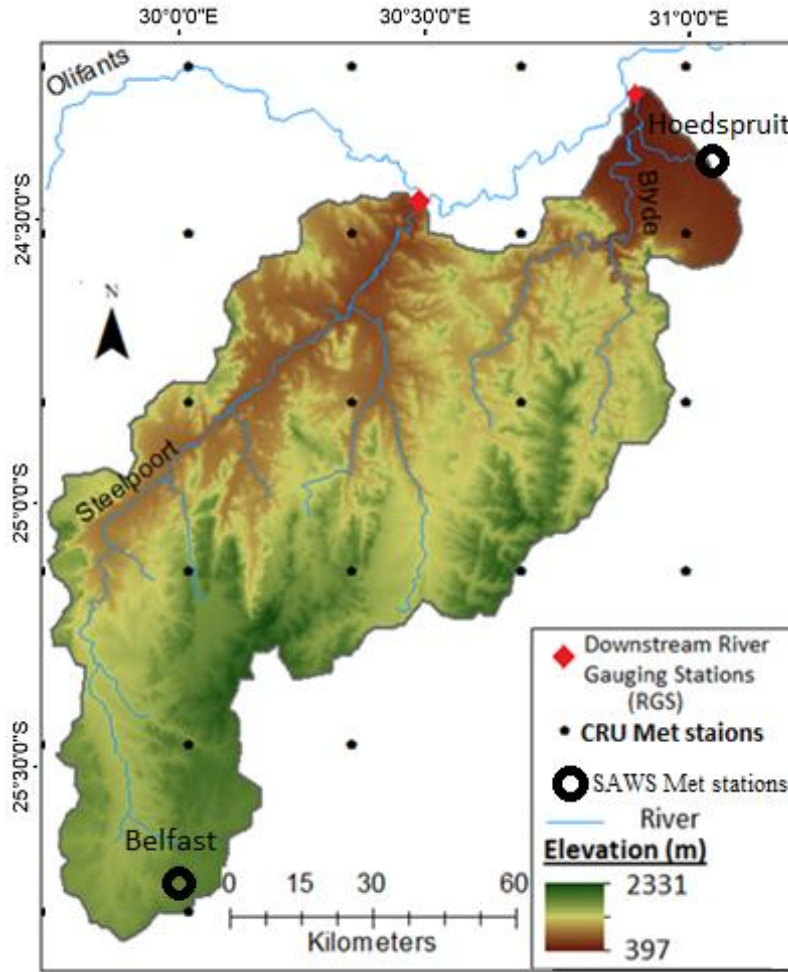


Figure 2-2: Data point locations from CRU TS

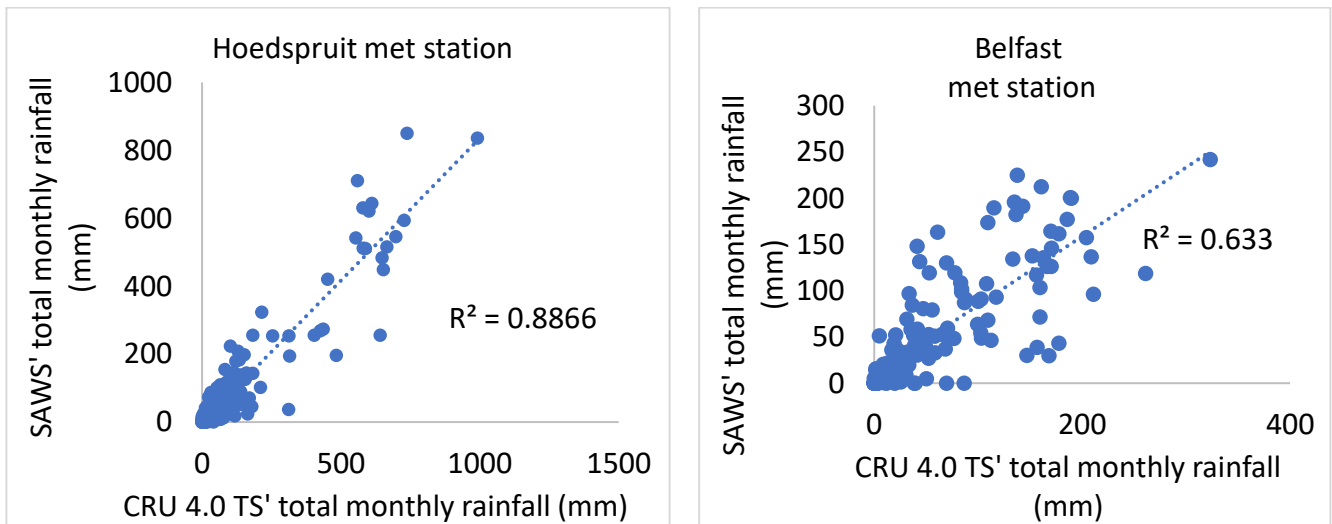


Figure 2-3: correlation between CRU 4.0 TS rainfall and observed rainfall from SAWS

Streamflow: Naturalized streamflow data were utilized in this stage of analysis in order to remove the effects of human influence and hydraulic structures. The data was obtained from South Africa's Water Research Commission (Bailey, 2012). The data is at a daily time step and has been extracted for the period beginning 1980 until 2009.

2.3 Hydro-climatic change: detection and attributions

Change detection and attributions play a significant role in assessing variation patterns in climatic parameters and their impacts on various hydrological parameters (Schipper, 2017). Change in time series occurs in various ways, for example, gradual change (trend), abrupt change (inhomogeneity), or in other complex forms leading to a shift in mean, variance, median, or any other aspect of the time series (Kundzewicz and Robson, 2004). In this research, the tests for abrupt changes, progressive change, and seasonal shifts are conducted.

In order to test the hydro-climatic time series for changes, two hypotheses are put into consideration; **null hypothesis** (H_0), which means that there is no change in the statistical properties of the data, and the **alternative hypothesis** (H_1), which means that there exist changes in the time series. In the first step, an assumption is made that the null hypothesis is true and then checks whether the observed data are consistent with this hypothesis. The null hypothesis is rejected if the data are not consistent. When the null hypothesis is rejected, a significance test is carried out to express the probability that the null hypothesis is incorrectly rejected. This involves checking whether the test statistic is very different from the range of values that would typically occur under the null hypothesis (Kundzewicz *et al.*, 2004). The significance test is expressed by p-value, which ranges between 0 and 1; p-value ≤ 0.05 provides strong evidence that for accepting alternative hypothesis, as the p-value becomes larger, evidence of alternative hypothesis becomes weaker (Ramsey, 2016).

2.3.1 Homogeneity Test

Homogeneity implies that the mean of a given time series does not change with time. Therefore tests carried out to check homogeneity involve analyzing the mean for any significant abrupt shifts or breaks in a time series (Adeloye and Montaseri, 2002). Various methods, like Pettitt's Test, Buishand's Test, T-test, Maximum Likelihood Test, and binary segmentation algorithms, have been adopted inhomogeneity test. In this research, the binary segmentation method is adopted because of its capability to detect multiple changepoints.

Binary segmentation iteratively applies the single change-point detection procedure on the entire time series, i.e., if a changepoint is detected, the data is split into two segments at the changepoint location. The single changepoint procedure is then repeated on the two new time series segments; this procedure continues until no further changepoints are found in any segments of the time series. The single changepoint is readily formulated under an alternative hypothesis, and hence if a change is detected, there are no tests for the p-value or significance level required (Killick and Eckley, 2014). The same procedure is also described by (Raveendran and Sofronov, 2017). The binary segmentation process is as depicted in Figure 2-4. The test statistic is constructed using the Likelihood Ratio (LR) test to calculate the maximum log-likelihood (ML) under alternative hypotheses. For a given an ordered data sequence $y_{1:n} = (y_1, \dots, y_n)$, a single changepoint occurs at T_1 , where $T_1 \in \{1, 2, \dots, n-1\}$, the maximum log likelihood at T_1 is computed as follows:

$$ML(T_1) = \log p(y_{1:T_1} | \hat{\theta}_1) + \log p(y_{(T_1+1):n} | \hat{\theta}_2) \quad (2.1)$$

Where $p(\cdot)$ is the probability density function of the time series and $\hat{\theta}$ is the maximum likelihood estimate of the parameters.

To detect the changepoint location in the time series, the maximum value of the maximum log-likelihood $\max_{T_1} ML_{T_1}$ is selected. The test statistic is computed as follows:

$$\lambda = 2[\max_{T_1} ML_{T_1} - \log p(y_{(y_{1:n})} | \hat{\theta})] \quad (2.2)$$

A threshold β is chosen, such that the null hypothesis is rejected when $\lambda > \beta$.

For a time series with multiple changepoints m , having changepoints positions $T_{1:m} = (T_1, \dots, T_m)$ with $T \in \{1, 2, \dots, n - 1\}$, the changepoints m will split data into $m + 1$ segments with the i^{th} segment containing data $y_{(T_{i-1}+1):T_i}$. When the method is extended to the detection of multiple changepoints, a search algorithm is used to identify the maximum of $ML_{T_{1:m}}$. The search algorithm used to detect the changepoints is given by the following the test statistic:

$$\sum_{i=1}^{m+1} [C(y_{(T_{i-1}+1):T_i})] + \beta f(m) \quad (2.3)$$

Where C is loss function for a segment, and $\beta f(m)$ is a threshold to check against overfitting. The significance test is not required with the binary segmentation method since the formulation is already under the alternative hypothesis.

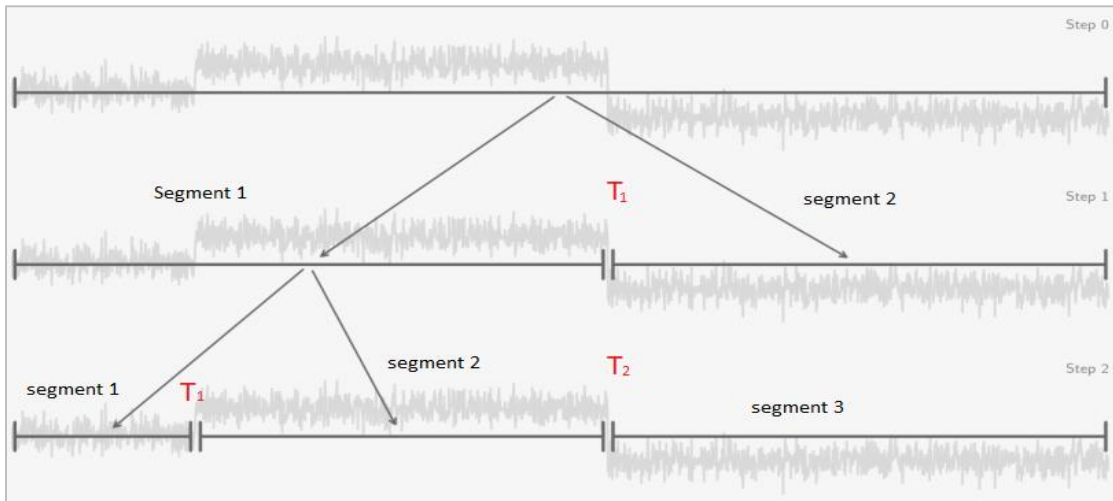


Figure 2-4: Illustration of changepoint detection using a binary segmentation algorithm

A multiple changepoint search algorithm developed by Killick *et al.*, 2014 based on the binary segmentation procedure described herein is adopted for this study.

A statistical test is first carried out on rainfall, discharge, temperature, and evapotranspiration to detect the existence of abrupt changes in the time series. The resultant changepoints are then compared to detect if there exist matching patterns in the timing of changes in other hydro-climatic parameters; rainfall is compared with discharge and temperature compared with evapotranspiration. A limit of two changepoints for rainfall and

discharge was chosen based on the presence of two adjacent peaks that are distinctly higher than the rest (in 1996 and 2000), as shown in Figure 2-5.

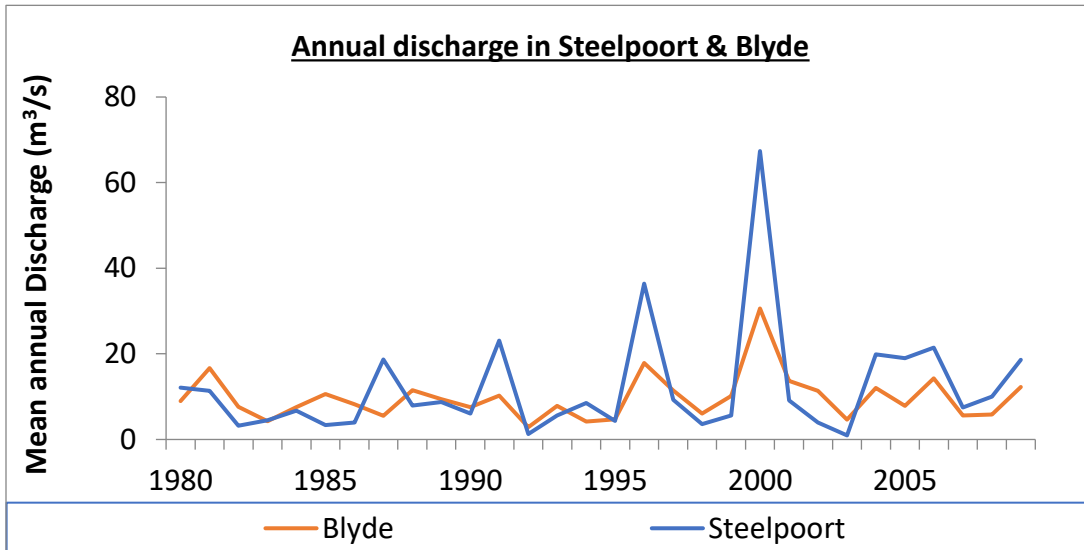


Figure 2-5: Average annual discharge in Blyde and Steelpoort

In the second step, if the rainfall time series is confirmed to have abrupt changes, further statistical analysis is carried out in order to determine to establish precipitation characteristics that are associated with the abrupt breaks. Two categories of tests are conducted on each identified segment in order to determine the percentage of **the number of wet days** and percentage of **extreme rainfall events** based on the rainfall frequency distribution: Rainfall distribution is conducted according to training module developed by DHV CONSULTANTS BV & DELFT HYDRAULICS, 2002 on analysis of rainfall data. Computation of the number of wet days and extreme rainfall are conducted for each rainfall station in order to check for any spatial variations in rainfall. The number of wet days is formulated as follows:

$$\% \text{ number of wet days} = \frac{\text{Number of days with rainfall} > 0 \text{ mm}}{\text{Total number of days in period}} * 100\% \quad (2.4)$$

2.3.1.1 Results: Changepoint Analysis

Figure 2-6 shows the plots for mean annual discharge for both Blyde and Steelpoort Rivers. In both cases, two change points are detected in 1996 and 2002, dividing the time series into three segments (1980-1995, 1996-2002, and 2003-2016). The source of these abrupt changes can be attributed to rainfall patterns, where the frequency of extreme rainfall events and the mean annual rainfall in the period 1996-2002 is much higher in comparison to the earlier period and later period; the variations in mean values are shown in Table 2-1 and the frequency distribution of rainfall shown in Figure 2-7.

Table 2-2 shows changepoint locations in relation to the percentage of wet days within the period depicted by the segment. The number of wet days in all the stations during the central (1996-2002) period is slightly lower those of the outer segments (1980-1555 and 2003-2016); therefore, this can not describe the increase in annual rainfall between 1996 and 2002 as shown in Figure 2.6.

Table 2-3 shows changepoint locations in relation to the percentage of extreme rainfall events (> 40mm/day). The percentage of extreme rainfall events in all the stations during the central (1996-2002) period is comparatively higher than those of the outer segments (1980-1995 and 2003-2016); Increase in annual rainfall between 1996-2002 as shown in Figure 2-6 can be attributed to the higher percentage of extreme rainfall events

According to Figure 2-8, abrupt changes are detected in 2003, where the mean temperature shifted from 17.21 to 17.84 in Blyde River Basin and from 17.02 to 17.64 in Steelpoort. However, these changes in temperature did not influence evapotranspiration at all since no changepoints are detected in both basins.

Though temperature controls the water balance through evapotranspiration processes, the influence of temperature increase is not detected in discharge. In conclusion, the shift in discharge patterns can only be attributed to the shift in rainfall patterns.

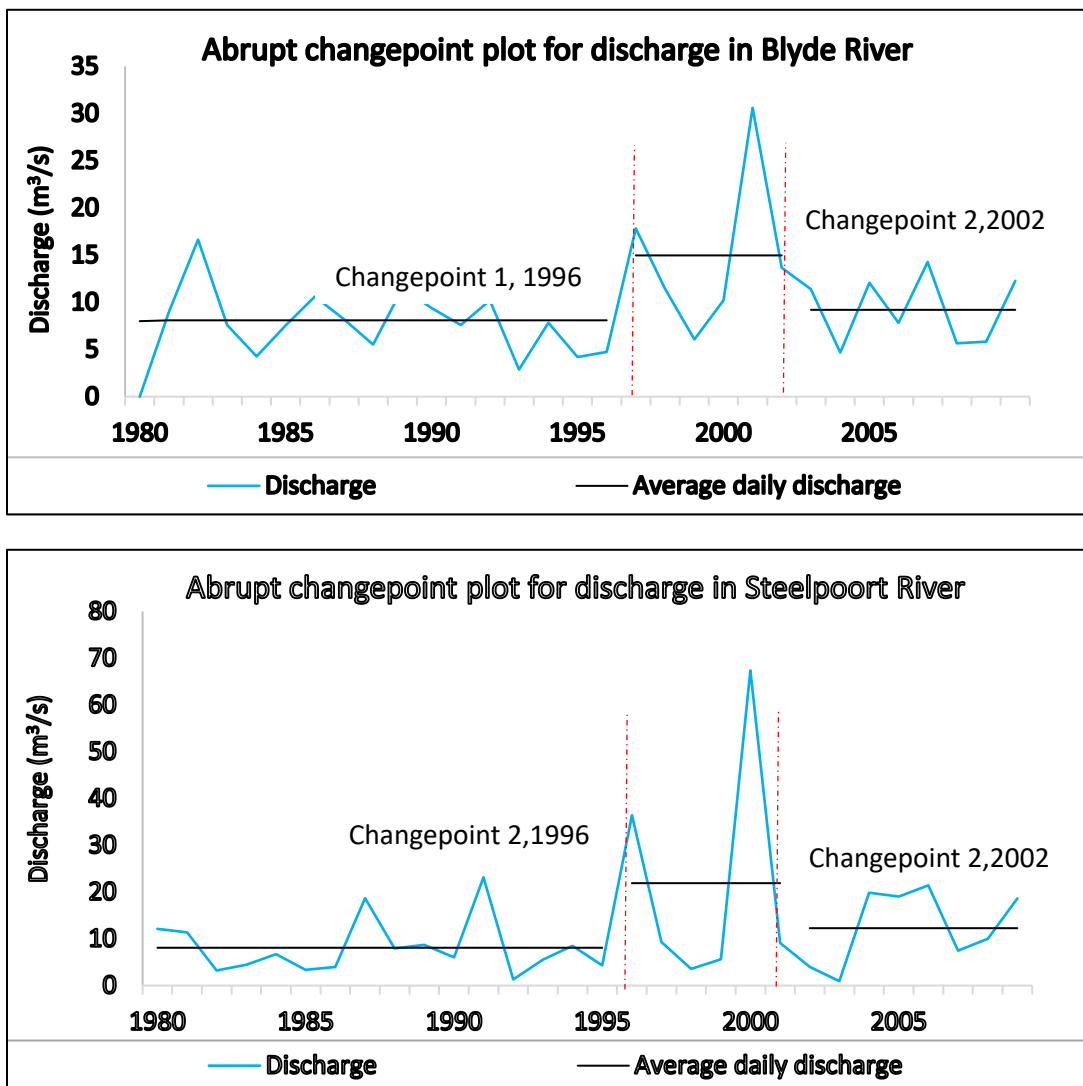


Figure 2-6: Abrupt changes in discharge in Blyde and Steelpoort Rivers; (black line shows the mean values for each segment)

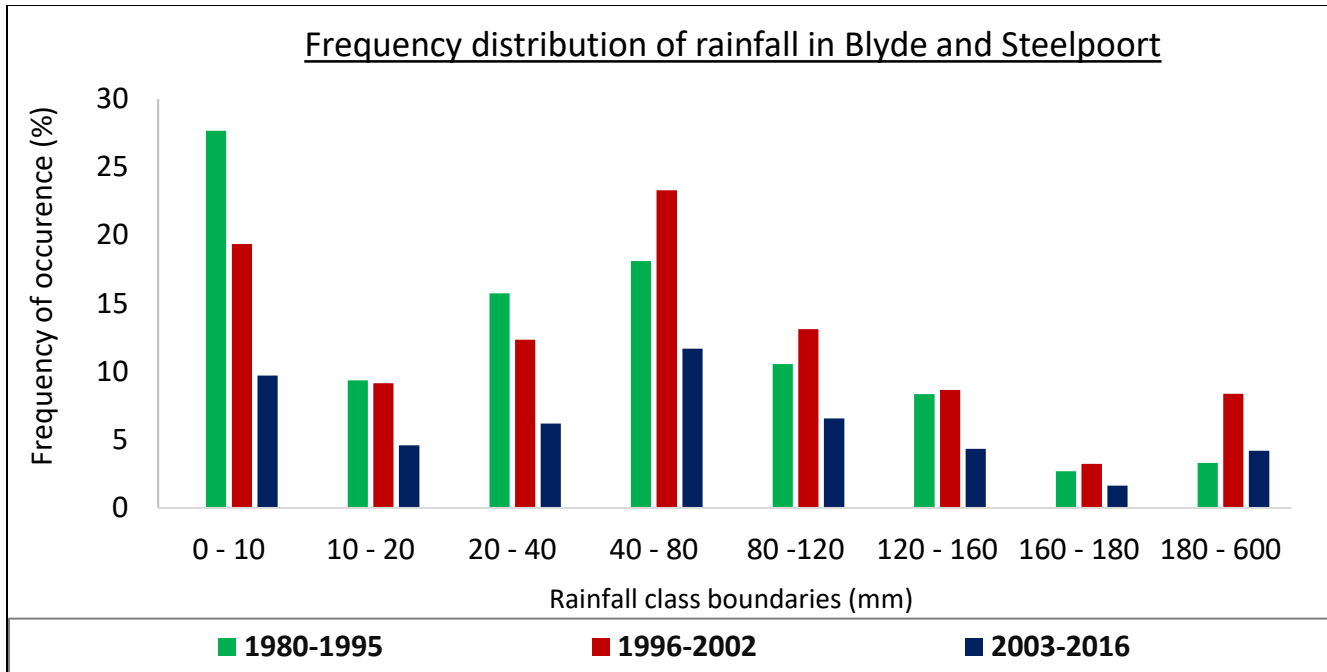


Figure 2-7: Frequency distribution of rainfall in Blyde and Steelpoort River Basins based on segments of abrupt changes

Table 2-1: Summary of changepoints in rainfall and discharge Blyde and Steelpoort

Parameter	Sub-basin	Changepoint locations	Mean values for each segment		
			1980-1995	1996-2002	2003-2016
Rainfall (mm)	Blyde	1995, 2002	136	150	117
	Steelpoort	1995, 2002	8	22	12
Discharge (m ³ /s)	Blyde	1995, 2002	8	15	9
	Steelpoort	1995, 2002	120	137	104

CLIMATE CHANGE AND ITS IMPACTS ON HYDROLOGY

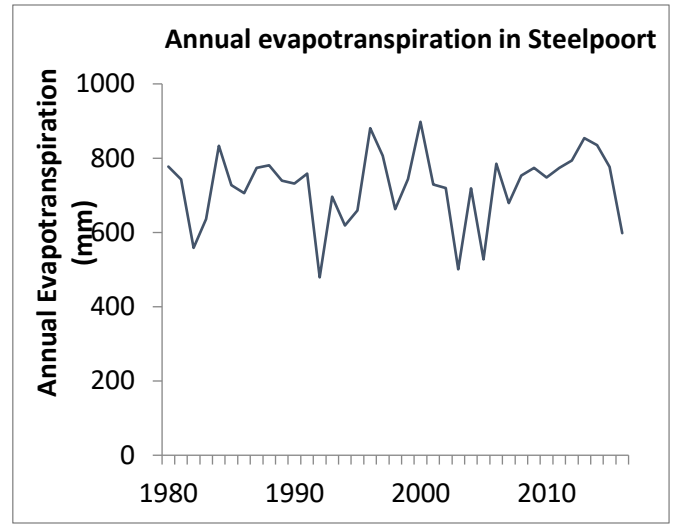
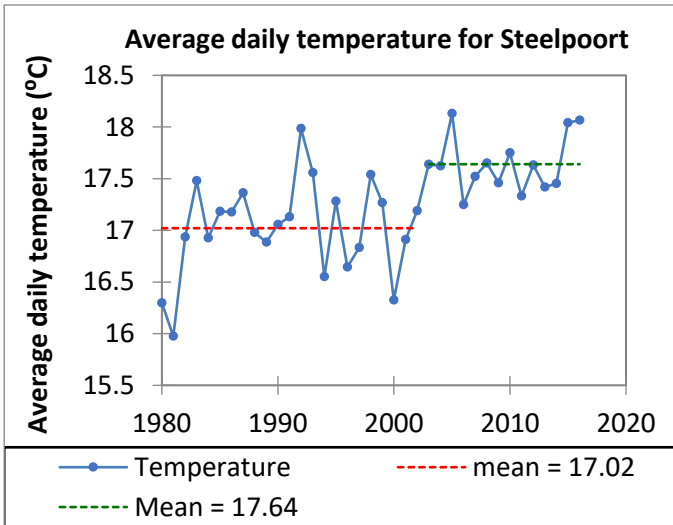
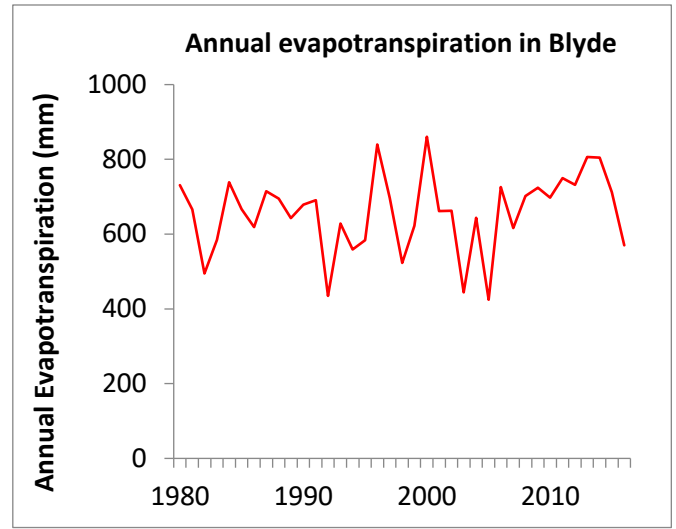
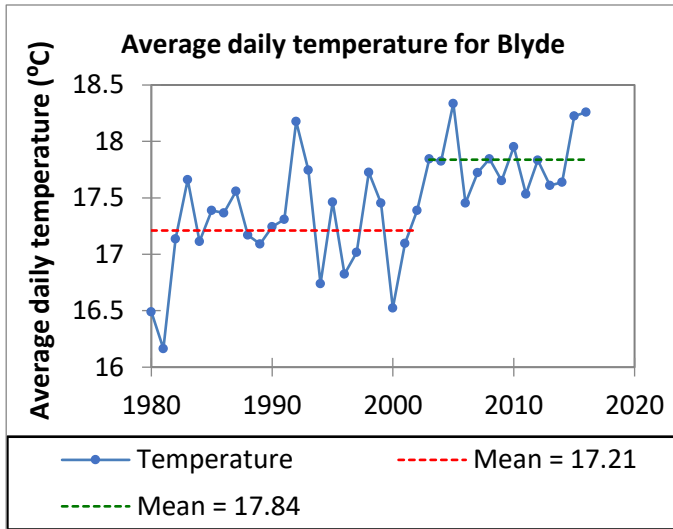


Figure 2-8: Abrupt shift in temperature and evapotranspiration

CLIMATE CHANGE AND ITS IMPACTS ON HYDROLOGY

Table 2-2: Rainfall changepoint locations in relation to the number of wet days

Station	Sub-basin	Changepoint 1		Changepoint 2		% number of wet days		
		year	% change in mean	year	% change in mean	1980-1995	1996-2002	2003-2016
P-248303	Blyde	1995	28	2002	-24	21	19	21
P-251303	Blyde	1995	35	2002	-27	25	22	25
P-254297	Blyde	1995	19	2002	-20	22	20	22
P-254300	Blyde	1995	35	2002	-27	24	23	23
P-254303	Blyde	1995	35	2002	-27	24	23	23
P-242309	Blyde	1995	32	2002	-26	18	17	18
P-245306	Blyde	1995	30	2002	-26	24	22	24
P-248306	Blyde	1995	30	2002	-26	24	22	24
P-245303	Steelpoort	1995	28	2002	-24	24	22	24
P-245309	Steelpoort	1995	30	2002	-26	21	19	21
P-248300	Steelpoort	1995	28	2002	-24	24	22	24
P-251300	Steelpoort	1995	35	2002	-27	21	19	21
P-251306	Steelpoort	1995	35	2002	-27	24	23	23

CLIMATE CHANGE AND ITS IMPACTS ON HYDROLOGY

Table 2-3: Changepoint locations in relation to the percentage of extreme rainfall events (> 40mm/day)

Station	Sub-basin	Changepoint 1.		Changepoint 2		Extreme events (% of the time)		
		year	% change in mean	year	% change in mean	1980-1995	1996-2002	2003-2016
P-248303	Blyde	1995	28	2002	-24	1	8	1
P-251303	Blyde	1995	35	2002	-27	2	13	2
P-254297	Blyde	1995	19	2002	-20	2	9	2
P-254300	Blyde	1995	35	2002	-27	2	10	3
P-254303	Blyde	1995	35	2002	-27	2	10	3
P-242309	Blyde	1995	32	2002	-26	2	9	2
P-245306	Blyde	1995	30	2002	-26	2	9	2
P-248306	Blyde	1995	30	2002	-26	2	9	2
P-245303	Steelpoort	1995	28	2002	-24	2	5	3
P-245309	Steelpoort	1995	30	2002	-26	2	9	2
P-248300	Steelpoort	1995	28	2002	-24	1	8	1
P-251300	Steelpoort	1995	35	2002	-27	2	10	3
P-251306	Steelpoort	1995	35	2002	-27	2	10	2
P-258300	Steelpoort	1995	30	2002	-26	2	13	2

2.3.2 Trend

Time series is said to have a trend when the observations/data change with time; the change can be in downwards or upwards direction and expressed using a linear or a non-linear model (Machiwal and Jha, 2012). There are various methods for testing the presence of a trend in time series, for example, Linear Regression, Mann-Kendall Test, Sum of First derivatives, LOESS, and Likelihood Ration Test (Gray, 2007). Mann-Kendall Test is adopted in this research to test annual and seasonal trends in rainfall, temperature, and discharge; this test analyzes the sign of the difference between later-measured data and earlier-measured data. Each value measured later is compared to all values measured earlier, resulting in a total of $n \left(\frac{n-1}{2} \right)$ possible pairs of data, where n is the total number of observations. Mann-Kendall Test statistic is given by:

$$S = \sum_{i=1}^{n-1} \sum_{j=i+1}^n \text{sign}(y_j - y_i) \quad (2.5)$$

Where $y \in \{1, 2, \dots, n\}$, $\text{sign}(y_j - y_i) < 0$ implies a downward trend, $\text{sign}(y_j - y_i) = 0$ implies no trend and $\text{sign}(y_j - y_i) > 0$ implies an upward trend. The null hypothesis (H_0) of no trend is rejected when S is significantly different from zero (Meals *et al.*, 2011). Trend is considered statistically significant when the absolute value of Z is above a given critical value Z (Meals *et al.*, 2011). Mann-Kendall test is the test statistic Z is given by:

$$Z = \begin{cases} \frac{S - 1}{\sqrt{\text{VAR}(S)}} & \text{if } S > 0 \\ 0 & \text{if } S = 0 \\ \frac{S + 1}{\sqrt{\text{VAR}(S)}} & \text{if } S < 0 \end{cases} \quad (2.6)$$

Where $\sqrt{\text{VAR}(S)}$ is the variance of S . According to Helsel and Hirsch (1992), if a significant trend is found, the rate of change can be calculated using the Sen's slope estimator; this is achieved by computing the median of slopes of all pairs of data used to compute S . For data with time Where $T \in \{1, 2, \dots, n\}$, Sen's Slope is given by:

$$\beta_1 = \text{median} \left(\frac{y_j - y_i}{T_j - T_i} \right) \quad (2.7)$$

Another statistic that is computed under the Mann-Kendall test is the test statistic Tau (τ), which measures the strength of the monotonic trend (Fathian *et al.*, 2016). is given by:

$$\tau = \frac{S}{\left(\frac{n(n-1)}{2} \right)} \quad (2.8)$$

Kendall's Tau (τ) has a range of -1 to $+1$ and is analogous to the correlation coefficient in regression analysis. The null hypothesis of no trend is rejected when S and τ are significantly different from zero

Both Seasonal and annual trend test is conducted on Rainfall, discharge, and temperature time series. The seasons are divided into four; autumn (March-May), winter (June –August), spring (September- November), and summer (December –February).

Mann-Kendall Trend Test was conducted using XLSTAT tool by Addinsoft (2019)

2.3.2.1 Results: Trend analysis

Figure 2-9 shows the outcome of the annual trend tests for rainfall, discharge, and temperature; there is a significant downward trend in rainfall in both Steelpoort and Blyde River Basins. Annual discharge, on the other hand, has an increasing trend. However, the trend from the Blyde River is not significant, as indicated by the p-value ≥ 0.2 . Based on the annual trend results, downward rainfall trends cannot be directly linked to the increasing discharge trends. Temperature shows an increasing annual trend with high significance indicated by the p-value of 0.05 for Blyde and 0.01 for Steelpoort; these changes cannot also be attributed to any pattern of change in river discharge.

In the summer season (December to February), the discharge has positive Mann Kendall Tau values. However, only Blyde River has a trend, though very marginal, as indicated by the p-value = 0.3. Steelpoort River has no trend in this season. Rainfall has a marginal downward trend, whereas temperature has a positive or upward trend. We concluded that in this season, the changes detected in the discharge of Blyde River could be attributed to neither temperature trends nor rainfall patterns

In the fall season (March to May), only Steelpoort River exhibits a positive trend, though weak. For both rivers, rainfall has positive Mann Kendall's Tau. However, the trend is present in only the Blyde River and absent in the Steelpoort River. Temperature exhibits upward trends in both river basins within this season. The trends detected in the discharge of the Steelpoort River cannot be explained by the lack of trend in rainfall and increasing temperature trends. Likewise, the rainfall trend detected in the Blyde River did not influence discharge trends of the river.

In the winter season (June to August), the Blyde River has a negative trend, whereas Steelpoort has a positive trend. Rainfall has a negative trend in the Steelpoort River Basin and no trend in Blyde River Basin. Temperature exhibits positive trends in both river basins in the winter season. The negative trend in discharge in Blyde river basin cannot be attributed to rainfall patterns, which had no trend. Increase in temperature may lead to an increase in water losses through evapotranspiration and may therefore be attributed to decreasing trend discharge of Blyde River. The positive trend in the Steelpoort river basin can be explained by neither temperature nor rainfall trends.

In spring (August – November), both Blyde and Steelpoort Rivers had negative Mann Kendall's Tau values. However, no trends were detected in rainfall based on the high p-values, whereas temperature had positive trends in both river basins. Discharge trends in this season cannot also be explained by the lack of trend in rainfall and increasing temperature trends.

Graphical representation of various seasonal trends of temperature, rainfall, and discharge are in Appendix I.

QUANTIFICATION OF LULC CHANGE AND ITS IMPACTS ON HYDROLOGY

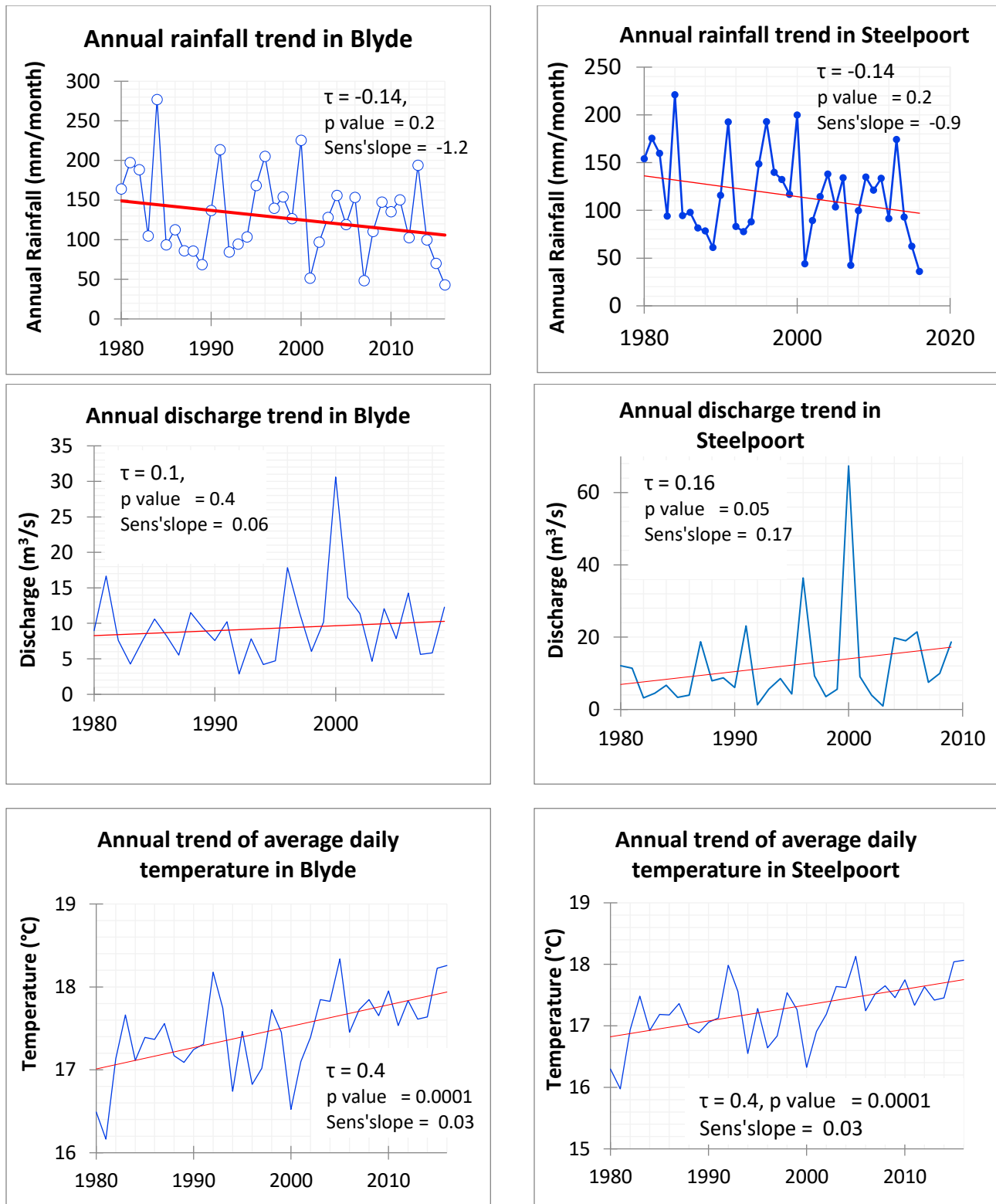


Figure 2-9: Trend of rainfall, discharge, and temperature in Blyde and Steelpoort River Basins

QUANTIFICATION OF LULC CHANGE AND ITS IMPACTS ON HYDROLOGY

Table 2-4: Summary of trend parameters for rainfall, discharge, and temperature in Blyde and Steelpoort

Season	Parameter	Temperature		Discharge		Rainfall	
		Blyde	Steelpoort	Blyde	Steelpoort	Blyde	Steelpoort
Annual	Tau (τ)	0.04	0.40	0.10	0.16	-0.14	-0.14
	P-value	< 0.05	< 0.05	0.4	0.05	0.20	0.20
	Sen's Slope	0.03	0.03	0.06	0.2	-1.2	-0.9
Dec-Feb	Tau (τ)	0.20	0.20	0.10	0.01	-0.02	-0.02
	P-value	< 0.05	< 0.05	0.30	0.90	0.10	0.03
	Sen's Slope	0.00006	0.00006	0.0003	0.00001	0.006	-0.006
Mar-May	Tau (τ)	0.04	0.04	0.02	0.13	-0.02	-0.02
	P-value	0.06	0.2	0.80	0.15	0.10	0.70
	Sen's Slope	0.00004	0.00004	0.00003	0.0003	-0.005	-0.006
Jun-Aug	Tau (τ)	0.04	0.2	-0.12	0.22	-0.006	-0.2
	P-value	0.06	0.06	0.20	0.1	0.90	0.03
	Sen's Slope	0.00004	0.00009	-0.0001	0.0002	-0.00006	-0.00001
Sep-Nov	Tau (τ)	0.20	0.20	-0.20	-0.20	-0.02	-0.02
	P-value	< 0.05	0.06	0.08	0.10	0.8	0.8
	Sen's Slope	0.0001	0.0001	-0.0002	-0.0003	-0.0003	-0.0003

2.3.3 Seasonality shift detection

Seasonality in hydrologic time series refers to regular fluctuations in a time series at a defined time interval (Machiwal *et al.*, 2012). Seasonality in hydrology studies is linked to the magnitude, timing, and duration of the associated hydro-climatic event like wet or dry season (Feng, Porporato and Rodriguez-Iturbe, 2013). Seasonality Index is used in this study for seasonality test; this method has been widely used in characterizing rainfall patterns and detecting shifts in seasonal patterns; for example, it has been used by Kumbuyo *et al.* (2014), Shamarti (2017), and Guhathakurta and Saji (2013). SI helps in identifying the rainfall regimes based on the monthly distribution of rainfall. It is computed using the following formula:

$$SI = \frac{1}{\bar{R}} \sum_{n=1}^{12} \left| X_n - \frac{R}{12} \right| \tag{2.9}$$

Where X_n is the average rainfall of the month n and R is the annual rainfall. Seasonality Index (SI) is divided into various classes shown in Table 2-5 that describe the rainfall regime.

Table 2-5: Seasonality index (SI) classes and the associated rainfall regimes

Rainfall Regime	Seasonality Index (SI)
Rainfall spread throughout the year	<0.19
Rainfall spread throughout the year with a definite wetter season	0.2-0.39
Rather seasonal with short drier periods	0.4-0.59
Seasonal	0.6-0.79
Markedly seasonal with long dry periods	0.8-0.99
Most rain in 3 months or less	1.0-1.19
Extreme seasonality with almost all rain in 2 months	>1.20

For seasonal shift detection, the rainfall time series is divided into three sub-series based on the changepoints detected in section (2.3.1). The SI values for each period are then compared for any significant variations. This test is only applied to rainfall since it is the only known hydrological parameters with defined seasonality index classes during this research period.

2.3.3.1 Results: Seasonality shift detection

Figure 2-10 shows the Seasonality Index (SI) plot for rainfall in Steelpoort and Blyde River Basins, with the dotted blue lines indicating the boundaries of various sub-series. It can be seen that throughout the study period, the seasonality index falls under a 0.8-0.99 category, which is described as “markedly seasonal with long dry periods.” Based on this pattern, it can be concluded that there were no seasonal shifts of rainfall during the study period.

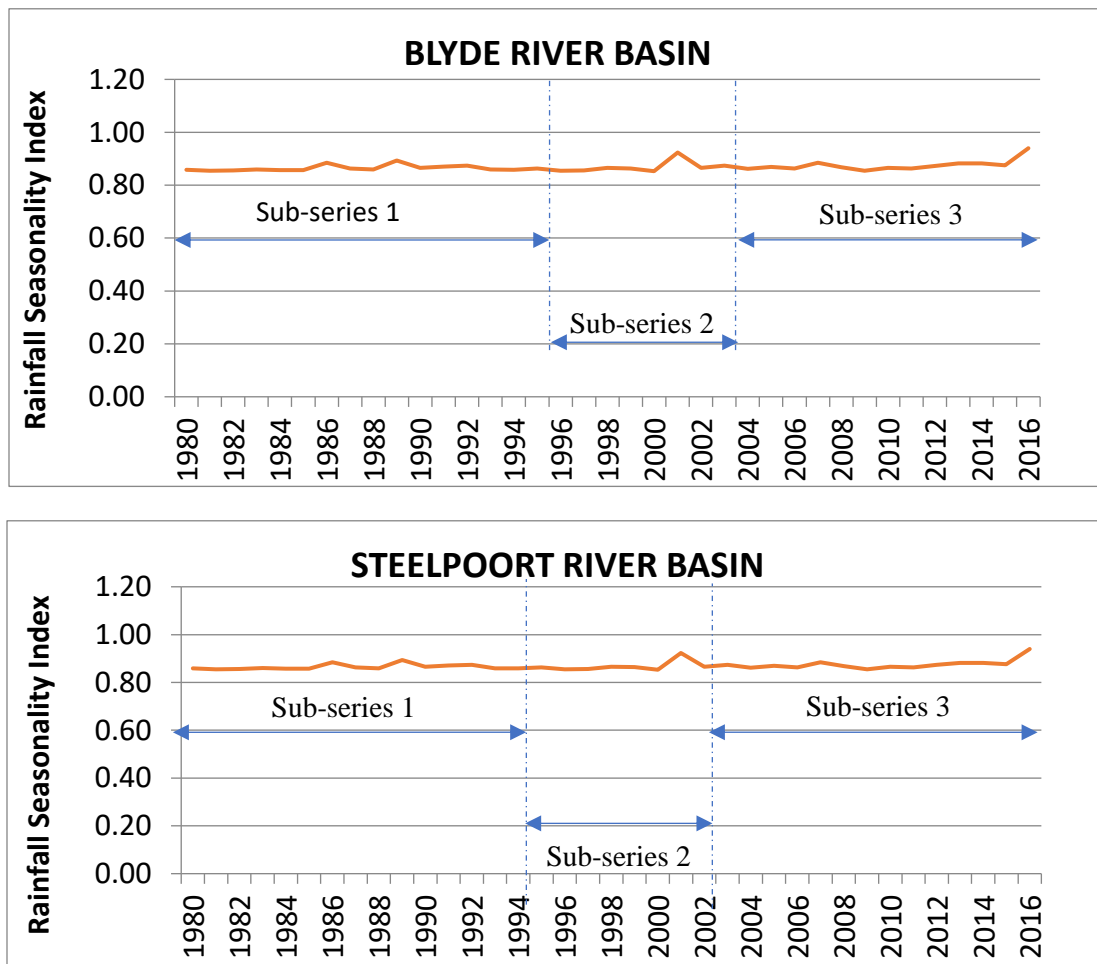


Figure 2-10: Distribution of seasonality Index over three sub-series (1980-1995, 1996-2002, 2003-2016) of rainfall

2.4 Discussions

The aim of this chapter is to quantify patterns of changes in climate regimes and attribute them to changes in streamflow and evapotranspiration. Climatic parameters under consideration in this research are rainfall and

temperature, whereas the resultant hydrological parameters are discharge and evapotranspiration. The period of this analysis was 37 years (1980 – 2016), and three statistical tests were adopted to detect abrupt shift (homogeneity test), progressive shift (trend test), and seasonal shifts (seasonality index). Analysis of the time series reveals the following:

Homogeneity test: This test is conducted on discharge, rainfall, temperature, and evapotranspiration to detect abrupt changes in the time series. Only temperature, discharge, and rainfall have abrupt changes in their time series, whereas evapotranspiration had none. To detect the source of these changes in discharge and evapotranspiration, the changepoint timing for discharge is compared to that of rainfall, whereas the changepoint for evapotranspiration is compared to that of temperature. Rainfall and discharge have two coinciding changepoints in 1995 and in 2002, which after further analysis, suggest that the source of these changes is extreme rainfall between 1996 and 2002. The temperature time series has only one changepoint in 2003, which cannot be directly linked to changes in discharge.

Trend test: This test is conducted on discharge, rainfall, temperature, and evapotranspiration to detect progressive changes in the time series at seasonal scale and annual scale. Temperature exhibited an increasing trend at both annual and seasonal scales, where an increase in temperature is observed in all the four seasons. Rainfall has a downward trend at an annual scale and generally exhibited a decreasing trend through the four seasons, except for the winter season (June to August), where there was no trend in the Blyde River Basin, and in spring (September – November) where there was no trend. Discharge exhibited an increasing trend in both river basins apart from the Blyde River, which revealed a decreasing trend from June to November, and Steelpoort, which had decreasing trend between September and November. The rate of change in discharge is very low, as depicted by the low slope. Most trends observed in discharge cannot be directly linked to rainfall patterns, apart from a decrease in discharge trend in the Blyde River Basin from June to November.

Seasonality shift detection test: this test is conducted on only rainfall to detect if there exists a shift in seasonal patterns of rainfall. The Seasonality Index (SI) ranges from 0.86 to 0.94, which falls into the “markedly seasonal with long dry periods” class. Based on this test, no seasonal shift was detected.

The outputs of this chapter provide strong evidence of changing climate, which directly influences streamflow. Changes in discharge are directly linked to rainfall rather than changes in temperature. However, changes discharge trend cannot be totally described by shifting climatic patterns, which therefore necessitates investigation of human influence on streamflow patterns.

3 QUANTIFICATION OF LULC CHANGE AND ITS IMPACTS ON HYDROLOGY

3.1 Background

LULC classification and change analysis is an important process in the quantification of the spatial distribution of various resources, physical features, and quantification of extents of human activities (Lam, 2008). Remotely sensed multi-spectral images had been widely applied in the classification of various LULC (Arveti and Etikala, 1992); Boschetti et al., 2014, Qi et al., 2009; Onjira and Sayama, 2014 use satellite images in flood mapping. Gyamfi et al., 2016 and Butt et al., 2015 use remote sensing to map multiple landuse classes.

LULC patterns and changes provide information about underlying human/natural processes, thus providing valuable information for monitoring and modelling various environmental processes (Song et al., 2011). Fluxes in surface water and various hydrological parameters resulting from LULC changes can be directly assessed using remotely sensed products as conducted by Razu Ahmed *et al.*, 2017, Boschetti *et al.*, 2014 and Uddin, Matin and Meyer, 2019 in flood mapping, by Avisse *et al.*, 2017 and Pipitone *et al.*, 2018 to monitor surface water storage. However, accurate estimation of streamflow at the local scale using coarse-resolution remotely sensed data is difficult (Carrier, 2000); hence when the river width is relatively smaller than the pixel values of the satellite images, errors are bound to arise. Also highlighted by Carrier, 2000, critical hydrological processes like deep soil moisture, snow water equivalent, sub-surface water fluxes, and interactions between surface and groundwater cannot be directly analyzed using satellite images. As a result, assessments of impacts of LULC change on hydrology (streamflow, lateral subsurface flow, groundwater fluxes) have been investigated using hydrological models that capture physical processes with LULC data as an input (Li et al., 2018).

The objective of this chapter is to quantify LULC changes using remote sensing images and quantify its impacts on hydrological partitioning in Steelpoort and Blyde River Basins. LULC maps for four epochs (1992, 1998, 2002, and 2014) are prepared using remotely sensed land products and changes between the successive maps analyzed. These maps are then used as input into a hydrological model for simulation of their resultant hydrological scenarios and subsequent analysis of hydrological anomalies.

Freely available and high-resolution images that cover the study period (1987-2014) and an open-source hydrological model that captures all physical processes and spatial variability of parameters are considered in this research.

3.2 LULC change mapping using remote sensing images

3.2.1 Overview of satellite remote sensing techniques

Remote sensing is the process of acquisition of information on physical characteristics of the earth using electromagnetic (EM) sensors onboard different platforms placed in space or air (Navalgund, Jararaman and Roy, 2007). These EM measurements can provide information about the position of objects and clues on the characteristics of the earth’s surface material (Zhu *et al.*, 2018). Remote sensing instruments are of two primary types - active and passive. Active sensors provide their own energy in order to scan objects and measure the amount of radiation that is reflected or backscattered. On the other hand, passive sensors gather radiation that is emitted or reflected by the object or surrounding areas (NASA, 2019) Figure 3-1 is a simple illustration of the operations of active and passive remote sensing.

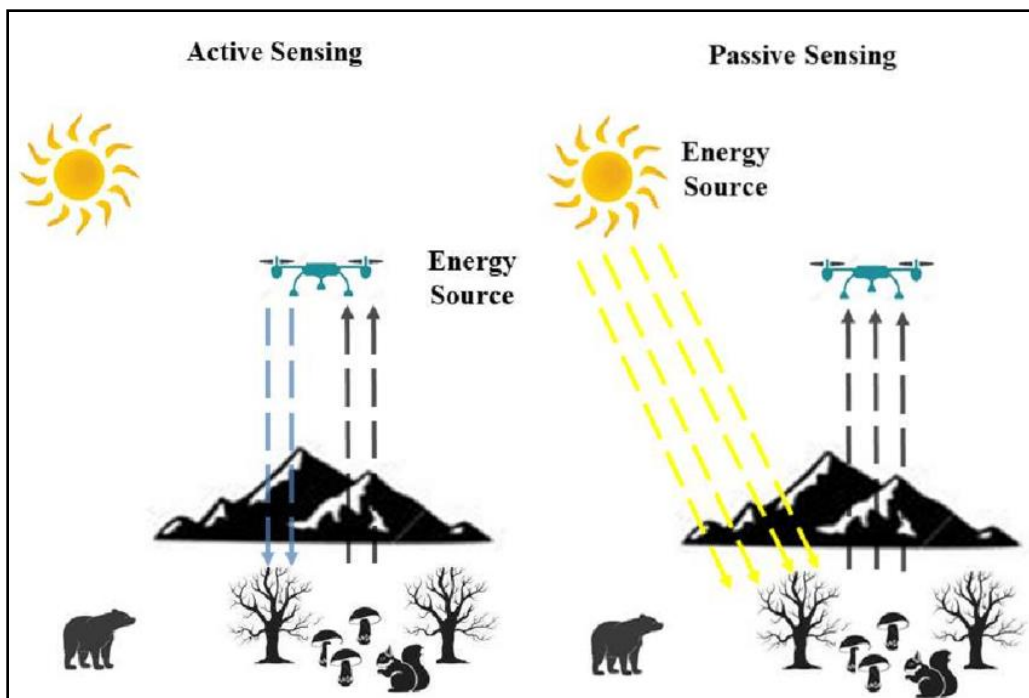


Figure 3-1: Illustration of active and passive remote sensing (Source: analytik.co.uk)

Identification of objects from remotely sensed images is made possible by the unique surface reflectance properties of various objects on the earth (Onjira *et al.*, 2014). Sensors record data in various sections of the electromagnetic spectrum (EMS) shown in Figure 3-2; the data is then stored in multi-band images (USGS, 2016). The EMS ranges from gamma rays to radio waves. However, the major application of remote sensing applications includes visible light, infrared, and microwave ranges (Zhu *et al.*, 2018).

QUANTIFICATION OF LULC CHANGE AND ITS IMPACTS ON HYDROLOGY

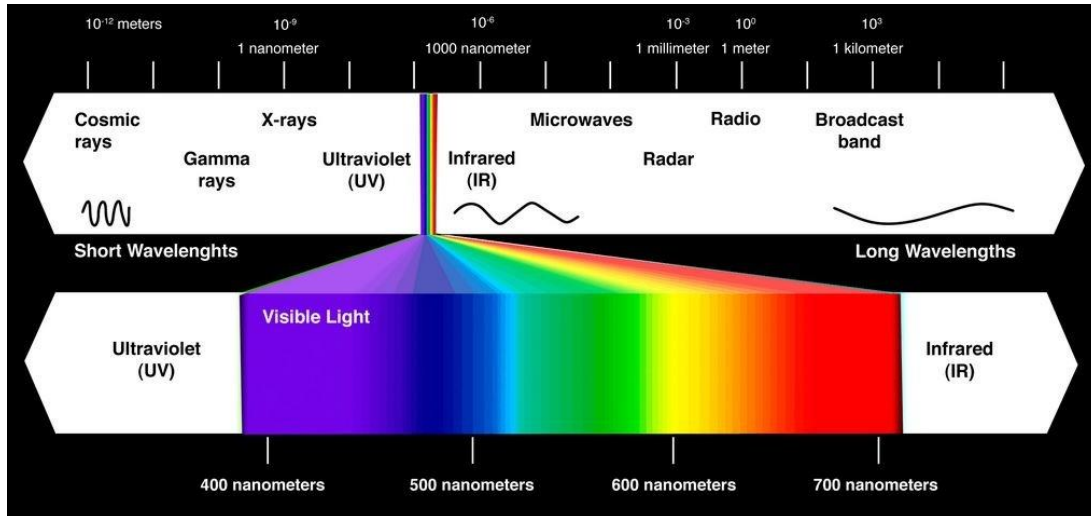


Figure 3-2: illustration of the electromagnetic spectrum (Source: Kiran, 2015)

Remote sensing instruments fall into two classes of sensors; non-imaging and imaging sensors (Zhu *et al.*, 2018). Table 3-1 summarizes the properties and typical remote sensing applications of the two classes of sensors. In this research, the interest is limited to LULC classification using remotely sensed images; hence only products from optical imaging sensors are selected because of their ability to recognize various objects.

Table 3-1: Categories of Remote Sensing sensors, EMS ranges, and typical applications

Remote sensing Instrument	Sensor Type	EMS Range	Application
Imaging Sensors	Optical	~400 – 750 nm	Object recognition, identification of material, detection of components of elements,
	Thermal	9 – 14 μm	Minerology, volcanology, hydrothermal studies, climatology & meteorology, DEM production,
	Radar	1 mm – 1 m	Aviation, meteorology, sounding satellites, DEM production, monitoring of glaciers, volcanic activities, landslides, and earthquakes
Non-Imaging sensors	Spectroradiometers & Radiometers		Telecommunication, bathymetry, laser operations, medical diagnosis, vegetation measurements, spectroscopic measurements

3.2.2 Data source selection

Several remote sensing instruments with optical imaging sensors have been launched in the past decades (Zhu *et al.*, 2018). Selection of data source for remotely sensed images for LULC classification under this research is based on the following criteria; **data availability** (covering period of study), **acceptable spatial resolution**, **acquisition cost** (freely available images), and **revisit time** (at least once per month)

Table 3-2 shows commonly used remote sensing instruments and their characteristics adopted from Zhu *et al.* (2018). The spectral sensors have been upgraded with time denoted by the suffix numbers under the mission column.

QUANTIFICATION OF LULC CHANGE AND ITS IMPACTS ON HYDROLOGY

Table 3-2: Major satellites used in remote sensing and their properties

	Mission	Launch year	Spatial resolution (m)	Availability	Revisit time (days)
1	LANDSAT 1-8	1972, 1975, 1978, 1982, 1984, 1993, 1999, 2013	30 – 250	Free	16
2	SPOT 1-6	1986, 1990, 1993, 1998, 2002, 2012	2.5 – 20	Commercial	1-3
3	ASTER	2000	15 – 90	Free	16
4	MODIS	1999, 2002	250 - 500	Free	8
5	SENTINEL 1-6	2014, 2015, 2016, 2017, 2021	5 – 60	Free	12, 10, 27
7	Quickbird	2000, 2001	0-61 – 2.62	Free	2.4-5.9
8	Envisat	2002	30 – 300	Free	35
9	GeoEye	2008	0.41 – 1.65	commercial	8.3
10	WorldView	2007– present	0.34 – 1.84	Commercial	1.7

According to Table 3-2, LANDSAT Mission meets all the four criteria set, and hence it is selected as the data source for this research. Images from LANDSAT 5, 7, and 8 are utilized in this research since they cumulatively have data covering the period of study; LANDSAT 4 has data from 1984 – 2013, LANDSAT 7 has data from 1999-2017, and LANDSAT 8 has data from 2013 to date (NASA, 2019).

LANDSAT sensors stores data in multiple bands where each band is collects data under a different EMS range. Table 3-3 the spectral bands in LANDSAT 5, 7, their corresponding wavelengths and EMS range (USGS, 2017).

Table 3-3: Properties of LANDSAT Images and their applications

EMS	LANDSAT 5 & 7		LANDSAT 8	
	Band No.	Wavelength	Band No.	Wavelength
Coastal aerosol	N/A	N/A	1	0.43-0.45
Blue	1	0.45-0.52	2	0.45-0.51
Green	2	0.52-0.60	3	0.53-0.59
Red	3	0.63-0.69	4	0.64-0.67
NIR	4	0.77-0.90	5	0.85-0.88
SWIR 1	5	1.55-1.75	6	1.57-1.65
Thermal Infrared	6	10.40-12.50	N/A	N/A
SWIR 2	7	2.09-2.35	7	2.11-2.29
Panchromatic	8	0.52-0.90	8	0.50-0.68
Cirrus	N/A	N/A	9	1.36-1.38
TIRS 1	N/A	N/A	10	10.60-11.19
TIRS 2	N/A	N/A	11	11.50-12.51

3.2.3 Image acquisition

LANDSAT 5, 7, and 8 satellite instruments orbit the earth at an altitude of 705 km (USGS, 2017). During the satellite revolves around the earth, the sensors “see” a portion of the earth, usually referred to as swath or scene, as shown in Figure 3-3. These satellites are stationary. Hence, the earth’s rotation enables them to scan the whole earth's surface within a given time (16 days).

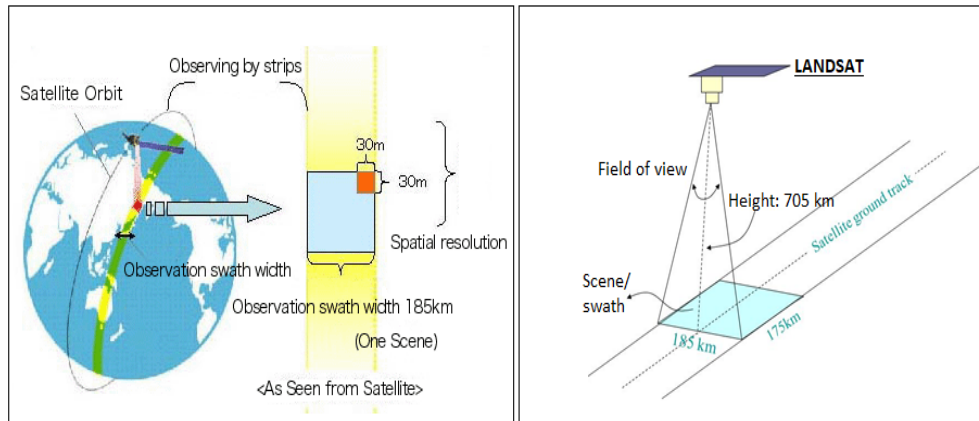


Figure 3-3: Illustration of a data collection plan of LANDSAT sensors (source: USGS, 2017)

Data for each scene is referenced using a global notation system called Worldwide Reference System (WRS), which identifies each scene by path and row numbers (Natural Resources Canada, 2015). This referencing system facilitates the easy acquisition of data. The Blyde and Steelpoort River Basins fall under two scenes, which are referenced by 168-77 and 169-77, as shown in Figure 3-4. 168 and 169 refer to the path numbers, while 77 refers to the row number.

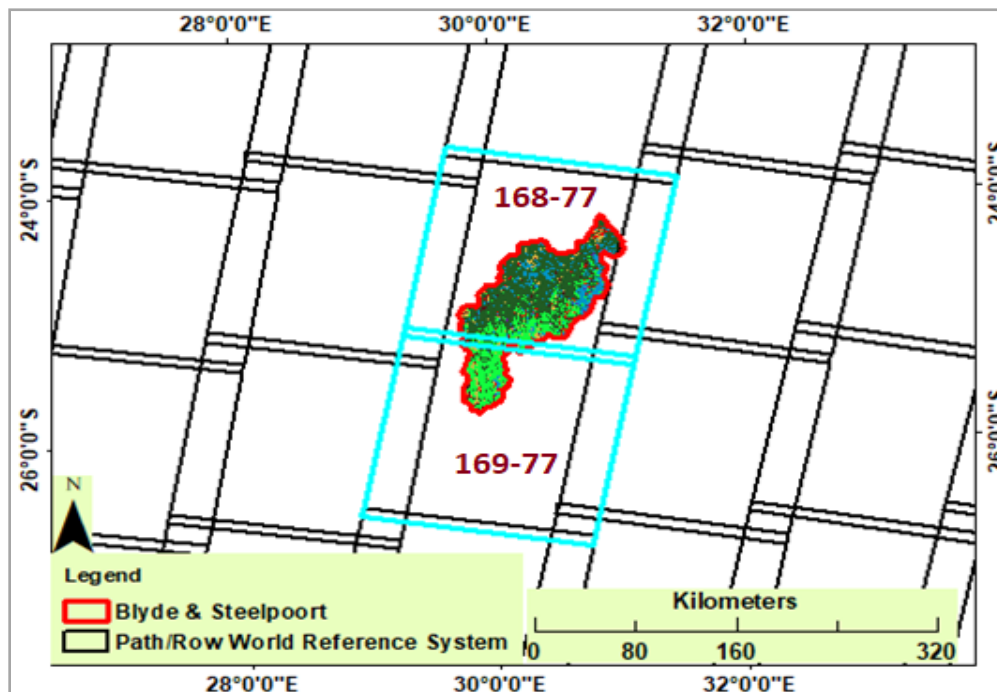


Figure 3-4: Location of Blyde and Steelpoort River Basins in the LANDSAT WRS

QUANTIFICATION OF LULC CHANGE AND ITS IMPACTS ON HYDROLOGY

Remotely sensed images for this research were acquired through the United States Geological Survey (USGS) website (<https://earthexplorer.usgs.gov/>). The search criteria applied in selecting images include images obtained between the dry months of May and October with less than 10% cloud cover; this is because there is minimal cloud cover in dry periods. The disparity in vegetation type can be well distinguished. Table 3-4 gives details of the images that were downloaded and used in this study.

Table 3-4: Summary of LANDSAT images acquired for LULC mapping

	LANDSAT Sensor	Path	Row	Acquisition Date	Ground Resolution (m)	% Cloud Cover
1	L4-5 TM	168	77	05/13/1992	30	5
2	L4-5 TM	169	77	05/20/1992	30	0
3	L7 ETM+	168	77	06/15/1998	30	0
4	L7 ETM+	169	77	06/22/1998	30	0
5	L7 ETM+	168	77	06/18/2002	30	0
6	L7 ETM+	169	77	06/09/2002	30	0
7	L8 OLI/TIRS	168	77	06/27/2014	30	0.05
8	L8 OLI/TIRS	169	77	06/18/2014	30	0

3.2.4 LULC classification

Various geospatial tools have been used in LULC classification using remote sensing data; Ansari and Golabi, 2019 use ERDAS and ArcGIS, Lekha and Kumar, 2018 use ENVI, Simonetti, Marelli, and Hugh, 2015 demonstrate the use of IMPACT Tool in digital image processing and classification, and Filipe and Correia, 2017 demonstrate the use of QGIS in LULC classification. IMPACT Tool, ENVI, and ArcGIS are used in this study since they are readily available. IMPACT Tool is used in pre-processing the images, ENVI is applied in the initial stages of classification, and features not well classified in ENVI are manually digitized in ArcGIS.

LULC classification from digital satellite images can be classified into two categories; Supervised classification and unsupervised classification (Mohammady *et al.*, 2015). According to Lusch, 2015, good knowledge of the area is required in supervised classification, where the analyzer provides training statistics that identify each class; the image analyst supervises the pixel categorization process by specifying the computer algorithm and numerical descriptor representing various land cover types in a scene (Patil, Desai and Umrikar, 2012). Unknown pixels are assigned into various categories based on their spectral properties by manually sampling and delineating the pixels. The spectral properties of those pixels are then extracted and used to classify unknown pixels in the whole image (Wai-Keung LAM and Lau, 2000). In unsupervised classification, prior knowledge of the area is not required (Mohammady *et al.*, 2015). LULC classes are automatically identified based on statistical structures or groups (Lusch, 2015).

According to Mohammady *et al.*, 2015, high accuracy in LULC classification is achieved in supervised classification, and therefore the method of LULC classification adopted in this study is supervised classification. Figure 3-5 shows the flowchart of the classification process used in this research.

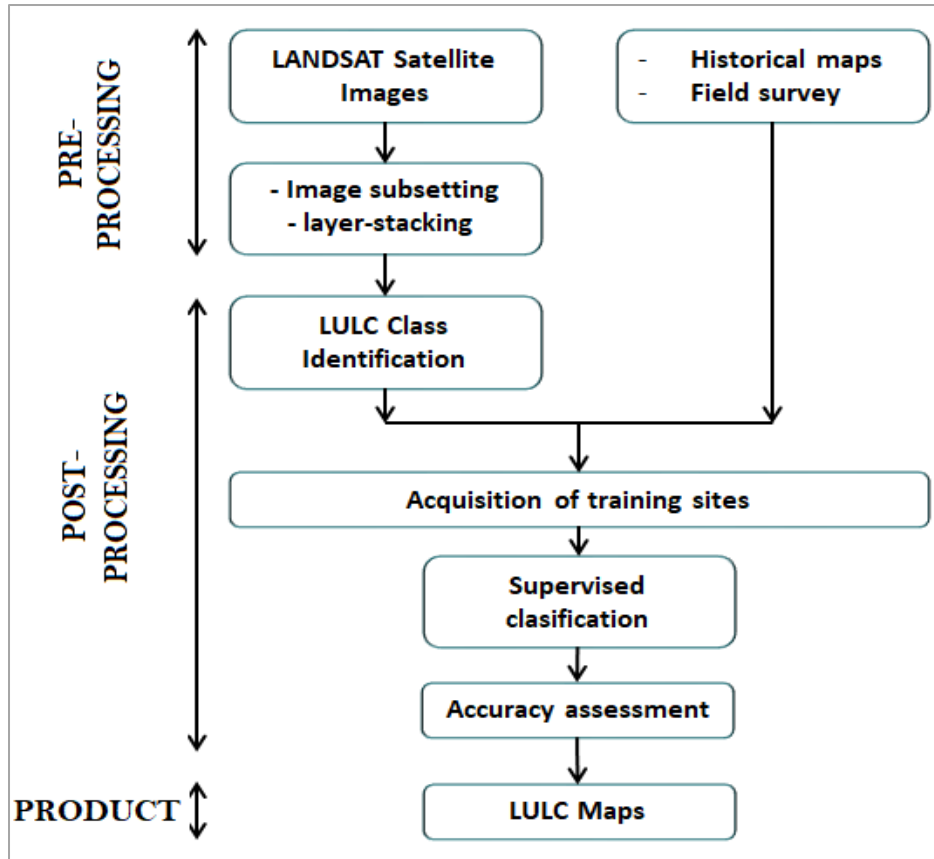


Figure 3-5: Flowchart for LULC Classification process

Image pre-processing: IMPACT Tool is used to executing the following three processes:

- **layer stacking**, where spectral bands are combined into one image with multiple bands
- **image sub-setting**, where the multi-band images are clipped to the study area
- **atmospheric correction** where raw digital number (DN) values to top-of-atmosphere (TOA) reflectance data are calibrated to a common radiometric scale to minimize spectral differences caused by acquisition time, sun elevation, and sun-earth distance (Simonetti *et al.*, 2015).

Identification of LULC classes: For image visualization in ArcGIS and ENVI, the following band combinations are used; 5-4-3 for Landsat 4-5 TM images, 5-4-3 for Landsat 7 images, and 6-5-4 for Landsat 8 images. Historical LULC maps, Google Earth imageries, and CCI LULC map of the 1998-2002 epoch (LAND_COVER_CCI Partnership, 2017) is then used as a baseline for the identification of various LULC classes. An example of a landuse class identification process is as shown in Figure 3-6 in which agricultural area features can be identified at the same location in the two base maps and correspondingly in the LANDSAT image.

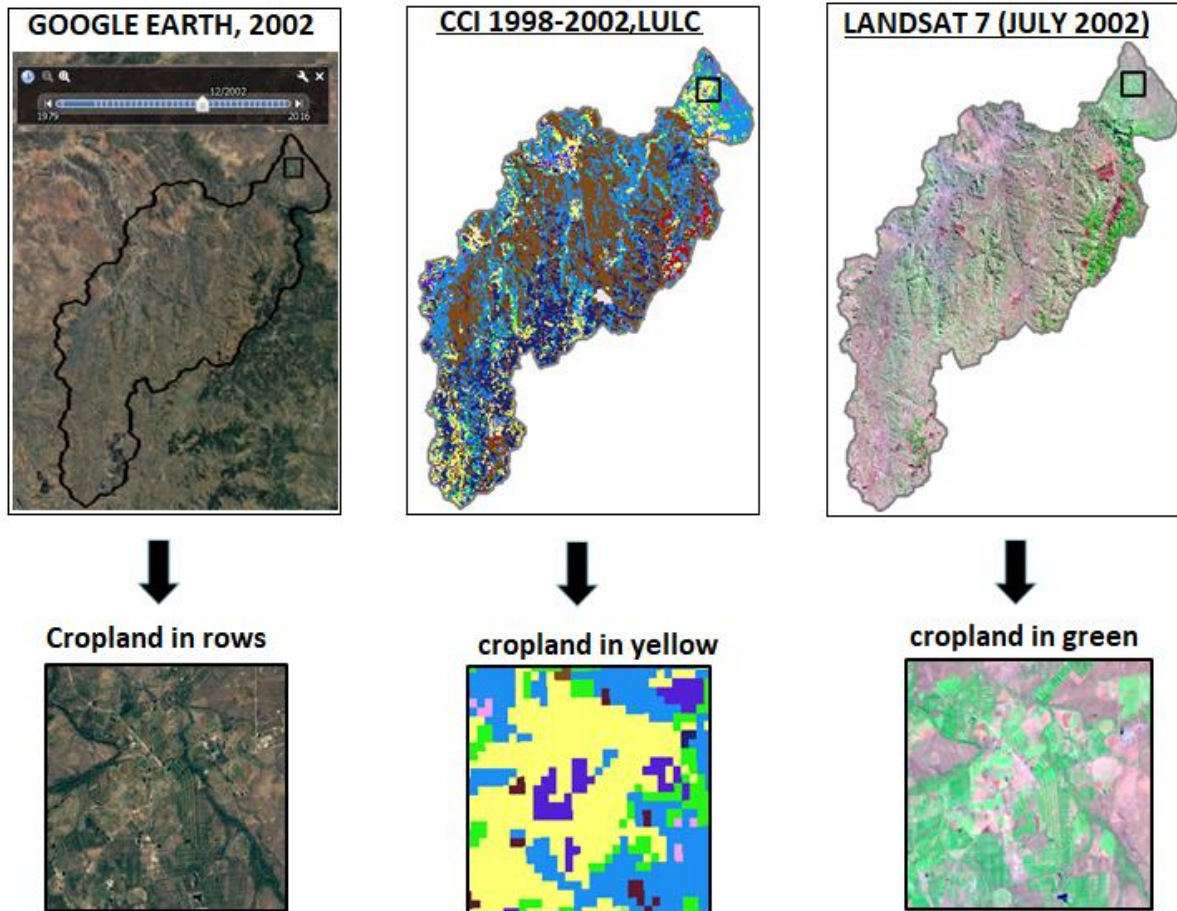


Figure 3-6: Illustration of LULC class identification process

By referencing these base maps, eight different landuse classes are identified in this research; agricultural area, waterbody, dense and sparse forest, shrubland, grassland and herbaceous vegetation (mixed vegetation), and urban areas (settlements).

Definition of training sites and extraction of signatures: Training sites are areas that are known to be representative of a particular land cover class. The computer determines the spectral signature of the pixels within each training area and uses this information to define the mean and variance of each of the classes (Humboldt State University, 2015). These locations are identified through visual interpretation of the image or based on historical maps.

After the creation of training sites, statistical characteristics of each class is created and stored for image classification (Rwanga and Ndambuki, 2017)

Image classification (Supervised classification): This approach has several classification techniques like a parallelepiped, minimum distance, Mahalanobis distance, maximum likelihood, Spectral Angle Mapper (SAM), Spectral Information Divergence (SID), and binary encoding (ENVI, 2009). In this research, classification is first conducted in ENVI using the **Maximum Likelihood** technique; this algorithm assumes that statistics in each class

has a normal distribution and computes the probability that a given pixel belongs to a specific class. Based on the signatures created in the previous step, each pixel is then assigned to a class that has the maximum probability (the maximum likelihood). If the highest probability is smaller than the specified threshold, the pixel remains unclassified. The unclassified pixels can be assigned to an unknown class or to any class that they may fit into depending on the knowledge of the area or the base maps (Humboldt State University, 2015).

Maximum likelihood classification is obtained by computing the following discriminating function:

$$f(x) = \ln p(\omega_i) - \frac{1}{2} \ln |\Sigma_i| - \frac{1}{2} (x - m_i)^T \Sigma_i^{-1} (x - m_i) \quad (3.1)$$

Where i is the class, x is the dimensional data (x), $p(\omega_i)$ is the probability that class ω_i occurs in the image and is assumed to be the same for all classes, $|\Sigma_i|$ is the determinant of the covariance matrix of the data in class ω_i , Σ_i^{-1} is the inverse matrix and m_i is the mean vector.

Once the classification is completed in ENVI, ArcGIS is used to enhance the quality of the classified data through the digitization process. The digitized data is converted to raster files and mosaicked with the data from ENVI. The data from this process is then adopted as interim LULC maps for the period and subjected verification process described under "Accuracy Assessment."

3.2.4.1 Classification Results and Discussions

LULC maps are prepared for Blyde and Steelpoort River Basins for the years 1992, 1998, 2002, and 2014 as shown in Figure 3-7. The area of each class was calculated, taking into account the pixel count and the total area. Thus, allocations of each classified area (km^2). For a description of the LULC changes observed, the basins are divided into three areas shown in the black triangle and denoted by numbers 1, 2, and 3 in figure 3-7. The various changes under each area are described as follows:

Area 1: There is an increase in agricultural land, which is very distinct between 1992 LULC and 1998 LULC.

Area 2: There is a gradual loss of forest, which distinctly occurs between 1998 LULC and 2002 LULC. Forest in this area is majorly transitioned to agriculture land. Another change observed in this area is the transition of shrubland into agricultural land, and part of agricultural land is transitioned into urban area between 2002 LULC and 2014 LULC.

Areas 3: There is an increase in agricultural land, which is progressing from 1992 LULC through to 2014 LULC. The major LULC transition in this area is from grassland to agriculture land.

Other changes observed include an increase in the water body, which is attributed to dam constriction in the Steelpoort River.

Therefore, we can conclude that dominant LULC changes in Blyde and Steelpoort are mainly induced by human activities. In general, the change statistics are summarized in Table 3-5 with dominant changes detected in an agricultural area where an increase of 95% of its original size is detected, water body increased by 136% of its original size due to the construction of reservoirs, and increase of urban area by 169% of its original size. Dominant forest loss is realized between 1992 and 1998, whereas the expansion of agricultural area and urban area is dominant between 2002 and 2014.

QUANTIFICATION OF LULC CHANGE AND ITS IMPACTS ON HYDROLOGY

Table 3-5: LULC change statistics, where (+) means increase and (-) means a decrease in respective LULC classes

	LANDUSE TYPE	1992 LULC (km²)	1998 LULC (km²)	2002 LULC (km²)	2014 LULC (km²)	Overall change (km²)
1	Agricultural area	539	710	788	1053	+513
2	Water body	39	40	40	59	+20
3	Forest	1127	1080	778	754	-373
4	Grassland	2674	2662	2647	2510	-164
5	Herbaceous Vegetation	259	190	182	130	-129
6	Sparse Forest	230	202	195	177	-53
7	Shrubland	4716	4691	4916	4732	-16
8	Urban Area	9	18	48	179	+169

QUANTIFICATION OF LULC CHANGE AND ITS IMPACTS ON HYDROLOGY

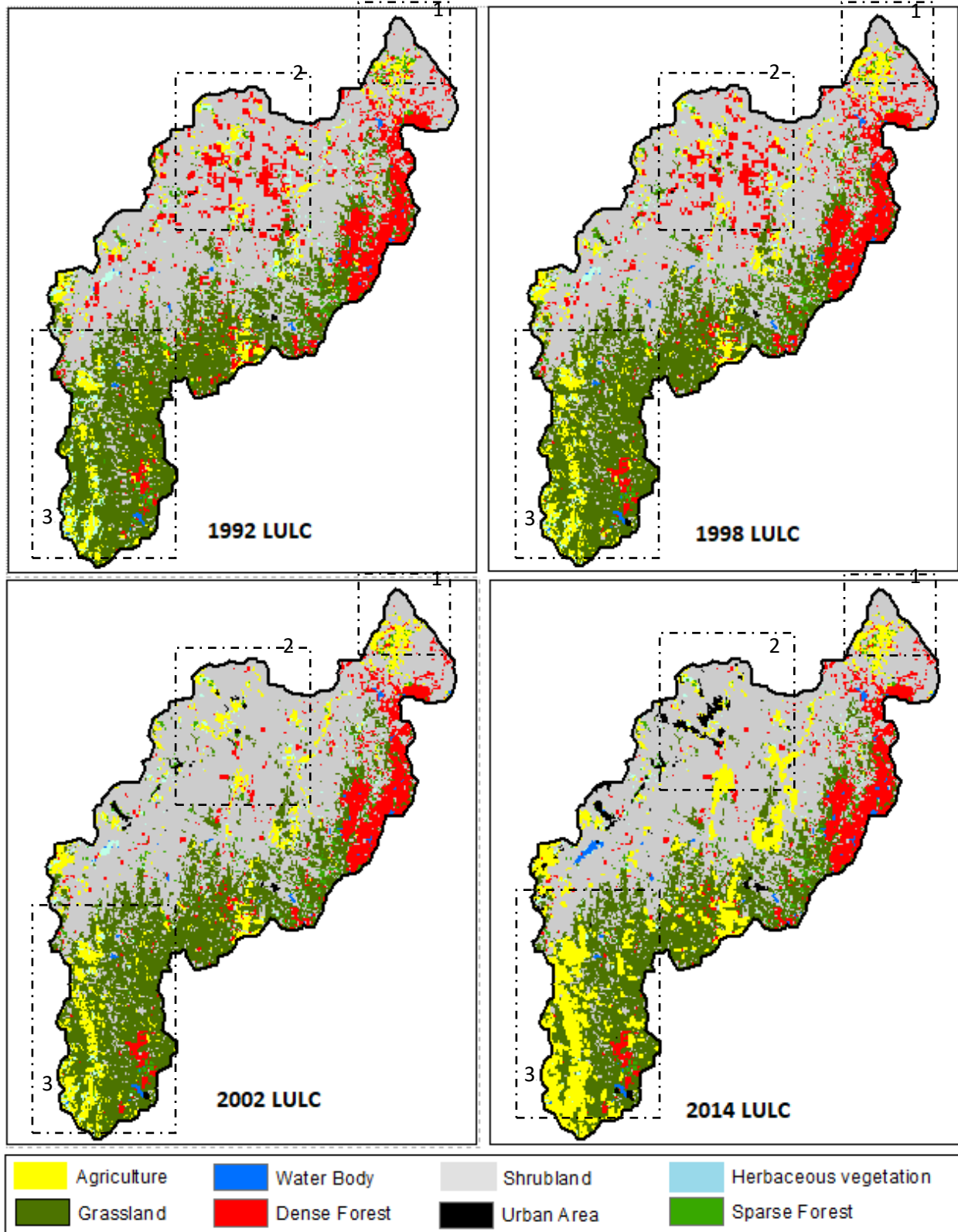


Figure 3-7: LULC map series for Steelpoort and Blyde River Basins

3.2.5 Accuracy assessment of LULC Maps

Accuracy of the LULC maps developed are evaluated to assess their accuracy; this is performed by comparing the degree at which the maps agree with the existing LULC maps or ground survey data. In this study, CCI LULC maps are used for verification of the results. This step is conducted in ArcGIS, where three geoprocessing tools are used to select assessment pixels randomly. Confusion matrix and Kappa coefficients are adopted as the metrics for accuracy assessment; this approach has been widely used in various research to verify LULC classification, for example, by Elsaid and Abdelkareem (2018), Patil *et al.* (2012), and by Rwanga *et al.* (2017). According to Pontius Jr., (2000), Kappa coefficient $K = 1$ means a perfect agreement, $K > 0.5$ is satisfactory, while a value close to zero means that the agreement is poor.

Kappa coefficient K is calculated using the following formula (Elsaid *et al.*, 2018):

$$K = \frac{N \sum_{i=1}^r X_{ii} - \sum_{i=1}^r (X_{i+} X_{+i})}{N^2 - \sum_{i=1}^r (X_{i+} X_{+i})} \quad (3.1)$$

Where r is the number of rows and columns in the confusion matrix, X_{ii} are the observation in row i and column i , N is the total number of observations (pixels), X_{i+} is the number of rows and X_{+i} is the number of columns i .

Under accuracy assessments, several statistical elements like Overall Accuracy, Producer's Accuracy, and User's Accuracy are also computed. Overall Accuracy is the percentage of correctly classified samples of an error (confusion) matrix. The producer's accuracy indicates the quality of the classification of training set pixels, and User's Accuracy indicates the probability that prediction represents reality.

These statistical metrics are expressed by the following equations:

$$\text{Overall accuracy} = \frac{1}{N} \sum_{k=1}^n a_{kk} \quad (3.2)$$

Where a is individual cell value, $k + a$ is the row total and $ka +$ is the column total, n total number of classes, and N is the number of samples.

$$\text{Producer's accuracy} = \frac{a_{ii}}{\sum_{i=1}^n a_{i+}} \quad (3.3)$$

$$\text{User's accuracy} = \frac{a_{ii}}{\sum_{i=1}^n a_{+i}} \quad (3.4)$$

Where a_{ii} is the number of samples correctly classified, a_{i+} is the column total for class i , a_{+i} row total for class i confusion matrix, producer's and user's accuracy are calculated for each class, as well as the overall accuracy (Rwanga *et al.*, 2017).

3.2.5.1 Results: Accuracy assessment

Table 3-7 summarizes the accuracy assessment results; the overall accuracy for each map indicates high accuracy at 78% in 1992, 76% in 1998, 80% in 2002, and 68% in 2014. Kappa Coefficients for all these three periods are above 0.5, which is also indicative of satisfactory classification. The user's accuracy for the agricultural area was quite low in all the LULC maps; this is because the agricultural area is vastly identified as herbaceous vegetation on the base map and hence could not correspond to the classified map.

QUANTIFICATION OF LULC CHANGE AND ITS IMPACTS ON HYDROLOGY

Based on Kappa statistics and overall accuracy, the LULC maps developed are considered to be a true representation of LULC evolution in Blyde and Steelpoort River Basins.

Table 3-6: Summary of accuracy assessment of land use land cover classification of Blyde and Steelpoort River Basins

Landuse Class	1992		1998		2002		2014	
	User's Accuracy	Producer's accuracy						
Agricultural area	17	75	10	62	12	65	7	83
water Body	42	50	43	60	62	80	28	50
Forest dense	76	66	68	62	80	65	68	42
Grassland	84	82	86	82	86	82	81	69
Herbaceous Vegetation	46	30	43	18	57	26	41	12
Sparse Forest	9	60	7	63	13	70	7	40
Shrubland	89	84	88	81	91	86	84	78
Urban Area	50	50	38	30	19	30	19	30
Overall accuracy	78		76		80		68	
Kappa Coefficient	0.66		0.63		0.68		0.52	

3.3 Hydrological Modelling

Modelling is an important aspect of hydrology for assessing the environmental well-being of our river basins and has, therefore, been vastly utilized in water resources planning and management (Jha, 2009). Development on hydrological modelling has seen an evolution from simplistic models which are capable of capturing the hydrologic cycle to models that capture various physical characteristics and are capable of simulating numerous physical processes like groundwater-surface water interactions, coupled hydrologic-atmospheric processes, and mass transport at various resolutions of time and space (Singh, 2018).

Hydrological models can be classified based on the presence of random variables, their distribution in space, and temporal variation; these are ***lumped*** and ***distributed*** models which are classified based on model parameters as a function of space and time, and ***deterministic*** and ***stochastic*** models which are based on randomness/non-randomness of variables. Distributed models make predictions by taking into account the spatial variability of physical attributes of the catchment, whereas lumped models consider the whole river basin as a single unit where spatial variability of physical parameters is disregarded (Chow, Maidment, and Mays, 1988; Dwarakish and Ganasri, 2015a).

Hydrological models can also be classified as ***empirical***, ***conceptual***, and ***physically based*** models based on the hydrological processes. Empirical models take into account the direct physical relationship between the input and

output without considerations for transformations functions. Conceptual models have the complex physical processes simplified and can have various processes represented empirically. Physically-based models are able to represent the idealized real phenomenon by taking into account the principles of physical processes.

Hydrological models may also give output at a different time step from the input data; the typically computational time steps range from hourly to monthly, which often is a function of the process representation and the models' intended use. In relation to time, models can be **event-based**, which are short term and used to simulate individual storm events and continuous models which simulate catchment behavior over a long period of time (Singh and Woolhiser, 2002).

The ability of physically-based distributed models to capture spatially variable morphological and climatic parameters enhances their effectiveness in accounting for water dynamics in our environmental systems (Devia, Ganasri and Dwarakish, 2015; Krogh *et al.*, 2015; Sitterson *et al.*, 2017; Sun *et al.*, 2017). Hydrological models under this category are considered ideal for modelling LULC changes impacts on hydrology.

3.3.1 Model Selection

Several hydrological models have been developed over the decades with varying capabilities, as highlighted in Section 3.3. Therefore, the desired process to be simulated and data availability informs model selection (Dwarakish and Ganasri, 2015b). A set of criteria was developed for selections of the model that can be effectively used to achieve the objectives of this research. Model selection is restricted to fully distributed or semi-distributed models for their ability to spatial variability of river basin characteristics. The following are the criteria used in model selection:

- Must have complete landuse tools (interception, plant water uptake, vegetation growth) to enable assessment of the impacts of land-use changes on water resources.
- It should be able to capture reservoir operation, water use, and irrigation processes.
- Must be able to simulate hydrological processes at a large scale (equivalent to the study area, 10,000 km^2).
- It should be able to output baseflow, evapotranspiration, surface runoff, and groundwater recharge.
- It should be able to output values at a daily time step
- Must be a continuous model
- The model must be freely available
- Has a GIS interface for enhanced spatial visualization and analysis

Six commonly used physically-based distributed and semi-distributed hydrological models are subjected to a selection process where the models are screened against the criteria. Four Models (HEC-HMS, SWAT, HBV, and Pitman Model) meet the set criteria, as shown in Table 3-7. However, the SWAT Model is selected for this research because of readily available support

QUANTIFICATION OF LULC CHANGE AND ITS IMPACTS ON HYDROLOGY

Table 3-7: Model screening against selection criteria

Model	Landuse Tools	Water use & dam operation	Large scale model	BF, SR, ET, GW	Outputs at daily time step	Continuous time scale	Freely Available	GIS Interface	Source
HEC-HMS	Yes	Yes	Yes	Yes	Yes	Yes	Yes	Yes	(Arlen D. Feldman, 2000)
MIKE-SHE	Yes:	Yes	Yes	Yes	Yes	Yes	No	Yes	(DHI, 2017)
SWAT	Yes	Yes	Yes	Yes	Yes	Yes	Yes	Yes	(Neitsch, J.G. Arnold, et al., 2009; Neitsch et al., 2011)
VIC	Yes	No	Yes	Yes	Yes	Yes	Yes	No	(Hamman et al., 2018)
HBV	Yes	Yes	Yes	Yes	Yes	Yes	Yes	Yes	(Pers, 2007)
Pittman Model	Yes	Yes	Yes	Yes	Yes	Yes	Yes	Yes	(HUGHES and METZLER, 1998)

3.3.2 Description of SWAT Model Processes

Soil and Water Analysis Tool (SWAT) is a hydrologic and hydraulic model that is widely applied in modelling impacts of LULC changes on hydrology by many researchers like Muthuwatta (2014), Paudel *et al.* (2011), Guzha *et al.* (2018), Wang *et al.* (2018), Reeves and Mager Daniel (2014) and Zhu *et al.* (2014) among others. The model is a physically-based semi-distributed hydrological model developed by the United States Department for Agriculture Research Service (USDA-ARS) for the purpose of predicting the impact of land management practices on water, sediment, and agricultural chemical yields in large watersheds with varying soil, land-use, and management conditions over long periods of time. It captures various physical processes like surface runoff, percolation, evapotranspiration, erosion, nutrient and pesticide loading/transport, crop growth and irrigation, groundwater flow, channel transmission losses, pond and reservoir storage, and channel routing (Neitsch, J.G. Arnold, *et al.*, 2009; Neitsch *et al.*, 2011).

The SWAT Model divides a basin into sub-basins, which are further into hydrological response units (HRUs) based on soil type distribution, LULC classes, and slope characteristics. The model works on the concept that a day’s rainfall can generate surface runoff, and a fraction can infiltrate into the soil depending on LULC and soil characteristics. Upon further water movements, a fraction of soil water content becomes available for evaporation plant evapotranspiration. The soil water is also partitioned into a sub-surface flow, which eventually enters a river/stream and groundwater recharge (Masud, Ferdous and Faramarzi, 2018).

Simulations of the hydrological processes in the SWAT model is divided into two phases; **land phase** and **routing phase**. The land phase controls water balance, sediment, nutrients, and pesticide loadings to the main channel. The hydrologic cycle in this phase is based on the water balance equation, which is given as follows:

$$S_t = S_o + \sum_{i=1}^t R_d - Q_s - ET - W_s - Q_{gw} \quad (3.2)$$

Where S_t is final soil water content, S_o is initial water content on day i , R_d is rainfall amount on day i , Q_s is the amount of surface runoff on day i , ET is the amount of evapotranspiration on day i , W_s is the amount of water entering the vadose zone from the soil profile on day i and Q_{gw} is the groundwater return flow on day i (Neitsch, J.G. Arnold, *et al.*, 2009; Neitsch *et al.*, 2011).

3.3.2.1 Evapotranspiration estimation

SWAT model has three methods of simulating potential evapotranspiration (PET); the Penman-Monteith, Priestley–Taylor, and Hargreaves method. In this research, the Hargreaves method is selected for evapotranspiration estimations. Hargreaves PET is formulated as follows:

$$PET = \lambda E_o = 0.0023 * H_o * (T_{mx} - T_{mn})^{0.5} * (\bar{T}_{av} + 17.8) \quad (3.3)$$

Where λ is the latent heat of vaporization in ($MJ kg^{-1}$), E_o is the potential evapotranspiration ($mm d^{-1}$), H_o is the extraterrestrial radiation ($MJ m^{-2}d^{-1}$), T_{mx} is the maximum temperature for a given day ($^{\circ}C$), T_{mn} is the minimum temperature for a given day ($^{\circ}C$), \bar{T}_{av} is the mean air temperature for a given day ($^{\circ}C$). The model simulates actual evapotranspiration (ET) based on PET, soil water availability, and the maximum amount of transpiration depending on the plant type and related daily above-ground and below-ground biomass production (Neitsch *et al.*, 2011).

3.3.2.2 Surface runoff estimation

SWAT Model provides two methods for surface runoff volume estimations; the modified Soil Conservation Service Curve Number (SCS-CN) method and the Green & Ampt (GA) infiltration method. The modified Soil Curve Number (SCS-CN) method is used in this research. The SCS-CN method is based on a conceptual model that is aided by verified data (Ponce and Hawkins, 1997; Dile *et al.*, 2016). SCS-CN is preferred since it only takes into account the total volume of rainfall, while the GA method takes into account factors like rainfall duration and intensity, which are not readily available in the water resources database for the study area. The SCS-CN Method is a function of LULC, land treatment, soil permeability, and antecedent soil water conditions (Neitsch *et al.*, 2011).

LULC represents the surface conditions with regard to the degree of cover. Land treatment includes anthropogenic practices that can compact the soil, modify surface conditions, and drainage characteristics. Soil properties also influence the amount of surface runoff generate. In the SCS-CN Method, these soil properties are represented by a hydrological parameter, which is indicative of the minimum rate of infiltration obtained for bare soil after prolonged wetting (Krishi, 2013). Therefore, the method includes both infiltration and horizontal transmission rates. This parameter, which defines the soils' surface runoff potential, is the qualitative basis of classification of soils into various groups known as Hydrological Soil groups (Chow *et al.*, 1988; United States Natural Resources Conservation Service, 1997; Krishi, 2013)

QUANTIFICATION OF LULC CHANGE AND ITS IMPACTS ON HYDROLOGY

According to NRCS (2007), Jin et al. (2015), Abraham et al. (2020), and Pancholi (2015), the SCS-CN method defines the Hydrological Soil Groups (HSGs) as summarized in Table 3-8.

The soil texture classification is conducted based on the silt, sand, and clay content, as shown in Figure 3-8.

Table 3-8: The USDA-NRCS Hydrologic Soil Group Classification

HSG	Soil type	Texture class	Runoff potential	Infiltration rate (mm/h)	Water transmission
A	Deep, well-drained soils	Sand, loamy sand, or sandy loam	Low	7.62–11.43	High rate (7.62 mm/hr)
B	Moderately deep, well-drained with moderately fine to coarse textures	Silt loam or loam	Moderate	3.81–7.62	Moderate rate (3.81-7.62 mm/hr)
C	Moderately fine to fine textures	Sandy clay loam	Moderate	1.27-3.81	Low rate (1.27-3.81 mm/hr)
D	Soils which swell significantly when wet, heavy plasticity and with a high permanent water table	Clay loam, silty clay, sandy clay, silty clay, and clay	high	0-1,27	Very low rate (0-1.27 mm/hr)

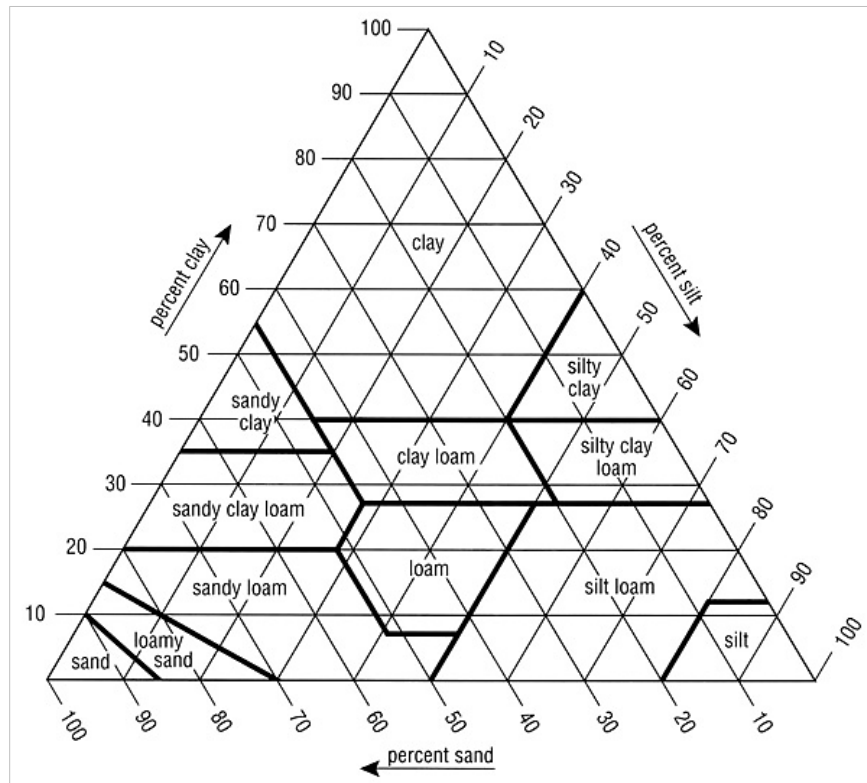


Figure 3-8: Soil textural triangle used for soil texture classification and

The curve number varies non-linearly with soil moisture; the curve number drops as the soil approached the wilting point and increases as the soil approaches saturation (Neitsch *et al.*, 2011).

According to Krishi (2013), the SCS-CN method is based on the water balance equation and two basic hypotheses. The first hypothesis equates the ratio of the actual amount of direct surface runoff Q_s to the total rainfall for the day R_d , or the maximum potential surface runoff to the ratio of the amount of actual infiltration F to the amount of the potential maximum water retention S of soil. The second hypothesis relates to the initial abstraction (I_a) to the potential maximum retention. Thus, the SCS-CN method is represented as follows:

Water balance equation:

$$R_d = I_a + F + Q_s \quad (3.4)$$

Proportional Equality Hypothesis:

$$\frac{Q_s}{R_d} - I_a = \frac{F}{S} \quad (3.5)$$

$I_a - S$ Hypothesis:

$$I_a = \alpha S \quad (3.6)$$

Upon combining equations 3.4 with 3.5, the SCS-CN equation becomes:

$$Q_s = \frac{(R_d - I_a)^2}{(R_d - I_a + S)} \quad (3.7)$$

Q_s is the amount of surface runoff on day i , I_a is the initial abstraction on day i , R_d is the rainfall amount on day i , and S is the water retention parameter (Neitsch, J.G. Arnold, *et al.*, 2009; Neitsch *et al.*, 2011). Equation 3.7 is only valid when $R_d \geq I_a$.

Water retention Parameter S for a given curve number CN for the day is represented by the following equation:

$$S = 25.4 \left(\frac{1000}{CN} - 10 \right) \quad (3.8)$$

The initial abstraction I_a is commonly approximated as $0.2S$; thus, equation 3.7 becomes:

$$Q_s = \frac{(R_d - 0.2S)^2}{(R_d - 0.8S)} \quad (3.9)$$

The SWAT Model automatically assigns the SCS-CN based on soil type, landuse type, and treatment of surface conditions. However, the SCS-CN computed by the SWAT model is based on watershed conditions in the United States (US) and does not accurately represent conditions in other parts of the world (Kim *et al.*, 2010). Therefore, the SWAT Model-assigned SCS-CN is adjusted to represent local conditions in Olifants during the calibration process, as described in sections 3.3.3 and 3.3.4.

Antecedent Soil Moisture Condition (AMC) refers to the water content of the upper soil layer in a watershed at a given time prior to a precipitation event (Chow *et al.*, 1988). The SCS defines three AMC conditions based on rainfall limits for dormant and growing season:

- AMC I represents dry soils that have reached or about to reach wilting point

- AMC II represent soils having average soil moisture
- AMC III represent wet soils that have reached field capacity

The SCS-CN values assigned by SWAT represent the AMC II and is denoted by CN_2 . The curve numbers for AMC I (denoted by CN_1) and AMC III (denoted by CN_3), are calculated using equations 3.10 and 3.11, respectively:

$$CN_1 = CN_2 - \frac{20 * (100 - CN_2)}{100 - CN_2 + \exp[2.533 - 0.636 * (100 - CN_2)]} \quad (3.10)$$

$$CN_3 = CN_2 * \exp[0.00673 * (100 - CN_2)] \quad (3.11)$$

According to Neitsch *et al.* (2011) and Pancholi (2015), the CN_2 provided by SWAT Model are for 5% slope. For slopes larger or smaller than 5%, the following formula is provided for adjustment:

$$CN_{2s} = [1 - 2. \exp(-13.86. slp)] + CN_2 \quad (3.12)$$

Where CN_{2s} is the AMC II curve number adjusted for slope, CN_3 is the AMC III curve number for 5% slope, CN_2 is the AMC II curve number for 5% slope, and slp is the average slope for the particular subbasin.

The Rational Method is used to compute the peak runoff rate at any location in the watershed. It is based on the assumption that a steady uniform rainfall rate in time and space will produce maximum runoff when all parts of the watershed are contributing to outflow. This condition is met when the storm duration exceeds the time of concentration. The rational formula is represented by the following equation:

The SCS-CN method translates the rainfall to surface runoff using the following formulation:

$$Q = K * Q_{sc} * i * A \quad (3.13)$$

Where Q is the maximum runoff rate (m^3/s), A is the watershed area (m^2), i is the rainfall intensity (mm/h), Q_{sc} is the surface runoff coefficient, K is the attenuation factor (Hadadin, 2013).

3.3.2.3 Channel flow routing

Flow routing refers to a procedure used to determine the time and magnitude of flow at a point in the watershed based on a known or assumed hydrograph at one or more upstream locations (Chow *et al.*, 1988). The routing phase in SWAT Model is divided into two major categories, namely main channel routing and reservoir routing. In this phase, the hydrologic cycle is defined by the movement of water, sediment, and solutes through the channels and reservoirs to the basin outlet. Channel routing is computed using the **Muskingum routing method** or **variable storage coefficient method**, which are estimated using various derivatives of the kinematic wave model (Neitsch, J.G. Arnold, et al., 2009). SWAT model uses steady-state simulations for channel routing. Steady-state refers to a condition where fluid properties like pressure, temperature, and velocity do not change over time (Julien, 2018).

The kinematic wave model is computed using St. Venant continuity and momentum equations for 1-D flow (Chow *et al.*, 1988; Goodrich, 1992). The continuity equation applies the mass conservation principle, which states, "in any control volume consisting of the fluid (water) under consideration, the net change of mass in the control volume due to inflow and outflow is equal to the net rate of change of mass in the control volume." The continuity equation is represented as follows:

$$\frac{\partial Q}{\partial x} + \frac{\partial A}{\partial t} - q = 0 \quad (3.14)$$

The momentum equation applies conservation of momentum laws, which states, “that the rate of change of momentum in the control volume is equal to the net forces acting on the control volume.” This equation considers external forces that contribute to water movement and is represented by the following formula:

$$\frac{1}{A} \frac{\partial Q}{\partial t} + \frac{1}{A} \frac{\partial}{\partial x} \left(\frac{Q^2}{A} \right) + g \frac{\partial y}{\partial x} - g(S_o - S_f) = 0 \quad (3.15)$$

Where Q is the discharge through the channel (m^3/s), q is lateral inflow (m/s), A is cross-section areas of flow (m^2), S_o is channel bed slope, g is the gravitational acceleration (m/s^2) and S_f is the friction slope.

The kinematic wave model assumes that $S_o = S_f$ and friction and gravity forces balance out each other; that is, it neglects local acceleration, convective acceleration, and pressure terms. Therefore, the equation is reduced to steady-state flow representation. (Chow *et al.*, 1988)

Variable Storage Routing Method:

Variable storage routing is based on the continuity equation described by Williams (1975) and Nguyen *et al.* (2018). The equation is represented as follows:

$$I - O = \frac{dS_\omega}{dt} \quad (3.16)$$

Where I and O respectively denote inflow and outflow rates (m^3/s) for a river reach, t is time, and S_ω is storage (m^3). When equation 3.15 is discretized by time Δt (s), it becomes:

$$\Delta t \cdot \frac{I_1 + I_2}{2} - \Delta t \cdot \frac{O_1 + O_2}{2} = S_{\omega 1} - S_{\omega 2} \quad (3.17)$$

Where subscripts 1 and 2 refer to start and end of the routing time interval Δt (s), respectively. Equation 3.16 can be rearranged to have the following terms:

$$I_a + \frac{S_{\omega 1}}{\Delta t} - \frac{O_1}{2} = \frac{S_{\omega 2}}{\Delta t} + \frac{O_2}{2} \quad (3.18)$$

Equation 3.18 can be re-written as follows to obtain a relationship between the storage coefficient and travel time as follows:

$$I_a + \frac{S_{\omega 1}}{\Delta t} - \frac{O_1}{2} = I_a + \frac{S_{\omega 2}}{\Delta t} + \frac{O_2}{2} \quad (3.19)$$

$$O_2 = \left(\frac{2\Delta t}{2T + \Delta t} \right) \cdot I_a - \left(1 - \frac{2\Delta t}{2T + \Delta t} \right) \cdot O_2 \quad (3.20)$$

$$O_2 = c \cdot \left(I_a + \frac{S_{\omega 1}}{\Delta t} \right) \quad (3.21)$$

Where C is the storage coefficient represented by the following equation:

$$C = \frac{2\Delta t}{2T + \Delta t} \quad (3.22)$$

Condition $s \leq 1$ must be satisfied in order to achieve a logical, physical representation (Nguyen *et al.*, 2018).

3.3.3 Model setup

The setup is performed in QSWAT (SWAT version 2012 in the QGIS environment). The overall model set-up and is illustrated in Figure 3-10. Following the guide provided by QSWAT User Manual by Arnold *et al.* (2012), Dile *et al.* (2015) Dile *et al.* (2017), SWAT Model was set-up in the following steps:

- Watershed delineation, where QSWAT uses GIS tools and the DEM to define the drainage characteristics of the river basin and its boundaries.
- Definition of Hydrological Response Units (HRUs); this refers to the sub-division of basins into smaller units, each of which has a particular soil, LULC class, and slope range.
- Database building, which involves uploading and writing of hydro-meteorological data, and editing of various known parameters to reflect conditions of the study area.
- Model calibration, validation, and sensitivity analysis

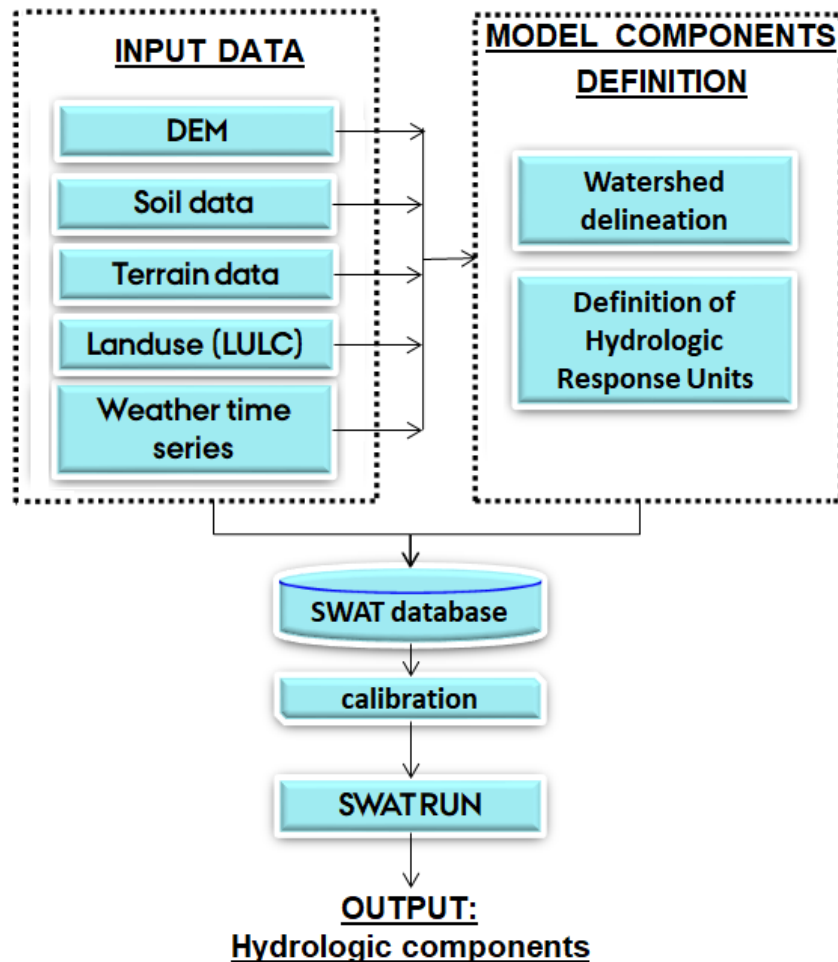


Figure 3-9: Schematic illustration of Model setup

3.3.3.1 Data description

The SWAT Model has five different categories of input data for purposes of hydrological modelling that is shown in Figure 3-9, and described as follows:

Digital Elevation Model (DEM): It is a gridded digital representation of terrain, with each pixel value that corresponds to a height above a given datum (Hawker *et al.*, 2018). DEM is used in SWAT Model in the watershed delineation phase to extract terrain information like slope and drainage pattern. DEM for this research was obtained from Advanced Land Observing Satellite (ALOS) (Earth Observation Research Center Japan Aerospace Exploration Agency (JAXA), 2019). The DEM has a spatial resolution of 30x30 m grid. Error correction, coordinate projection, and conditioning of the DEM is conducted using the watershed delineation Tool in SWAT Model. The DEM used in this research and the river network developed from it is shown in Figure 3-10.

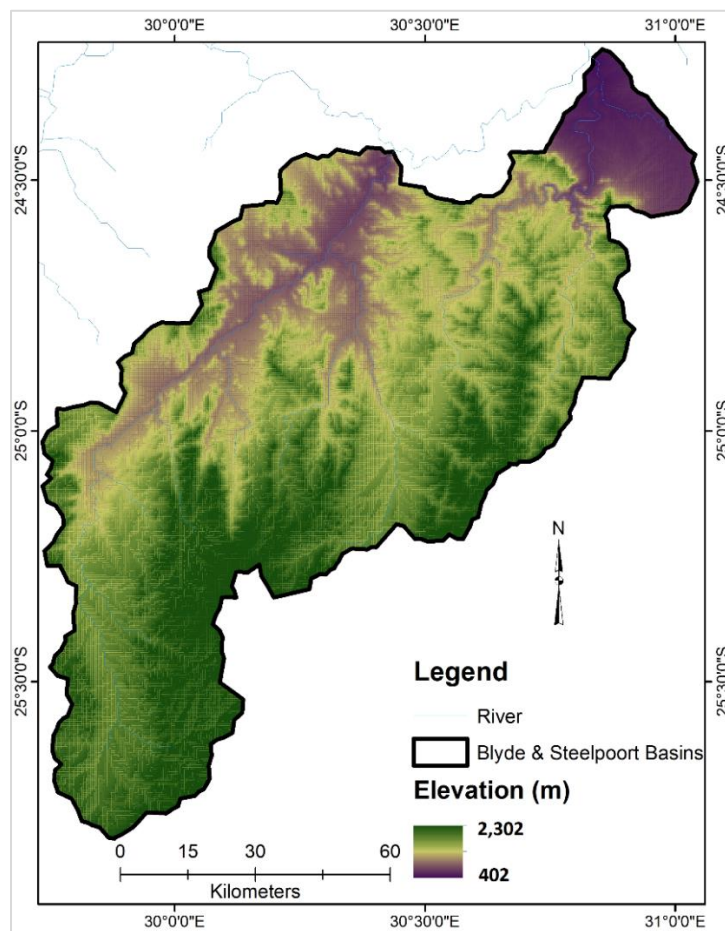


Figure 3-10: Elevation and river network map(Source: ALOS DEM)

Soil distribution map: was obtained from the Food and Agriculture Organization (FAO). The mask for the study area has seven different soil classes, which are described in Table 3-9 and illustrated in Figure 3-10. The soil has a spatial resolution of 7x7 km grid, and its properties have been compiled from UNESCO and FAO (1995, 2003), NRCS (2007), Jin *et al.* (2015), and Abraham *et al.* (2020).

QUANTIFICATION OF LULC CHANGE AND ITS IMPACTS ON HYDROLOGY

Table 3-9: Soil classes in Steelpoort and Blyde River Basins with their corresponding texture classes and hydrologic group

	Soil Code in Fig 3-10	Soil composition	Texture	HSG
1	887	Chromic vertisols	Clay	D
2	886	Orthic Acrisols	Sandy_Loam	C
3	725	Chromic Luvisols	Sandy_Clay_Loam	C
4	722	Chromic Luvisols with traces of Orthic Luvisols, Ferric Luvisols, and Lithosols	Sandy_Clay_Loam	C
5	575	Cambic Arenosols with traces of Orthic Solonetz and Eutric Planosols	Sandy_Loam	C
6	434	Cambic Arenosols with traces of Luthosols, Chromic Luvisols, and Ferric Luvisols	Sandy_Loam	C
7	262	Chromic Vertisols	Clay	D

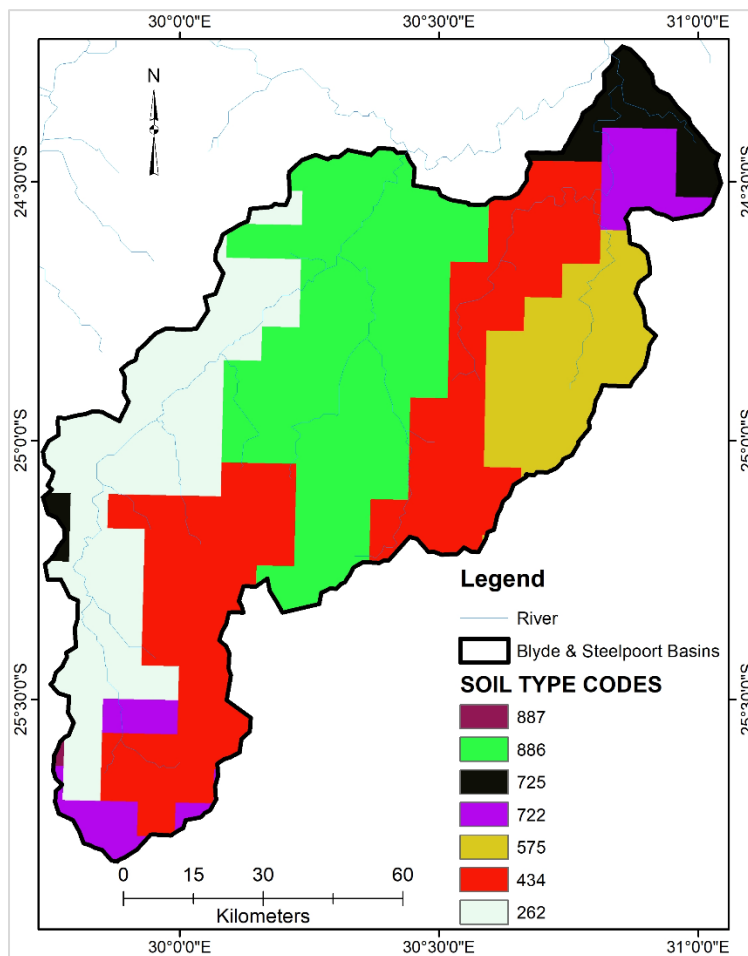


Figure 3-11: soil distribution map for Steelpoort and Blyde River Basins (Source: FAO)

LULC data: it is prepared from LANDSAT 5, 7 & 8 satellite images as described in section 3.1. LULC is static during the modelling period. The LULC data have a spatial resolution of 30X30 m grid and are as shown in Figure 3-7 in section 3.2.4.

Maximum temperature (°C), minimum temperature (°C), and precipitation (mm); these data sets were obtained from the University of East Anglia Climate Research Unit (CRU TS 4.0) database. The raw data is gridded, has a monthly temporal resolution and a spatial resolution of 0.5°. Since the required weather input in SWAT Model should be in daily time-step, the CRU data was decoupled to daily time steps using the MODAWEC program. The decoupling process is described in section 2.1. The data were interpolated to a resolution of 0.125° using Inverse Distance Weighting (IDW) tool in ArcGIS.

IDW was developed by the U.S National weather Services in 1972 and is based on Tobler’s first law of geography, which states that “everything is related to everything, but near things are more related than distant things (Chen and Liu, 2012; Ahrens, 2005). The IDW is formulated as follows:

$$R_0 = \frac{\sum_{\alpha=1}^n R_{\alpha} W_{\alpha}}{\sum_{\alpha=1}^n W_{\alpha}} \quad (3.23)$$

$$W_{\alpha} = \frac{d_i^{-\alpha}}{\sum_{i=1}^n d_i^{-\alpha}} \quad (3.24)$$

Where R_0 is the unknown rainfall data (mm), R_{α} is the known rainfall data, n is the number of rainfall stations, W_{α} is the weighting for each rainfall station, d_i is the distance from each rainfall station with known data to the station with unknown data, γ is the power and control parameter.

Relative humidity (%), wind speed (m/s), and solar radiation (Wm^{-2}) were simulated from SWAT in-built weather generator (Neitsch, J.G. Arnold, *et al.*, 2009). To simulate meteorological data in the SWAT Model, a weather database, which shows the average annual values of each type of data for at least ten years, should be created. Because of data scarcity, the Climate Forecast System Reanalysis (CFSR) data were used to prepare the weather database for using the SWAT Weather Database program. CFSR is a product of the National Centers for Environmental Prediction (NCEP) and has been successfully applied in hydrological modelling by many researchers like Fuka *et al.* (2014) and Dile *et al.* (2016). SWAT Weather Database is a tool developed by Essenfelder (2018) and is a recognized supporting tool for data preparation in SWAT Modelling.

Reservoir operations and water use data were obtained from South Africa’s Department of Water and Sanitation (DWS) and WRSM2012/ Pitman database (Middleton and Bailey, 2008; Bailey, 2012).

3.3.3.2 Definition of Hydrologic Response Units (HRUs)

HRU definition phase allows the user to upload LULC and soil distribution files. The Model automatically subdivides the watershed into smaller areas based on soil type, slope class, and LULC class. SWAT Model allows the user to define six slope classes between 0-100%. Figure 3-12 shows the map of slope classes used in this research.

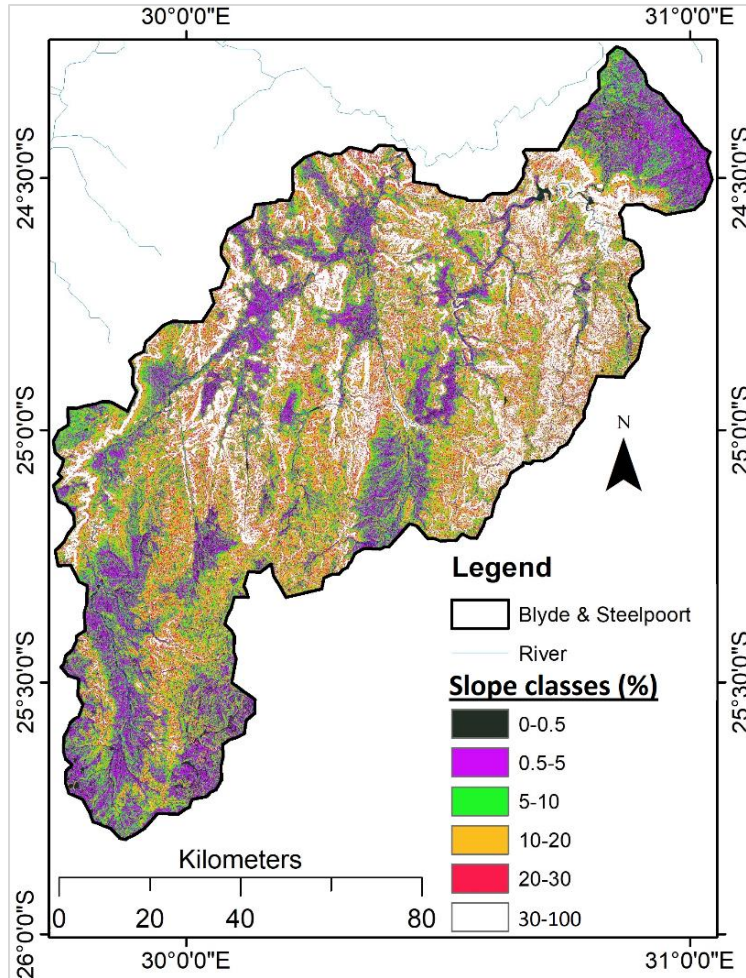


Figure 3-12: Slope classes derived from DEM

3.3.3.3 Building of SWAT Model Database

This step involves uploading of meteorological time series, reservoir operation, water use data, and adjustment of CN_2 value to reflect the slope conditions of the study area. CN_2 is adjusted using equation 3.12. final CN_2 values for the various slope classes are summarized in Table 3-9.

QUANTIFICATION OF LULC CHANGE AND ITS IMPACTS ON HYDROLOGY

Table 3-10: Summary of Hydrologic Soil Groups and their corresponding original and slope-adjusted CN_2

LULC	H S G	AREA (km^2)	CN_2	CN_1	CN_3	CN_2 for various slope classes					
						0-0.5% slope	0.5-5% slope	5-10% slope	10-20% slope	20-30% slope	30-100% slope
Agriculture	C	378	83	71	93	80	82	85	86	86	86
	D	182	87	76	95	85	86	88	89	90	90
Dense Forest	C	1076	70	55	86	65	68	73	75	75	75
	D	101	77	63	90	73	76	79	81	81	81
Grassland	C	2268	79	66	91	75	78	81	82	83	83
	D	514	84	72	94	81	83	86	87	87	87
Herbaceous Vegetation	C	159	79	66	91	75	78	81	82	83	83
	D	106	84	72	94	81	83	86	87	87	87
Sparse Forest	C	207	77	63	90	72	75	79	80	81	81
	D	33	82	70	93	79	81	84	85	85	86
Shrubland	C	3810	74	60	88	70	72	76	78	79	79
	D	1110	80	67	92	76	79	82	83	84	84
Urban area	C	8	72	57	87	67	70	74	76	77	77
	D	2	79	66	91	75	78	81	82	83	83

3.3.4 Model Calibration and sensitivity analysis

Hydrological simulations were conducted for 25 years (1990-2014), with a warm-up period of three years (1987-1989). Model calibration was based on a 13-year (1990-2002) simulations, while validation was based on a 12-year (2003-2014) simulations. To investigate the influence of LULC change on hydrology in the Steelpoort and Blyde River Basins, the SWAT Model is set-up for three scenarios based on 1992, 2002, and 2014 LULCs. The 1998 LULC was not used because of minimal differences from the preceding 1992 LULC. The 1992 LULC was selected as the baseline scenario, with which both calibration and validation of the model were conducted.

The calibration process was done using both the manual approach and Sequential Uncertainties Fitting Algorithm, Ver-2 (SUFI-2). SUFI-2 is a semi-automated approach used for calibration, validation, uncertainty analysis, and sensitivity analysis (Abbaspour, Vaghefi, and Srinivasan, 2017; Kouchi *et al.*, 2017). Calibration of the hydrologic model is conducted based on discharge data at eleven gauging stations; B6H005, B4H003, B6H001, B4H010, B4H003, B4H005, B4H007, B4H009, B42H, B60J, and B4H025 shown in Figure 3-14. Simulated discharge data from WRSM/Pitman Model (Middleton *et al.*, 2008) are used for discharge calibration at stations B42H and B60J, and for gap-filling of calibration data from station B4H025.

The goodness fit of the model is then assessed using Nash-Sutcliffe Efficiency (NSE) and the coefficient of determination (R^2). Coefficient of determination measures the degree of linear association between modelled and observed values and is defined by the following equation:

$$R = \frac{\sum_{t=1}^n (x_t - \bar{x})(y_t - \bar{y})}{\sqrt{\sum_{t=1}^n ((x_t - \bar{x})^2) \sum_{t=1}^n (y_t - \bar{y})^2}} \quad (3.25)$$

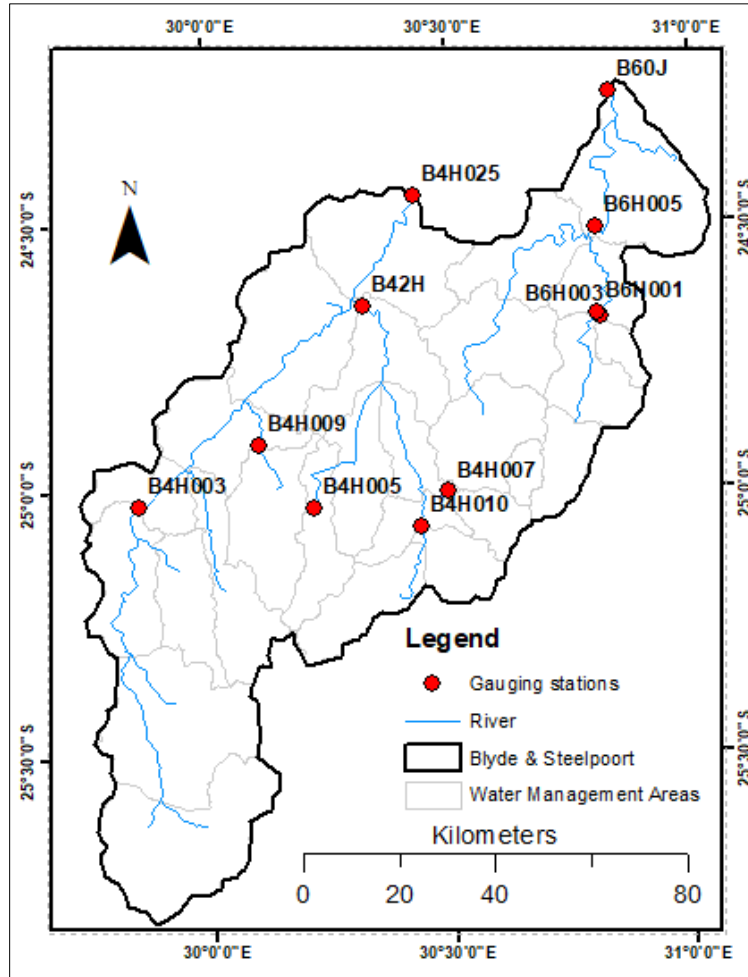


Figure 3-13: Location map of River gauging stations used for model calibration

Where x_t and y_t are the modelled (GCM) and observed variable at t time step (months), \bar{y} is the mean of observed data, \bar{x} is the mean of modelled data, and n is the total number of observations. The coefficient of determination varies within the interval $[-1, 1]$, where values close to 1 indicate a good fit (López *et al.*, 2017).

Nash-Sutcliffe Efficiency (NSE) was proposed by Nash and Sutcliffe (1970), it is a normalized statistic that describes the relative magnitude of the residual variance as compared to the observed and demonstrates how well the plot of observed versus simulated value fits the 1:1 line. The following formula represents NSE:

$$NSE = 1 - \frac{\sum_{t=1}^n [x_t - y_t]^2}{\sum_{t=1}^n [y_t - \bar{y}]^2} \quad (3.26)$$

Where x_t and y_t are the modelled (GCM) and observed variable at t time step (months), \bar{y} is the mean of observed data, \bar{x} is the mean of modelled data, and n is the total number of observations. NSE varies from $-\infty$ to 1, with values close to 1 indicate a good fit (López *et al.*, 2017).

In SUFI-2, parameter uncertainty accounts for all sources of uncertainties, such as the model forcing and model processes. The level of uncertainty is measured by a statistical parameter referred to as 'p-factor,' which is the percentage of measured data falling within the 95% prediction uncertainty (95PPU). The

QUANTIFICATION OF LULC CHANGE AND ITS IMPACTS ON HYDROLOGY

95PPU is calculated at 2.5% and 97.5% of the cumulative distribution of an output variable obtained through Latin hypercube sampling (Singh *et al.*, 2014). The Latin hypercube sampling (LHS) is a statistical approach used to generate a near-random sample of parameter values from a multidimensional distribution. In SUFI-2, the LHS is used to generate the parameters that are selected for calibration with a specified parameter range (Yang *et al.*, 2008).

The p-factor is the fraction of measured data and its error, bracketed by the 95PPU band. The p-factor varies from 0 -1, where 1 indicates 100% of the measured data falls within the 95PPU bracket and represents a perfect model simulation (K.C. Abbaspour *et al.*, 2015; López *et al.*, 2017). According to K.C. Abbaspour *et al.* (2015), a p-factor > 0.7 is considered adequate for hydrological modelling

The 'r-factor', also computed by SUFI-2; it is the ratio of the average width of the PPU band and the standard deviation of the measured variable. A value < 1 is a desirable measure for the r-factor. The degree to which the values deviate from these numbers can be used to judge the strength of the calibration (K.C. Abbaspour *et al.*, 2015; López *et al.*, 2017; Abbaspour *et al.*, 2019; Rouholahnejad *et al.*, 2012; Vasel *et al.*, 2015; López *et al.*, 2017). The p-factor and the r-factor are used to measure the strength of the calibration

K.C. Abbaspour *et al.*, 2015 stresses the necessity of striving to balance the r-factor and p-factor, since a large value of p-factor can be achieved at the expense of the r-factor

3.3.5 Results: Model calibration and validation

Table 3-11 shows the calibration and validation results of river discharge at eleven various locations; satisfactory model performance is achieved at seven stations during the calibration period; out of these eleven stations, the model performed satisfactorily at eight stations during the validation period. The model had p-factor > 0.7 at four stations during the calibration period and r-factor < 1 at five stations. The r-factor and p-factor were only obtained during the calibration period with the best parameters obtained directly used in model validation.

In conclusion, the model generally showed good capability to simulate streamflow at most locations of the river basins.

Table 3-11: Discharge calibration and validation model performance statistics

	Station	Calibration (1990-2002)				Validation (2003-2014)	
		NSE	R^2	p-factor	r-factor	NSE	R^2
1	B6H005	0.67	0.67	0.55	0.94	0.65	0.68
2	B6H003	0.55	0.69	0.24	0.37	0.52	0.63
3	B6H001	0.75	0.81	0.53	0.8	0.71	0.80
4	B6H025	0.5	0.5	0.46	0.46	0.42	0.4
5	B4H010	0.50	0.58	0.76	1.99	0.46	0.60
6	B4H009	0.23	0.4	0.73	1.87	0.20	0.2
7	B4H007	0.64	0.6	0.52	0.37	0.62	0.62
8	B4H005	0.63	0.7	0.92	2.62	0.63	0.72
9	B4H003	0.36	0.41	0.86	6.5	0.3	0.40
10	B42H	0.77	0.81	0.09	1.19	0.70	0.79
11	B60J	0.79	0.79	0.1	1.51	0.81	0.77

QUANTIFICATION OF LULC CHANGE AND ITS IMPACTS ON HYDROLOGY

Table 3-12 summarizes the average values of parameters that were finally obtained after calibration of the SWAT Model. The calibrated parameters for the individual sub-basin are summarized in Appendix II. Table 3-12 also shows the ranking of parameter sensitivity as obtained from the SUFI-2 Algorithm. Nineteen parameters were used, where Curve Number (CN_2) and Soil Available Water (SAW) exhibiting the highest overall sensitivity in all the sub-basins.

Table 3-12: Average calibrated parameters' values

Rank	Parameter	Parameter description	Allowable Range	Calibrated values
1	CN_2	Curve number	35 - 98	61.05
2	SOL_AWC	Soil available water	0 - 1	0.20
3	SOL_Z	Active soil depth	0 - 3,500	456.90
4	ALPHA_BF	Baseflow factor	0 - 1	0.31
5	GWQMN	Water depth threshold in shallow aquifer required for return flow to occur	0 – 5,000	2013.32
6	ESCO	Soil evaporation compensation factor	0 – 1	0.33
7	EPCO	Plant uptake compensation factor	0 – 1	0.28
8	SOL_K	Saturated hydraulic conductivity	0 – 2,000	17.97
9	CH_N2	Manning's roughness for channel flow	-0.01 – 0.3	0.18
10	OV_N	Manning's roughness for overland flow	0.01 – 1	0.51
11	GWHT	Initial groundwater height	0 - 25	13.57
12	HRU_SLP	HRU slope	0 - 1	0.15
13	GW_SPYLD	Specific yield from shallow aquifer	0 – 0.4	0.20
14	SURLAG	Lag time of surface runoff	0 - 25	2.08
15	GW_DELAY	Groundwater delay	0 - 500	186.51
16	REVAPMN	Water depth threshold in shallow aquifer required for "revap" to occur	0 – 1,000	475.65
17	GW_REVAP	Factor of water movement from shallow aquifer to top soil layer	0.02 – 0.2	0.08
18	CH_K2	Channel's effective hydraulic conductivity	-0-01 - 500	87.77
19	SLSUBBSN	Average slope length for flow saturation	10 - 150	55.44

According to Abbaspour *et al.* (2019), Rafiei Emam *et al.* (2018), Liu and Gupta (2007), Renard *et al.* (2010), and Abbaspour *et al.* (2017), outputs of hydrological modelling are subject to uncertainty due to errors from different sources; these errors can arise from the data, model structure and model parameters. Evaluation of this uncertainty in hydrological modelling informs the consumers of the information the degree of reliability of the outputs (Rafiei Emam *et al.*, 2018). In this research, the potential sources of uncertainties in the hydrological outputs are as follows:

Meteorological data:

Rainfall and temperature data are obtained from the University of East Anglia Climate Research Unit. This data is in monthly time step but decoupled using the MODAWEC (Liu, Williams, *et al.*, 2008) program; the program uses the probability of wet days tie series to produce daily rainfall and temperature data stochastically. While the outputs of MODAWEC in the current study and other in different studies by Liu,

Fritz, *et al.* (2008) Liu, Williams, *et al.* (2008) have shown good performance in producing the daily time series, some biases are still detected which could transfer to the hydrological simulations.

The solar radiation, wind speed, and relative humidity belong to the Climate Forecast System Reanalysis data group; this data is from satellite sources, compiled by National Centers for Environmental. According to Tian *et al.* (2009 and Ramírez- Beltrán *et al.* (2019), satellite data are prone to bias errors, which are subsequently transferred to the model outputs.

LULC data, Soil data, and Elevation data:

LULC maps prepared in Section 3.2 are used in hydrological modelling; despite acceptable results during validation (Section 3.2.1), these maps are subject to errors as shown by the degree of accuracy. These errors are transferred to the model processes and subsequently to the output as well. The exact contribution of these errors to hydrological modelling cannot be single out. However, under the modelling process, all sources of errors are quantified using the SUFI-2 algorithm.

The soil map has a very coarse resolution of 7 km grid, which presents a generalized classification; this does not present the actual variability that exists on the ground. This errors can be transferred to the mode leading to additional uncertainties.

A DEM of 30 km grid has been used in the modelling exercise; this may be too coarse when defining features that have smaller widths.

Quantification of uncertainties:

The SUFI-2 algorithm, which is used in the SWAT Model calibration, also estimates parameter uncertainties. The indices that are used to measure the uncertainty in model prediction are the r-factor and the p-factor. Calibration was conducted at 11 stations, out of which four stations had p-factor > 0.7 and had five stations r-factor < 1. Therefore, it can be concluded that the calibration outputs from 9 stations are relatively reliable, whereas the output from two stations have high uncertainty and hence low reliability.

These uncertainties have implications on the discharge and are also transferred to subsequent processes modelled using the calibrated model.

3.3.6 Results: Hydrological impacts of LULC change

Calibrated parameters were used to set-up the SWAT Model for two additional scenarios based on 2002 and 2014 LULCs. The meteorological data was kept constant (data used in the calibration step was also applied in simulating the two new scenarios). Hydrological change analysis due to LULC change was conducted by:

Comparing the average annual values for evapotranspiration, surface runoff, and groundwater recharge, lateral flow, and groundwater flow.

Assessing shifts in monthly discharge curves based in 1992 and 2014 LULC data. Discharge at four locations was analyzed; B4H025 (Outlet of Steelpoort River), B4H003 (Steelpoort mid-section), B42H outlet (Steelpoort mid-section), and B60J outlet of Blyde River.

Figure 3-14 shows the graphical presentation of various hydrological parameters based on 1992, 2002, and 2014 LULC scenarios: Surface runoff is with continued LULC changes. There were slight changes in

QUANTIFICATION OF LULC CHANGE AND ITS IMPACTS ON HYDROLOGY

aquifer recharge and lateral flow where there was a decrease throughout the season. There was variability in evapotranspiration with a general decrease from the initial state; the biggest changes were seen under 2002_LULC where there were major loss of forests in the

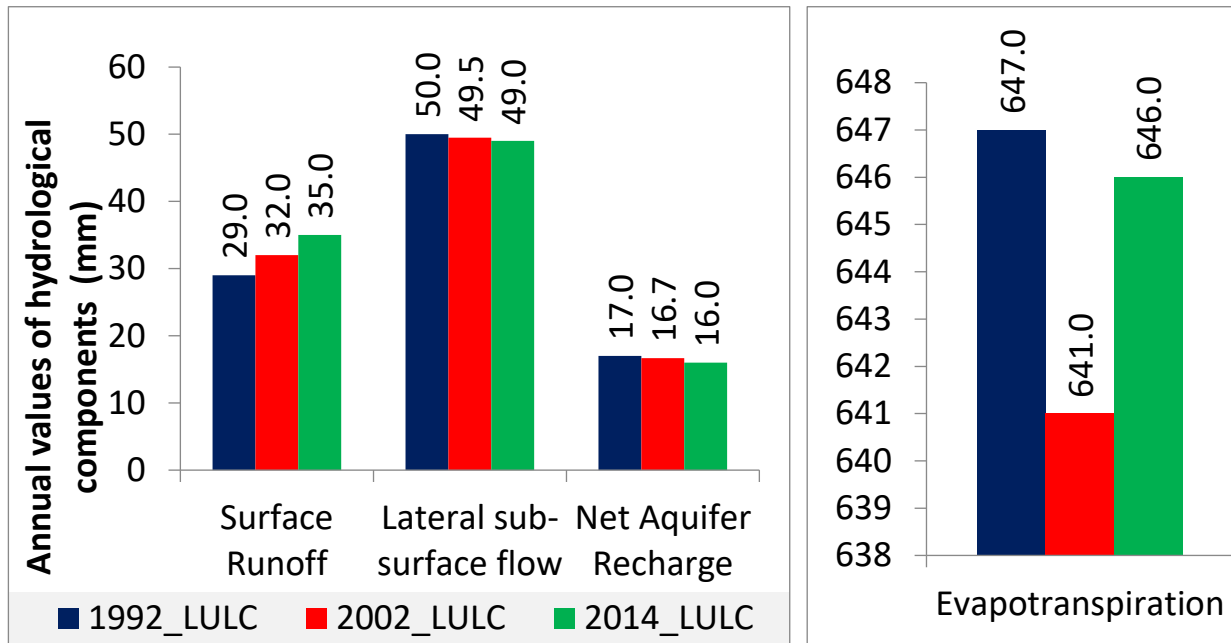


Figure 3-14: Changes in hydrological parameters due to LULC changes

Figure 3-15 shows the shift discharge curves at various locations in the two river basins. Based on the 2014 LULC data, there is an increase of discharge at stations B4H003, B4H025, B42H Outlet, and Blyde (B60J) outlet. The timing of these shifts and their magnitudes are different and could be attributed to the location and extent of LULC changes, which are shown in Figure 3-7.

An upward shift in the discharge at station B4H003 can be attributed to an extensive expansion of agriculture in the upstream section (identified by Area 3 in Figure 3-7) of the station. The area lies in the headwaters; therefore, the increase in discharge is much larger in comparison to discharge at other locations.

The smaller shift in discharge curves at station B42H can be attributed to a lesser expansion of agriculture in Area 2 in comparison to Area 3. Agricultural expansion in Area 2 also occurs closer to the sub-basin outlet and not headwaters; hence the impact on discharge can be lower. In Area 2, extensive loss of forest, which is usually responsible for high evapotranspiration rates, also occurs between 1992 and 2002 LULC; hence evapotranspiration rates are significantly reduced under the 2002 LULC scenario.

In the Blyde River Basin, expansion of agriculture is in the lower areas; near the basin outlet, therefore the shift in discharge curve comes earlier in the season and normalizes during the peak, as shown in Figure 3-15.

While the peak seasons (beginning of October until end of May) exhibit increase in discharge due to LULC changes in all the four stations, there were no distinct changes in low flow seasons (from May to September); this means that the impact on baseflow is very minimal

QUANTIFICATION OF LULC CHANGE AND ITS IMPACTS ON HYDROLOGY

Figure 3-16 shows the spatial distribution of changes in various hydrological components resulting from LULC changes. Changes in surface runoff are prominent in areas where landuse is transitioned to agricultural land. There was a predominant decrease in evapotranspiration in areas where forest losses were observed and an increase in areas where agricultural land was expanded. Generally, there were minimal changes in lateral flow.

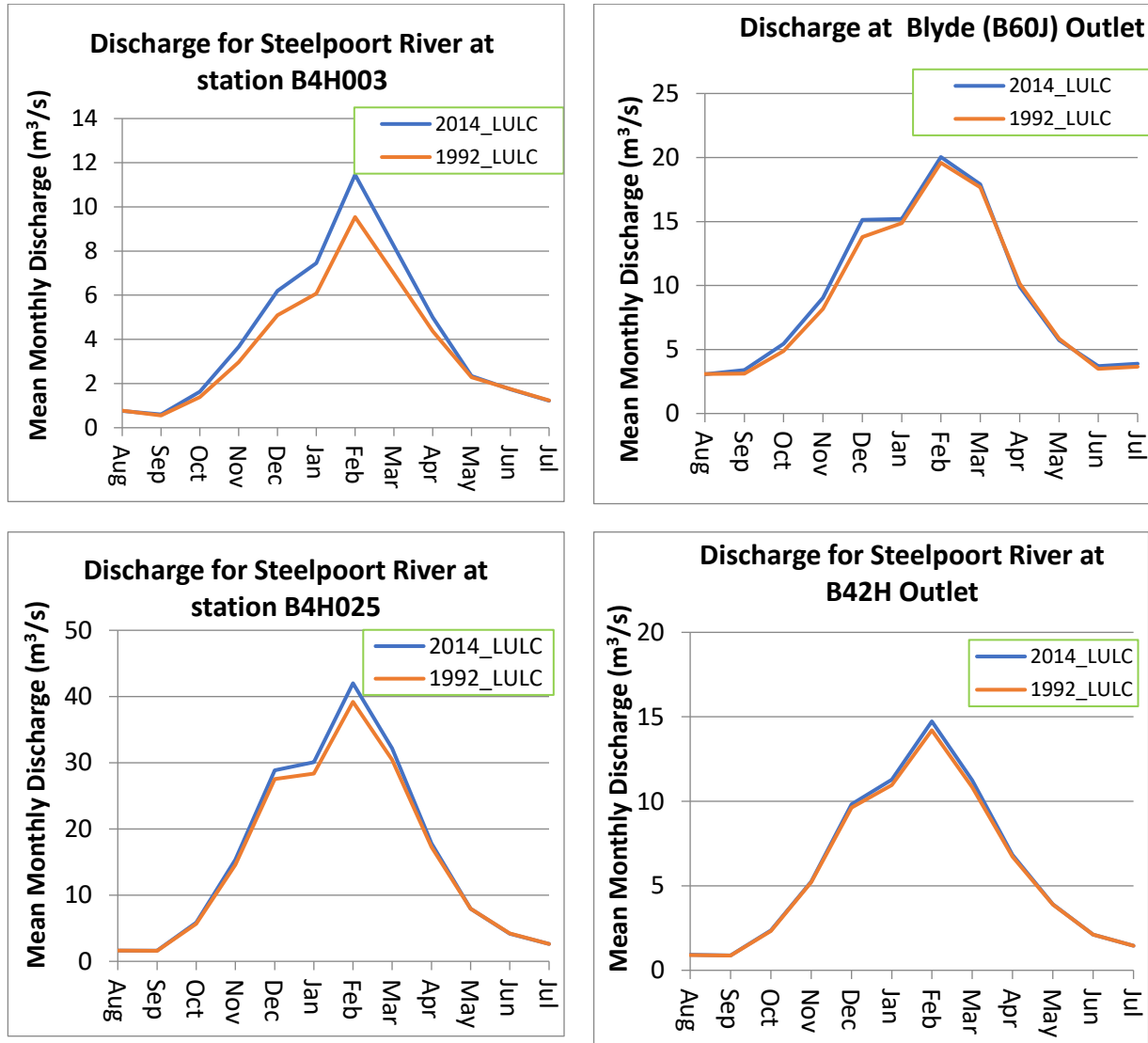


Figure 3-15: Shift in mean monthly discharge curves in the basins due to 1992-2014 LULC change

QUANTIFICATION OF LULC CHANGE AND ITS IMPACTS ON HYDROLOGY

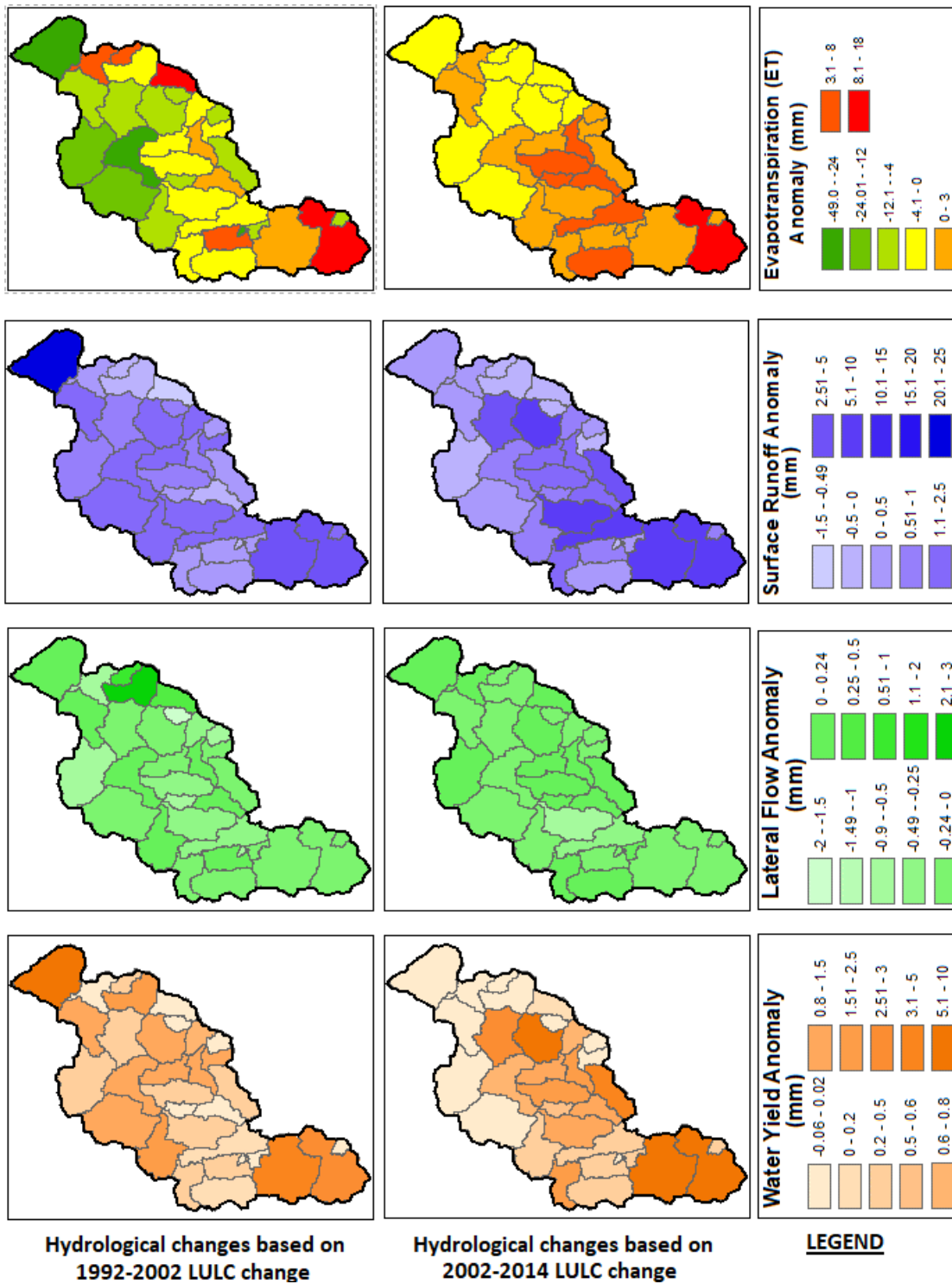


Figure 3-16: Spatial anomalies of various hydrological components due to LULC changes

3.4 Discussions

The objective of this chapter is to quantify LULC changes using remote sensing images and quantify its impacts on hydrological partitioning in Steelpoort and Blyde River Basins. Remotely sensed images from LANDSAT 5, 7 & 8 were used to prepare LULC maps for four different epochs (1992, 1998, 2002 and 2014). LULC change detection revealed that major changes were largely driven by agricultural landuse activities with an increase of 514 km² from 1992 to 2014. Other increments in LULC were in water bodies due to the construction of water storage facilities and in urban areas. Major losses in landuse are in forest cover, grassland, and shrubland; these losses are largely attributed to agriculture expansion.

To assess the impacts of LULC on the hydrology of the Blyde and Steelpoort River Basins, SWAT Model was used in hydrological simulations for three scenarios based on 1992, 2002, and 2014 LULC data. 1998 LULC was not used since there were very minimal differences observed in this period, as seen in Figure 3-7 and Table 3-5. 1992 LULC was used as the baseline scenario, where calibration and validation of the model were conducted.

Analysis of the hydrological outputs from the three scenarios of the SWAT Model revealed the following general changes:

- Increase in peak discharge
- Increase in surface runoff and decrease in aquifer recharge, especially in areas where agricultural expansion occurred.
- Evapotranspiration decreased significantly, especially in the period (1992-2002) when the loss of forest cover was significant.

The outcomes of this chapter have revealed that changes in landuse in the Blyde and Steelpoort River Basins have significant impacts on hydrology, especially on surface runoff patterns and evapotranspiration. Human activities like agriculture are the main drivers of LULC changes in the river basins; therefore, it should be undertaken with careful planning and moderation to conserve the ecosystem.

In this LULC planning approach, the identification of morphological parameters is conducted at the sub-basin scale, which has a coarse spatial resolution. The output is then scaled down to a higher resolution of 1200 m. Low-resolution data can be a large cause of prediction uncertainty in hydrology (Hawker *et al.*, 2018).

4 ADAPTATION OF AGRICULTURAL LANDUSE PLANNING TO IMPROVE MITIGATION OF IMPACTS ON HYDROLOGY

4.1 Background

Human's effort to meet their livelihood needs has led to extensive modification of landscapes around the world. The ecological consequences of these actions include the translocation of nutrients, altered hydrological systems, and the loss/change of biodiversity. The increasing global population is driving up demand for land and therefore necessitating a careful balance between competing for landuse activities and ecological needs. Landuse planning, therefore, emerges from the societal aspiration to improve management, sustainably harness the land resources, and to prevent/mitigate negative environmental impacts of landuse activities (Food and Agriculture Organization, 1993).

FAO, 1993 describes landuse planning as a structured evaluation of land and water potential, alternatives for landuse activities, and socio-economic conditions to identify and adopt ecologically sustainable options. The previous chapter of this research reveals extensive human-driven landuse changes in the Blyde and Steelpoort river basins, which subsequently lead to alteration of the hydrological regimes. An increase in surface runoff is the major change observed and is attributed to the expansion of agricultural activities. In this region where river flow is dominated by baseflow, an increase of surface runoff translates to a decrease in baseflow, potentially resulting in increased water scarcity in low flow seasons. The background of this research also highlights the susceptibility of this study area to further changes in landuse from agricultural development, which would subsequently magnify the impacts on the hydrological regime.

The existing approach for identifying sites suitable for agriculture follows an on-demand and mostly site-specific studies through Environmental Impacts Assessment. The shortcomings of this approach are that limited alternative sites are because of time and economic factors, whereas there could exist more suitable sites.

Besides, the parameters used to assess impacts on hydrological flows are not extensively explored since they are limited to slope characteristics and soil drainage conditions. However, other morphological parameters define hydrological characteristics of the basin, and they could be utilized as additional analyzers in EIA studies. There is also a limited exploration of the role of morphology, which has the potential to limit or augment the hydrological reactions.

Therefore, the objective of this chapter is to develop an approach for agricultural landuse planning to enhance mitigation of changes in the hydrological regime that result from agricultural expansion, identify

ADAPTATION OF AGRICULTURAL LANDUSE PLANNING TO IMPROVE MITIGATION OF IMPACTS ON HYDROLOGY

morphological parameters and their approximate thresholds to be utilized in site evaluation for agricultural use, and to develop future landuse scenarios and their corresponding hydrological scenarios. To achieve this, the entire study area is analyzed to identify the best areas for agricultural use following steps:

- Identification of LULC classes that exhibit a similar hydrological response to agriculture; these LULC classes will be selected for replacement with agriculture to achieve minimal changes in hydrology.
- Identification of “hydrologically suitable” morphological features for agricultural use; Morphological features that exhibit minimal anomalies under agricultural expansion are identified and selected as the best sites for agricultural land establishment.

This approach will be developed and tested by recreating the 2014 LULC using the 1992 LULC as the baseline scenario. The target area for agricultural expansion is approximately 513 km^2 , an equivalent to expansions observed in the actual scenario outlined in section 3.2.4. The hypothetical 2014 LULC will be used in hydrological simulations that will then be evaluated against the hydrological outputs from the actual 2014 LULC and 1992 LULC.

4.2 Identification of LULC classes that exhibit similar hydrological responses to agriculture

The hydrological response is highly sensitive to and dependent on landuse type; each landuse class has a unique hydrological response pattern (Schulze, 2016). To minimize changes in discharge following agricultural expansion, landuse class/classes that exhibit closer or similar hydrological characteristics with agricultural land could be cleared for agricultural use. Identification of landuse type with closer hydrological reactions is quite a complex matter since the influencing factors range from regional climate to underlying morphological conditions;

Studies by Kabantu (2016), Alemayehu *et al.* (2017) and Li *et al.* (2017) indicate that evapotranspiration (ET) from agricultural land relative to ET from the forest, grassland, and shrubland differ in different regions of the world; Figure 4-1 summarizes the findings of this studies.

ADAPTATION OF AGRICULTURAL LANDUSE PLANNING TO IMPROVE MITIGATION OF IMPACTS ON
HYDROLOGY

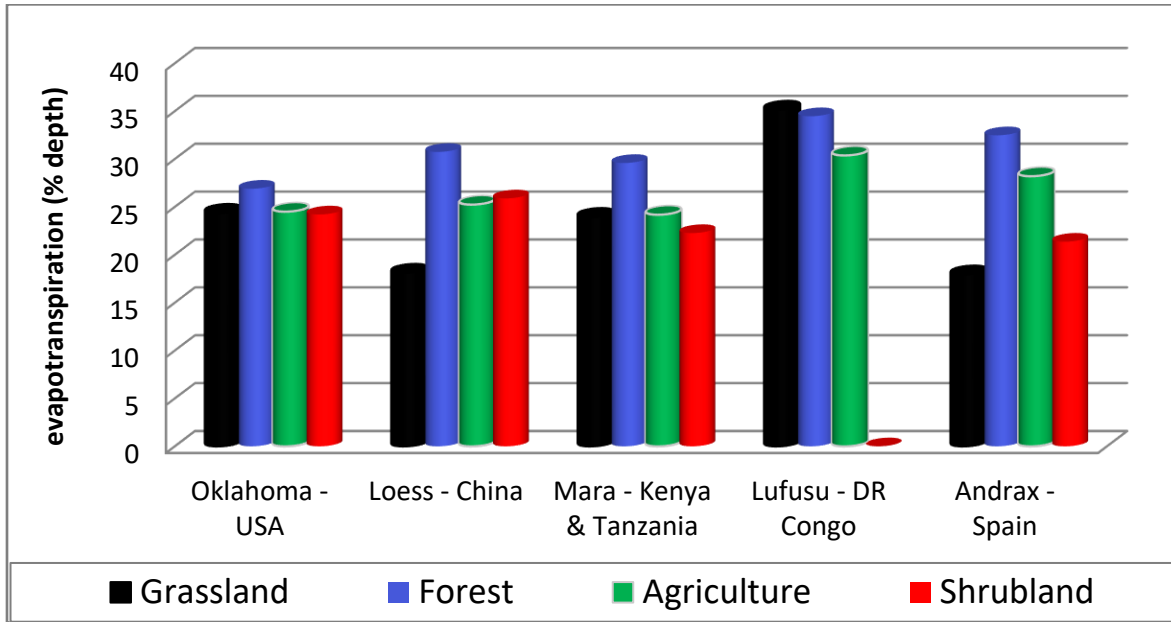


Figure 4-1: Evapotranspiration rates for various landuse categories in different regions

The work of Wang *et al.* (2018) also indicated that forests under steep slopes increase the volume of runoff generation and discharge variability; this pattern of discharge is also observed in gently sloping areas under agriculture. The following are the various characteristics of vegetation that influences hydrological response:

Canopy and Leaf Area Index (LAI): canopy can also refer to the portion of a plant community found above ground formed by the crowns of individual plants; LAI refers to the leaf area per unit ground area. In a vegetated environment, canopy and LAI are responsible for partitioning rainfall into canopy storage (S_c), throughfall (R_T) and stemflow (Q_{st}), as shown in Figure 4-2. Larger canopies and LAI translate to higher evaporation rates and reduced surface wetting (Chow *et al.*, 1988; O'connor *et al.*, 2019; Li, Lin and Levia, 2012; Kunert *et al.*, 2015; Tarigan *et al.*, 2018).

ADAPTATION OF AGRICULTURAL LANDUSE PLANNING TO IMPROVE MITIGATION OF IMPACTS ON HYDROLOGY

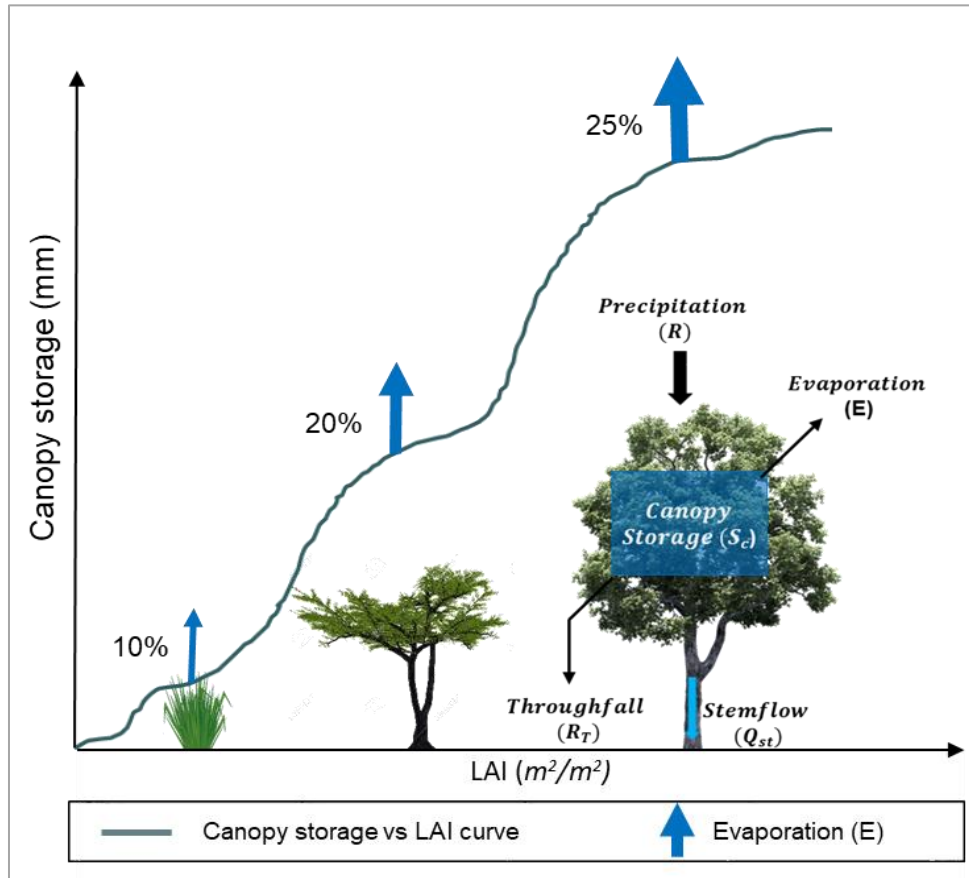


Figure 4-2: Conceptual illustration of canopy storage relationship with leaf area Index, and rainfall partitioning by vegetation canopy

Root depth and density: Deep roots facilitate access to deep soil moisture, which helps to maintain photosynthesis even in dry seasons. Denser roots increase the surface area of water absorption, which results in increasing the water uptake ratio, as shown in Figure 4-3. Evapotranspiration from forests is always high year-round because of their deep and, in some cases, dense root system. Because of this feature, plants with deeper roots tend to cause more lowering of the water table (Kunert *et al.*, 2015; Bates, 2017; Fan *et al.*, 2017; O’connor *et al.*, 2019). Flow-through the soil is also influenced by the root channels, which contribute to the preferential flow pathway (Ghestem, Sidle and Stokes, 2011).

ADAPTATION OF AGRICULTURAL LANDUSE PLANNING TO IMPROVE MITIGATION OF IMPACTS ON
HYDROLOGY

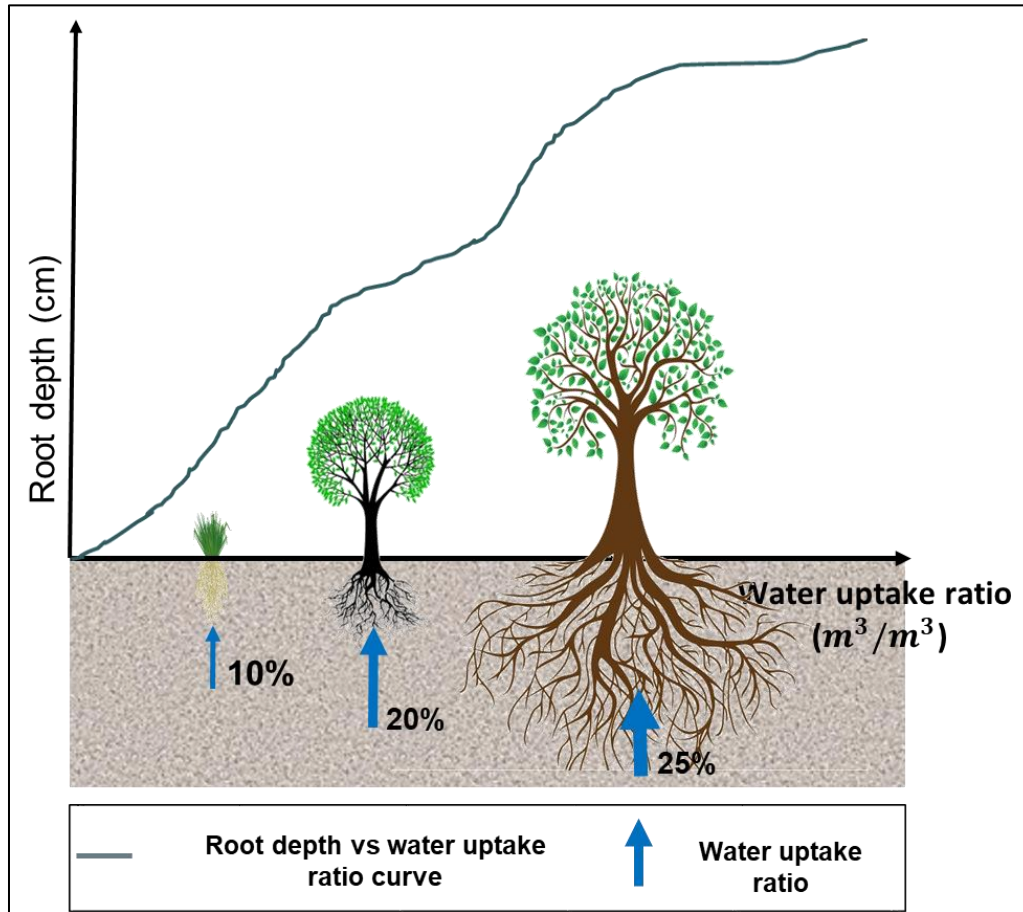


Figure 4-3: conceptual illustration of water uptake relationship with root depth

Surface cover: surface cover by vegetation influences hydrological aspects and surface runoff volume, peak flow rates, and infiltration (Loch, 2000; Boland-Brien, Basu, and Schilling, 2014; Gyamfi *et al.*, 2016; Wang *et al.*, 2017). Figure 4-4 illustrates how vegetation cover influences the volume of surface runoff generated from a rainfall event.

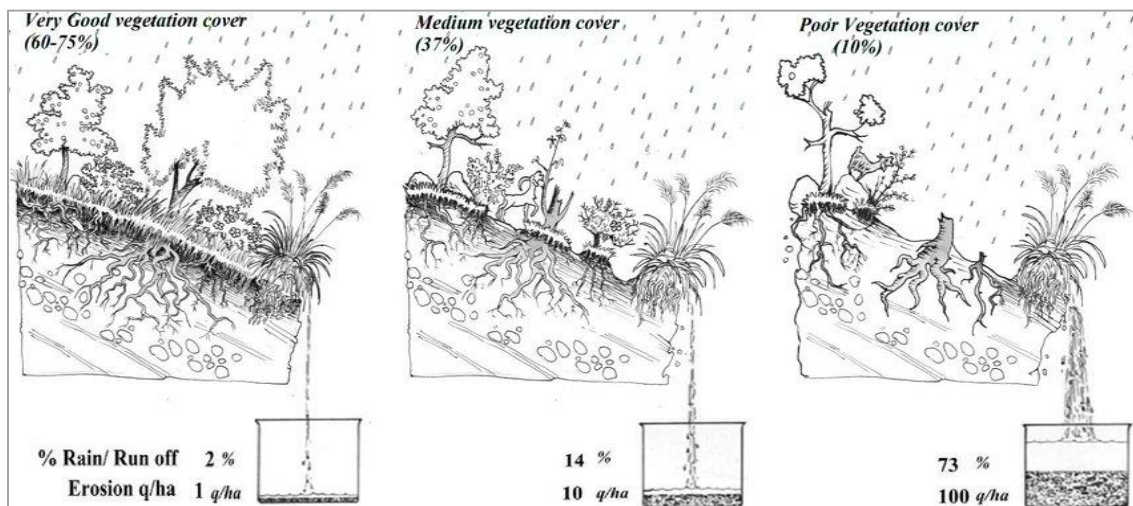


Figure 4-4: Illustration of soil cover relationship with surface runoff (Marongiu and Cenceti, 2015)

ADAPTATION OF AGRICULTURAL LANDUSE PLANNING TO IMPROVE MITIGATION OF IMPACTS ON HYDROLOGY

4.2.1 Methods

Hydrological responses of the various LULC classes in the Blyde and Steelpoort River Basins are analyzed to identify the LULC class that has minimal hydrological anomalies with agricultural land. Only LULC classes that are selected for this step have to cover an area slightly larger than the targeted 513 km^2 ; these LULC classes are herein referred to as “dominant LULCs,” and include forests (dense and sparse combined), grassland, shrubland, and agriculture land. The hydrological components that are considered are evapotranspiration, groundwater recharge, lateral sub-surface flow, and surface runoff. The following three steps are adopted in the process:

STEP 1: Four homogeneous LULC scenarios (with 100% coverage) are prepared based on the four dominant LULC classes (dense Forest, Shrubland, Grassland, and Agriculture land) identified during classification. Figure 4-5 shows the LULC scenarios with 100% coverage of each of the for LULC classes selected for analysis in this step

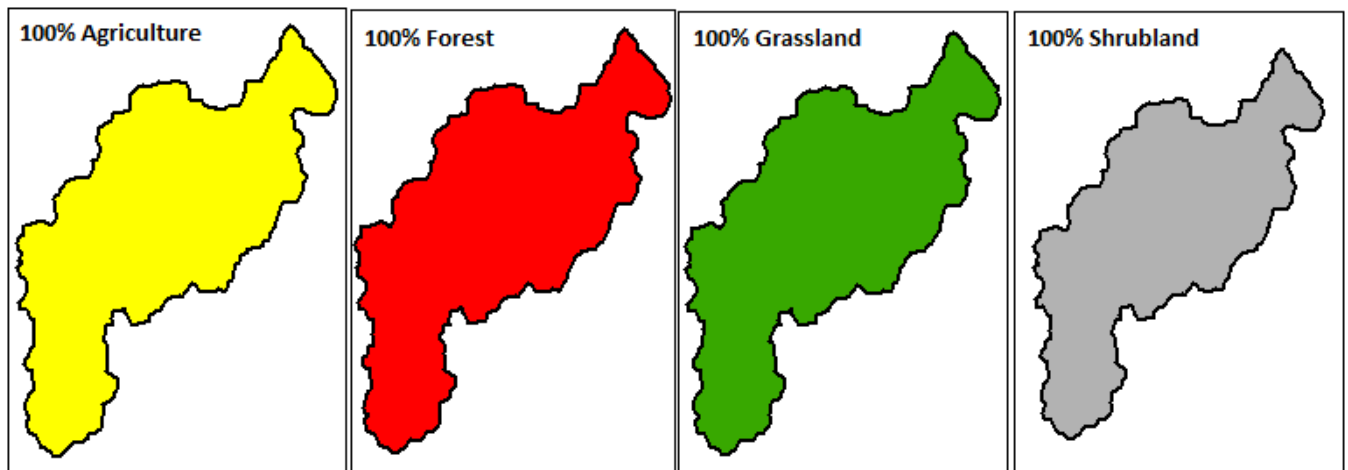


Figure 4-5: Landuse Scenarios prepared with 100% coverage of Agriculture, Forest, Grassland and Shrubland

STEP 2: Four scenarios of the SWAT Model are set-up based on the four homogeneous LULC prepared in STEP 1. Calibrated parameters’ values obtained in section 3.3.4 are applied in the parameterization of the four modelling scenarios.

STEP 3: The hydrological outputs of these simulations are then assessed to establish LULC class with minimal hydrological anomalies from agricultural land. The landuse class that exhibits minimal difference with agricultural land is then selected as the most appropriate to be cleared for agricultural use; this is because the impact on hydrological flows will subsequently be minimal. Minimum hydrological anomaly rather than the “best” hydrological conserving LULC class is utilized in this step; since minimal anomaly is an indication of similarities in requirements for growth factors. For example, Brouwer and Heibloem, (1986) indicate that both climate and crop type influence crop water requirements which are reflected in crop evapotranspiration rates. During the field Survey, DAFF also indicated that areas having vegetation with similar crop water requirements as the intended crop to be planted, are considered most suitable. Therefore, the closeness in evapotranspiration rates from grassland and agricultural area demonstrate their similarities in crop water need and subsequently an indication of similarities in growth factor requirements.

ADAPTATION OF AGRICULTURAL LANDUSE PLANNING TO IMPROVE MITIGATION OF IMPACTS ON HYDROLOGY

4.2.2 Results

Figure 4-6 illustrates the process flow used in the identification of landuse class that can be replaced by agriculture. The variations in simulated hydrological components from Agriculture LULC differs greatly with those from Forest and Grassland LULCs. Minimal anomalies in the simulated hydrological components are detected in Agriculture-Grassland anomalies (Output 1-Output 2) as shown in Figure 4-6

The surface runoff generated from grassland is lower than that generated from agricultural land: Based on the surface runoff controls, this is attributed to the degree of surface cover in the study area, which is higher in grassland. Evapotranspiration from the agricultural area is much higher than that of grassland; this can be attributed to canopy storage, which is larger in agricultural crops because of higher crop heights. On the other hand, higher lateral flow and groundwater recharge are observed under grassland, this can be attributed to enhanced surface roughness that increased residence time of surface runoff and promotes increased infiltration. Grass, in comparison to major crops grown in the river basin, have shallower roots, and hence it does not quickly deplete soil water content.

It can be seen in Figure 4-6 that shrubland appears to increase the hydrological conservation capacity of the basin. However, grassland is selected as the appropriate LULC class to be replaced since its closeness in hydrological characteristics also indicates physical and environmental suitability for agriculture.

Hydrological outputs from the Forest LULC indicate very minimal surface runoff, extremely high evapotranspiration, which can be attributed to large canopy storage and minimized surface wetting. The simulated high groundwater recharge and lateral flow can be attributed to increased residence time.

ADAPTATION OF AGRICULTURAL LANDUSE PLANNING TO IMPROVE MITIGATION OF IMPACTS ON HYDROLOGY

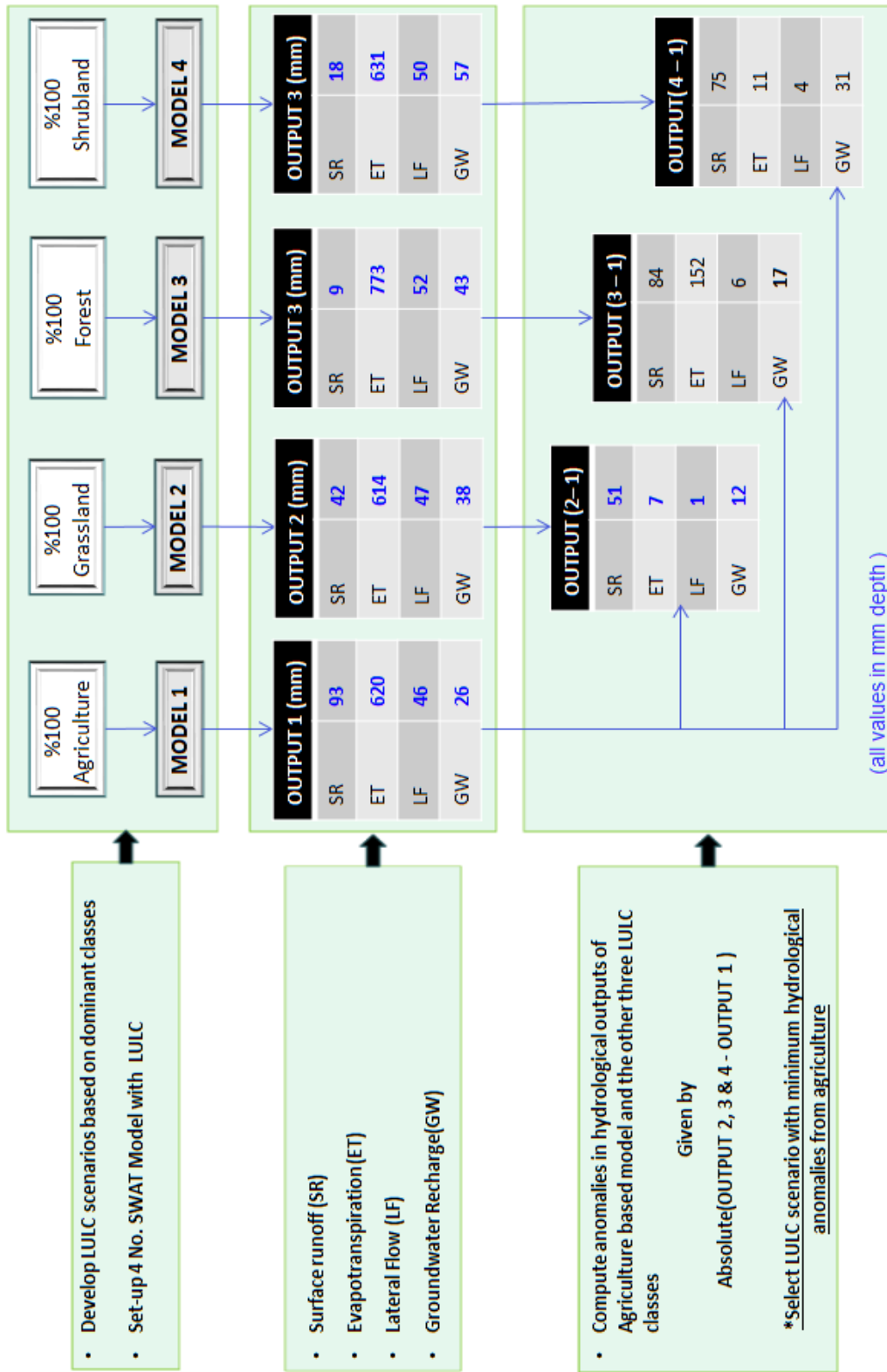


Figure 4-6: Process flow for selection of landuse class that exhibit similar hydrological response to agriculture; output shows grassland exhibits minimal anomalies

4.3 Identification of “hydrologically suitable” morphological features for agricultural use

Morphology is a key aspect that, in addition to LULC, controls hydrological regimes (Voepel *et al.*, 2011). Studies carried out by Price (2011), Boland-Brien, Basu and Schilling (2014), and Wang *et al.* (2018) indicate that the physical characteristics of the river basin can influence the magnitude of hydrological to similar landuse classes. Boland-Brien *et al.* (2014) demonstrated that the baseflow ratio in agricultural fields is dependent on the size of the watershed, sub-surface formations, and slope; however, the magnitude of the response was also dependent on the cropping pattern and degree of surface cover. Therefore, in an environment or a region where landuse changes or development is prominent, quantification of the influence of morphology on the magnitude of hydrological reaction to landuse change could guide the landuse-planning process for mitigation of hydrological variability.

The prediction of the hydrological response of agricultural LULC based on a single morphological parameter can be a simple task. However, the complexities in the prediction increase as the number of parameters increase. Figure 4-7. Uses three morphological parameters (soil structure, slope, and depth of water table) to illustrate how the number of parameters influences complexity in hydrological predictions.

The SWAT Model is capable of capturing the roles each morphological parameter plays on hydrological partitioning. A river basin in its natural or modifies state has heterogeneous morphology, which varies spatially in the level of occurrence; these morphological parameters interact with each other and produce ta unique hydrological response. Some morphological parameters have a greater and spatially consistent pattern of influence in hydrological response, whereas some less significance in hydrological influence or a consistent pattern of influence cannot be detected across the entire river basins. Based on this description, identification of morphological parameters that can be utilized in EIA studies can only be based on dominant morphological parameters that best describe the hydrological response of the watershed.

The SWAT Model is semi-distributed and outputs hydrological information at HRU and sub-basin scale (Neitsch *et al.*, 2011). Therefore, the identification of hydrologically low impact areas will provide information at a larger scale, which may not be effective, considering the large area of the sub-basins (Figure 4-8) and their morphological heterogeneity. Therefore, statistical methods will be used to detect correlations between various morphological parameters and the hydrological outputs; the statistical/mathematical relationships obtained in this step will be used to characterize the reaction of the entire basin from a small scale to a large scale.

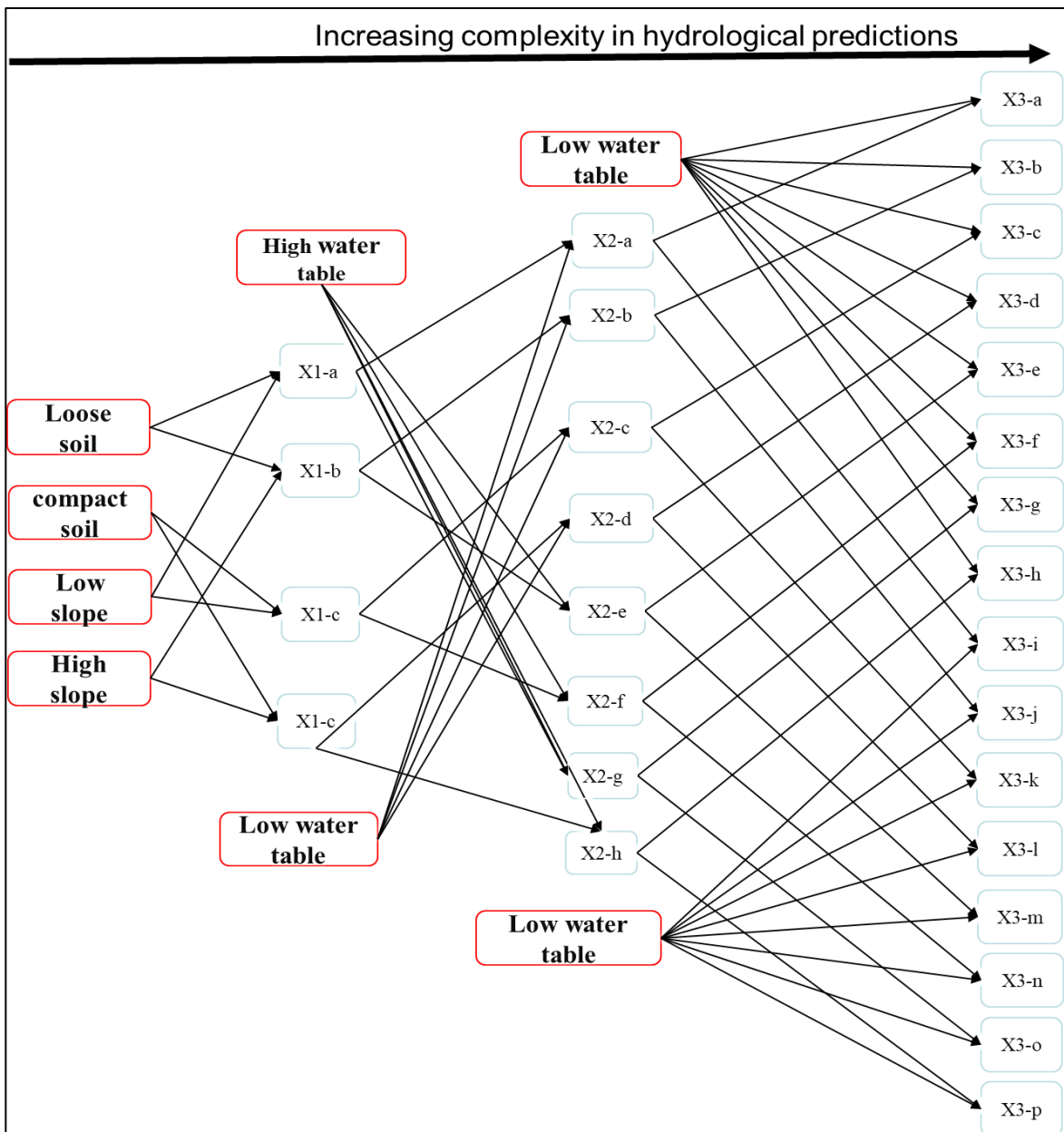
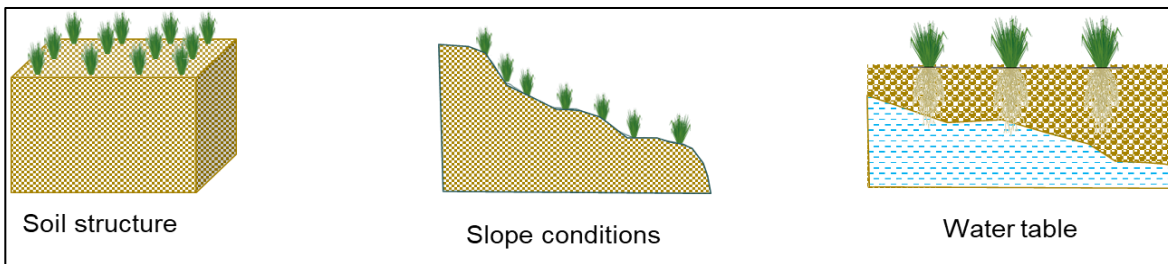


Figure 4-7: Illustration of increasing complexity in hydrological prediction with an increase in controlling morphological features

4.3.1 Methods

In Blyde and Steelpoort River Basins, grassland is already identified in the previous section as most suitable for replacement by agriculture. In this section seeks to identify the dominant morphological parameters that describe hydrological partitioning in the river basin, and also identify morphological conditions that produce minimum hydrological anomaly when transitioned from grassland to agricultural land. The following four steps are adopted in the process:

Step 1: In this step, dominant morphological conditions that best describe hydrological partitioning of the river basin are first identified using correlation matrices and construction of scatterplots; Voepel *et al.* (2011) successfully used the method adopted here to characterize the role of morphology in hydrological partitioning. Voepel *et al.* (2011) correlation matrices and scatterplots construct to identify dominant climatic and morphological parameters that define water partitioning across the various watershed in the United States.

To obtain enough sample size for correlation analysis, the river basins are split into 32 sub-basins based on water management areas as delineated by the Republic of South Africa as shown in Figure 4-3

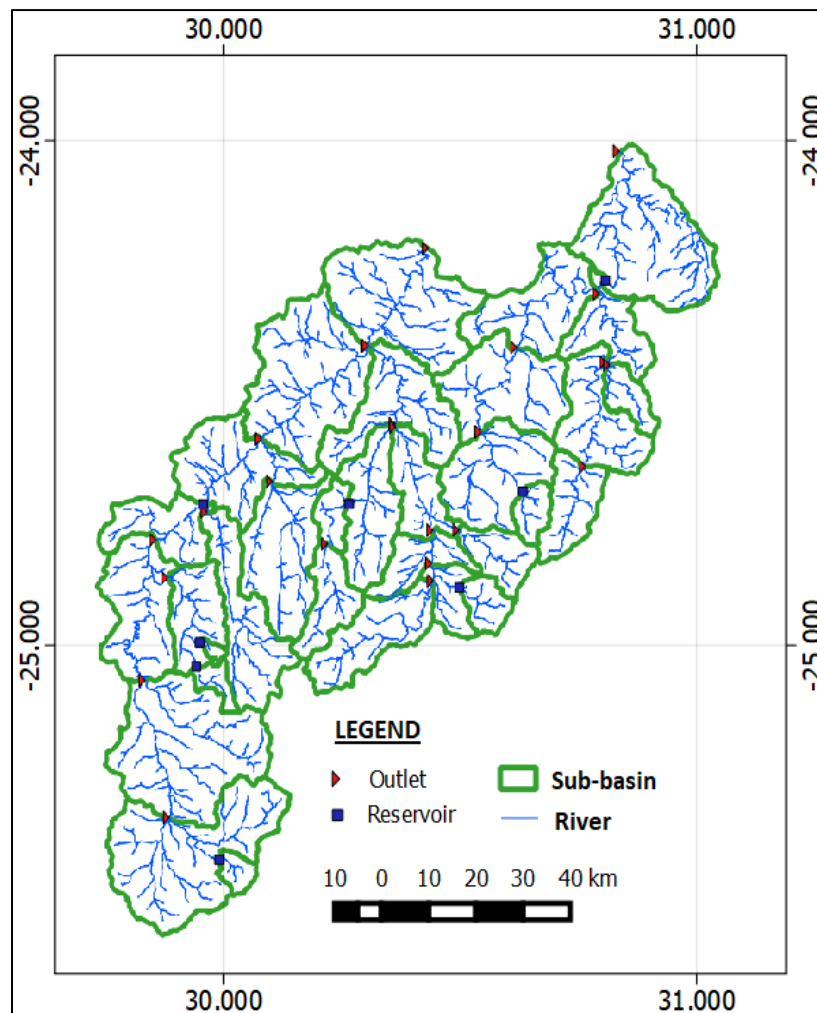


Figure 4-8: Sub-basins used in correlation analysis for identifying dominant morphological parameters

Morphological parameters that are tested are derived from terrain (DEM), soil properties, and geological conditions. Only observed data is used since model-derived parameters may introduce further biases due to parameter uncertainty. The morphological parameters that are tested are as follows:

Terrain derived parameters include:

Terrain Ruggedness Index (TRI): Expresses the amount of elevation difference between adjacent cells of a DEM (Riley, DeGloria and Elliot, 1999; United States Naval Academy, 2016). The TRI is computed for each grid cell of the DEM by calculating the sum of elevation difference between the grid cell and the eight surrounding grid cells. According to the description provided by Riley *et al.* (1999), TRI is computed as follows:

$$TRI = \sum_{i=1}^8 ABS(X_i - X_c) \tag{4.1}$$

Where X is the elevation for a particular DEM cell, X_c is the elevation for the grid cell at the center (whose TRI is being computed), and i is the index of the neighboring grid cell.

Figure 4-9 shows various hypothetical DEMs and their corresponding TRI values as computed by equation 4.1

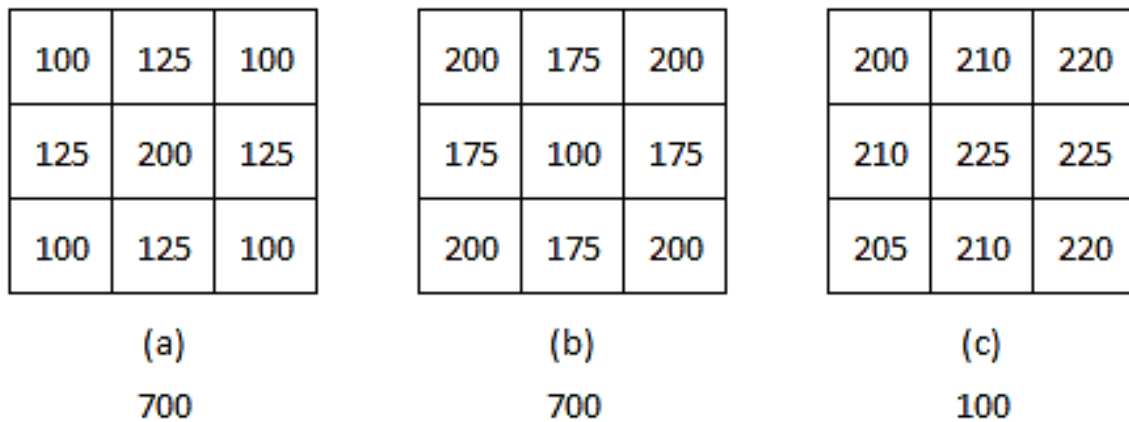


Figure 4-9: Hypothetical square grids DEMs and their corresponding TRIs, where a) is peak type topography that is highly rugged, b) is pit type topography that is highly rugged, and c) is a gently undulating topography.

According to Figure 4-10, high TRI values occur in areas with higher elevation. Low TRI corresponds to lower elevation areas and is continuous along the riverine. TRI defines the rate of water evacuation from one grid cell to another and the storage capacity of a particular cell.

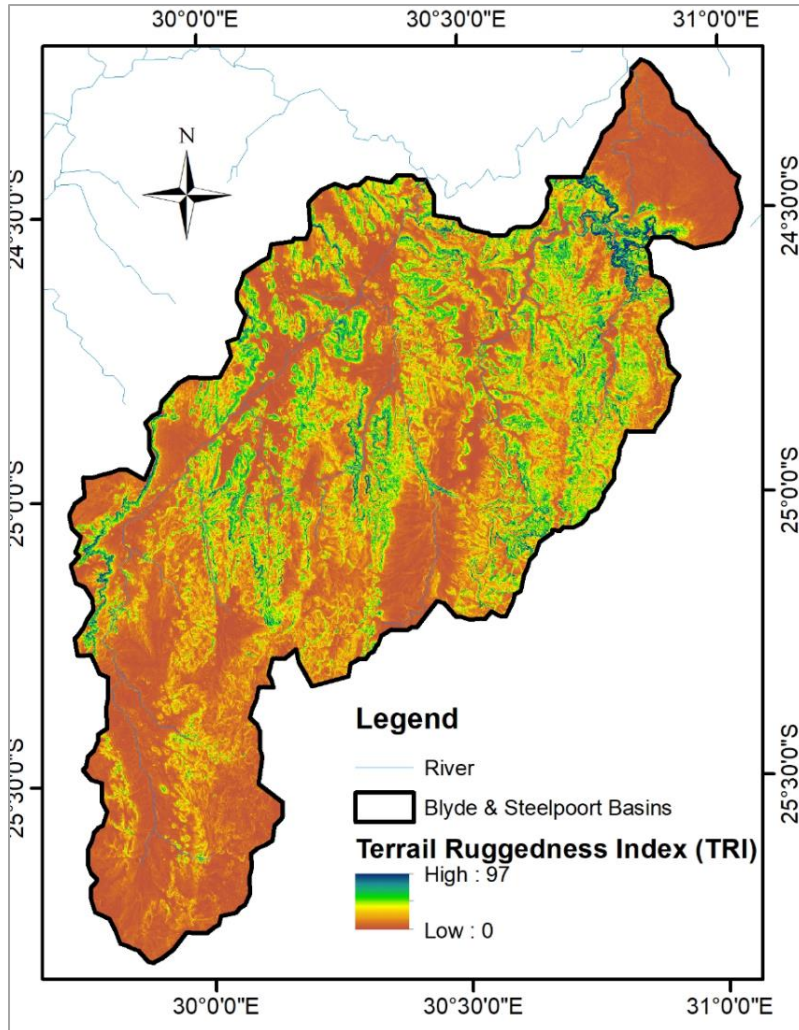


Figure 4-10: Terrain Ruggedness Index of Steelport and Blyde River Basins

Terrain Convergence Index (TCI): A terrain parameter that shows the structure of the relief as a set of convergent areas (channels or ponds) and divergent areas (ridges). It represents the degree of agreement of aspect of surrounding cells with the theoretical matrix. Aspect is the orientation of slope, measured clockwise in degrees from 0° to 360°, where 0° is north-facing, 90° is east-facing, 180° is south-facing, and 270° is west-facing. The calculation uses the aspects of surrounding cells, i.e. it looks to which degree surrounding cells point to the center cell (Köthe and Lehmeier, 1996; Kiss, 2004). TCI for each grid cell computed as follows:

$$TCI = \left[\frac{1}{8} \sum_{i=1}^8 \phi \right] - 90^\circ \tag{4.2}$$

Where ϕ denotes the average angle between the aspect of adjacent cells and the aspect to the central cell. TCI values range from -90 to +90, where the extreme (-ve) values represent highly divergent areas, values around 0 represent planar areas, and extreme (+ve) values represent highly convergent areas.

Figure 4-10 illustrates the varied aspects for each grid cell, with their corresponding TCIs

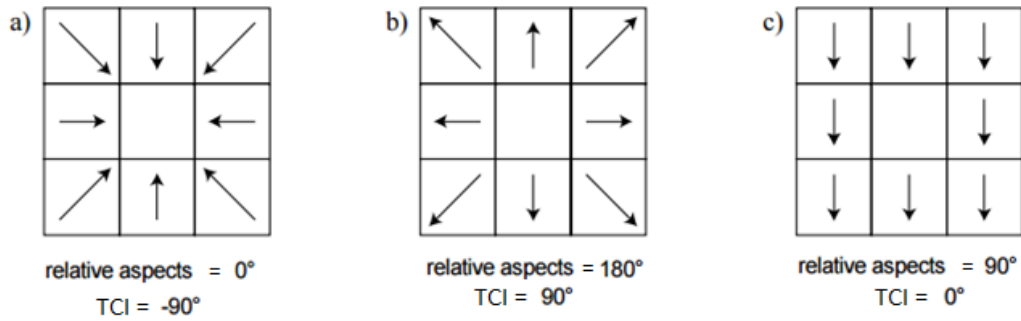


Figure 4-11: Hypothetical illustration of the varied aspects for each grid cell, with their corresponding TCI s (source: Kiss, 2004)

According to figure 4-12, the TCI of Blyde and Olifants River Basins indicate an almost uniformly distributed convergent and divergent areas. Slope aspect influences surface energy balance, hence influencing water balance at a particular point (Jackson, 1967; Faber, 2004)

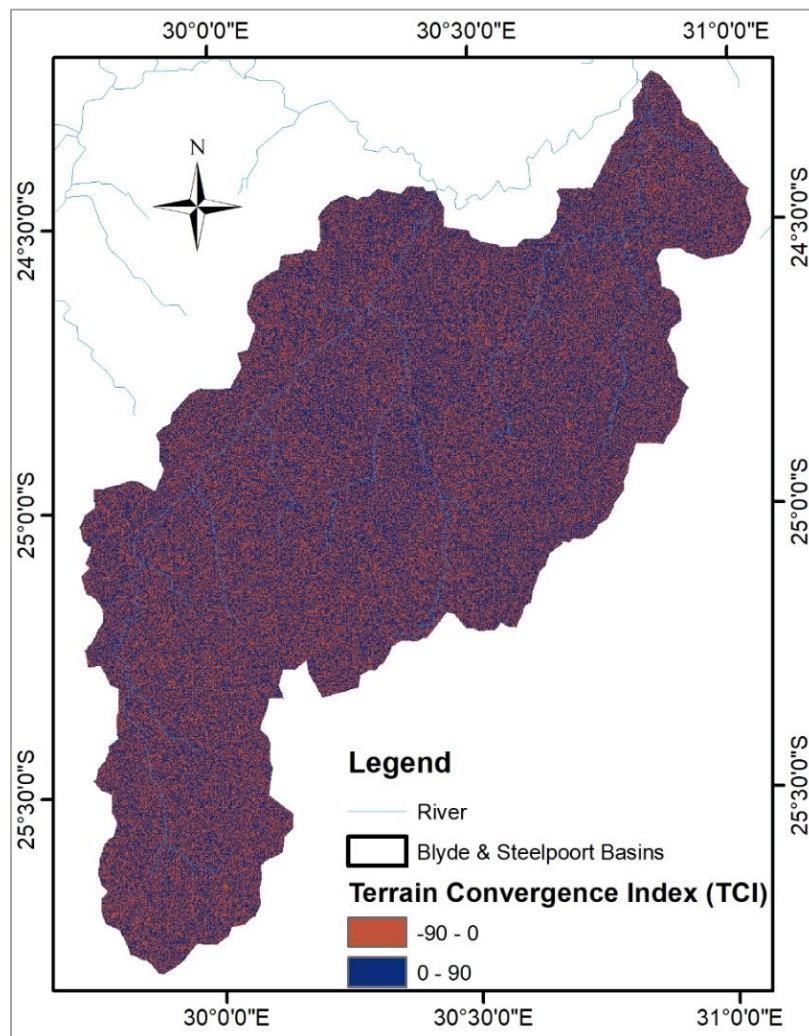


Figure 4-12: Terrain Convergences Index of Steelpoort and Blyde River Basins

Slope: it is the steepness or the degree of incline of a surface Slope for a given surface is calculated by computing the ratio of the vertical change (Δy) to the horizontal change Δx between two given points. Slope influences surface runoff velocity and peak surface runoff rate and volume of surface runoff generated (Chow *et al.*, 1988). It is represented as follows:

$$slope = \frac{\Delta y}{\Delta x} \quad 4.3$$

Elevation: it is the height of a particular grid cell above or below a fixed reference point (above sea level). The elevation of the river basins is shown in Figure 3-10.

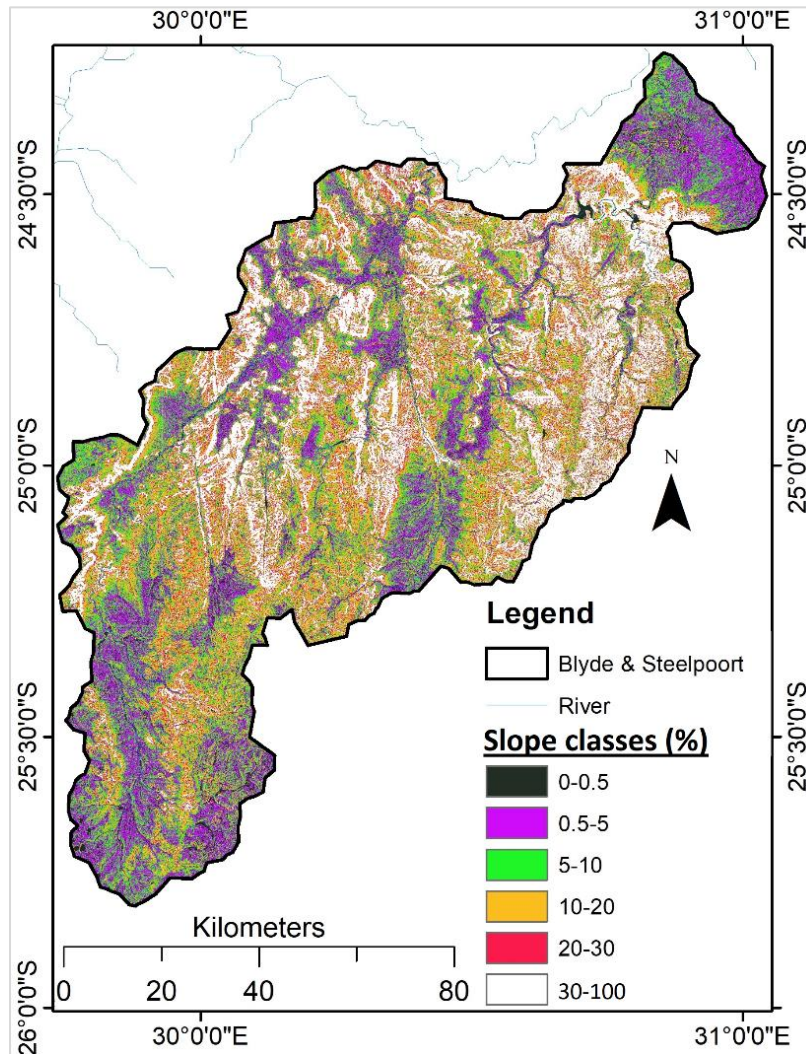


Figure 4-13: Illustration of slope classes for Steelport and Blyde River Basins

Bulk density (kg/m^3): Soil bulk density refers to the ratio of the dry mass of solids to bulk volume of a soil sample (Akker, JJ H Van ; Soane, 2005; Batjes *et al.*, 2017). Bulk density influences the soil temperature and hence impacts on the distribution and decay of soil water content (Neitsch *et al.*, 2011; Arnold *et al.*, 2012). Bulk density is calculated as follows:

$$\rho_b = \frac{M_s}{V_s} \tag{4.4}$$

Where ρ_b is the soil bulk density (kg/m^3), M_s is the dry mass of solid, and V_s is the total volume of the soil sample. Higher Bulk density represents high compaction (Sandhage-Hofmann, 2016), which translates to low infiltration rates and high surface runoff generation.

The temperature of a soil layer is a function of the surface temperature, mean annual air temperature and depth in the soil at which variation on temperature due to changes in climatic conditions no longer occur. This depth is referred to as damping depth. It is dependent on Bulk density.

Soil temperature influences water movement and the soil and rate of decay of water residue

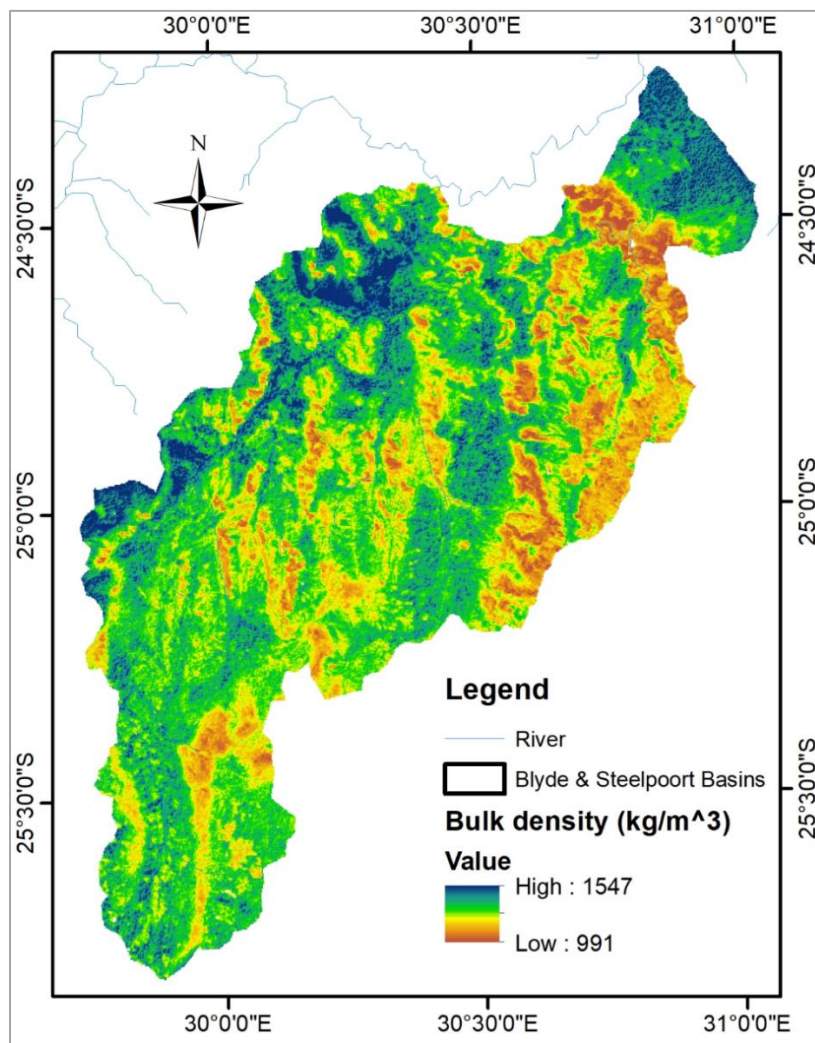


Figure 4-14: Map of the Bulk density of Steelpoort and Blyde River Basins

Porosity: Measure of void spaces in the soil; this dataset was extracted from SWAT Tables. Soils with higher porosity have high infiltration rates (USDA_NRCS, 2014)

SWAT Model assigns porosity values for each specific soils based on their textures. For the FAO, soil classes and corresponding textures have been pre-determined and input into the SWAT database. The raw values are used to prevent biases that may result from parameter changes in the calibration step.

Soil Available Water (mm/m): maximum amount of plant-available water a type soil can provide. This dataset was extracted from SWAT Tables. The higher the field capacity, the higher the amount of water that can be drained from it. Figure 4-15 illustrates the SAW and FC of various soils.

Field capacity (mm/m): the amount of soil moisture or water content held in the soil after excess water has drained away, and the rate of downward movement has decreased; this dataset was extracted from SWAT Tables.

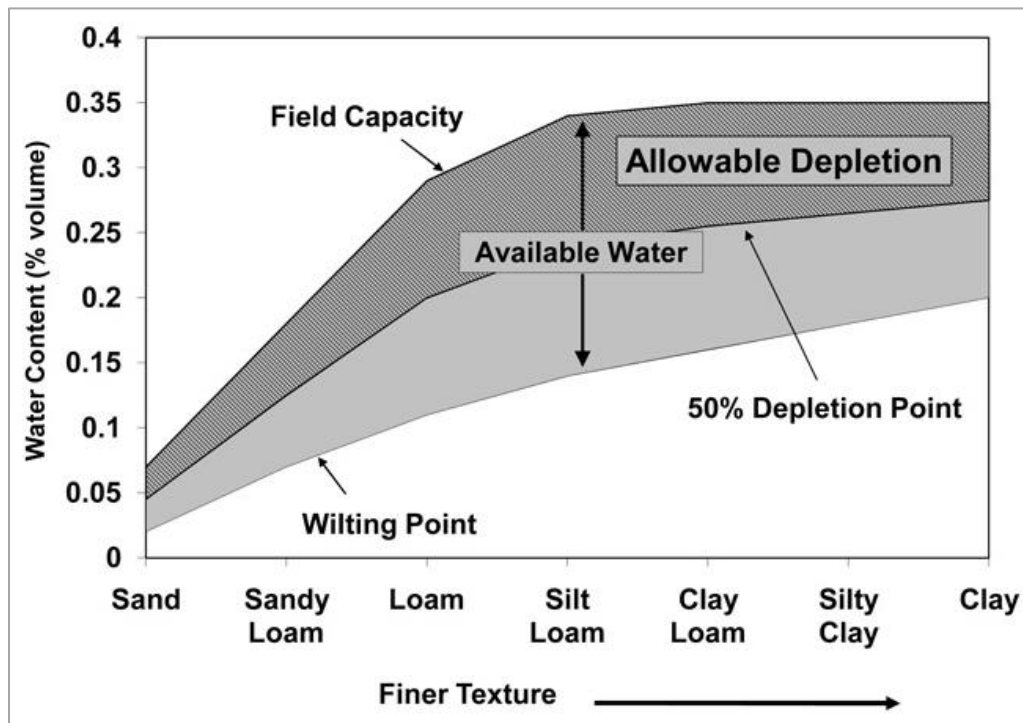


Figure 4-15: illustration of Soil Available Water and Field Capacity (Utah State University, no date)

Hydraulic conductivity (mm/hr): describes the ease with which water can move through pore spaces or fractures. This dataset was also extracted from SWAT Tables

Borehole yield (l/s): in this research, borehole yield refers to the maximum rate at which a borehole can be pumped on a sustainable basis. The spatial illustration of the borehole yield is shown in Figure 1-13.

The above morphological parameters are averaged over each sub-basin and tested for correlation with various hydrological indices. The indices used in this step refer to the fraction of mean annual rainfall that is partitioned to specific hydrologic components and is defined as follows:

Surface runoff coefficient (SR_c), which is represented by the following formula:

$$SR_c = \frac{Q_s}{R_a} * 100 \quad 4.5$$

Where Q_s is the mean annual surface runoff and R_a is the mean annual rainfall.

Groundwater recharge to rainfall ratio, which will be referred to as Groundwater Recharge Index and denoted by *GWRI*:

$$GWRI = \frac{GWR}{R_a} * 100 \quad 4.6$$

Where *GWR* is the mean annual groundwater recharge (mm) and *R_a* is the mean annual rainfall (mm).

Lateral flow to rainfall ratio, which will be referred to as Lateral Flow Index and denoted by *LFI*:

$$LFI = \frac{LF}{R_a} * 100 \quad 4.7$$

Where *LF* is the mean annual lateral flow (mm) and *R_a* is the mean annual rainfall (mm).

Percolation to rainfall ratio, which will be referred to as Percolation Index and denoted by *PI*:

$$PI = \frac{P}{R_a} * 100 \quad 4.8$$

Where *P* is the mean annual percolation (mm) and *R_a* is the mean annual rainfall (mm).

The morphological parameters that exhibit co-relationship with various hydrological indices are considered dominant. Coefficient of determination, *R*² is used as the measure of correlation; when *R*² >= 0.5, then a strong correlation exists. The (-) sign indicates that the variables are moving in opposite directions.

Step 2: Once the dominant morphological parameters are identified, their influence on the magnitude of hydrological changes is then assessed as well using correlation analysis. In this step, correlation analysis is conducted between the morphological parameters and the anomalies of the various hydrological indices. Since the focus is on grassland to agriculture transition, only the hydrological outputs based on the two homogeneous LULC are used to calculate the indices.

Statistical relationships that exist between the two variables tested indicate how each morphological parameter influences the magnitude of change in the hydrological components when grassland is converted to agricultural land.

The anomalies of the hydrological indices are calculated for each sub-basin for enough statistical sampling and are represented by the following formulae:

The anomaly of Surface Runoff Coefficient (*SR_{can}*):

$$SR_{can} = SR_{cag} - SR_{cgr} \quad 4.9$$

Where *SR_{cag}* is the Surface Runoff Coefficient from the homogeneous agriculture LULC and *SR_{cgr}* is the Surface Runoff Coefficient from the homogeneous grassland LULC.

The anomaly of Groundwater Recharge Index (*GWRI_{an}*):

$$GWRI_{an} = GWRI_{ag} - GWRI_{gr} \quad 4.10$$

Where *GWRI_{ag}* is the Groundwater Recharge Index from the homogeneous agriculture LULC and *GWRI_{gr}* is the Groundwater Recharge Index from the homogeneous grassland LULC.

The anomaly of the Lateral Flow Index (LFI_{can}):

$$LFI_{an} = LFI_{ag} - LFI_{gr} \quad 4.11$$

Where LFI_{ag} is the Lateral Flow Index from the homogeneous agriculture LULC and LFI_{gr} is the Lateral Flow Index from the homogeneous grassland LULC.

The anomaly of Percolation Index (PI_{an}):

$$PI_{an} = PI_{ag} - PI_{gr} \quad 4.12$$

Where PI_{ag} is the Percolation Index from the homogeneous agriculture LULC and PI_{gr} is the Percolation Index from the homogeneous grassland LULC.

Step 3: The scatter plots of the dominant morphological parameters vs. anomalies of the hydrological indices are prepared and equations describing each relationship obtained. Only the dominant parameters that exhibit correlation with the hydrological anomaly ratios are utilized in this step.

The thresholds for morphological parameters that would ensure minimal changes in hydrology are obtained by randomly setting the targeted change to a fraction of the mean annual basin value of the various ratios of the anomalies.

Step 4: To identify the exact location for the expansion of agricultural land, the spatial properties of the river basins are then explored to identify areas that have a combination of the set of morphological parameters that are within the limits identified by the thresholds set. These areas are then checked for the following conformities/criteria:

- Must have slope < 20% as stipulated by South Africa's Department of Agriculture, Forestry and Fisheries (DAFF)
- Must be covered by grassland
- Must not be in protected areas like Forests and game reserves

4.3.2 Results

Step 1: Table 4-1 shows a set of morphological parameters that were tested and their corresponding values of R^2 . In the work of Kelleher *et al.* (2015), the high variability of parameters may result in low correlation, hence R^2 values of about 0.3 can be considered dominant: this approach is also employed in this step. Most DEM-derived parameters (TCI, TRI, and slope) exhibited a correlation with some hydrological indices.

Bulk density was the only soil parameter which exhibited a correlation with LFI whereas geological parameter (groundwater yield) did not correlate with the hydrological ratios.

TCI, TRI, slope, Bulk density ρ_b , were adopted as the dominant morphological parameters and are therefore in combination with LFI and SR_c adopted for the analysis in **Step 2** and **Step 3**.

Various scatterplots showing the statistical relationships established between the selected morphological parameters and various hydrological indices are outlined in Appendix III.

Step 2: The objective of this step is to reduce the anomalies in lateral flow and surface runoff; therefore, the LFI_{an} and SR_{can} are reducing by a random factor ranging between $\frac{1}{4}$ to $\frac{1}{2}$ to obtain the targeted LFI_{an} and SR_{can} . These targets values are denoted by $Target\ LFI_{an}$ and $Target\ SR_{can}$. The target values are then applied in **Step 3** to establish the morphological thresholds using equations that will result from the graphical relationships.

Table 4-2 shows the simulated mean annual values of lateral flow and surface runoff obtained from the homogeneous LULC scenarios of grassland and agriculture and their corresponding anomalies

Step 3: Figure 4-4 shows the scatter plots of the various indices of hydrological anomalies obtained in **Step 2**.

The anomaly of the Lateral Flow Index LFI_{an} exhibited an exponential relationship with bulk density, where LFI_{an} decreases exponentially with an increasing bulk density.

The anomaly of Surface Runoff Coefficient SR_{can} exhibited an exponential relationship slope, where SR_{can} increases exponentially with increasing slope.

The anomaly of the Lateral Flow Index LFI_{an} exhibited a polynomial relationship with slope and terrain Terrain Ruggedness Index (TRI), where LFI_{an} increases with increasing slope and TRI.

Figure 4-17 shows the maps of the dominant morphological parameters showing only the areas meeting the threshold values.

Table 4-3 shows the equations obtained from the graphical plots in Figure 4-16; the y value in the graphical equations are substituted by their respective targeted anomalies of Lateral Flow Index $Target\ LFI_{an}$ and Surface Runoff Coefficient $Target\ SR_{can}$. The y values represent the morphological thresholds.

Table 4-1: Correlation of various morphological parameters and hydrological components

S.No	Morphological Parameters	LFI	SR _c	PI
1	Terrain Convergence Index (TCI)	0.69	0.30	No correlation
2	Terrain Ruggedness Index (TRI)	0.52	No correlation	No correlation
3	Slope	0.37	No correlation	No correlation
4	Elevation	No correlation	No correlation	No correlation
5	Porosity	No correlation	No correlation	No correlation
6	Field capacity	No correlation	No correlation	No correlation
7	Hydraulic Conductivity (mm/hr)	No correlation	No correlation	No correlation
8	Bulk density (kg m ⁻³)	0.6	No correlation	No correlation
9	Aquifer yield (l/s)	No correlation	No correlation	No correlation

ADAPTATION OF AGRICULTURAL LANDUSE PLANNING TO IMPROVE MITIGATION OF IMPACTS ON HYDROLOGY

Table 4-2: Summary of hydrological components from grassland and agriculture LULC and the anomalies of their ratios

Sub-basin	Rainfall (mm)	Agriculture		Grassland		Agriculture-Grassland anomaly	
		Surface Runoff (mm)	Lateral flow (mm)	Surface Runoff (mm)	Lateral flow (mm)	<i>Target SR_{can}</i>	<i>Target LFI_{an}</i>
1	908	31	36	9	39	2.44	-0.35
2	1114	94	216	19	227	6.71	-0.98
3	1081	78	108	34	117	4.03	-0.76
4	999	295	42	185	54	11.00	-1.19
5	921	38	81	17	87	2.28	-0.65
6	821	581	1	267	4	38.32	-0.42
7	1113	77	94	24	99	4.82	-0.50
8	834	58	38	21	45	4.43	-0.84
9	909	28	68	10	69	2.04	-0.11
10	863	60	50	26	65	3.87	-1.72
11	1019	70	16	55	18	1.54	-0.11
12	946	38	390	10	402	2.89	-1.22
13	958	102	47	58	55	4.66	-0.81
14	947	306	49	135	78	18.08	-3.07
15	1066	629	13	483	37	13.71	-2.21
16	879	3	171	2	171	0.14	-0.05
17	869	110	18	36	21	8.54	-0.38
18	822	53	24	22	25	3.69	-0.17
19	985	86	45	56	52	3.00	-0.70
20	1019	180	56	45	76	13.20	-1.96
21	1091	380	64	169	107	19.33	-3.94
22	1017	107	50	59	52	4.75	-0.20
23	1041	51	81	34	84	1.62	-0.26
24	1048	174	168	65	183	10.40	-1.48
25	902	136	63	44	73	10.20	-1.14
26	1009	74	6	64	7	0.97	-0.10
27	885	90	73	27	80	7.03	-0.79
28	951	95	12	82	14	1.35	-0.27
29	894	58	31	32	37	2.84	-0.68
30	909	29	40	17	41	1.31	-0.08
31	981	292	58	178	77	11.65	-1.93
32	929	27	37	12	38	1.61	-0.08
Average						6.95	-0.91
Surface runoff targeted (<i>Target SR_{can}</i>) change = 1/4 * (Average)						1.74	
Lateral flow targeted change (<i>Target LFI_{an}</i>) = 1/3 * (Average)							-0.30

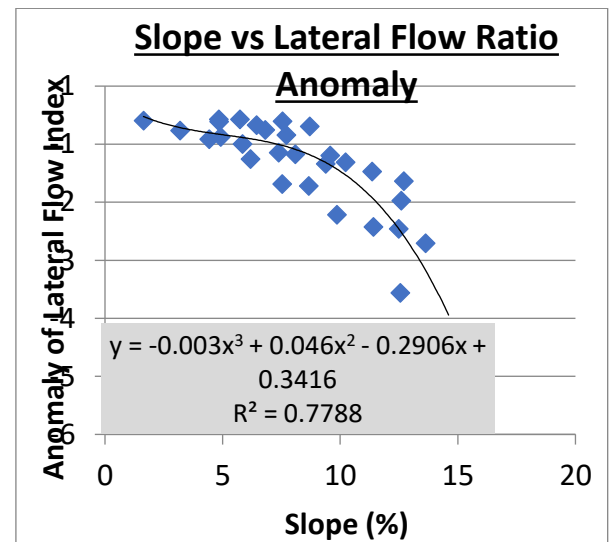
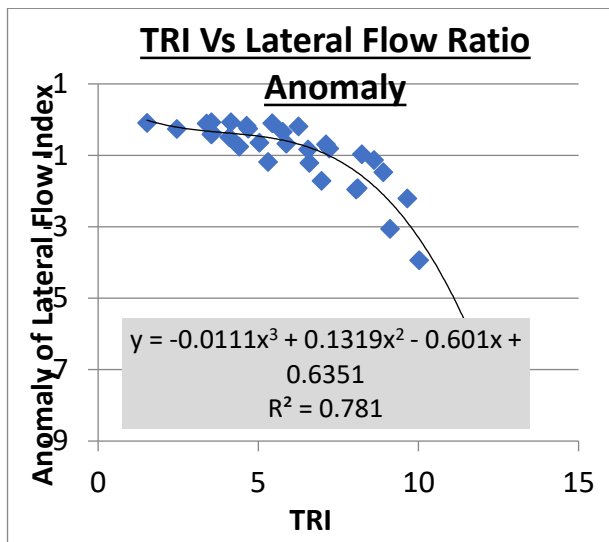
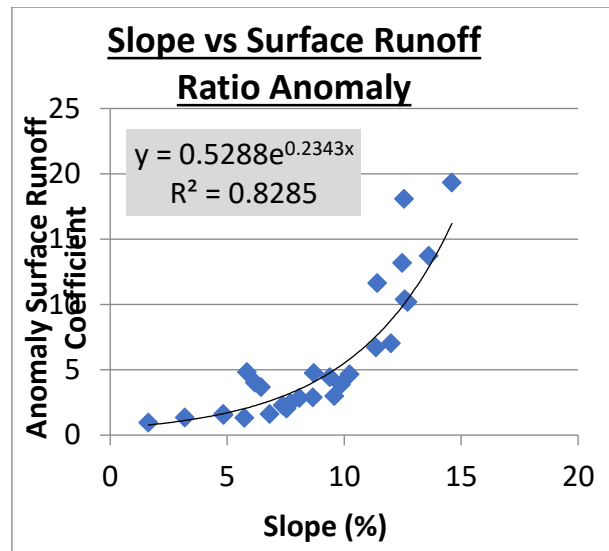
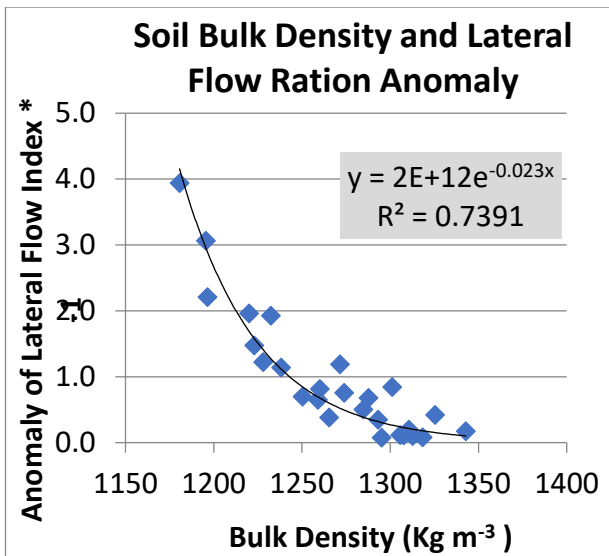


Figure 4-16: Graphs show relationship between morphological parameters and hydrological anomalies from grassland and agriculture LULC based simulations

Table 4-3: Summary of morphological parameters, hydrological parameters and anomalies and equations used in the identification of limits morphological parameters

Graph	Equation	Targeted change = y	Morphological parameter	Morphological thresholds = x
TRI Vs LFI_{an}	$y = -0.0111x^3 + 0.1319x^2 - 0.601x + 0.6351$	Target $LFI_{an} = 0.3$	TRI	≤ 3
Slope vs LFI_{an}	$y = -0.003x^3 + 0.046x^2 - 0.2906x + 0.3416$	Target $LFI_{an} = 0.3$	slope	≤ 4.4
Bulk Density and LFI_{an}	$y = 2E+12e^{-0.023x}$	Target $LFI_{an} = 0.3$	Bulk density	≥ 1282
Slope vs SR_{can}	$y = 0.5288e^{0.2343x}$	Target $SR_{can} = 1,7$	slope	≤ 4.9

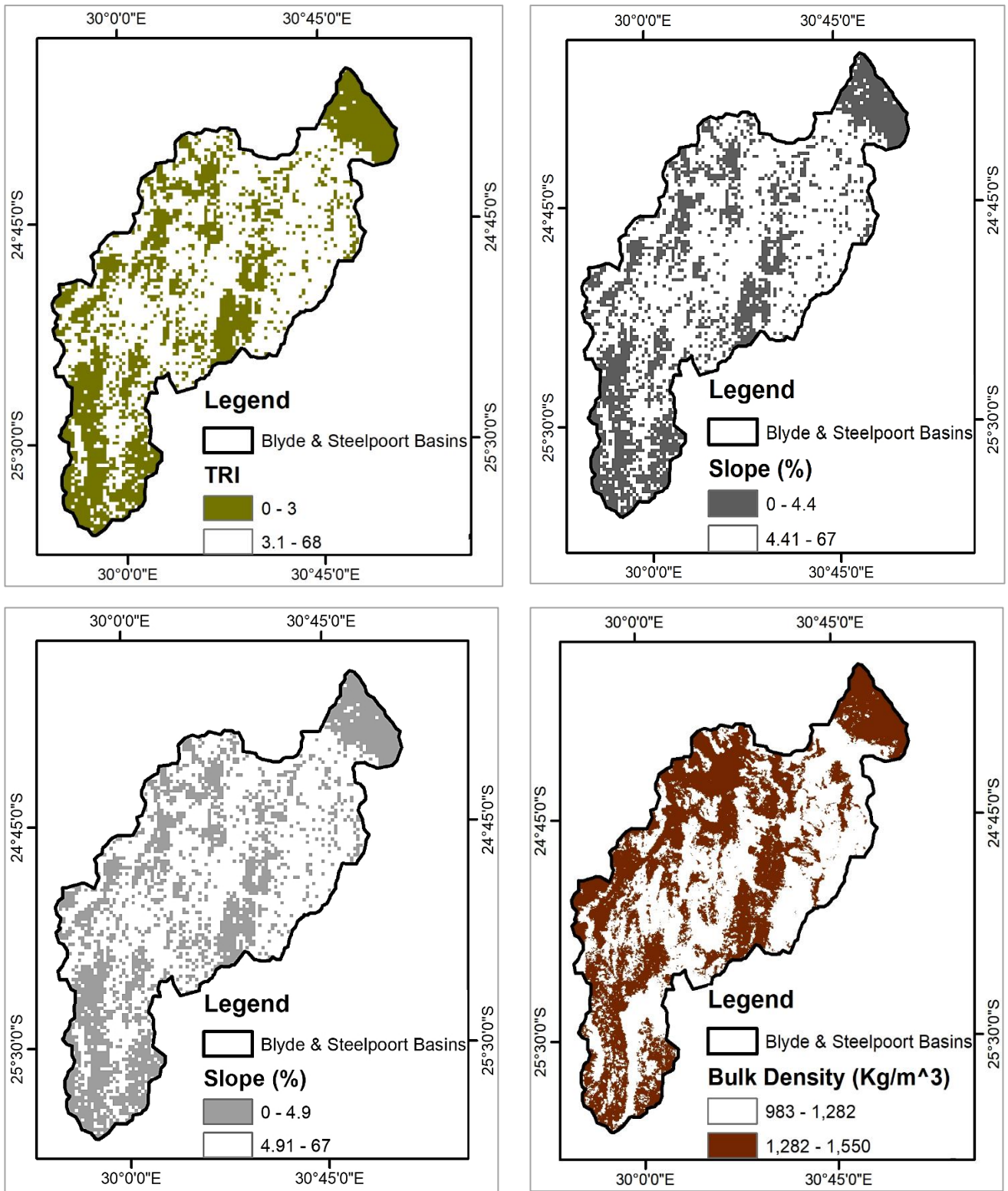


Figure 4-17: Maps showing the spatial distribution of TRI that meet hydrological conservation thresholds

Step 4: To identify the exact locations for the expansion of agricultural land, the morphological thresholds developed in the previous step are combined with criteria for agricultural land development described in section 4.3.1. These criteria stipulate that agricultural establishments must be on slopes < 20% (DAFF criterion), must only be expanded into grassland, and must not be in protected areas. Since the slope limit provided by DAFF is larger, the slope thresholds used in this step are the values identified in the previous step.

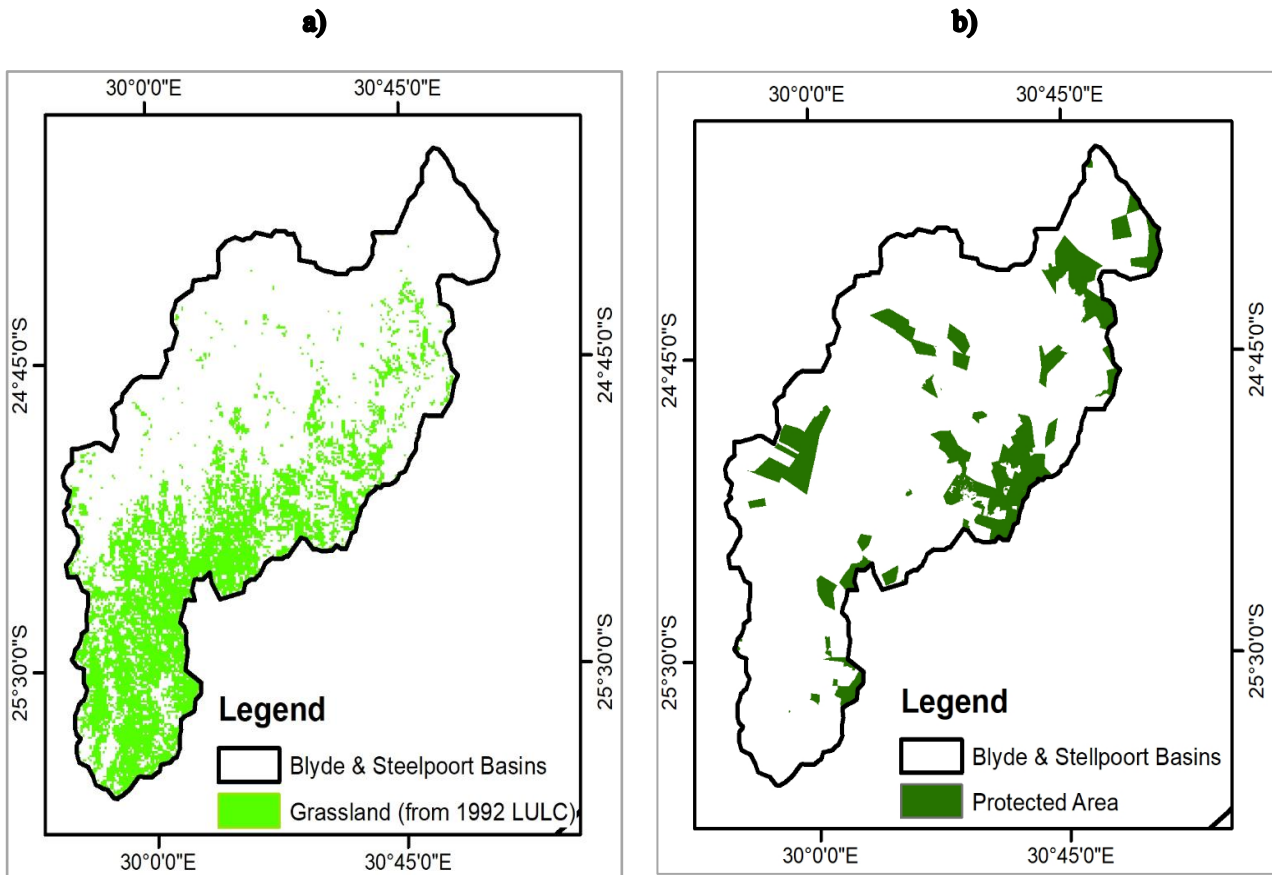


Figure 4-18: map of grassland under 1992 LUL (a)C and protected areas (b) in Blyde and Steelpoort River Basins.

The map of protected area and grassland under the 1992 LULC are as shown in Figure 4-18

The maps in Figure 4-17 are then intersected with the grassland map of 1992. Areas that fall under protected areas are then clipped out of this intersection to give the “suitable” agricultural areas, which is shown in Figure 4-19. The area is considered suitable for agricultural use for its ability to mitigate impacts on hydrological regimes; this area is 657 km².

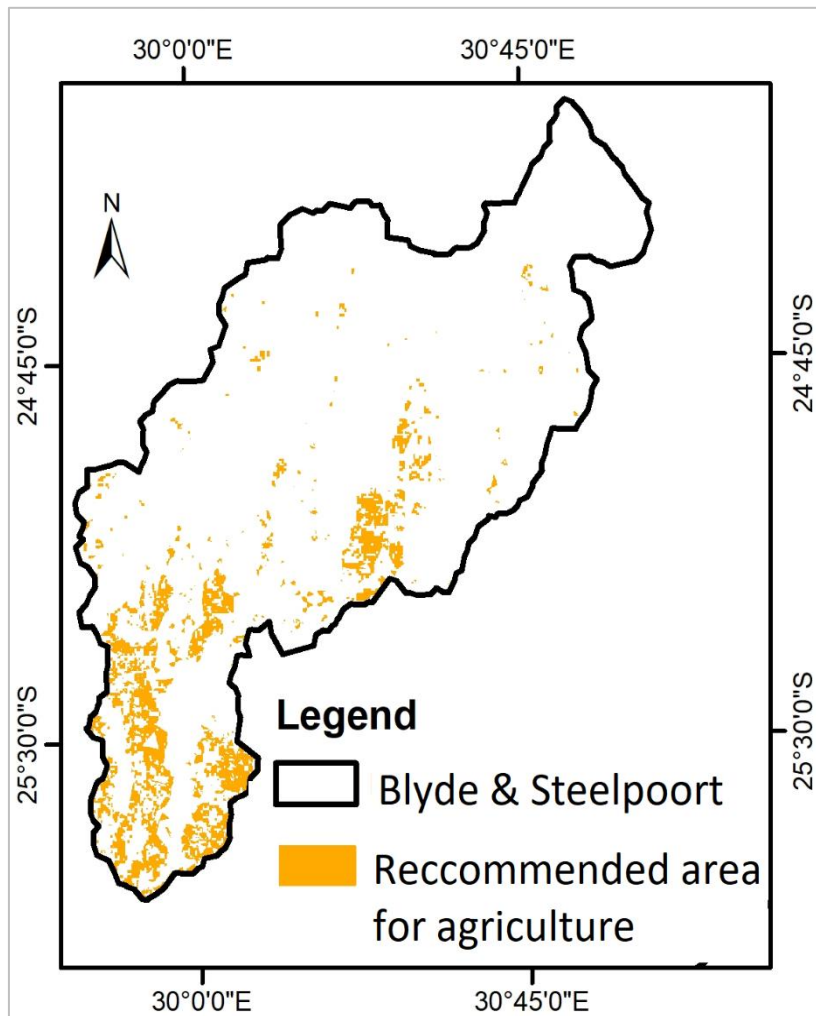


Figure 4-19: Map of suitable areas for agricultural use

4.4 LULC scenario development

The suitable agricultural area identified in the previous section is used to develop a hypothetical LULC scenario of 2014. The detected increase in agricultural land between 1992 and 2014 is 513 km^2 , whereas the area identified as suitable for agricultural use is 657 km^2 . In developing a hypothetical 2014 LULC scenario, the entire 657 km^2 is taken into account.

This process involves only modifying the agricultural expansions that took place between 1992 and 2014 to take the form of the “suitable agricultural area.” All other non-agricultural changes detected in this period, like the expansion of urban area and water body, are kept constant.

The procedure is conducted in ArcGIS using the Mosaic Tool.

4.4.1 Results

Figure 4-20 (a) shows a mosaic of “suitable” agricultural area, water body, and urban area under the actual 2014 LULC, which are kept constant in the hypothetical LULC scenario development process. The hypothetical 2014 LULC scenario is as shown in Figure 4-20 (c), is prepared by mosaicking the map in Figure 4-20 (a) onto 4-20 (b), which is the 1992 LULC (also the baseline LULC scenario).

Major differences between the actual 2014 LULC scenario (Figure 4-20 b.) and the hypothetical 2014 LULC scenario occur mainly in three areas highlighted by dotted rectangles and denoted by numbers 1, 2, and 3. These changes are explained as follows:

Area 1: The actual 2014 LULC (4-20 .b) has a slightly larger agricultural area in comparison to the hypothetical 2014 LULC map (4-20 .c); this is because of the sparse forest, which has a very aerial small coverage, was cleared for agriculture use. However, this option has been blocked by the new landuse planning approach, which restricts expansion only to Grassland. Since Grassland does not occur in this area, the state of agricultural land remains as it was in the baseline LULC scenario of 1992 (4-20 .a).

Area 2: Actual 2014 LULC scenario (4-20 .b) has larger tracts of agricultural land; this is because the large forest which was found in this area under 1992 LULC was cleared to make room for. Agricultural activities in this area were also established in areas that initially had herbaceous vegetation and Shrubland. Since the agricultural expansion is limited to grassland LULC is very limited in the area, expansion of agricultural establishment under the hypothetical 2014 LULC is less (4-20 .c) in comparison to the actual 2014 LULC scenario.

Area 3: The new approach breaks up agricultural areas into smaller discrete areas. There are also additional areas that have been identified as suitable for agriculture. The areas that have been used for agriculture under the actual 2014 LULC scenario (in Figure 4-20 .b) are quite suitable. However, there is room for improving the conservation of hydrological regimes using the new approach; this gives a higher resolution scenario.

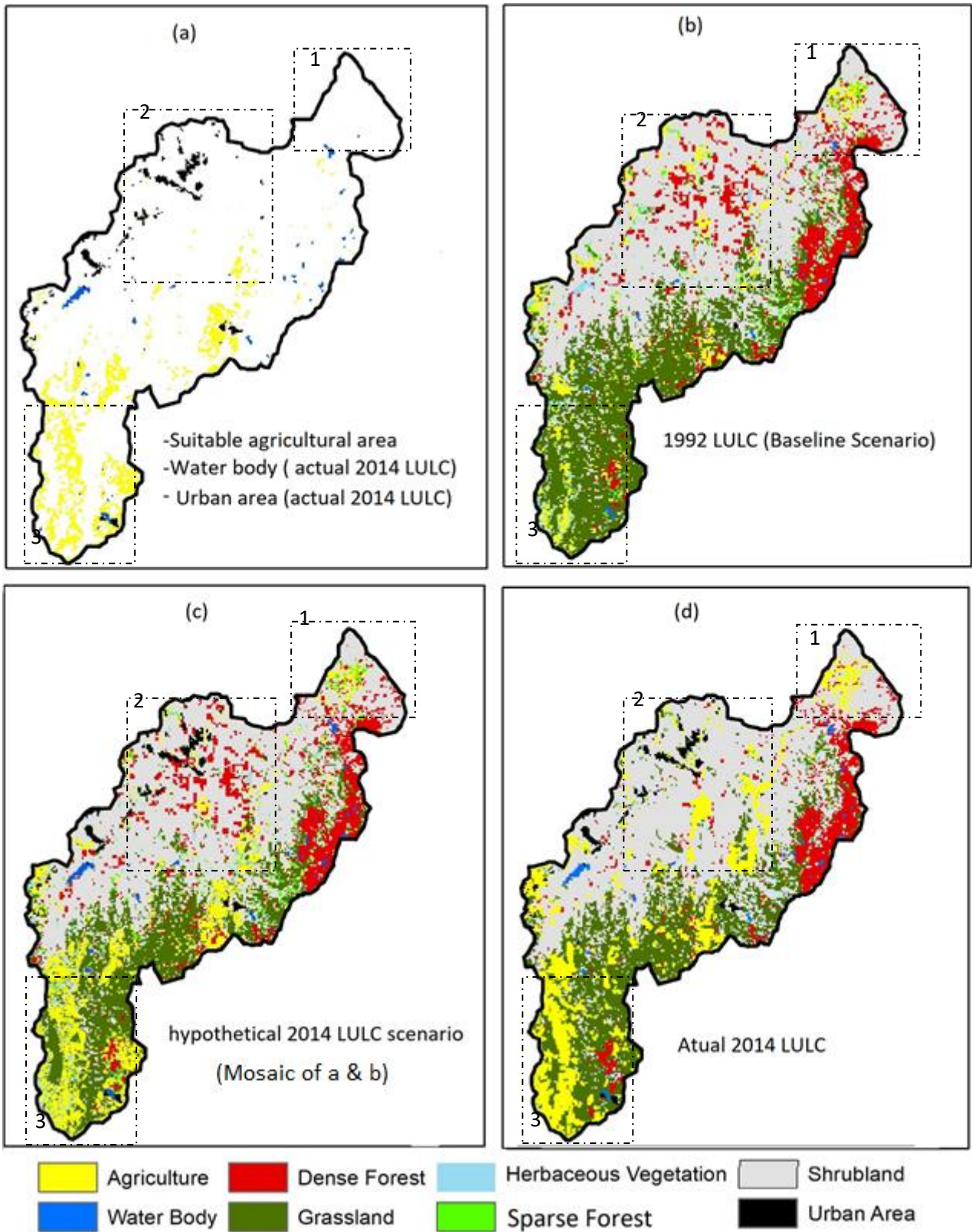


Figure 4-20: Development of hypothetical 2014 LULC scenario and the difference maps of the 1992 LULC baseline scenario (b), 2014 LULC real scenario and 2014 LULC scenario developed using the new approach

4.5 Evaluation of the proposed LULC planning approach

The effectiveness of the agricultural LULC planning approach in mitigating changes in the hydrological regime in Blyde and Steelpoort River Basin is evaluated by using the SWAT Model; the model is set up using the hypothetical 2014 LULC scenario developed in the previous chapter (Figure 4-21 c.). The meteorological data is the same as that described and used in model set-up in Section 3.3.3. Model parameterization is based on calibrated parameters obtained in Section 3.3.4.

Hydrological simulations were conducted for 25 years (1990-2014), with a warm-up period of three years (1987-1989).

4.5.1 Results

Figure 4-21 shows the various hydrological components under the 1992 LULC scenario, the actual 2014 LULC scenario, and the hypothetical 2014 LULC scenario. The surface under the hypothetical 2014 LULC is lower than that of the actual 2014 LULC scenario but higher than that of the 1992 LULC scenario; this is an indication that the new LULC planning approach is effective in mitigating changes in surface runoff.

There are no changes in lateral flow under the actual 2014 LULC scenario and the hypothetical 2014 LULC scenario.

Net aquifer recharge under the hypothetical 2014 LULC scenario is a little much higher than that of the actual 2014 LULC and that of 1992 LULC; this is an indication that the developed agricultural LULC planning approach is effective in enhancing groundwater recharge.

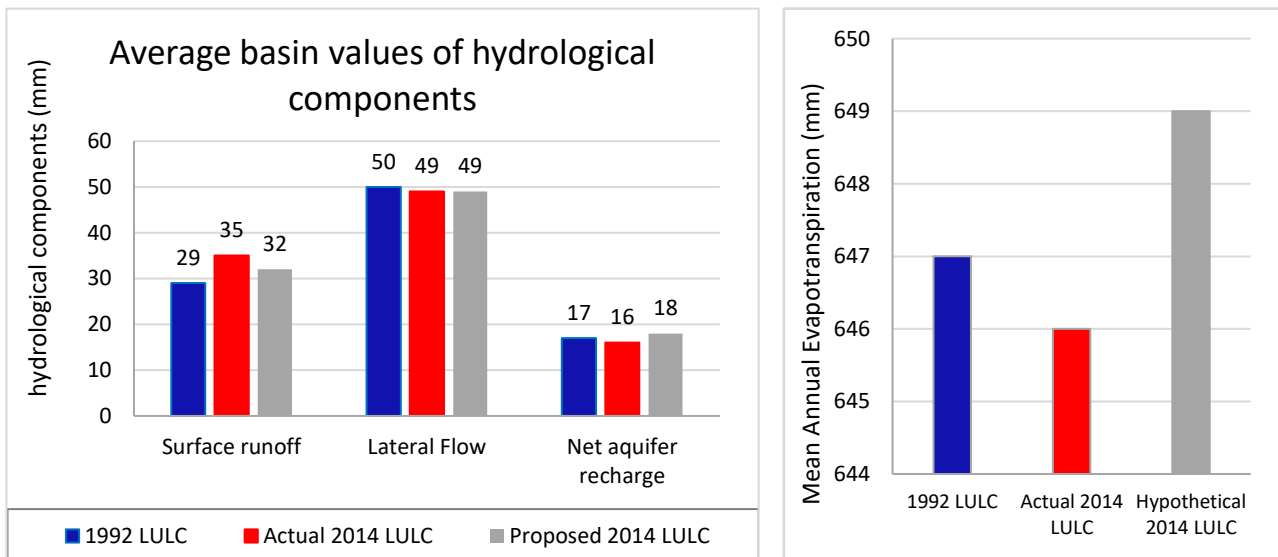


Figure 4-21: comparison of various hydrological components under the 1992 LULC, the actual 2014 LULC, and the hypothetical 2014 LULC scenarios

Figure 4-22 shows the various discharge curves under the 1992 LULC scenario, the actual 2014 LULC scenario, and the hypothetical 2014 LULC scenario. At station B4H003, the discharge under the hypothetical 2014 LULC is lesser than that of the actual 2014 LULC and more than that of the 1992 LULC; this illustrated that the newly developed LULC approach is reduced the volume of surface runoff generated despite the upstream area (Area

3 in Figure 4-20) having larger agricultural development under the hypothetical 2014 LULC than that detected in the actual scenario.

At the outlet of Blyde (B60J), the discharge curve under the hypothetical LULC scenario resembles the curve under the 1992 LULC scenario; this is because the upstream area (Area 1 in Figure 4-20) which underwent extensive agricultural development under the actual 2014 LULC scenario did not meet criteria for agricultural use under the new LULC planning approach, and hence the agricultural LULC impacts on hydrology do not exist under the hypothetical 2014 LULC.

At the B42H Outlet, the discharge curve only shifts slightly downwards during the peak season; this can be attributed to the minimal agricultural development under Area 2 in Figure 4-20. Changes in discharge between the 1992 LULC scenario (baseline) and those from the actual 2014 LULC scenario and the hypothetical 2014 LULC scenarios are very minimal at this station.

At station B4H025, the discharge curve under the hypothetical 2014 LULC shifts upwards at the beginning of the rain season in October with higher flows in the recession period (March, April, May); this discharge pattern can be attributed to factors like increase in the lateral flow which subsequently increases the baseflow.

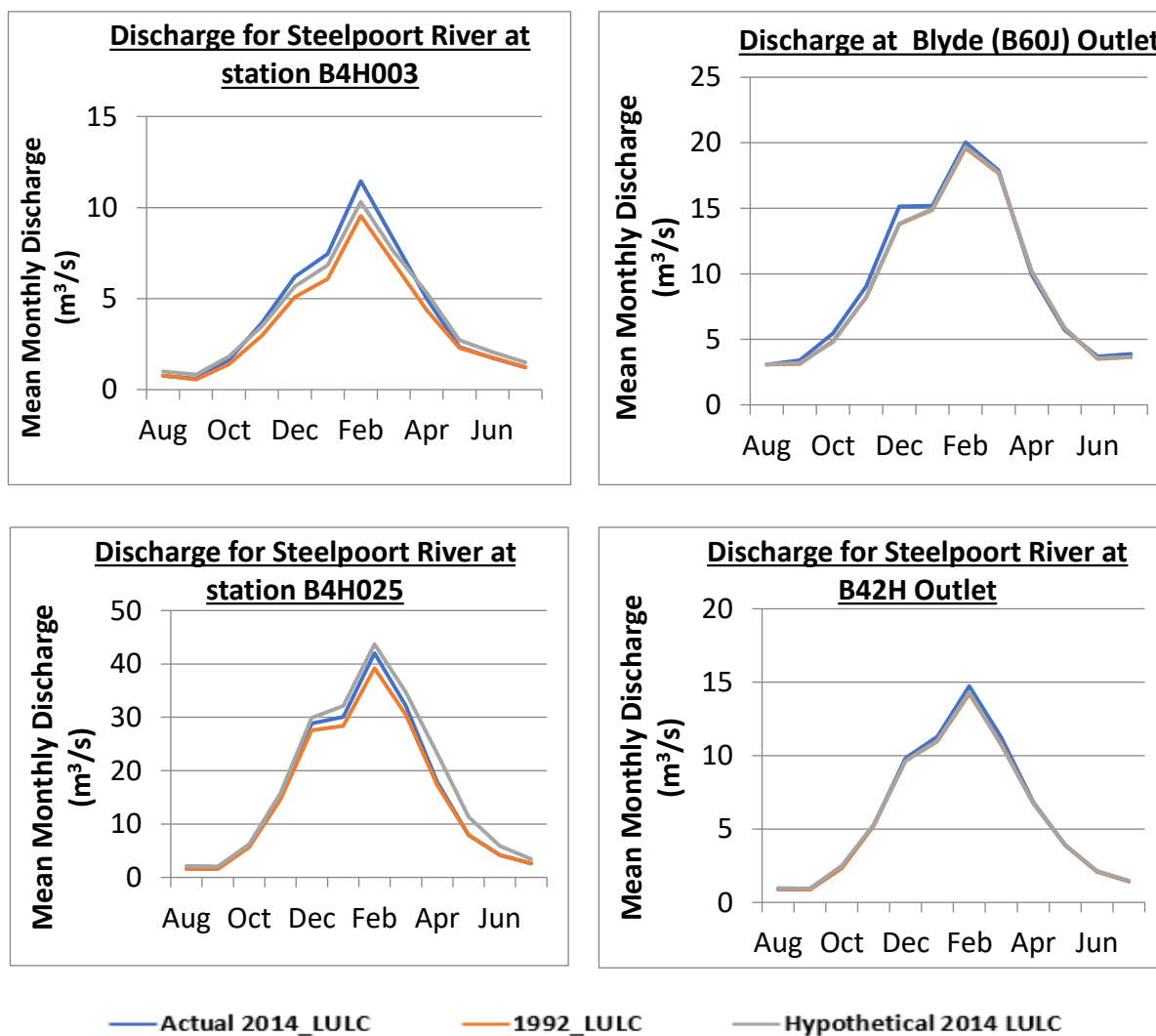


Figure 4-22: Illustration of the shift in discharge curves under the 1992 LULC, the actual 2014 LULC and the hypothetical 2014 LULC

4.6 Discussions

Hydrological regimes of many river basins are under threat due to constant landuse development. The Blyde and Steelpoort River Basins have experienced an extensive expansion of agriculture within a very short period, as shown in Chapter 3 of this research. The drivers of these LULC changes indicate that further changes in the future are inevitable.

The EIA studies, which are in some cases employed when a developer/farmer wishes to establish agricultural activities, are conducted on a need-basis and cannot provide an overview of the whole river basin. The basin-wide overview is necessary to improve IWRM planning and in the long term. A review of the EIA procedure indicates that in the quantification of the impacts of agricultural establishment on hydrology, the terrain slope is almost the only morphological parameter that is given consideration. However, numerous morphological features that contribute to hydrological partitioning that are not included in the EIAs can provide information to help enhance the mitigation of changes in hydrology.

On the other hand, the existing agricultural LULC development approaches do not give much emphasis on the LULC class that can be replaced without much impact hydrology. EIA studies and small scale farmers. Providing these farmers and other stakeholders with a map designating the best areas for agricultural use can change the course of the resource management to promote conservation of the hydrological regimes and other services depending on it.

This chapter proposes an agricultural LULC planning approach in which both morphological aspects and the hydrological characteristics of the LULC class to be replaced are taken into account. The method utilized morphology-landuse-hydrology interactions to identify LULC classes and physical conditions under which agriculture can be established with minimal hydrological implications. Hydrological characteristics of the dominant LULC classes in the study area were compared through hydrological simulations to identify LULC classes with closer response patterns to agricultural land. The findings revealed that grassland responds almost closely to agriculture and can be cleared for agricultural activities.

Morphology, which is considered an essential element in water partitioning, was also assessed to establish the physical basin characteristics under which agriculture exhibits the least hydrological changes. Dominant morphological parameters that define water partitioning in these basins are first identified, and they are utilized to characterize their influence on the magnitude of hydrological changes between when landuse is transitioned from grassland to agriculture. Following a two-step analysis, anomalies in lateral flow ratio and surface runoff ratio were found to have a statistical correlation with Terrain Ruggedness Index, slope, and bulk density. The three criteria developed for identifying “hydrologically suitable” areas for agriculture are as follows:

- Slope $\leq 4.4\%$, Terrain Ruggedness Index (TRI) ≤ 3 , and Bulk density $\geq 1282 \text{ kg/m}^3$

The results of Chapter 3 indicate that at slopes $> 4.4\%$, the volume of surface runoff generated is high; this figure is much lower than the value stipulated by DAFF. The slope influences the velocity of surface runoff; therefore, a decrease in the surface cover through agriculture further increases the surface runoff velocity by reducing Manning’s roughness of the surface.

High terrain ruggedness can indicate the presence of depression on the ground or crests on the ground; these depressions can be rivers or ponds, while the ridges can be cliffs or peaks of elevated areas. The high TRI areas are not suitable for agriculture since agriculture on the riverine is not recommended for conservation purposes, whereas the cresting grounds have high slopes, which result in high surface runoff.

High bulk density indicates high compaction of the ground; this usually results in poor infiltration, lateral flow, and high surface runoff generation. At higher bulk density, the changes in lateral flow due to agricultural LULC are very minimal; however, a field experiment may be required to determine to explain this phenomenon.

The LULC class identified for replacement and the three morphological parameters identified as suitable for agricultural use can be adopted for use in EIA studies and in mapping out potential agricultural areas in other river basins with similar vegetation communities.

The three morphological parameters and their statistical relationships (equations in Table 4-3) were adopted for the identification of “hydrologically suitable” areas for agriculture by applying a threshold that reduced the magnitude of hydrological changes

The above criteria were then used to develop a hypothetical scenario of 2014 LULC. The difference map in Figure 4-20 indicated a large disparity in agricultural land, especially in Areas 1 and 2. This disparity was mainly brought about by insufficient grassland in this area that could be cleared for agricultural development.

The hydrological output of the hypothetical 2014 LULC scenario was then compared that of 1992 LULC as the baseline scenario; in comparison to the actual 2014 LULC scenario, the general pattern revealed that most expansions in the upper section of the basin (Area 3 in Figure 4-20) were a little well sited with small exceptions. However, in the mid and lower parts, the significant disparity is brought about by the absence of grassland, which could be cleared for agricultural use.

The effectiveness of the approach developed was also evaluated by setting up the SWAT model using the developed hypothetical 2014 LULC scenario. Comparison of the hydrological outputs from the hypothetical 2014 LULC with those from the actual 2014 LULC and 1992 LULU revealed that the new LULC planning approach is capable of mitigating changes in various hydrological components like evapotranspiration and surface runoff. There was a slight increase in lateral flow and net groundwater recharge; these changes were, however, not so significant in comparison to minimized changes achieved in evapotranspiration and surface runoff. Therefore, the approach developed proved to be an effective landuse planning method with the aim of mitigation of changes in hydrological regimes. The reduction in lateral flow and net aquifer recharge could be an indication that various processes are connected and may depend on other parameters that could be further investigated.

While the slope is the only major topographic aspect integrated into EIA studies in cases of agricultural land establishment, this study demonstrates that bulk density and terrain ruggedness index can well define the magnitude of hydrological changes when grassland is transitioned into agricultural land. Global raster data for bulk density is freely available, while slope and terrain ruggedness can be derived from freely available DEM in GIS application software. Therefore; it can be concluded that bulk density and terrain ruggedness can be used for preliminary mapping of potential agricultural areas for the safeguarding of hydrological regimes

Based on the findings in this Chapter, water resources and land managers can adopt the morphological parameters identified herein and their corresponding thresholds for agricultural landuse planning so as to mitigate significant impacts on hydrological regimes. The LULC planning approach can be adopted for agricultural landuse planning in various parts of the world or be modified for a different type of landuse planning. However, the use of the morphological thresholds developed should be restricted to areas with similar vegetation communities and the same climatic pattern as the study.

5 TRANSFER OF FINDINGS TO MAPPING SUITABLE AREA FOR FUTURE AGRICULTURAL USE AND PROJECTION OF ITS CORRESPONDING HYDROLOGICAL SCENARIOS UNDER CLIMATE CHANGE

5.1 Background

The previous chapters of this research have revealed the extensive expansion of agriculture in Blyde and Steelpoort River Basins. During the data collection exercise, discussions with Ms. Anneliza Collett of the Department of Agriculture Forestry and Fisheries (DAFF) indicated that population growth and food demand are the main drivers of agricultural landuse expansion. WWF (2016) indicate that South Africa had a population of about 49 million according to the 2009 census and projected that there would be 82 million people living in South Africa by 2035. The Olifants River Basin receives higher rainfall than most parts of the country (Figure 5-1), which is an indicator of relatively conducive conditions for agriculture; this environmental aspect, coupled with increasing demand for food, makes the basin prone to further expansions of agriculture. Also demonstrated in the previous chapters is the influence of these changes on the hydrology of the river basin, which in turn influences water availability and the ecology.

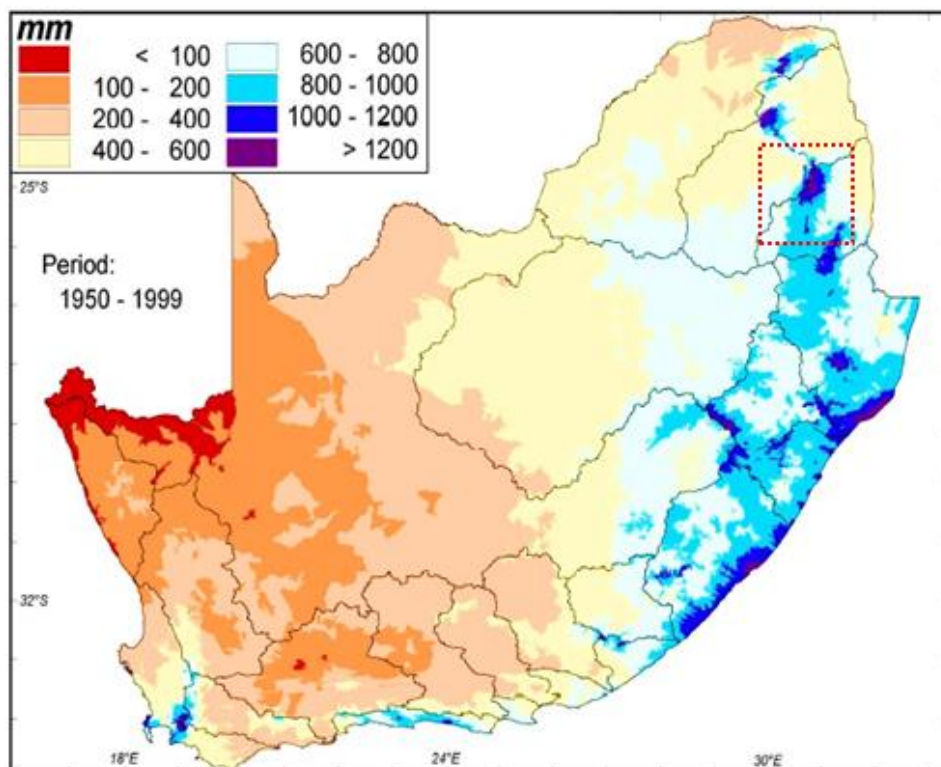


Figure 5-1: Rainfall distribution in South Africa

TRANSFER OF FINDINGS TO MAPPING SUITABLE AREA FOR FUTURE AGRICULTURAL USE AND PROJECTION OF ITS CORRESPONDING HYDROLOGICAL SCENARIOS UNDER CLIMATE CHANGE

The proposed agricultural landuse approach developed in the previous chapter has proved effective in minimizing changes in hydrology due to landuse changes. This method has also been utilized in the previous chapter to map out potential areas for future agricultural use, as shown in Figure 4-7. The main objective of proposing a new landuse planning approach being the minimization of hydrological changes. Therefore, it is also necessary to assess the future hydrological scenarios under this landuse expansion scenario (Figure 4-7) to aide a wholesome integrated water-landuse planning.

According to Bates *et al.* (2008) and IPCC (2014), all scenarios of climate projections show significant changes in hydrological regimes and induce various water stresses in most parts of the world.

The objective of this chapter is to apply the findings of the research to the preparation of future LULC maps with proposed areas for agriculture and simulating the resultant hydrological scenarios under the influence of climate change under various warming scenarios. The study period for the future hydrological scenarios is restricted to 21 years (until from 2015 to 2035).

5.2 Climate change and global warming scenarios

Climate change is a phenomenon that is brought about by global warming, which has accelerated since industrialization in the mid-20th Century (Department for Business Energy & Industrial Strategy, 2014; EPA, 2016; IPCC, 2014). Various stresses have been induced by climate change, and the desire to mitigate further changes and managed the risk triggered the scientific community to develop various future warming scenarios as a guide for developing target measures. These scenarios are developed by considering various factors like socio-economic development and their corresponding contribution of greenhouse gasses (GHG) and aerosols and chemically active gases concentration in the atmosphere (Moss *et al.*, 2008; Wayne, 2013; IPCC, 2014).

The increase of atmospheric gasses, including GHG concentration, alters the global energy balance by trapping more incoming energy. The measure of the influence the GHG and other gases have on the global energy balance is referred to as radiative forcing expressed in Watts per square meter (W/m^2), while the amount of carbon emission is expressed as Pentagram of Carbon per year ($PgC\ yr^{-1}$) (IPCC), 2008).

The warming scenarios developed by the Intergovernmental Panel for Climate Change (IPCC) are referred to as Representative Concentration Pathways (RCPs) and are represented by various trajectories of radiative forcing. Four different RCP scenarios of 2.6, 4.5, and 8.5 $PgC\ yr^{-1}$ are developed as illustrated in Figure 5-2 and described as follows.

RCP 2.6: Assumes a near-term and consistent decrease of CO_2 emissions; the radiative forcing pathway leads to 2.6 W/m^2 before 2100. Under this scenario, the change in global temperature is projected to be between 0.4^o to 1.6^o C

RCP 4.5 & RCP 6: This is intermediate scenarios where radiative forcings assume a gradual increase in emissions until mid to late century, followed by a gradual decrease until they are stabilized at approximately 4.5 W/m^2 and 6.0 W/m^2 after 2100. Changes in average global temperature for RCP 4.5 is projected to be between 0.9^o to 2^o C, while that of RCP 6 is projected to range between 0.8^o to 1.8^o C

RCP 8.5: This is the highest pathway for which radiative forcing reaches greater than 8.5 W/m^2 by 2099 and continues to rise for some amount of time

In this research, hydrological assessments are based on only three radiative forcing scenarios; RCP 2.6, RCP 4.5, and RCP 8.5.

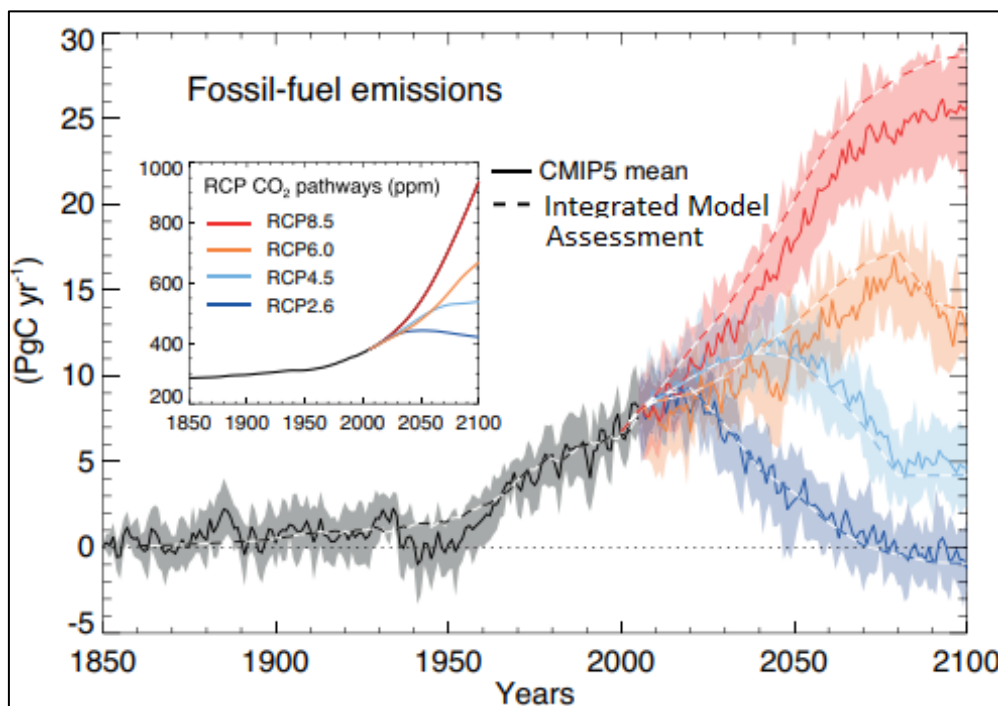


Figure 5-2: Illustration of RCPs (Intergovernmental Panel for Climate Change (IPCC), 2013)

5.2.1 Data acquisition and pre-processing

General Circulation Models (GCMs) are important tools that are used to investigate the past and future climatic patterns. The CIMP5 has forty GCMs that have been developed from various research groups around the world (Taylor, Stouffer, and Meehl, 2011). According to Kamworapan and Surussavadee (2019), GCMs perform differently in different regions. Therefore, in this research, data from four GCMs are evaluated to identify GCM that simulates the local climatic conditions well before applications in hydrological modelling and assessments. Projected climate data has been provided Water, Weather Energy, and Ecosystem (WWEE) supported by Coupled Model Intercomparison Project 5 (CMIP5) (Abbaspour *et al.*, 2019). The GCMs are as described in Table 5-1.

Table 5-1: Sources and resolutions of databases provided by WWEE

Data Type	Period extracted	Spatial Resolution	Temporal Resolution	Scenarios	Source
GFDL-ESM2M	1979–2035	0.5°	Daily	2.6, 4.5 & 8.5	NOAA/Geophysical Fluid Dynamics Laboratory
HadGEM2-ES	1979–2035	0.5°	Daily	2.6, 4.5 & 8.5	Met Office Hadley Center
IPSL-CM5A-L	1979–2035	0.5°	Daily	2.6, 4.5 & 8.5	L’Institut Pierre-Simon Laplace
MIROC	1979–2035	0.5°	Daily	2.6, 4.5 & 8.5	AORI, NIES and JAMSTEC

All four GCMs have historical (1970–2005) and future data (2005–2099). Because of continuously dynamic environmental conditions highlighted in previous chapters, analysis of future climatic and hydrological conditions are only limited to the year 2035. Historical data was also obtained in addition to projected data to support the correction of bias errors. The type of data acquired includes temperature and precipitation in daily

TRANSFER OF FINDINGS TO MAPPING SUITABLE AREA FOR FUTURE AGRICULTURAL USE AND PROJECTION OF ITS CORRESPONDING HYDROLOGICAL SCENARIOS UNDER CLIMATE CHANGE

time steps with a grid resolution of $0.5^{\circ} \times 0.5^{\circ}$. According to Ehret *et al.* (2012), GCM data is too coarse for realistic representation, especially in hydrological applications; therefore, correction of GCM data before use in hydrological analysis is necessary.

Climate Change Toolkit (CCT), which is also provided by WWEE, is used to check and correct the bias errors in the data and interpolate the data to a higher resolution of $0.25^{\circ} \times 0.25^{\circ}$ (Vaghefi, Abbaspour, and Kamali, 2017). Bias correction utilizes a transformation algorithm to adjust GCM data. The algorithm identifies biases between observed and simulated historical climate data, which parameterize the algorithm for correcting historical data. The parameterized algorithm is also applied to the correction of future climate data (Rathjens *et al.*, 2016). CCT Model presents two bias correction methods; the Ratio Method, which employs multiplicative factors for the correction of precipitation, and Additive Method for the correction of temperature (Abbaspour *et al.*, 2019).

The baseline period for bias correction has been selected based on time coverage of historical data (from 1979-2005).

5.2.2 Results: Bias correction of rainfall and temperature

Figure 5-3 shows the comparison of monthly distribution of raw historical rainfall from four GCM with observed rainfall and bias-corrected GCM rainfall. Raw rainfall data from GFDL-ESM2M has a minimal variation between in winter (May-September) when it is drier. The pattern changes in October until the end of January, where GFDL-ESM2M rainfall is much higher than observed rainfall. Thereafter slight variations in rainfall are observed in March and April. After corrections, GFDL-ESM2M rainfall data exhibits almost similar seasonal patterns with observed data but with only very little variations during the peak season.

Raw HadGEM2-ES exhibit closer patterns with observed rainfall between May and September. The peak of the raw data comes in November with a very quick recession soon after. The CCT algorithm well corrected the smaller variations in the rising and receding limbs of the rainfall curves. However, the algorithm introduced some variations in the peak that did not match the observed data.

Raw IPSL-CM5A-L data has much closer patterns with observed rainfall between February and September. The seasonal pattern deviates from observed data from October to January, where the raw GCM data is much higher than the observed data. The timing of the highest peak coincides with that of the observed data. After corrections, the high peaks in the data are much reduced, with very little variations still observed at the peaks.

Raw MIROC data starts to deviate from observed data very early in the season (July), where the GCM data is much higher. The deviation is highest at the peak. After corrections, the deviations in the rising limb are corrected, the higher peak is reduced and becomes slightly lower than that of observed in January.

Based on the results presented herein, it can be seen that the bias correction algorithm employed generally improved rainfall distribution in all the GCMs apart from HadGEM2-ES, where the peak was more distorted.

TRANSFER OF FINDINGS TO MAPPING SUITABLE AREA FOR FUTURE AGRICULTURAL USE AND PROJECTION OF ITS CORRESPONDING HYDROLOGICAL SCENARIOS UNDER CLIMATE CHANGE

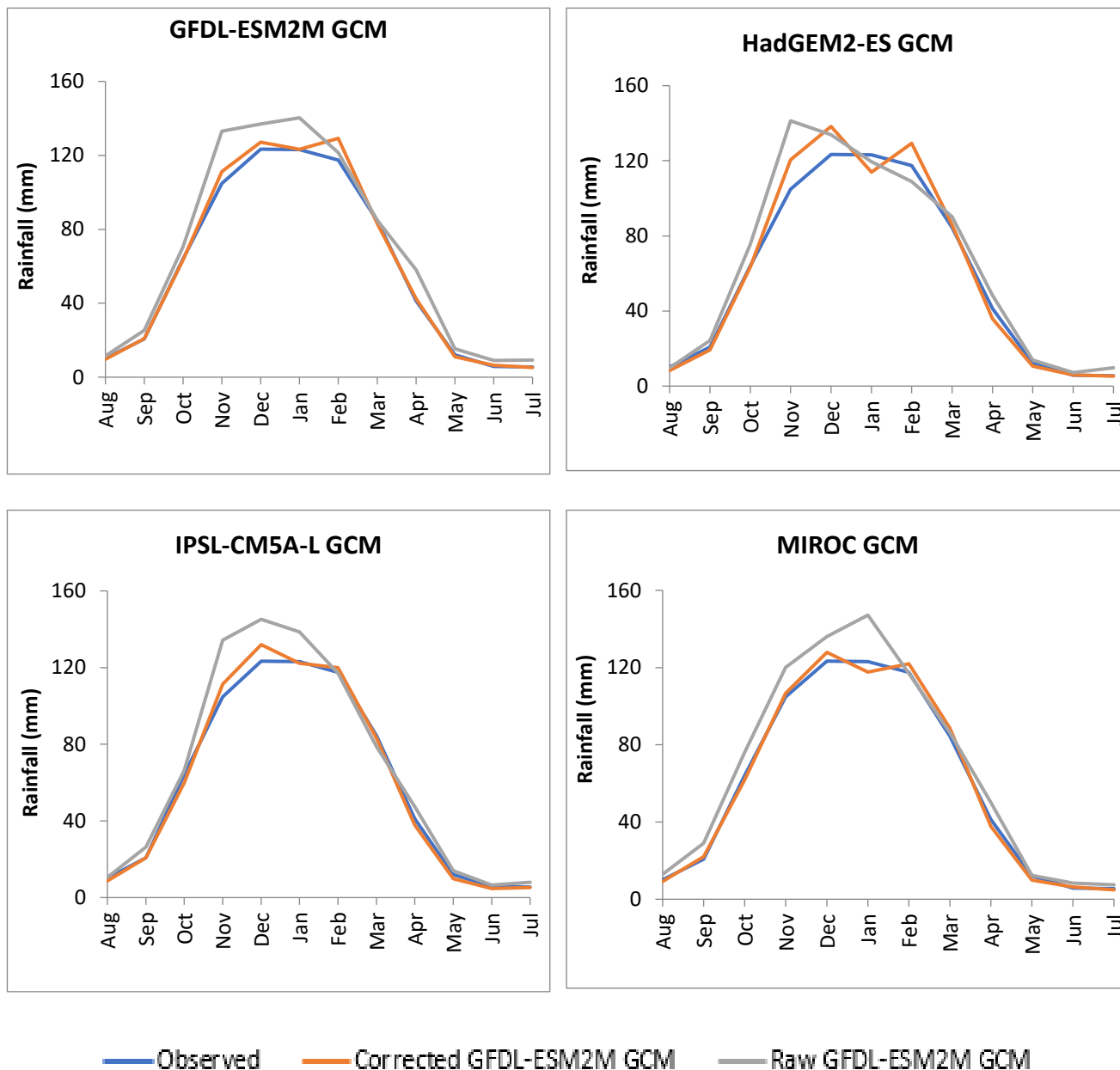


Figure 5-3: comparison of monthly distribution of raw historical rainfall from four GCM with observed rainfall and bias-corrected

Figure 5-4 shows the monthly distribution of raw historical average daily temperature from four GCM in comparison with observed and bias-corrected GCM temperature. Raw temperature data from all the four GCMs is generally higher than that of observed data most of the time. Bias correction algorithm improves the temperature data in all the four GCMs with best curve improvement observed under GFDL-ESM2M and IPSL-CM5A-L GCMs

TRANSFER OF FINDINGS TO MAPPING SUITABLE AREA FOR FUTURE AGRICULTURAL USE AND PROJECTION OF ITS CORRESPONDING HYDROLOGICAL SCENARIOS UNDER CLIMATE CHANGE

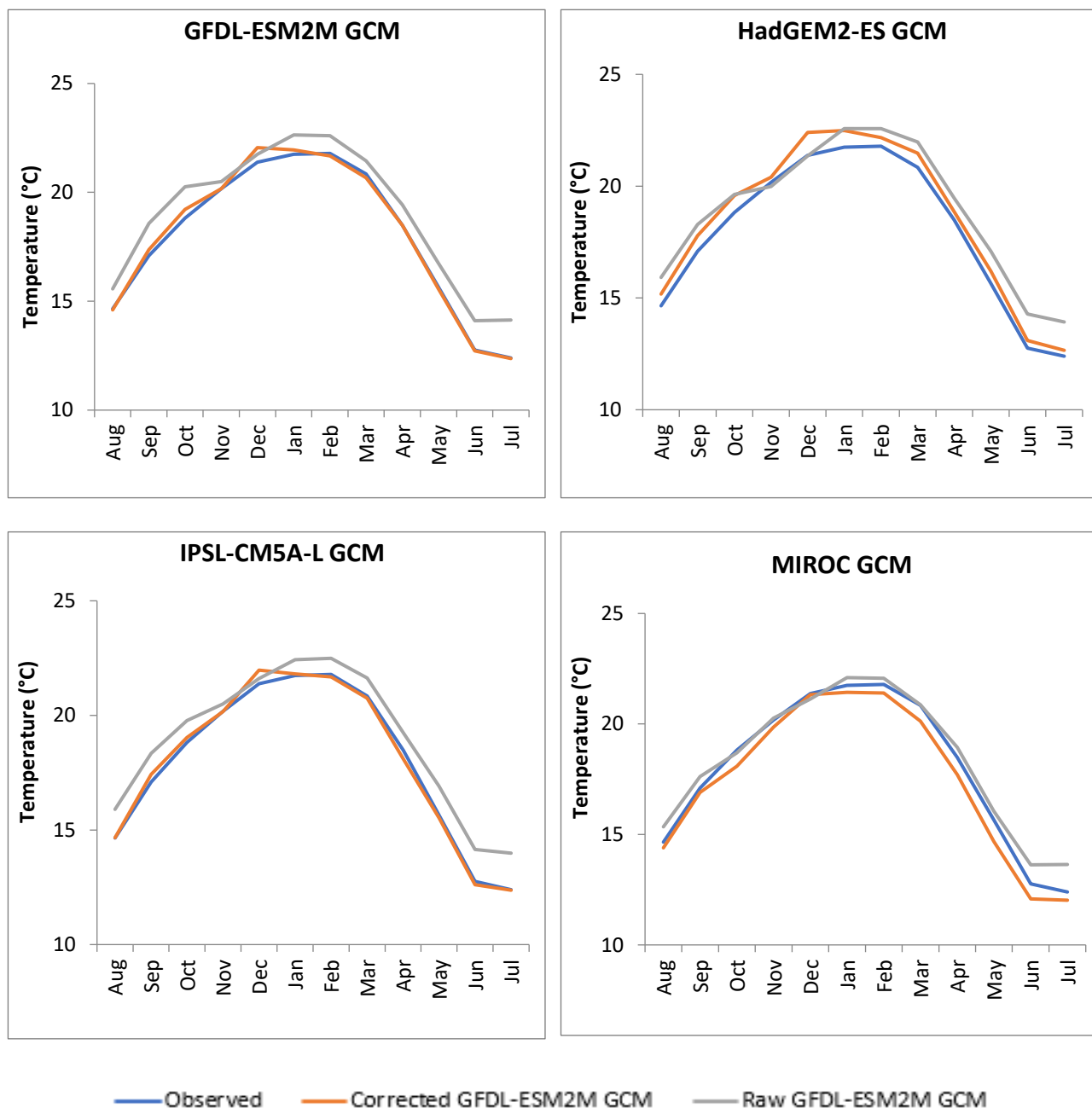


Figure 5-4: comparison of monthly distribution of raw historical average daily rainfall from four GCM with observed and bias-corrected temperatures (average daily)

5.2.3 GCM selection

Evaluation of GCMs' performance before applications in further studies is becoming a widely accepted scientific practice (Shi *et al.*, 2018). Statistical tests have been in the past utilized to evaluate the performance of GCMs, for example, by Ruan *et al.* (2018), Shi *et al.* (2018), Bokke *et al.* (2017), and Fu *et al.* (2013). In this research, multiple statistical tests are selected as criteria in assessing the performance of the selected GCMs. This includes percentage bias (PBIAS), Pearson's correlation coefficient (R), Kling Gupta efficiency (KGE), Index of Agreement (IA), Nash-Sutcliffe Efficiency (NSE), and root mean square error (RMSE).

TRANSFER OF FINDINGS TO MAPPING SUITABLE AREA FOR FUTURE AGRICULTURAL USE AND PROJECTION OF ITS CORRESPONDING HYDROLOGICAL SCENARIOS UNDER CLIMATE CHANGE

The rainfall and temperature data used in this step are from the four GCMs and have already been bias-corrected and interpolated to a grid size of 0.25°.

The statistical tests are applied to monthly time series, and each statistical test is assigned an equal weight. Therefore, a simple ranking of each test across the four GCMs is conducted. Based on the ranking scores, the overall ranks are computed for each GCM. GCM with the highest rank is then selected for further applications. The statistical tests are described as follows:

Pearson's correlation coefficient (R) measures the degree of linear association between modelled and observed values and is defined by:

$$R = \frac{\sum_{t=1}^n (x_t - \bar{x})(y_t - \bar{y})}{\sqrt{\sum_{t=1}^n (x_t - \bar{x})^2} \sqrt{\sum_{t=1}^n (y_t - \bar{y})^2}} \quad 5.1$$

Where x_t and y_t are the modelled (GCM) and observed variable at t time step (months), \bar{y} is the mean of observed data, \bar{x} is the mean of modelled data, and n is the total number of observations. The coefficient of determination varies within the interval $[-1, 1]$, where values close to 1 indicate a good fit (López *et al.*, 2017).

Nash-Sutcliffe Efficiency (NSE) describes the relative magnitude of the residual variance as compared to the observed and demonstrates how well the plot of observed versus simulated value fits the 1:1 line. The following formula represents NSE:

$$NSE = 1 - \frac{\sum_{t=1}^n [x_t - y_t]^2}{\sum_{t=1}^n [y_t - \bar{y}]^2} \quad 5.2$$

Where x_t and y_t are the modelled (GCM) and observed variable at t time step (months), and n is the total number of observations. NSE varies from $-\infty$ to 1, with values close to 1 indicate a good fit (López *et al.*, 2017).

PBIAS is used to estimate the average bias between observed and GCM values. PBIAS (%) is computed as follows:

$$PBIAS(\%) = \frac{1}{n} \sum_{t=1}^n x_t - y_t \quad 5.3$$

Where x and y_t are the modelled (GCM) and observed variable at t time step (months) and n is the total number of observations. A positive bias error indicates that the GCM dataset is overestimated, whereas a negative error indicates an underestimation of the GCM dataset (von Storch and Zwiers, 1999; Fikre, 2017; Ruan *et al.*, 2018).

The Root Mean Square Error (RMSE) is used to measure the error between model (GCM) predicted values and the observed value. These individual differences are also called residuals, and the RMSE aggregates them into a single measure of predictive power. It is computed as follows:

$$RMSE = \frac{\sum_{t=1}^n [y_t - x_t]^2}{n} \quad 5.4$$

Where x_t and y_t are the modelled (GCM) and observed variable at t time step (months), and n is the total number of observations. RMSE varies from 0 to $+\infty$. Lower values of RMSE are associated with the best results (von Storch *et al.*, 1999; Fikre, 2017; Ruan *et al.*, 2018).

KGE This goodness-of-fit measure was first developed by Gupta *et al.*, (2009) to provide a diagnostically interesting decomposition of the NSE. It facilitates the analysis of the relative importance of correlation, bias,

and variability in the context of hydrological modelling. Kling, Fuchs, and Paulin (2012), proposed a revised version of this index, to ensure that the bias and variability ratios are not cross-correlated. KGE is computed as follows:

$$KGE = 1 - \sqrt{(R - 1)^2 + \left(\frac{\delta_x}{\delta_y} - 1\right)^2 + \left(\frac{\bar{x}}{\bar{y}} - 1\right)^2} \quad 5.5$$

Where x and y are modelled (GCM) and observed variables, \bar{y} is the mean of observed data, \bar{x} is the mean of modelled data, and n is the total number of observations. KGE ranges from $-\infty$ to 1. Essentially, the closer to 1, the more accurate the model is (Gupta *et al.*, 2009).

Index of Agreement (d) is a standardized measure of the degree of model prediction error. d is computed using the following formula:

$$d = 1 - \frac{\sum_{t=1}^n [y_t - x]^2}{\sum_{t=1}^n [|x - \bar{y}| + |y_t - \bar{y}|]^2}, \quad 0 \leq d \leq 1 \quad 5.6$$

Where x and y_t are the modelled (GCM) and observed variable at t time step (months), \bar{y} is the mean of observed data, \bar{x} is the mean of modelled data, and n is the total number of observations. Index of Agreement (d) varies between 0 and 1. A value of 1 indicates a perfect match, and 0 indicates no agreement at all (Willmott, 1981).

5.2.3.1 Results: GCM selection

Figure 5-5 shows the performance evaluation of the seasonal distribution of bias-corrected rainfall data from the four GCMs. Rainfall is well represented by the four GCMS between March until October when the simulated rainfall deviates from observed. HadGEM2-ES and IPSL-CM5A-L exhibited the largest deviations and variability at the peaks relative to the observed data. The rainfall patterns from GFDL-ESM2M and MIROC exhibited closer seasonal patterns with observed data at the peak, though with some variations.

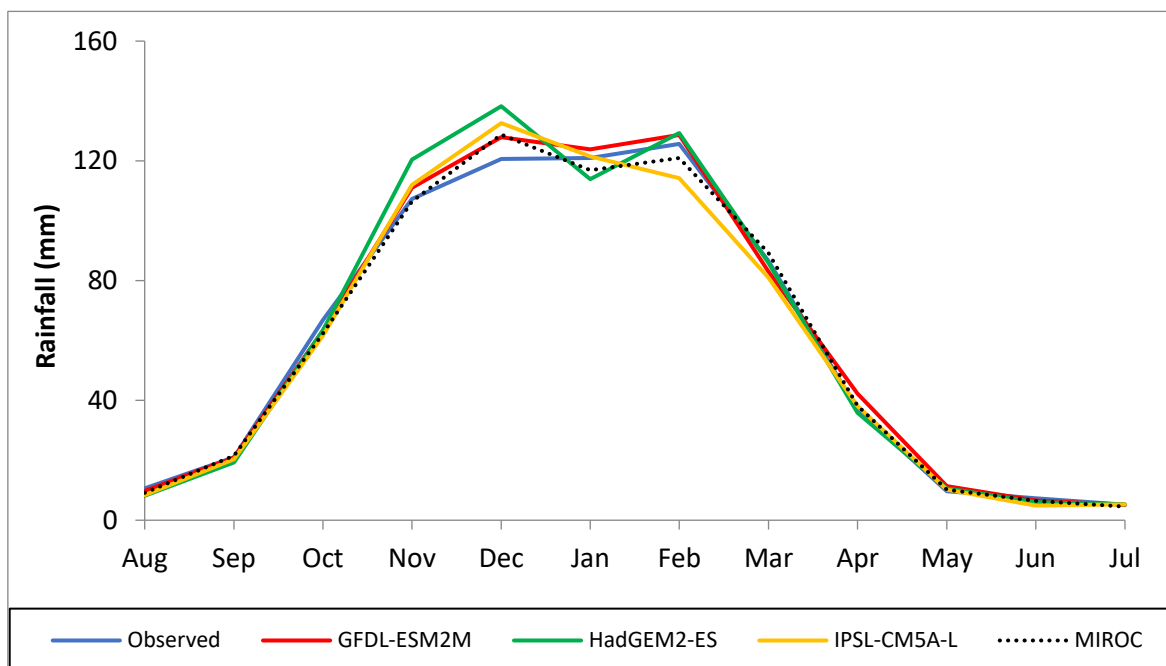


Figure 5-5: GCM performance evaluation of the seasonal distribution of bias-corrected rainfall over the study area.

TRANSFER OF FINDINGS TO MAPPING SUITABLE AREA FOR FUTURE AGRICULTURAL USE AND PROJECTION OF ITS CORRESPONDING HYDROLOGICAL SCENARIOS UNDER CLIMATE CHANGE

Table 5-2 shows the values of each statistical tests conducted for each bias-corrected GCM rainfall and their rankings in terms of their performance in simulating rainfall in the study area. The overall performance of bias-corrected rainfall data indicates that IPSL-CM5A-L and MIROC performed best (rank 1), having each of the test interchangeably taking the first and the second ranks. HadGEM2-ES and GFDL-ESM2M had relatively lower performance in each of the tests carried out.

Table 5-2: Ranking of criteria used for selection of GCM source for rainfall data

Statistical Test	GFDL-ESM2M		HadGEM2-Es		IPSL-CM5A-L		MIROC	
	Value	Rank	Value	Rank	Value	Rank	Value	Rank
R	0.59	3	0.57	4	0.67	1	0.64	2
PBIAS(%)	2.83	4	2.50	3	0.39	2	0.30	1
NSE	0.23	4	0.14	4	0.35	2	0.36	1
KGE	0.56	3	0.56	3	0.70	1	0.57	2
Index of Agreement (d)	0.74	3	0.72	4	0.8	1	0.78	2
RMSE	56.03	3	59.90	4	51.64	2	51.30	1
Total Points		20		22		9		9
Overall Rank		3		2		1		1

Figure 5-6 shows the performance evaluation of the seasonal distribution of bias-corrected temperature data from the four GCMs. Bias corrected temperature from HadGEM2-Es is higher than the observed temperature throughout the season. Bias corrected temperature from GFDL-ESM2M and IPSL-CM5A-L closely represent the observed data throughout the season. Bias corrected temperature from MIROC is underestimated.

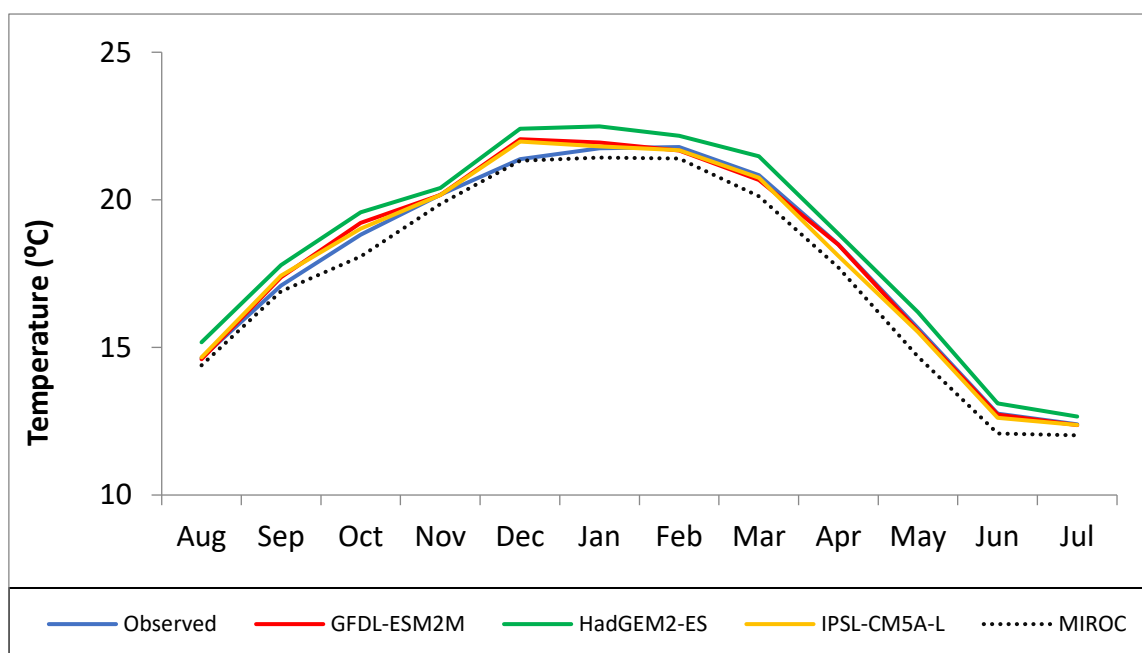


Figure 5-6: GCM performance evaluation of the seasonal distribution of bias-corrected temperature over the study area.

Table 5-3 Summarizes the output of each statistical test carried out on bias-corrected GCM temperature and their corresponding ranks in terms of their performance in simulating the temperature of the study area. The overall rank of bias-corrected rainfall data indicates that HadGEM2-ES performed best, followed by IPSL-CM5A-L. MIROC and GFDL-ESM2M had a relatively lower performance with poor performance, especially in RMSE, PBIAS, and NSE.

TRANSFER OF FINDINGS TO MAPPING SUITABLE AREA FOR FUTURE AGRICULTURAL USE AND PROJECTION OF ITS CORRESPONDING HYDROLOGICAL SCENARIOS UNDER CLIMATE CHANGE

Table 5-3: Ranking of criteria used for selection of GCM source for temperature data

StatisticalTest	GFDL-ESM2M		HadGEM2-ES		IPSL-CM5A-L		MIROC	
	Value	Rank	Value	Rank	Value	Rank	Value	Rank
R	0.16	3	0.19	2	0.16	3	0.57	1
PBIAS(%)	-2.82	3	-1.01	1	-1.28	2	-9.09	4
NSE	0.90	3	0.92	1	0.91	2	0.12	4
KGE	0.55	1	0.55	1	0.55	1	0.54	2
Index of Agreement (d)	0.71	3	0.72	2	0.74	1	0.71	3
RMSE	3.88	3	3.66	1	3.78	2	4.33	4
Total Points		16		8		11		18
Overall Rank		3		1		2		4

Since the time series used in statistical analysis are at monthly time steps, the results obtained using this approach provides a better representation of the whole dataset in comparison to the evaluation of the monthly distribution of rainfall and temperature curves. Therefore, bias-corrected data from IPSL-CM5A-L is selected for further analysis and subsequent application studies in the next steps.

5.2.4 Analysis of projected climate data

Patterns of projected rainfall and temperature under the three warming scenarios that are under consideration in this study are analyzed to identify patterns of variability from observed historical datasets. In the first step, curves of long-term seasonal distribution of projected rainfall and temperature are evaluated to identify anomalies from each other and observed datasets. Figure 5-7 shows curves of long-term seasonal distribution of projected rainfall and temperature vs. observed data; the mean monthly rainfall curves under RCP 2.6, 4.5, and 8.5 indicate minimum anomaly from each other and observed rainfall between April and September. The three scenarios of projected rainfall highly vary from each other and observed data at the peak.

On the other hand, projected temperatures under each RCP are much higher than the observed temperature with RCP 2.8, having the highest temperatures and RCP 2.6 the lowest temperatures.

TRANSFER OF FINDINGS TO MAPPING SUITABLE AREA FOR FUTURE AGRICULTURAL USE AND PROJECTION OF ITS CORRESPONDING HYDROLOGICAL SCENARIOS UNDER CLIMATE CHANGE

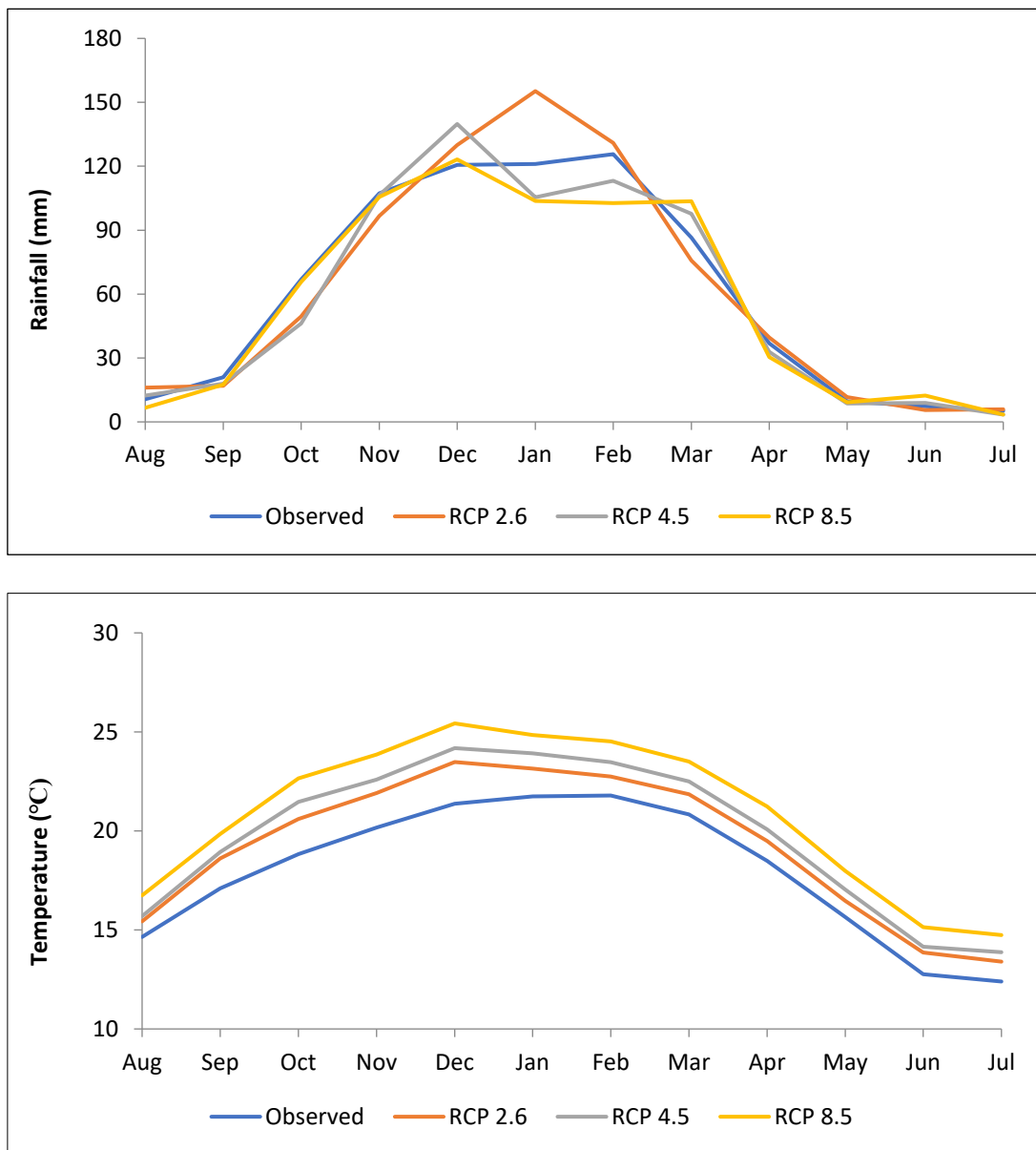


Figure 5-7: comparison of long-term seasonal distribution of projected rainfall (RCP 2.6, 4.5 & 8.5) with observed rainfall data

Figure 5-8 shows box plots of long-term seasonal distribution of projected rainfall under RCPs 2.6, 4.5, and 8.5 (blue) and observed historical (red). Under RCP 2.6, there is an indication that the beginning of the rainy season (September, October, and November) will experience reduced and variable rainfall, whereas the peak season (December, January, and February) will experience higher rainfall relative to the observed data. Under RCPs 4.5 and 8.5, average monthly rainfall is projected to be generally lower than observed data most of the season. There is no shift in peak season or dry season under the three future scenarios.

TRANSFER OF FINDINGS TO MAPPING SUITABLE AREA FOR FUTURE AGRICULTURAL USE AND PROJECTION OF ITS CORRESPONDING HYDROLOGICAL SCENARIOS UNDER CLIMATE CHANGE

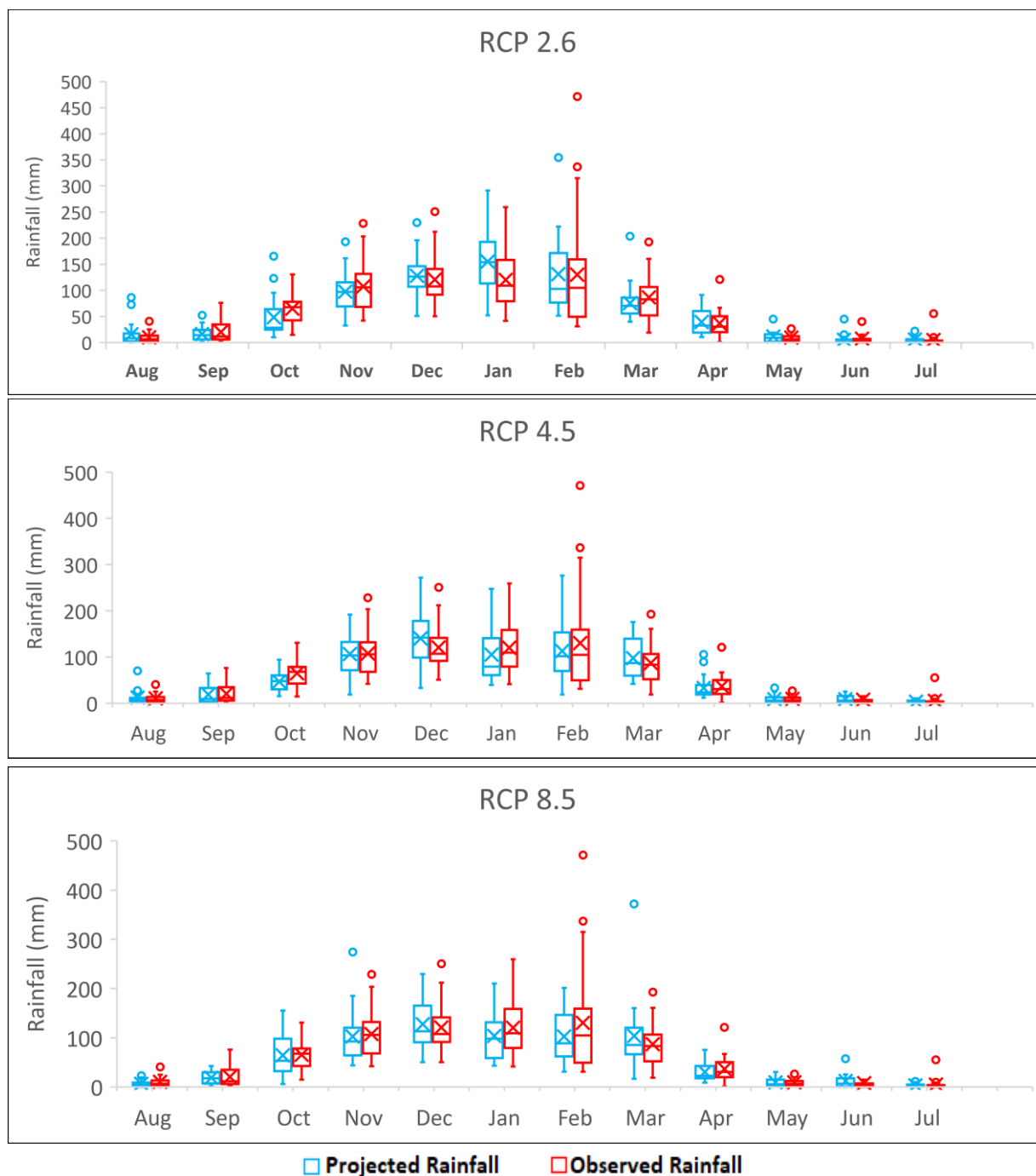


Figure 5-8: Box plots of long-term seasonal distribution of projected rainfall under RCP 2.6, 4.5 and 8.5 (2015-2035; in blue) and observed historical (1979-2005; in red). (x) represents monthly mean and (-) monthly median rainfall values

In the second step, the mean monthly rainfall distribution for each year under the three RCPs was compared against the long-term mean of observed data, as shown in Figure 5-9. There is a dominant interannual variability of rainfall under all three scenarios. The long-term monthly average rainfall marked by the red dotted line is 62mm, and it appears above the mean values of monthly rainfall under the three RCPs for most of the time in the year.

The projected long-term monthly average rainfall is 61mm under RCP 2.6, 58mm under RCP 4.5, and 57mm under RCP 8.5. The low average values in projected rainfall may indicate exacerbated drought conditions in the future and subsequently increased water scarcity in the study area.

TRANSFER OF FINDINGS TO MAPPING SUITABLE AREA FOR FUTURE AGRICULTURAL USE AND PROJECTION OF ITS CORRESPONDING HYDROLOGICAL SCENARIOS UNDER CLIMATE CHANGE

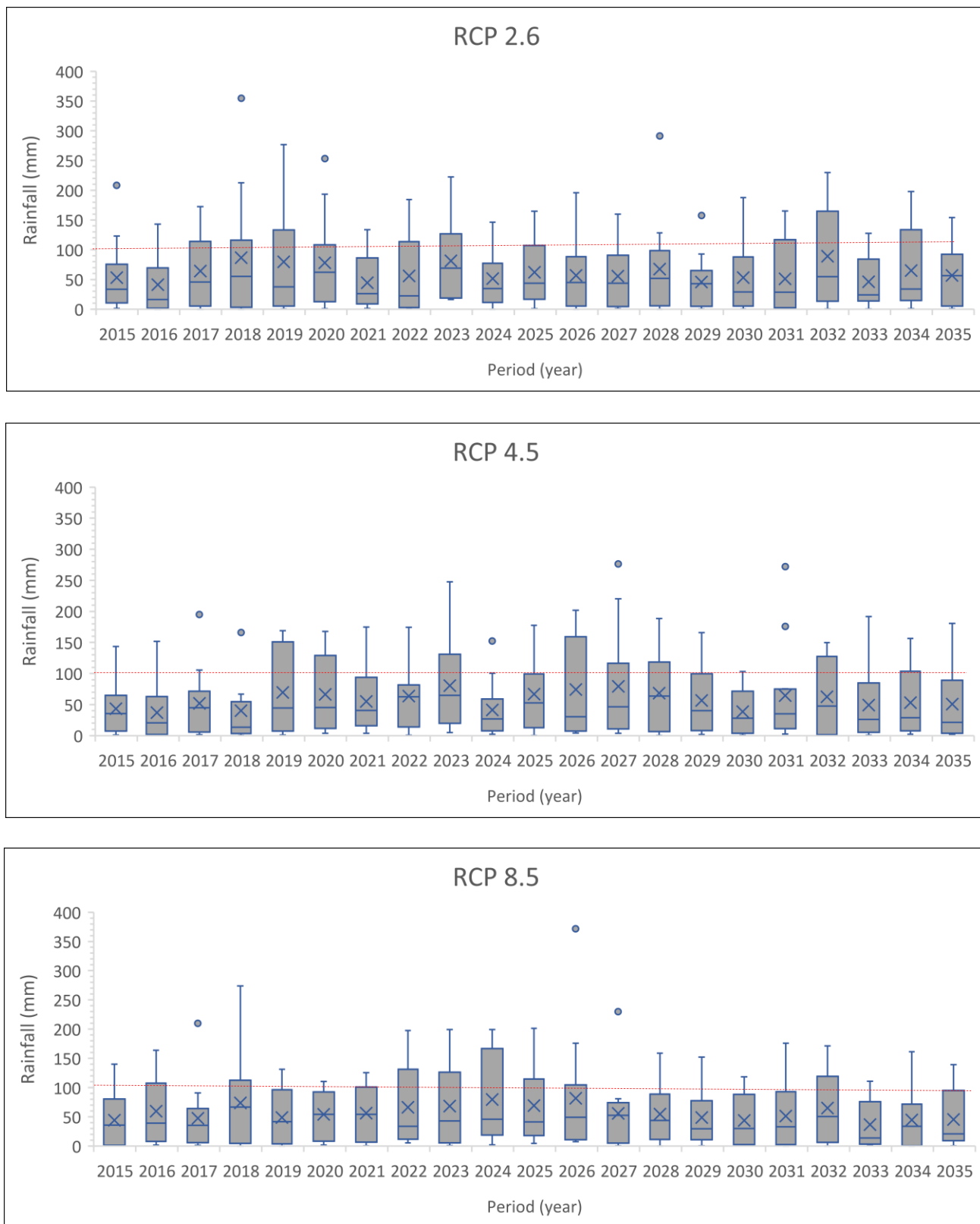


Figure 5-9: Box plots of 31 years (2015-2035) mean monthly rainfall under RCP 2.6, 4.5, and 8.5; (x) represents monthly mean and (-) monthly rainfall values for each year

TRANSFER OF FINDINGS TO MAPPING SUITABLE AREA FOR FUTURE AGRICULTURAL USE AND PROJECTION OF ITS CORRESPONDING HYDROLOGICAL SCENARIOS UNDER CLIMATE CHANGE

Figure 5-10 shows box plots of long-term seasonal distribution of projected temperature under RCPs 2.6, 4.5, and 8.5 (blue) and observed historical (red). The graphs indicate that under all the three RCPs, temperatures will be much higher than the observed historical temperature. Figure 5-11 indicates that the future average daily temperature under the three RCP scenarios will be slightly higher than that of the observed data throughout the year.

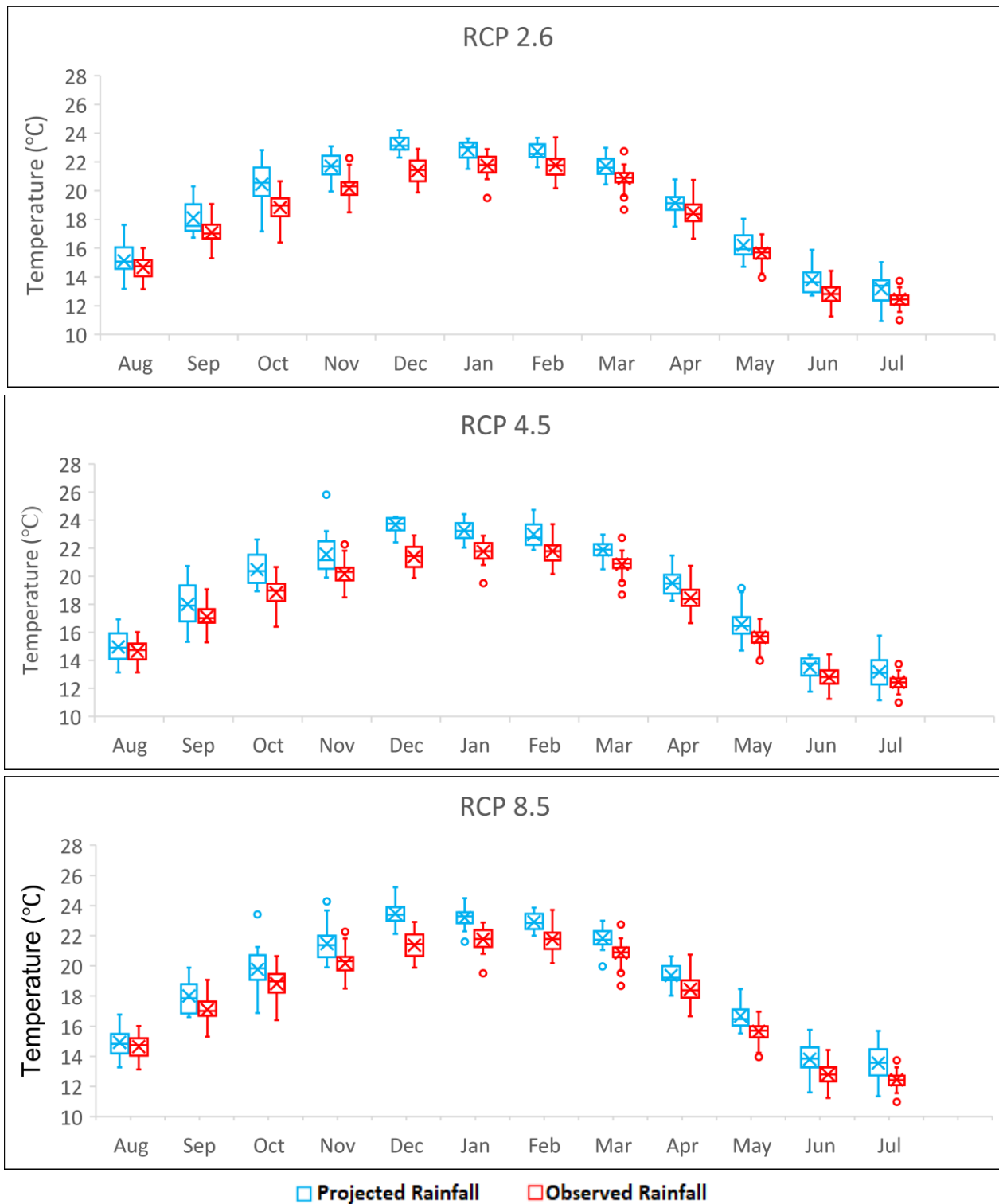
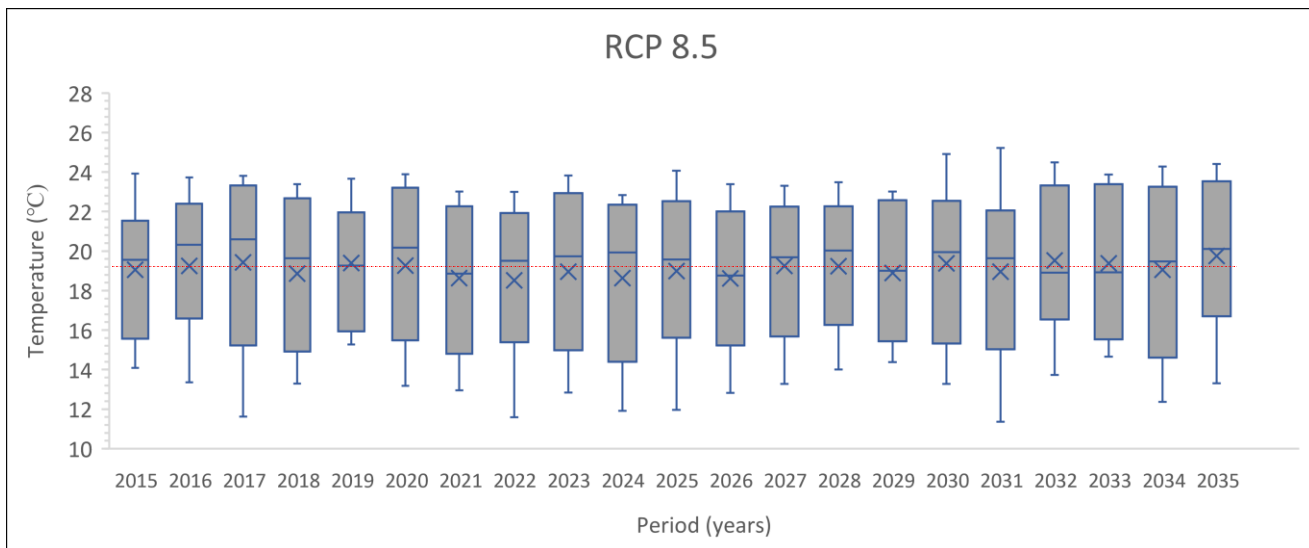
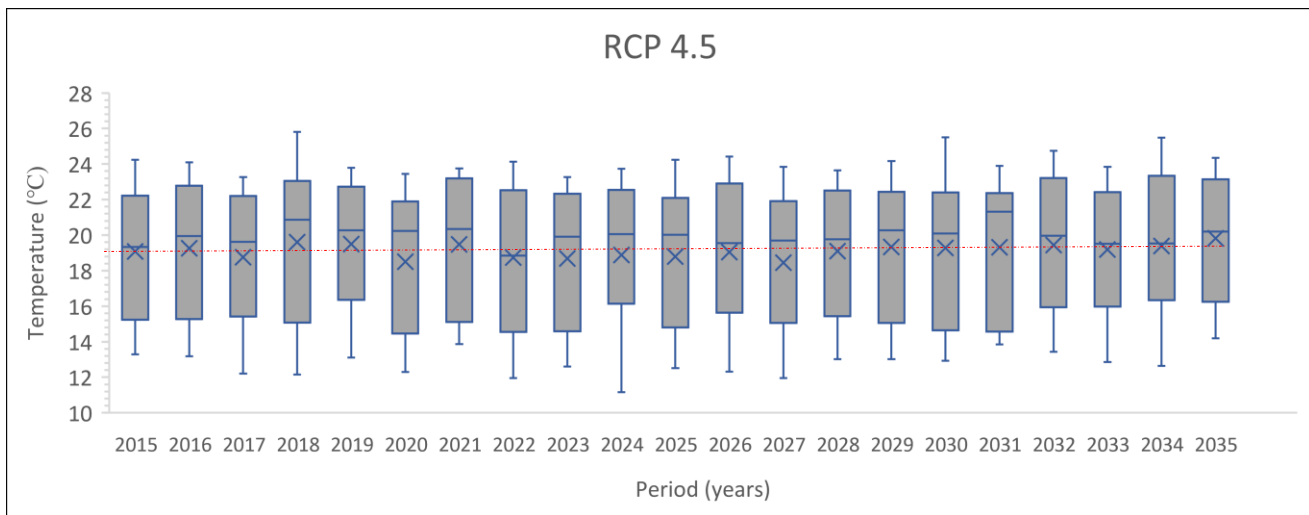
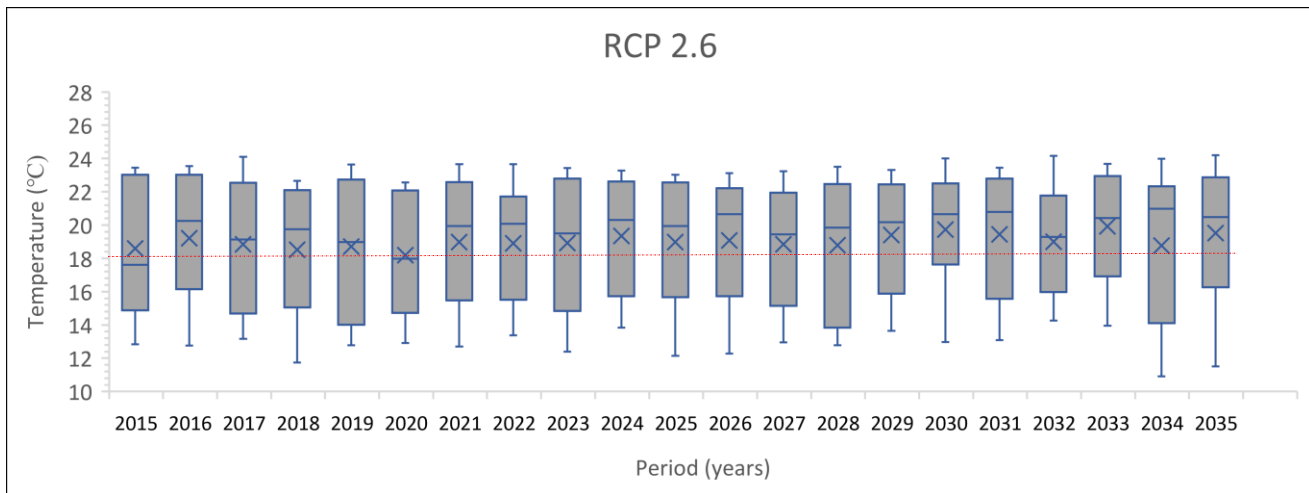


Figure 5-10: Box plots of long-term seasonal distribution of projected temperature under RCP 2.6, 4.5 and 8.5 (2015-2035; in grey) and observed historical (1979-2005; in red). (x) represents mean and (-) represents median temperature

TRANSFER OF FINDINGS TO MAPPING SUITABLE AREA FOR FUTURE AGRICULTURAL USE AND PROJECTION OF ITS CORRESPONDING HYDROLOGICAL SCENARIOS UNDER CLIMATE CHANGE



■ Projected Rainfall - - - - - Long term monthly mean of observed rainfall

Figure 5-11: Box plots of 31 years (2015-2035) mean monthly rainfall under RCP 2.6, 4.5, and 8.5;(x) represents monthly mean and (-) monthly rainfall values for each year

5.3 Future LULC scenario

In view of the future expansion of agriculture with 2014 LULC as the baseline scenario, there is still room for additional expansion of approximately 422 km² areas. The agricultural area under the 2014 LULC scenario (in Figure 5-13) and the suitable (recommended) areas for agriculture use are shown in figure 5-12.

With a focus only on agricultural expansion, the development of the future LULC scenario is achieved by mosaicking available 422 km² onto the actual 2014 LULC scenario. The Mosaic procedure is conducted in ArcGIS using the Mosaic Tool. The Map developed from this process is shown in Figure 5-14.

If major expansions exceeding 422 km² are desired, then shrubland would be the next LULC for consideration. Shrubland which also exhibits little hydrological anomaly with agriculture after grassland

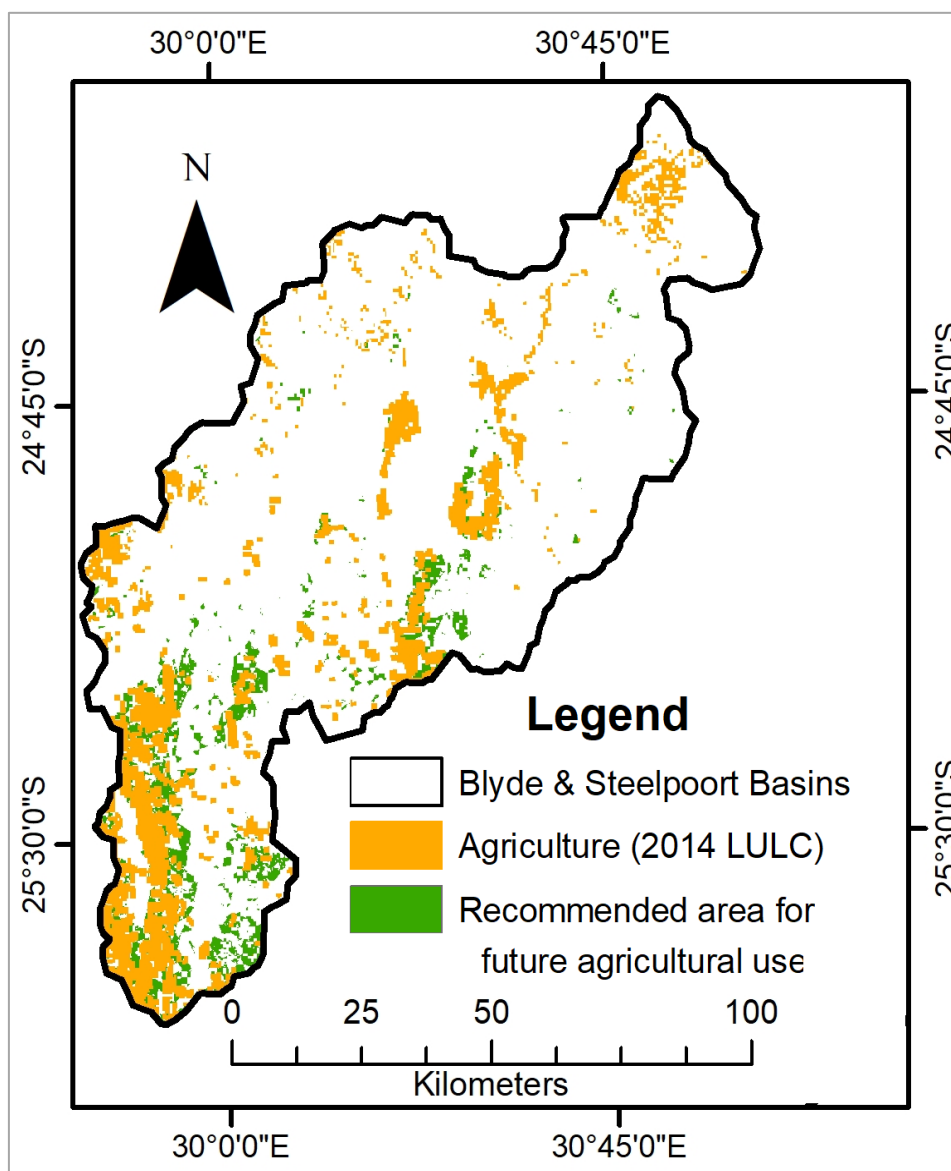


Figure 5-12: Map of Agricultural areas under 2014 LULC and the recommended areas for future agricultural use

TRANSFER OF FINDINGS TO MAPPING SUITABLE AREA FOR FUTURE AGRICULTURAL USE AND PROJECTION OF ITS CORRESPONDING HYDROLOGICAL SCENARIOS UNDER CLIMATE CHANGE

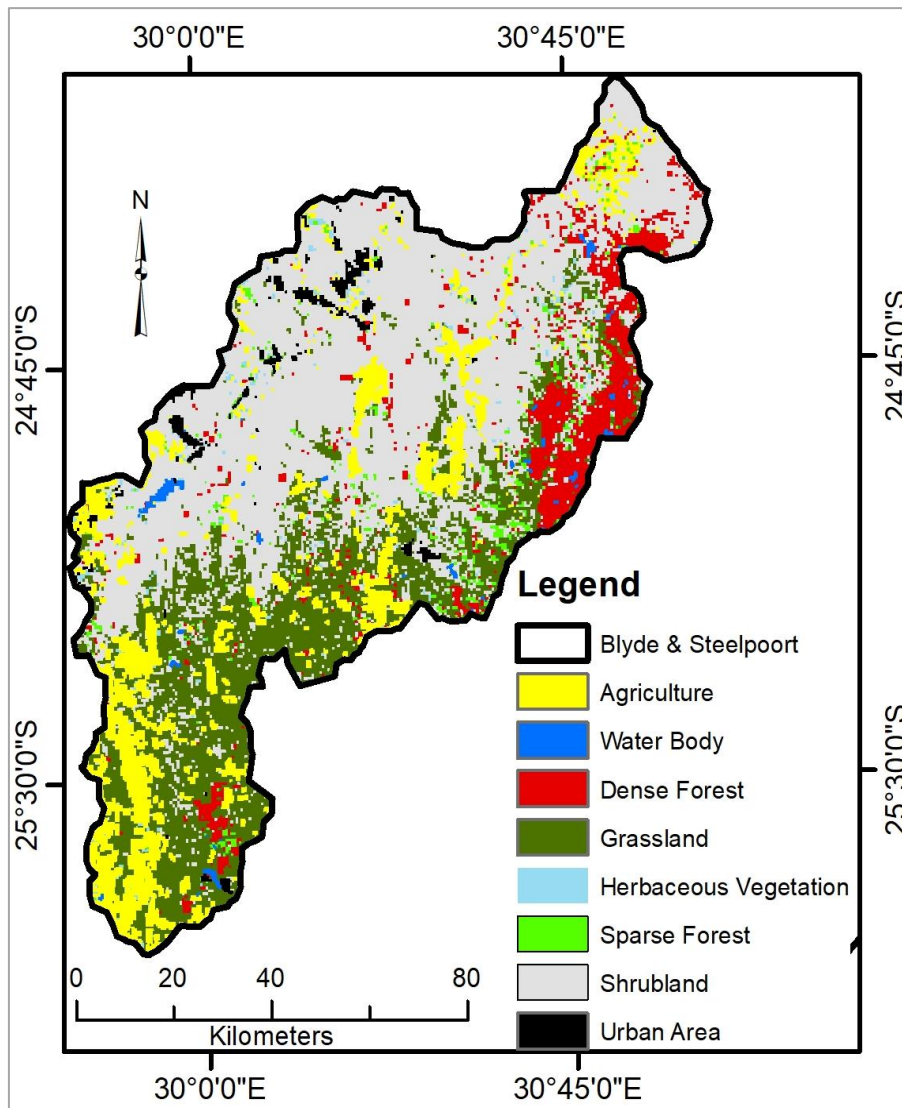


Figure 5-13: The actual 2014 LULC map

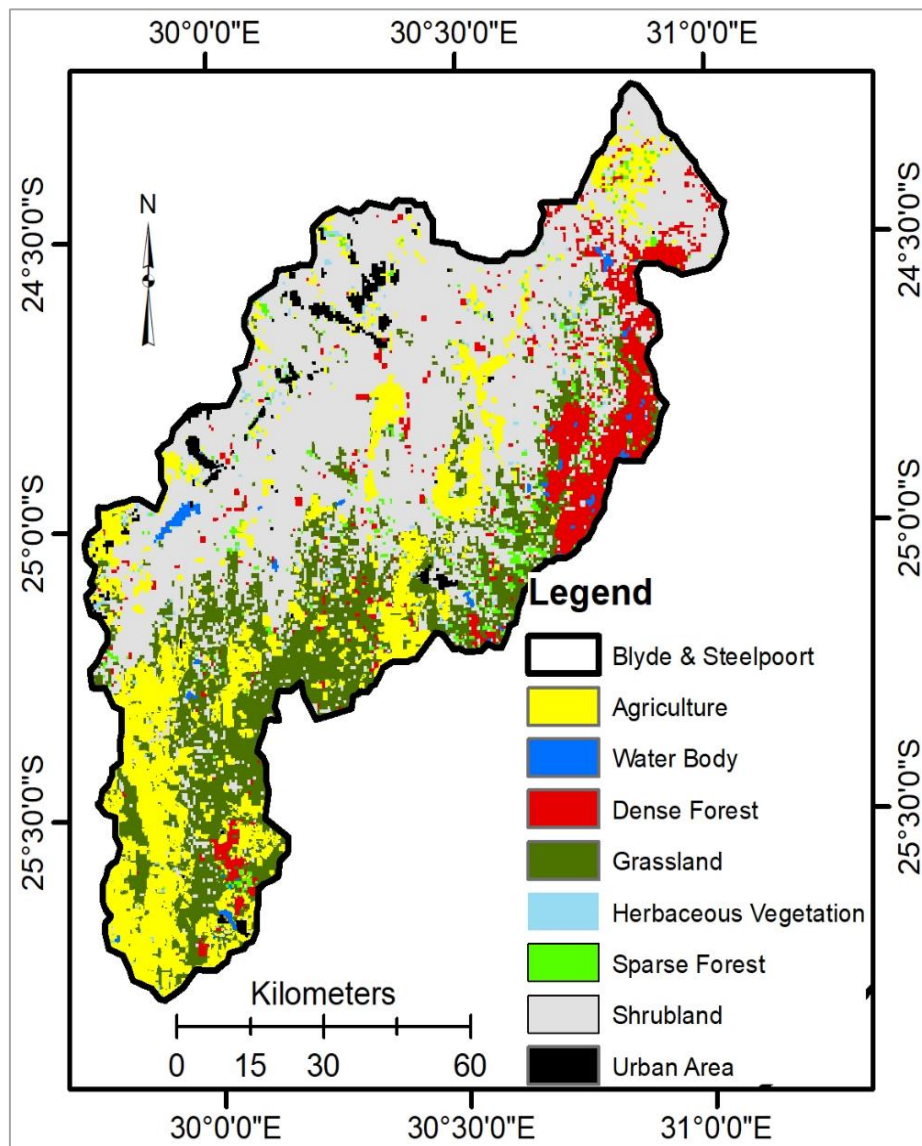


Figure 5-14: LULC map showing combined current (2014 LULC) and recommended future agricultural development

5.4 Simulations of hydrological scenarios future scenarios

Simulation of future hydrological scenarios is conducted using SWAT Model. The model is set up for three scenarios are based on projected climatic data of the bias-corrected RCP 2.6, RCP 4.5, and RCP 8.5 obtained in the previous step. Model setup for 21 years (from 2015 until 2035) and parameterization are based on calibrated parameters obtained in Chapter 3. The general procedure adopted in this step is as outlined in Figure 5-15. The operating rules of various reservoirs in the river basin and other water management operations for the future projections are based on the water management practices of the year 2015.

In this step, the hydrological outputs from the actual LULC of 2014 are used as the baseline for comparison of the expected future anomalies.

TRANSFER OF FINDINGS TO MAPPING SUITABLE AREA FOR FUTURE AGRICULTURAL USE AND PROJECTION OF ITS CORRESPONDING HYDROLOGICAL SCENARIOS UNDER CLIMATE CHANGE

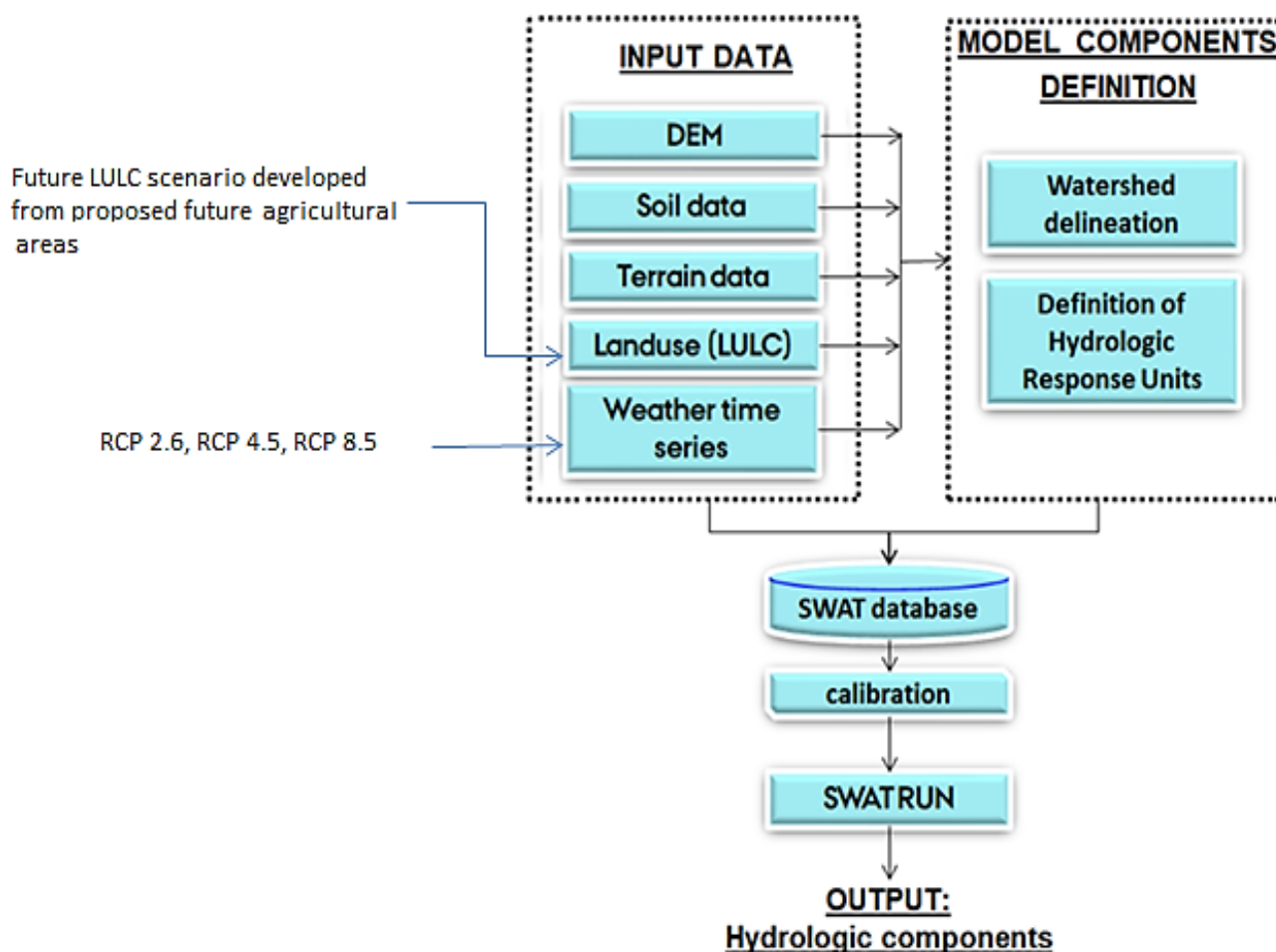


Figure 5-15: Flow process for hydrological modelling

5.4.1 Results: Simulations of hydrological scenarios future scenarios

Figure 5-16 shows graphs of the monthly distribution of discharge at various stations in the Blyde and Steelpoort Rivers. The peak discharge is highest under RCP 2.6 in comparison to baseline scenario and RCPs 4.5 and 8.5; The upward shift in peak under RCP 2.6 is also reflected in the rainfall pattern shown in Figure 5-8, where mean monthly rainfall in December, January, and February are slightly higher than the observed rainfall used in simulation of the baseline scenario. In comparison to discharge under the baseline scenario, discharge under RCPs 4.5 and 8.5 appear to have a slightly lower peak at three stations.

Discharge at three (B4H003, B4H025, and Blyde Outlet (B60J)) out of the four stations evaluated indicate the deviation of discharge from the baseline scenario early in the season; this may be as a result of the new landuse scenario and also changes in rainfall and temperature.

Minimal changes are noted in the low flow months of July, August, and September of the two rivers; however, the high peaks appearing in February under RCP 2.6 may be a potential indicator of floods in the future. Station B4H015 and Blyde outlet (B60J) are located downstream of large dams, which also play a role in regulating flow. Therefore, to avoid the negative impacts of changing flow patterns, the operating rules of reservoirs and the effectiveness of water management practices should be evaluated.

TRANSFER OF FINDINGS TO MAPPING SUITABLE AREA FOR FUTURE AGRICULTURAL USE AND PROJECTION OF ITS CORRESPONDING HYDROLOGICAL SCENARIOS UNDER CLIMATE CHANGE

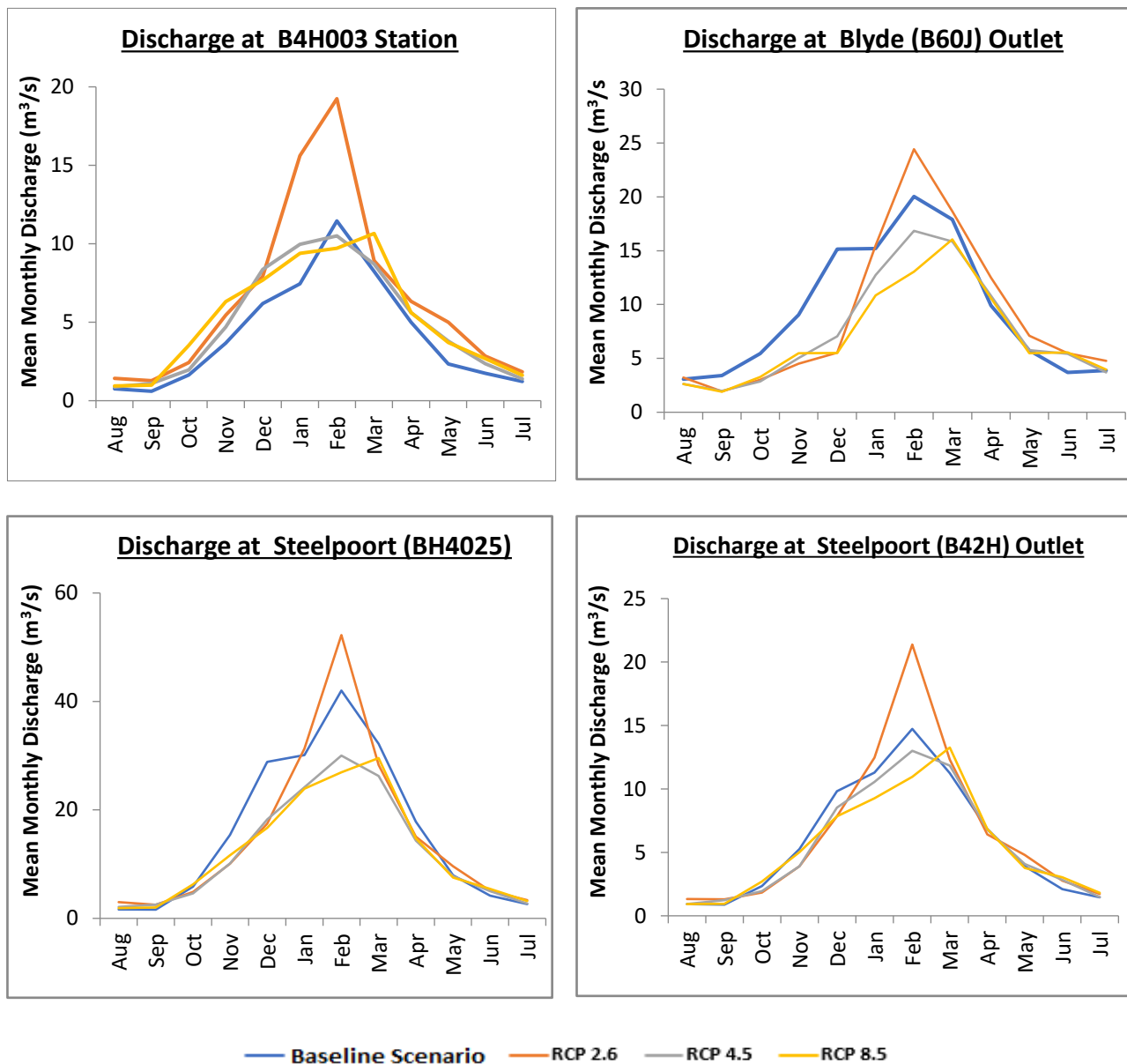


Figure 5-16: Monthly distributions of observed and bias-corrected projected (RCP 2.6, 4.5 & 8.5) discharge at four gauging stations in Blyde and Steelpoort River Basins.

Figure 5-15 shows a comparison of the spatial distribution of evapotranspiration, surface runoff, rainfall, and groundwater recharge under historical scenario and future projections under RCP 2.6, RCP 4.5, and RCP 8.0. Future projections indicate a general increase of rainfall across the whole river basins under all the three RCPs with the highest increase projected under RCR 2.6 at the higher elevations. Under RCPs 4.5 and 8.5, there are sections of the river basin that will experience reduced rainfall, whereas some areas indicate an increase in rainfall. Evapotranspiration, on the other hand, is projected by the simulations to increase under the three warming scenarios, with the highest increase under RCP 2.6.

The simulations outputs also indicate that surface runoff is bound to slightly increase under RCP 2.6 and significantly reduce under RCP 4.5 and RCP 8.5. Figure 5-15 also shows that groundwater flow will increase under all the three RCPs, with the highest increase noted under RCP 2. 6.

TRANSFER OF FINDINGS TO MAPPING SUITABLE AREA FOR FUTURE AGRICULTURAL USE AND PROJECTION OF ITS CORRESPONDING HYDROLOGICAL SCENARIOS UNDER CLIMATE CHANGE

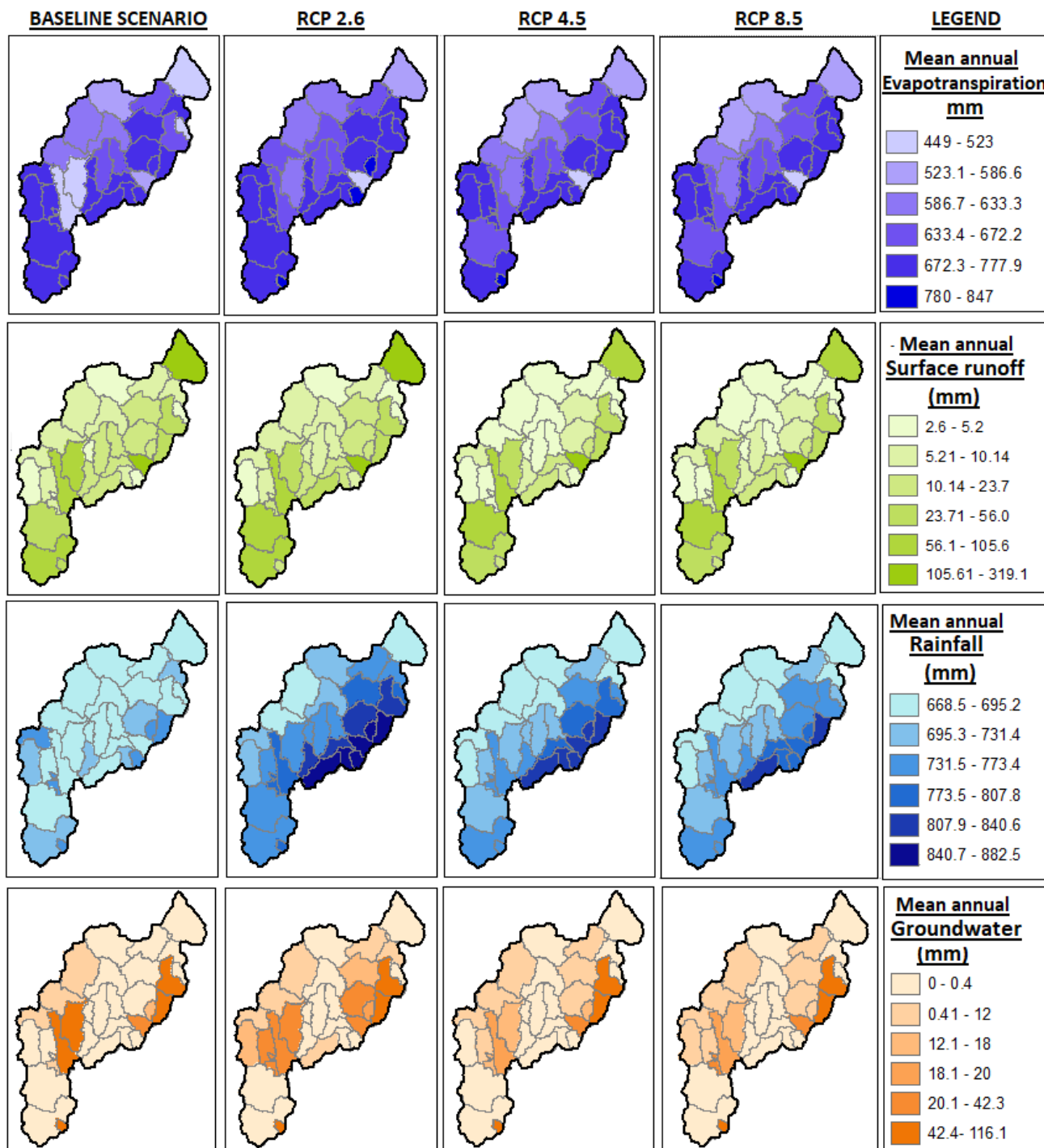


Figure 5-17: Spatial distribution of evapotranspiration, surface runoff, rainfall, and groundwater recharge

5.5 Discussions

The objective of this chapter is to apply the findings of the research to the preparation of future LULC maps with proposed areas for agriculture and simulating the resultant hydrological scenarios under the influence of climate change. Projected temperature and rainfall are obtained from four GCMs; GFDL-ESM2M, GFDL-ESM2M, IPSL-CM5A-L, and MIROC GCMs.

Climate Change Toolkit is then used to correct bias errors and downscale the data to a resolution of 0.125°. The correction of bias errors was based on the observed CRU data and GCMs' data of the overlapping period

TRANSFER OF FINDINGS TO MAPPING SUITABLE AREA FOR FUTURE AGRICULTURAL USE AND PROJECTION OF ITS CORRESPONDING HYDROLOGICAL SCENARIOS UNDER CLIMATE CHANGE

(1979 to 2005). Rainfall from the four GCMs showed biases from observed rain, mainly in the peak seasons, where higher peaks are observed, as shown in Figure 5-4. The temperature generally had slight deviations from observed data. The errors or differences identified during this stage were also successfully corrected by the CCT tool to an acceptable level of application in hydrological modelling.

It has been demonstrated in the previous chapter that available land for future agricultural development is approximately 422 km^2 . . With a focus on agricultural expansion, the development of future LULC maps is achieved by mosaicking the map of proposed future agricultural areas onto the actual 2014 LULC map (obtained in Chapter 3) in the ArcGIS environment as illustrated in Figure 5-12.

To simulate future scenarios of hydrology with climatic projections and projected expansions in agriculture, the SWAT model was set up using the bias-corrected climate data and a scenario of future LULC map. The LULC map was developed with the actual 2014 scenario as the baseline with a mosaic of proposed future agricultural areas (422 km^2). The simulated future scenarios revealed that under the three warming scenarios, there would be an increase in precipitation, an increase in surface runoff in peak season, an increase in groundwater recharge, but also with an increase in losses through evapotranspiration. The changes that are detected in the hydrology of the two river basins are indicative of surplus water relative to the baseline scenario; this shift is bound to influence seasonal availability of water and may render reservoir operation rules and management practices ineffective. Water managers should, therefore, revise the management practices in the river basins based on the hydrological projections.

The output of this chapter can be adopted in future planning for water resources; hydrological flows can provide information that can be used for reservoir planning and operations, flood and drought management planning. The study also provides information on the spatial distribution of various hydrological components, which is useful for water balancing. The morphological parameters that explain the hydrological anomaly patterns when agricultural land is expanded can be utilized in hydrological assessments under EIA studies in projects where agriculture establishment is desired.

The shortcomings of this approach are that if the future agricultural expansion of 422 km^2 is made as proposed, changes in hydrological will be minimized, but there is a looming danger of loss of biodiversity since all grassland will be replaced. Hence, stakeholder involvement will still be required to ensure moderation in the implementation of the approach.

Bias correction of GCM data is an acceptable way of improving data accuracy; however, the lack of physical means of verification. Therefore, there exists no means of quantifying the uncertainties in the climatic projections (Ehret *et al.*, 2012).

6 RESEARCH CONCLUSIONS

Climate change/variability and anthropogenic activities have continued to exert pressure on water resources globally. South Africa is one of the countries that are currently experiencing negative climatic impacts with predominantly prolonged droughts and occasional extreme rainfall events. The impacts of climate change, coupled with anthropogenic activities, are exacerbating the already stressed water resources. The Olifants River Basin, which has plenty of discharge in comparison to other river basins in the country, is vulnerable to the hazards posed by human activities and climate change. This situation necessitates water resources managers to develop an adapted approach to water resources management.

This research is conducted in the Blyde and Steelpoort Sub-basins of Olifants River Basin, where sustained agricultural activities and their subsequent impacts on hydrology are reported. The most impacted hydrological component being surface runoff, where there is a record increase in discharge, particularly in the peak rainfall season. The drivers of agricultural development and expansion in Blyde and Steelpoort River Basins indicate that further growth in agriculture; this is bound to further alter hydrological flows in the river basins. Therefore, to meet human demand for agricultural development without significant alteration of the hydrology, water managers must assess how physical features, landuse, and climatic conditions interact to influence hydrological partitioning. The findings of these studies can be used to inform planning activities in water resources management.

Rainfall and temperature data were acquired from CRU 4.0 TS, which is in gridded format and monthly time steps. A code was developed in R programming language to extract the data by point location from NetCDF format into ASCII file format (in Appendix IV); this code/approach can be used by other researchers in the extraction and preparation of climate time series data from NetCDF (Network Common Data Form) files. The data in ASCII format was decoupled from monthly to daily time steps using Daily Weather Converter (MODAWEC). The MODAWEC algorithm produced acceptable output that was successfully used in hydrological simulations; this indicated that the CRU 4.0 TS data could effectively be used in data-scarce situations to fill gaps or to represent the complete time series required

The evaluation conducted in Chapter 3 indicates that the river discharge experienced abrupt and gradual changes. Abrupt changes were attributed to the high frequency of extreme rainfall events that persisted for seven years from 2006 to 2012. Sources of gradual changes in discharge were not detected in climate patterns, but rather in landuse activities, which are also presented in Chapter 3. A gradual increase in temperature is detected, but this had no detectable influence on the shifts in hydrological patterns

Quantification of LULC changes in the river basins highlighted revealed that dominant changes were human-driven where forest, shrubland, grassland were mainly transformed into agriculture land over the years with a very small increase in urban area/settlement; this demonstrated the necessity for active participation of farmers in water resources and environmental planning activity.

SWAT Model was in simulating the hydrology of the study area and detecting shifts resulting from these changes; the capability of SWAT to uniquely capture growth parameters of each vegetation class, water use, and reservoir operations make it an essential tool in hydrological modelling, with LULC change as a factor under evaluation. The model has produced acceptable results based on measured river discharge at eight different locations in the study area. The parameter ranges obtained during this research can feed into the SWAT model that is currently under setup for the whole of the Olifants River Basin. Simulation output from SWAT Model revealed a reduction in evapotranspiration, especially in areas where forests were replaced with agriculture and a general increase in surface runoff, which is attributed to a reduction in surface cover.

The research explores the interactions of morphology, hydrology, and landuse in order to develop an approach for identification of areas that are “hydrologically suitable” for agriculture; this was achieved by identifying which landuse classes can be replaced without significant impacts on hydrology, and under which morphological conditions would minimal changes be met. A model-based comparative analysis of the hydrological reaction of the various LULC classes is conducted in order to obtain LULC class with minimum anomalies in hydrological components to agricultural land. A fraction of hydrological anomalies between grassland and agricultural LULC scenarios is used as the targeted hydrologic change in the event of agricultural development. This threshold is applied to statistical relationships established between morphological parameters and hydrological anomalies between grassland and agricultural land in order to find threshold values for Morphological parameters under which agricultural development with minimal hydrological impacts can be undertaken. This procedure can be followed in agricultural LULC planning in other river basins.

The thresholds of morphological parameters and the relationship between grassland and agricultural land can be adopted in first-hand assessment of large areas for “hydrological suitability” under agricultural use.

Analysis of historical climatic variables revealed an increase in temperature, which had no impacts on evapotranspiration rates, and increased river discharge, which resulted from the high frequency of extreme rainfall events. The simulated future scenarios revealed that under the three warming scenarios, there would be an increase in precipitation, an increase in surface runoff in peak season, an increase in groundwater recharge, but also with an increase in losses through evapotranspiration. The changes that are detected in the hydrology of the two river basins are indicative of surplus water relative to the baseline scenario; this shift is bound to influence seasonal availability of water and may render reservoir operation rules and management practices ineffective. Planners can use this information for hydraulic investigations and planning, reservoir operation planning, and future flood management planning

This study proposes a scientific approach for landuse planning in the Blyde and Steelpoort River Basins to mitigate changes in hydrology. The research has also revealed the shortcomings of the approach where there would be a loss of vegetation diversity. Therefore, further studies are recommended to investigate the environmental impacts of the transformation of the whole grassland to agriculture; this would provide a complete overview of the hydrological state and impacts of the new planning procedure on the ecosystem.

Various outputs of this research are subject to uncertainties resulting from data, model structure, and methodology. Coarse-resolution data, especially the DEM and soil distribution map, do not represent the spatial distribution of parameters. The LULC maps developed in Chapter 3 have an acceptable level of accuracy; however, the errors they possess can be transferred to hydrological simulations, causing further uncertainties. These uncertainties that are transferred to hydrological simulations are estimated using the SUFI-2 Algorithm during model calibration. Eleven stations were used in model calibration; the SUFI-s Algorithm indicated that nine out of the eleven stations had reliable outputs.

7 REFERENCES

- Abbaspour, K. C. *et al.* (2015) 'A continental-scale hydrology and water quality model for Europe: Calibration and uncertainty of a high-resolution large-scale SWAT model', *Journal of Hydrology*. Elsevier B.V., 524, pp. 733–752. doi: 10.1016/j.jhydrol.2015.03.027.
- Abbaspour, K.C. *et al.* (2015) 'A continental-scale hydrology and water quality model for Europe: Calibration and uncertainty of a high-resolution large-scale SWAT model', *Journal of Hydrology*, 524, pp. 733–752. doi: 10.1016/j.jhydrol.2015.03.027.
- Abbaspour, K. C. *et al.* (2019) 'Global soil , landuse , evapotranspiration , historical and future weather databases for SWAT Applications', pp. 1–11. doi: 10.1038/s41597-019-0282-4.
- Abbaspour, K., Vaghefi, S. and Srinivasan, R. (2017) 'A Guideline for Successful Calibration and Uncertainty Analysis for Soil and Water Assessment: A Review of Papers from the 2016 International SWAT Conference', *Water*, 10(1), p. 6. doi: 10.3390/w10010006.
- Abraham, S., Huynh, C. and Vu, H. (2020) 'Classification of soils into hydrologic groups using machine learning', *Data*, 5(1). doi: 10.3390/data5010002.
- Addinsoft (2019) *XLSTAT | Statistical Software for Excel*. Available at: <https://www.xlstat.com/en/> (Accessed: 10 February 2020).
- Adeloye, A. J. and Montaseri, M. (2002) *Preliminary streamflow data analyses prior to water resources planning study*. Available at: <https://www.tandfonline.com/doi/pdf/10.1080/02626660209492973?needAccess=true> (Accessed: 17 June 2019).
- African Development Bank (2000) 'African development bank: african development fund policy for integrated water resources management', *Constraints*, (March).
- Akker, JJ H Van ; Soane, B. (2005) 'Factors and Processes Affecting Distribution and Intensity of Compaction', pp. 285–293.
- Alemayehu, T. *et al.* (2017) 'Evapotranspiration Mapping in a Heterogeneous Landscape Using Remote Sensing and Global Weather Datasets: Application to the Mara Basin, East Africa', *Remote Sensing*, 9(4), p. 390. doi: 10.3390/rs9040390.
- Alexander, C. (2019) 'Cape Town's "Day Zero" Water Crisis, One Year Later', *CITYLAB*, May. Available at: <https://www.citylab.com/environment/2019/04/cape-town-water-conservation-south-africa-drought/587011/>.
- Ansari, A. and Golabi, M. H. (2019) 'Prediction of spatial land use changes based on LCM in a GIS environment for Desert Wetlands – A case study: Meighan Wetland, Iran', *International Soil and Water Conservation Research*, 7(1), pp. 64–70. doi: 10.1016/j.iswcr.2018.10.001.
- Arlen D. Feldman (2000) 'Hydrologic Modelling System Technical Reference Manual', *Computer Software Technical Reference Manual*, (March), p. 145. Available at: [https://www.hec.usace.army.mil/software/hechms/documentation/HEC-HMS_Technical Reference Manual_\(CPD-74B\).pdf](https://www.hec.usace.army.mil/software/hechms/documentation/HEC-HMS_Technical Reference Manual_(CPD-74B).pdf).

- Arnold, J. G. *et al.* (2012) 'Soil and Water Assessment Tool "SWAT": Input/Output Documentation', *Texas Water Resources Institute*, pp. 1068–1068. doi: 10.1007/978-0-387-35973-1_1231.
- Arveti, N. and Etikala, B. (1992) 'Introduction to Land Use / Land Cover (LULC) Classification'.
- Avisse, N. *et al.* (2017) 'Monitoring small reservoirs storage from satellite remote sensing in inaccessible areas', *Hydrology and Earth System Sciences Discussions*, pp. 1–23. doi: 10.5194/hess-2017-373.
- Bailey, A. (2012) *Water Resources of South Africa, 2012 Study - Resource Centre, Water Research Commission*. Available at: <https://waterresourceswr2012.co.za/resource-centre/> (Accessed: 17 March 2020).
- Basson, M. S. and Rossouw, J. D. (2003) *Olifants Water Management Area: Overview of Water resources Availability and Utilization*. Available at: <http://www.dwaf.gov.za/Documents/Other/WMA/4/optimised/overview/OLIFANTS REPORT.pdf>.
- Bates, B. C. *et al.* (2008) 'Climate Change and Water. Technical Paper of Intergovernmental Panel on Climate Change', *ISBN*, (978-92-9169-123-4). doi: 10.1007/978-94-007-5796-7.
- Bates, T. B. (2017) *Deep Roots in Plants Driven by Soil Hydrology | Rutgers Today*. Available at: <https://news.rutgers.edu/deep-roots-plants-driven-soil-hydrology/20170915#.XIVKBqKgVA> (Accessed: 25 February 2020).
- Batjes, N. H. *et al.* (2017) 'WoSIS: providing standardised soil profile data for the world', *Earth Syst. Sci. Data*, 9, pp. 1–14. doi: 10.5194/essd-9-1-2017.
- Blanton, B. N. (2014) *Trace: Tennessee Research and Creative Exchange Effect of Urbanization on Base Flow Hydrology Among Ecoregion II Catchments in Eastern United States Recommended Citation*. The University of Tennessee. Available at: https://trace.tennessee.edu/utk_gradthes/3140 (Accessed: 10 May 2019).
- Boccaletti, G., Stuchtey, M. and van Olst, M. (2010) *Confronting South Africa's water challenge | McKinsey*. Available at: <https://www.mckinsey.com/business-functions/sustainability/our-insights/confronting-south-africas-water-challenge> (Accessed: 26 September 2019).
- Bokke, A. S. *et al.* (2017) 'Validation of General Climate Models (GCMs) over Upper Blue Nile River Basin, Ethiopia', *Atmospheric and Climate Sciences*, 07(01), pp. 65–75. doi: 10.4236/acs.2017.71006.
- Boland-Brien, S. J., Basu, N. B. and Schilling, K. E. (2014) 'Homogenization of spatial patterns of hydrologic response in artificially drained agricultural catchments', *Hydrological Processes*, 28(19), pp. 5010–5020. doi: 10.1002/hyp.9967.
- Boschetti, M. *et al.* (2014) 'Comparative Analysis of Normalised Difference Spectral Indices Derived from MODIS for Detecting Surface Water in Flooded Rice Cropping Systems', *PLoS ONE*. Edited by G. J.-P. Schumann. Public Library of Science, 9(2), p. e88741. doi: 10.1371/journal.pone.0088741.
- Botai, C. M., Botai, J. O. and Adeola, A. M. (2018) 'Spatial distribution of temporal precipitation contrasts in South Africa', *South African Journal of Science*, 114(7–8), pp. 1–9. doi: 10.17159/sajs.2018/20170391.
- Brouwer, C. and Heibloem, M. (1986) *Irrigation Water Management: Irrigation Water Needs, Food and Agriculture Organization*. Available at: <http://www.fao.org/3/S2022E/s2022e00.htm#Contents> (Accessed: 31 October 2019).
- Bruijnzeel, L. A. (2004) 'Hydrological functions of tropical forests: not seeing the soil for the trees?', *Agriculture, Ecosystems & Environment*. Elsevier, 104(1), pp. 185–228. doi: 10.1016/J.AGEE.2004.01.015.
- Butt, A. *et al.* (2015) 'Land use change mapping and analysis using Remote Sensing and GIS: A case study of Simly watershed, Islamabad, Pakistan', *Egyptian Journal of Remote Sensing and Space Science*. Authority for Remote Sensing and Space Sciences, 18(2), pp. 251–259. doi: 10.1016/j.ejrs.2015.07.003.

- Carlier, A. (2000) 'The future of earth observation is in smallsats', *Air & Space Europe*, 2(4), pp. 42–44. doi: 10.1016/s1290-0958(01)80013-7.
- Chen, F. W. and Liu, C. W. (2012) 'Estimation of the spatial rainfall distribution using inverse distance weighting (IDW) in the middle of Taiwan', *Paddy and Water Environment*, 10(3), pp. 209–222. doi: 10.1007/s10333-012-0319-1.
- Chow, V. Te, Maidment, D. R. and Mays, L. W. (1988) *Applied Hydrology*.
- Claassen, M. (2013) 'Integrated Water Resource Management in South Africa', *International Journal of Water Governance*, 1(3), pp. 323–338. doi: 10.7564/13-IJWG12.
- Crafford, J. *et al.* (2011) 'Report on Socio-Economic Evaluation Framework and the Decision Analysis Framework Analysis Scoring System', Draft(Wma 4).
- Department for Business Energy & Industrial Strategy (2014) *Climate change explained - GOV.UK*. Available at: <https://www.gov.uk/guidance/climate-change-explained> (Accessed: 17 June 2019).
- Department of Environmental Affairs (1998) *National Environmental Management Act, 1998*.
- Department of Water and Sanitation (2006) 'Overview of the South African Water Sector'. doi: 10.1089/scd.2012.0638.
- Devia, G. K., Ganasri, B. and Dwarakish, G. (2015) 'A Review on Hydrological Models', *Aquatic Procedia*, 4, pp. 1001–1007. doi: 10.1016/j.aqpro.2015.02.126.
- DHI (2017) 'Mike She Volume 1: User Guide. The Experts in WATER ENVIRONMENTS', *DHI Software Licence Agreement*, 27(1), pp. 91–95.
- DHV CONSULTANTS BV & DELFT HYDRAULICS (2002) 'How to analyse rainfall data', (February).
- Dile, Y., Srinivasan, R. and George, C. (2017) 'QGIS Interface for SWAT (QSWAT)', February(v 1.4), p. 77. doi: 10.13140/RG.2.1.1060.7201.
- Dile, Y. T. *et al.* (2016) 'Investigation of the Curve Number Method For Surface Runoff Estimation In Tropical Regions', *Journal of the American Water Resources Association*, 52(5), pp. 1155–1169. doi: 10.1111/1752-1688.12446.
- Dwarakish, G. S. and Ganasri, B. P. (2015) 'Impact of land use change on hydrological systems: A review of current modelling approaches', *Cogent Geoscience*. Cogent, 1(1), pp. 1–18. doi: 10.1080/23312041.2015.1115691.
- Earth Observation Research Center Japan Aerospace Exploration Agency (2019) 'ALOS Global Digital Surface Model (DSM) "ALOS World 3D-30m (AW3D30) Ver.2.2"', (February), pp. 1–12. Available at: https://www.eorc.jaxa.jp/ALOS/en/aw3d30/aw3d30v22_product_e.pdf.
- Ehret, U. *et al.* (2012) 'HESS Opinions "should we apply bias correction to global and regional climate model data?"', *Hydrology and Earth System Sciences*, 16(9), pp. 3391–3404. doi: 10.5194/hess-16-3391-2012.
- Eini, M. R., Javadi, S. and Delavar, M. (2018) 'Evaluating the performance of CRU and NCEP CFSR global reanalysis climate datasets, in hydrological simulation by SWAT model, Case Study: Maharlu basin', *Iran Water Resources Research*, 14(1), pp. 32–44. Available at: http://www.iwrr.ir/article_48378_en.html (Accessed: 13 August 2019).
- Elsaid, O. and Abdelkareem, A. (2018) 'Accuracy Assessment of Land Use Land Cover in Umabdalla Natural Reserved Accuracy Assessment of Land Use Land Cover in Umabdalla Natural Reserved Forest , South Kordofan , Sudan', (January).
- ENVI (2009) 'ENVI User's Guide Restricted Rights Notice'. Available at: www.apache.org/.

- EPA (2016) *Causes of Climate Change*. Available at: https://19january2017snapshot.epa.gov/climate-change-science/causes-climate-change_.html (Accessed: 17 June 2019).
- Faber, B. A. (2004) 'Slope and aspect effect on evaporation as measured by atmometer', *Acta Horticulturae*, 664, pp. 213–216. doi: 10.17660/ActaHortic.2004.664.24.
- Fan, Y. *et al.* (2017) 'Hydrologic regulation of plant rooting depth', *Proceedings of the National Academy of Sciences of the United States of America*, 114(40), pp. 10572–10577. doi: 10.1073/pnas.1712381114.
- Fathian, F. *et al.* (2016) 'Trends in hydrological and climatic variables affected by four variations of the Mann-Kendall approach in Urmia Lake basin, Iran', *Hydrological Sciences Journal*, 61(5), pp. 892–904. doi: 10.1080/02626667.2014.932911.
- Feng, X., Porporato, A. and Rodriguez-Iturbe, I. (2013) 'Changes in rainfall seasonality in the tropics', *Nature Climate Change*. Nature Publishing Group, 3(9), pp. 811–815. doi: 10.1038/nclimate1907.
- Fikre, A. (2017) 'Selection of Best Fitted Probability Distribution Function for Daily Extreme Rainfall of Bale Zone, Ethiopia', *Civil and Environmental REsearch*, 8 No 12(January 2016), pp. 13–21.
- Filipe, R. and Correia, C. (2017) 'Processing Image to Geographical Information Systems (PI2GIS)-a learning tool in QGIS'. Available at: <https://pdfs.semanticscholar.org/4a59/fe9c0270e909767e08b7443dde9ed453e.pdf> (Accessed: 15 June 2019).
- Food and Agriculture Organization (1993) *Guidelines for land-use planning*. Food and Agriculture Organization of the United Nations.
- Food and Agriculture Organization (2004) 'Integrated water Resource Management for Food security in Africa', in. Available at: <http://www.fao.org/3/J1645e/J1645e00.htm> (Accessed: 17 January 2020).
- Fu, G. *et al.* (2013) 'A score-based method for assessing the performance of GCMs: A case study of southeastern Australia', *Journal of Geophysical Research Atmospheres*, 118(10), pp. 4154–4167. doi: 10.1002/jgrd.50269.
- Fuka, D. R. *et al.* (2014) 'Using the Climate Forecast System Reanalysis as weather input data for watershed models', *Hydrological Processes*, 28(22), pp. 5613–5623. doi: 10.1002/hyp.10073.
- Geoterragelimage (2015) '1990 South African National Land Cover Dataset', 2(July), pp. 1–43. Available at: https://www.environment.gov.za/projectsprogrammes/egis_landcover_datasets.
- Ghestem, M., Sidle, R. C. and Stokes, A. (2011) 'The Influence of Plant Root Systems on Subsurface Flow: Implications for Slope Stability', *BioScience*, 61(11), pp. 869–879. doi: 10.1525/bio.2011.61.11.6.
- Goodrich, D. C. (1992) *The kinematic wave controversy*, *Journal of Hydraulic Engineering*. doi: 10.1061/(ASCE)0733-9429(1992)118:9(1334).
- Gray, K. L. K. (2007) 'Comparison of Trend Detection Methods'. Available at: <http://etd.lib.umd.edu/theses/available/etd-09262007-104625/>.
- Guhathakurta, P. and Saji, E. (2013) 'Detecting changes in rainfall pattern and seasonality index vis-à-vis increasing water scarcity in Maharashtra', *Journal of Earth System Science*, 122(3), pp. 639–649. doi: 10.1007/s12040-013-0294-y.
- Guide, A QuickEssenfelder, A. H. (2018) 'Weather Database', (June).
- Gupta, H. V. *et al.* (2009) 'Decomposition of the mean squared error and NSE performance criteria: Implications for improving hydrological modelling', *Journal of Hydrology*. Elsevier B.V., 377(1–2), pp. 80–91. doi: 10.1016/j.jhydrol.2009.08.003.

- Guzha, A. C. *et al.* (2018) 'Impacts of land use and land cover change on surface runoff, discharge and low flows: Evidence from East Africa', *Journal of Hydrology: Regional Studies*, 15(December 2017), pp. 49–67. doi: 10.1016/j.ejrh.2017.11.005.
- Gyamfi, C., Ndambuki, J. M. and Salim, R. W. (2016) 'Hydrological responses to land use/cover changes in the Olifants River Basin, South Africa', *Water (Switzerland)*, 8(12). doi: 10.3390/w8120588.
- Hadadin, N. (2013) 'Evaluation of several techniques for estimating stormwater runoff in arid watersheds', *Environmental Earth Sciences*, 69(5), pp. 1773–1782. doi: 10.1007/s12665-012-2010-7.
- Hamman, J. J. *et al.* (2018) 'The Variable Infiltration Capacity model version 5 (VIC-5): infrastructure improvements for new applications and reproducibility', *Geoscientific Model Development*, 11(8), pp. 3481–3496. doi: 10.5194/gmd-11-3481-2018.
- Harris, I. *et al.* (2014) 'Updated high-resolution grids of monthly climatic observations - the CRU TS3.10 Dataset', *International Journal of Climatology*, 34(3), pp. 623–642. doi: 10.1002/joc.3711.
- Hawker, L. *et al.* (2018) 'Perspectives on Digital Elevation Model (DEM) Simulation for Flood Modelling in the Absence of a High-Accuracy Open Access Global DEM', *Frontiers in Earth Science*, 6(December), pp. 1–9. doi: 10.3389/feart.2018.00233.
- Helsel, D. R. and Hirsch, R. M. (1992) 'Statistical methods in water resources', *Statistical methods in water resources*, (January 1992). doi: 10.2307/1269385.
- Hijmans, R. J., Guarino, L. and Mathur, P. (2012) *DIVA-GIS*. Available at: <http://www.geocities.com/SiliconValley/Network/2114/> (Accessed: 2 December 2019).
- Hoerling, M. *et al.* (2006) 'Detection and Attribution of Twentieth-Century Northern and Southern African', *American Meteorological Society*, pp. 3989–4008.
- Hoffman, T. and Todd, S. (1999) *The Southern Africa Environment and Landuse*. Available at: http://www.humanities.uct.ac.za/sites/default/files/image_tool/images/192/TechCh03.doc.
- HUGHES, D. A. and METZLER, W. (1998) 'Assessment of three monthly rainfall-runoff models for estimating the water resource yield of semiarid catchments in Namibia', *Hydrological Sciences Journal*, 43(2), pp. 283–297. doi: 10.1080/02626669809492122.
- Humboldt State University (2015) *Supervised Classification*. Available at: http://gsp.humboldt.edu/olm_2015/Courses/GSP_216_Online/lesson6-1/supervised.html (Accessed: 15 June 2019).
- Intergovernmental Panel for Climate Change (IPCC) (2013) *Climate change, Physical Science Basis: IPCC Fifth Assessment Report on Climate Change*. Available at: https://www.ipcc.ch/site/assets/uploads/2018/02/WG1AR5_all_final.pdf.
- Intergovernmental Panel on Climate Change (IPCC) (2008) *Climate change 2007: Synthesis report, Intergovernmental Panel on Climate Change [Core Writing Team IPCC*. doi: 10.1256/004316502320517344.
- IPCC (2014) 'Climate Change: Synthesis Report for Policy Makers'. doi: 10.1017/CBO9781107415324.
- Jackson, R. J. (1967) 'THE EFFECT OF SLOPE, ASPECT AND ALBEDO ON POTENTIAL EVAPOTRANSPIRATION FROM HILLSLOPES AND CATCHMENTS', *Journal of Hydrology (New Zealand)*. New Zealand Hydrological Society, pp. 60–69. doi: 10.2307/43944123.
- Jha, M. (2009) 'Hydrologic simulations of the Maquoketa river watershed Using SWAT', (June). Available at: http://econ2.econ.iastate.edu/research/webpapers/paper_13081.pdf.
- Jin, Z. *et al.* (2015) 'Effects of water transfer on water quality and estimation of the pollutant fluxes from

- different sources into West Lake, Hangzhou City, China', *Environmental Earth Sciences*, 73(3), pp. 1091–1101. doi: 10.1007/s12665-014-3456-6.
- Jonker, L. (2014) *Integrated Water Resource Management (IWRM): From Theory To Practice, From Policy To Outcomes*.
- Jovanovic, N. *et al.* (2015) 'Dynamics of MODIS evapotranspiration in South Africa', *Water SA*, 41(1), p. 79. doi: 10.4314/wsa.v41i1.11.
- Julien, P. Y. (2018) 'Steady Flow in Rivers', in *River Mechanics*. Cambridge University Press, pp. 116–152. doi: 10.1017/9781316107072.006.
- Kabantu, T. M. (2016) *Response of evapotranspiration to changes in land use and land cover and climate in China during 2001–2013*. University of Zimbabwe.
- Kamworapan, S. and Surussavadee, C. (2019) 'Evaluation of CMIP5 global climate models for simulating climatological temperature and precipitation for southeast Asia', *Advances in Meteorology*. Hindawi Limited, 2019. doi: 10.1155/2019/1067365.
- Kelleher, C., Wagener, T. and McGlynn, B. (2015) 'Model-based analysis of the influence of catchment properties on hydrologic partitioning across five mountain headwater subcatchments', *Water Resources Research*, 51(6), pp. 4109–4136. doi: 10.1002/2014WR016147.
- Killick, R. and Eckley, I. (2014) 'changepoint: a comprehensive changepoint analysis package for R', *Journal of Statistical Software*, 58(3). doi: 10.18637/jss.v058.i03.
- Kim, N. W. *et al.* (2010) 'SWAT application to estimate design runoff curve number for South Korean conditions', *Hydrological Processes*, 24(15), pp. 2156–2170. doi: 10.1002/hyp.7638.
- Kings, S. (2017) 'A river of shit, chemicals, metals flows through our land', *Mail & Guardian*. Available at: <https://mg.co.za/article/2017-04-13-00-a-river-of-shit-chemicals-metals-flows-through-our-land>.
- Kiran, M. (2015) *How useful is the electromagnetic spectrum to remote sensing? - Quora*. Available at: <https://www.quora.com/How-useful-is-the-electromagnetic-spectrum-to-remote-sensing> (Accessed: 31 July 2019).
- Kiss, R. (2004) 'Determination of drainage network in digital elevation models, utilities and limitations', *Journal of Hungarian Geomathematics*, 2, pp. 16–29.
- Kling, H., Fuchs, M. and Paulin, M. (2012) 'Runoff conditions in the upper Danube basin under an ensemble of climate change scenarios', *Journal of Hydrology*, 424–425, pp. 264–277. doi: 10.1016/j.jhydrol.2012.01.011.
- Köthe, R. and Lehmeier, F. (1996) *System zur Automatischen Relief-Analyse. User Manual, 2. Edition*. University of Göttingen.
- Kouchi, D. H. *et al.* (2017) 'Sensitivity of calibrated parameters and water resource estimates on different objective functions and optimization algorithms', *Water (Switzerland)*, 9(6). doi: 10.3390/w9060384.
- Krogh, S. A. *et al.* (2015) 'Physically Based Mountain Hydrological Modelling Using Reanalysis Data in Patagonia', *Journal of Hydrometeorology*, 16(1), pp. 172–193. doi: 10.1175/JHM-D-13-0178.1.
- Kumbuyo, C. P. *et al.* (2014) 'Fluctuation of rainfall time series in Malawi: An analysis of selected areas', 31. doi: 10.15233/gfz.2014.31.1.
- Kundzewicz, Z. W. and Robson, A. J. (2004) 'Change detection in hydrological records - A review of the methodology', *Hydrological Sciences Journal*, 49(1), pp. 7–20. doi: 10.1623/hysj.49.1.7.53993.
- Kunert, N. *et al.* (2015) 'Modelling potential impacts of planting palms or tree in small holder fruit plantations on ecohydrological processes in the central Amazon', *Forests*, 6(8), pp. 2530–2544. doi: 10.3390/f6082530.

- Lam, N. S.-N. (2008) 'Methodologies for Mapping Land Cover/Land Use and its Change', *Advances in Land Remote Sensing*, pp. 341–367. doi: 10.1007/978-1-4020-6450-0_13.
- LAND_COVER_CCI Partnership (2017) 'P Roduct U Ser G Uide'. Available at: <https://www.esa-landcover-cci.org/?q=node/164>.
- Lange, M. De *et al.* (2003) 'Water Resources Planning and Management in the Olifants River Basin of South Africa: Past, Present and Future. Chapter 10 of the IWMI Book on River Basin Management Table of Contents', *Management*, (January), p. 30. Available at: <http://citeseerx.ist.psu.edu/viewdoc/download?doi=10.1.1.499.2019&rep=rep1&type=pdf>.
- Lekha, S. L. S. and Kumar, S. S. (2018) 'Classification and Mapping of Land Use Land Cover change in Kanyakumari district with Remote Sensing and GIS techniques', *International Journal of Applied Engineering Research*, 13(1), pp. 158–166. Available at: <http://www.ripublication.com>.
- Li, G. *et al.* (2017) 'Response of evapotranspiration to changes in land use and land cover and climate in China during 2001–2013', *Science of the Total Environment*. Elsevier B.V., 596–597(October), pp. 256–265. doi: 10.1016/j.scitotenv.2017.04.080.
- Li, P. *et al.* (2018) 'Assessing the Hydrologic Impacts of Land Use Change in the Taihu Lake Basin of China from 1985 to 2010', *Water*, 10(11), p. 1512. doi: 10.3390/w10111512.
- Liu, J., Fritz, S., *et al.* (2008) 'A spatially explicit assessment of current and future hotspots of hunger in Sub-Saharan Africa in the context of global change', *Global and Planetary Change*. Elsevier B.V., 64(3–4), pp. 222–235. doi: 10.1016/j.gloplacha.2008.09.007.
- Liu, J., Williams, J. R., *et al.* (2008) 'Using MODAWEC to generate daily weather data for the EPIC model', *Environmental Modelling and Software*, 24, pp. 655–664. doi: 10.1016/j.envsoft.2008.10.008.
- Liu, Y. and Gupta, H. V. (2007) 'Uncertainty in hydrologic modelling: Toward an integrated data assimilation framework', *Water Resources Research*, 43(7), pp. 1–18. doi: 10.1029/2006WR005756.
- Loch, R. J. (2000) 'Effects of vegetation cover on runoff and erosion under simulated rain and overland flow on a rehabilitated site on the Meandu Mine, Tarong, Queensland', *Australian Journal of Soil Research*. CSIRO PUBLISHING, 38(2), pp. 299–312. doi: 10.1071/SR99030.
- López, P. L. *et al.* (2017) 'Calibration of a large-scale hydrological model using satellite-based soil moisture and evapotranspiration products', *Hydrology and Earth System Sciences*, 21(6), pp. 3125–3144. doi: 10.5194/hess-21-3125-2017.
- Lusch, D. P. (2015) *Digital Image Classification 2 / 72*. Available at: http://lees.geo.msu.edu/courses/geo827/lecture_10_classification.pdf (Accessed: 15 June 2019).
- Machiwal, D. and Jha, M. K. (2012) 'Introduction', in *Hydrologic Time Series Analysis: Theory and Practice*. Dordrecht: Springer Netherlands, pp. 1–12. doi: 10.1007/978-94-007-1861-6_1.
- Marongiu, I. and Cenceti, T. (2015) *Natural Resource Management - Hand book*. 'Soil Bio-engineering techniques for Slope protection and Stabilization'.
- Masud, M. B., Ferdous, J. and Faramarzi, M. (2018) 'Projected changes in hydrological variables in the agricultural region of Alberta, Canada', *Water (Switzerland)*, 10(12). doi: 10.3390/w10121810.
- McCartney, M. (2003) *Technical Note : Hydrological Review of the Olifants River Catchment*. Available at: http://www.iwmi.cgiar.org/assessment/files_new/research_projects/River_Basin_Development_and_Management/Olifants_Hydrology_6june.pdf.
- McCartney, M. P. and Arranz, R. (2007) *Evaluation of historic, current and future water demand in the Olifants River Catchment, South Africa, IWMI Research Report 118*. doi: 10.3910/2009.118.

- Meals, W. D. *et al.* (2011) 'Statistical Naalysis for Monotonic Trend'. Available at: <https://www.epa>. (Accessed: 7 July 2019).
- Menzel, L. *et al.* (2007) 'Impact of socio-economic development and climate change on water resources and water stress', *Water, (Caiwa)*, pp. 1–21.
- Middleton, B. J. and Bailey, A. K. (2008) *Water resources of South Africa, 2005 study (WR2005)*. Available at: <http://www.wrc.org.za>.
- Mitchell, B. (2005) 'Integrated water resource management, institutional arrangements, and land-use planning', *Environment and Planning A*, 37(8), pp. 1335–1352. doi: 10.1068/a37224.
- Mohammady, M. *et al.* (2015) 'A comparison of supervised, unsupervised and synthetic land use classification methods in the north of Iran', *International Journal of Environmental Science and Technology*, 12(5), pp. 1515–1526. doi: 10.1007/s13762-014-0728-3.
- Moss, R. *et al.* (2008) *Towards New Scenarios for Analysis of Emissions, Climate Change, Impacts and Response Strategies, IPCC Expert Meeting Report*. Available at: http://www.osti.gov/energycitations/product.biblio.jsp?osti_id=940991.
- Muthuwatta, L. P. (2014) *Integrating water resources modelling and remote sensing in Karkheh river basin, Iran*. doi: 10.3990/9789036537940.
- NASA (2019) *Remote Sensors | Earthdata*. Available at: <https://earthdata.nasa.gov/learn/remote-sensors> (Accessed: 8 June 2019).
- Nash, J. and Sutcliffe, J. (1970) 'Peramalan aliran sungai melalui model konseptual bagian I — Sebuah diskusi tentang prinsip-prinsip', *Jurnal hidrologi*, 10, pp. 282–290. Available at: <https://www.sciencedirect.com/science/article/pii/0022169470902556>.
- National Resources Conservation Service (2007) 'National Engineering Handbook', *National Engineering Handbook*, pp. 7-1,7-5.
- Natural Resources Canada (2015) *Satellite Characteristics: Orbits and Swaths | Natural Resources Canada*. Available at: <https://www.nrcan.gc.ca/earth-sciences/geomatics/satellite-imagery-air-photos/satellite-imagery-products/educational-resources/9283> (Accessed: 9 June 2019).
- Navalgund, R. R., Jararaman, V. and Roy, P. s (2007) 'Remote sensing applications: An Overview', *INDIAN SPACE PROGRAM*.
- Neitsch, S. . *et al.* (2011) *SWAT Theoretical Documentation Version 2009, Texas Water Resources Institute*. doi: 10.1016/j.scitotenv.2015.11.063.
- Neitsch, S. L., Arnold, Jeffrey G, *et al.* (2009) 'Soil & Water Assessment Tool', *Texas Water Resources Institute Technical Report*, TR-406, p. 647. doi: 10.1007/978-0-387-35973-1_1231.
- Neitsch, S. L., Arnold, J.G., *et al.* (2009) 'Soil & Water Assessment Tool Theoretical Documentation', *Blackland Research Center, Temple, TX*, p. 647.
- Nguyen, V. T. *et al.* (2018) 'Verification and correction of the hydrologic routing in the soil and Water Assessment Tool', *Water (Switzerland)*, 10(10). doi: 10.3390/w10101419.
- Nugroho, P. *et al.* (2013) 'Impact of Land-use Changes on Water Balance', *Procedia Environmental Sciences*. Elsevier B.V., 17, pp. 256–262. doi: 10.1016/j.proenv.2013.02.036.
- O'connor, J. *et al.* (2019) 'The influence of water table depth on evapotranspiration in the Amazon arc of deforestation', *Hydrology and Earth System Sciences*, 23(9), pp. 3917–3931. doi: 10.5194/hess-23-3917-2019.
- Onjira, I. P. P. and Sayama, T. (2014) *APPLICATION OF REMOTE SENSING AND RAINFALL-RUNOFF-INUNDATION*

MODEL TO NEAR REALTIME FLOOD INUNDATION MAPPING IN KENYA. International center for water Hazard and Risk Management. Available at: <http://e4ftl01.cr.usgs.gov/MOLT/MOD44W.005/2000.02.24/> (Accessed: 7 June 2019).

Pancholi, V. (2015) 'Analysis of Runoff for Vishwamitri River'.

Patil, M. B., Desai, C. G. and Umrikar, B. N. (2012) 'Image Classification Tool for Land Use / Land Cover Analysis : A Comparative Study of Maximum Likelihood', *International Journal of Geology, Earth, and Environmental Sciences*, 2(3), pp. 189–196.

Paudel, M. *et al.* (2011) 'Comparing the capability of distributed and lumped hydrologic models for analyzing the effects of land use change', *Journal of Hydroinformatics*, 13(3), p. 461. doi: 10.2166/hydro.2010.100.

Pers, C. (2007) 'HBV-NP Model Manual', *SMHI Hydrologi*, 103(103).

Pipitone, C. *et al.* (2018) 'Monitoring water surface and level of a reservoir using different remote sensing approaches and comparison with dam displacements evaluated via GNSS', *Remote Sensing*, 10(1), pp. 1–24. doi: 10.3390/rs10010071.

Ponce, V. M. and Hawkins, R. H. (1997) 'Runoff curve number: Has it reached maturity?', *Journal of Hydrologic Engineering*, 2(3), pp. 145–148. doi: 10.1061/(ASCE)1084-0699(1997)2:3(145).

Pontius Jr., R. G. (2000) 'Quantification error versus location error in comparison of categorical maps', *Photogrammetric Engineering and Remote Sensing*, 66(8), pp. 1011–1016.

Price, K. (2011) 'Effects of watershed topography, soils, land use, and climate on baseflow hydrology in humid regions: A review', *Progress in Physical Geography*, 35(4), pp. 465–492. doi: 10.1177/0309133311402714.

Qi, S. *et al.* (2009) 'Inundation Extent and Flood Frequency Mapping Using LANDSAT Imagery and Digital Elevation Models', *GIScience & Remote Sensing*, 46(1), pp. 101–127. doi: 10.2747/1548-1603.46.1.101.

Rafiei Emam, A. *et al.* (2018) 'Uncertainty analysis of hydrological modelling in a tropical area using different algorithms', *Frontiers of Earth Science*, 12(4), pp. 661–671. doi: 10.1007/s11707-018-0695-y.

Ramírez- Beltrán, N. D. *et al.* (2019) 'A satellite algorithm for estimating relative humidity, based on GOES and MODIS satellite data', *International Journal of Remote Sensing*. Taylor & Francis, 40(24), pp. 9237–9259. doi: 10.1080/01431161.2019.1629715.

Ramsey, D. J. (2016) *Statistics For Dummies, 2nd edition*. Second. Available at: <https://www.dummies.com/store/product/Statistics-For-Dummies-2nd-Edition.productCd-1119293529,navId-322493,descCd-DOWNLOAD.html> (Accessed: 10 February 2020).

Rathjens, H. *et al.* (2016) 'CMhyd User Manual Documentation for preparing simulated climate change data for hydrologic impact studies'.

Raveendran, N. and Sofronov, G. (2017) 'Binary Segmentation Methods for Identifying Boundaries of Spatial Domains', *Communiation Papers of the 2017 Federated Conference on Computer Science and Information Systems*, 13(December), pp. 95–102. doi: 10.15439/2017f206.

Razu Ahmed, M. *et al.* (2017) 'Remote sensing-based quantification of the impact of flash flooding on the rice production: A case study over Northeastern Bangladesh', *Sensors (Switzerland)*, 17(10). doi: 10.3390/s17102347.

Reeves, E. and Mager Daniel, S. K. (2014) 'Modelling the hydrological impacts of land use change and intergrating cultural perspectives in the Waikouaiti Catchment, Otago New Zealand', *Geography*, Master of(April).

Renard, B. *et al.* (2010) 'Understanding predictive uncertainty in hydrologic modelling: The challenge of

- identifying input and structural errors', *Water Resources Research*, 46(5), pp. 1–22. doi: 10.1029/2009WR008328.
- Riley, S. J., DeGloria, S. D. and Elliot, R. (1999) 'A Terrain Ruggedness Index that Quantifies Topographic Heterogeneity', *Intermountain Journal of Sciences*, 5(1–4), pp. 23–27. doi: citeulike-article-id:8858430.
- Rouholahnejad, E. *et al.* (2012) 'A parallelization framework for calibration of hydrological models', *Environmental Modelling and Software*. Elsevier Ltd, 31, pp. 28–36. doi: 10.1016/j.envsoft.2011.12.001.
- Ruan, Y. *et al.* (2018) 'Ranking of CMIP5 GCM skills in simulating observed precipitation over the Lower Mekong Basin, using an improved score-based method', *Water (Switzerland)*, 10(12). doi: 10.3390/w10121868.
- Rudel, T. K. (2013) 'The national determinants of deforestation in sub-Saharan Africa', *Philosophical Transactions of the Royal Society B: Biological Sciences*, 368(1625). doi: 10.1098/rstb.2012.0405.
- Rwanga, S. S. and Ndambuki, J. M. (2017) 'Accuracy Assessment of Land Use/Land Cover Classification Using Remote Sensing and GIS', *International Journal of Geosciences*, 08(04), pp. 611–622. doi: 10.4236/ijg.2017.84033.
- SADC *et al.* (2013) *Limpopo River Awareness Kit*. Available at: http://www.limpopo.riverawarenesskit.org/LIMPOPORAK_COM/EN/DEFAULT.HTM (Accessed: 14 February 2020).
- Sandhage-Hofmann, A. (2016) 'Rangeland Management', in *Reference Module in Earth Systems and Environmental Sciences*. Elsevier. doi: 10.1016/b978-0-12-409548-9.10455-5.
- Schipper, T. C. (2017) 'The attribution of changes in streamflow to climate and land use change for 472 catchments in the United States'. Available at: <https://www.utwente.nl/en/et/wem/education/msc-thesis/2017/schipper.pdf>.
- Schulze, R. E. (2016) 'Royal Swedish Academy of Sciences Modelling Hydrological Responses to Land Use and Climate Change : A Southern African Perspective Published by : Springer on behalf of Royal Swedish Academy of Sciences Stable URL : <http://www.jstor.org/stable/4314988> Your', 29(1), pp. 12–22. Available at: https://www.jstor.org/stable/4314988?seq=1#metadata_info_tab_contents.
- Schulze, R. E. and Lynch, S. D. (2011) *South African Risk and Vulnerability Atlas*. Available at: [http://sarva2.dirisa.org/resources/documents/beeH/Section 06.2 Ann Precip.pdf](http://sarva2.dirisa.org/resources/documents/beeH/Section%2006.2%20Ann%20Precip.pdf).
- Shamarti, H. (2017) 'Analysis of Rainfall Seasonality Index in Iraq', *Diyala Journal For Pure Science*, 13(1), pp. 188–202. doi: 10.24237/djps.1301.158a.
- Shao, G. *et al.* (2018) 'The impacts of climate variability and land use change on streamflow in the Hailiutu River Basin', *Water (Switzerland)*, 10(6). doi: 10.3390/w10060814.
- Shi, F. *et al.* (2018) 'An assessment of GCM performance at a regional scale using a score-based method', *Advances in Meteorology*, 2018. doi: 10.1155/2018/7641019.
- Shiksha Krishi (2013) *GRCS: Lesson 12 Runoff Estimation– SCS Curve Number Method*. Available at: <http://ecoursesonline.iasri.res.in/mod/page/view.php?id=1900> (Accessed: 20 February 2020).
- Simonetti, D., Marelli, A. and Hugh, E. (2015) *IMPACT: Portable GIS Toolbox for image processing and land cover mapping, EUR - Scientific and Technical Research Reports*. doi: 10.2788/143497.
- Singh, A. *et al.* (2014) 'Evaluation de la performance et de l'incertitude des modèles de simulation de la production de sédiments SWAT et RBNN, dans le bassin versant de Nagwa (Inde)', *Hydrological Sciences Journal*. Taylor & Francis, 59(2), pp. 351–364. doi: 10.1080/02626667.2013.872787.
- Singh, V. P. (2018) 'Hydrologic modelling: progress and future directions', *Geoscience Letters*. Springer

International Publishing, 5(1). doi: 10.1186/s40562-018-0113-z.

Singh, V. P. and Woolhiser, D. A. (2002) 'Mathematical Modelling of Watershed Hydrology', *Journal of Hydrologic Engineering*, 7(4), pp. 270–292. doi: 10.1061/(ASCE)1084-0699(2002)7:4(270).

Sitterson, J. *et al.* (2017) 'An Overview of Rainfall-Runoff Model Types An Overview of Rainfall-Runoff Model Types', *U.S. Environmental Protection Agency*, (September), pp. 0–29.

Siyabona Africa (2017) *Kruger Park Times | Huge fish deaths in Olifants | Online News Publication...* Available at: <http://www.krugerpark.co.za/krugerpark-times-2-11-fish-deaths-in-olifants-19861.html> (Accessed: 3 December 2018).

Song, K. *et al.* (2011) 'Land use/land cover (LULC) classification with MODIS time series data and validation in the Amur River Basin', *Geography and Natural Resources*, 32(1), pp. 9–15. doi: 10.1134/S1875372811010021.

Srinivasan, R. and George, C. (2015) 'QGIS Interface for SWAT (QSWAT) October 2015', *Setup for Robit Watershed, Lake Tana Basin*, (October), pp. 20–21. doi: 10.13140/RG.2.1.1060.7201.

von Storch, H. and Zwiers, F. W. (1999) *Statistical Analysis in Climate Research*. The Press Syndicate of the University of Cambridge.

Sun, G. *et al.* (2013) 'Impacts of climate change and variability on water resources in the Southeast USA', *Climate of the Southeast United States: Variability, Change, Impacts, and Vulnerability*, (January), pp. 210–236. doi: 10.5822/978-1-61091-509-0_10.

Sun, W. *et al.* (2017) 'Physically based distributed hydrological model calibration based on a short period of streamflow data: case studies in four Chinese basins', *Hydrol. Earth Syst. Sci*, 21, pp. 251–265. doi: 10.5194/hess-21-251-2017.

Tadono, T. *et al.* (2014) 'PRECISE GLOBAL DEM GENERATION BY ALOS PRISM'. doi: 10.5194/isprsannals-II-4-71-2014.

Takaku, J., Tadono, T., Tsutsui, K., *et al.* (2016) 'VALIDATION OF "AW3D" GLOBAL DSM GENERATED FROM ALOS PRISM'. doi: 10.5194/isprsannals-III-4-25-2016.

Takaku, J., Tadono, T. and Tsutsui, K. (2016) 'GENERATION OF HIGH RESOLUTION GLOBAL DSM FROM ALOS PRISM'. doi: 10.5194/isprsarchives-XL-4-243-2014.

Taylor, K. E., Stouffer, R. J. and Meehl, G. A. (2011) 'An Overview of CMIP5 and the Experiment Design'. doi: 10.1175/BAMS-D-11-00094.1.

The World Bank (2019) *South Africa | Data*. Available at: <https://data.worldbank.org/country/south-africa> (Accessed: 13 January 2020).

Tian, Y. *et al.* (2009) 'Component analysis of errors in Satellite-based precipitation estimates', *Journal of Geophysical Research Atmospheres*. doi: 10.1029/2009JD011949.

Du Tiot, W. H. and Sonnekus, C. J. (2014) 'AN EXPLANATION OF THE 1 : 500 000 GENERAL HYDROGEOLOGICAL MAP - Nelspruit 2530', (October), pp. 0–136.

Toit, W. H. D. U. and Sonnekus, C. J. (2014) 'EXPLANATION OF THE 1:500 000 HYDROGEOLOGICAL MAP 2326 POLOKWANE', (October), pp. 1–175.

Turton, A. (2015) 'The looming water crisis, and its causes - IRR - NEWS & ANALYSIS | Politicsweb', November. Available at: <https://www.politicsweb.co.za/news-and-analysis/water-the-next-eskom--irr> (Accessed: 1 June 2019).

Uddin, K., Matin, M. A. and Meyer, F. J. (2019) 'Operational Flood Mapping Using Multi-Temporal Sentinel-1 SAR Images: A Case Study from Bangladesh', *Remote Sensing*, 11(13), p. 1581. doi: 10.3390/rs11131581.

UN (2018) *Devastating Impacts of Climate Change Threatening Farm Outputs, Increasing Global Hunger, Delegates Say as Second Committee Takes Up Agriculture, Food Security | Meetings Coverage and Press Releases*. Available at: <https://www.un.org/press/en/2018/gaef3499.doc.htm> (Accessed: 17 June 2019).

UN CC:Learn (2015) *THE SCIENTIFIC FUNDAMENTALS OF CLIMATE CHANGE Resource Guide for Advanced Learning on*. Available at: https://www.uncclearn.org/sites/default/files/guide_scientific_fundamentals.pdf (Accessed: 17 June 2019).

UNESCO and FAO (1995) *FAO/UNESCO SOIL MAP UNITS*. Available at: http://www.fao.org/fileadmin/user_upload/soils/docs/Soil_map_FAOUNESCO/new_maps/VI_back_petit.jpg (Accessed: 12 February 2020).

UNESCO and FAO (2003) 'THE DIGITAL SOIL MAP OF THE WORLD FOOD', 19(8), pp. 159–170.

UNFCCC (2011) *United Nations Framework Convention on Climate Change*. Available at: https://unfccc.int/files/press/backgrounders/application/pdf/press_factsh_science.pdf (Accessed: 17 June 2019).

United States Natural Resources Conservation Service (1997) *National Engineering Handbook*.

United States Naval Academy (2016) *Topographic Ruggedness Index*. Available at: https://www.usna.edu/Users/oceano/pguth/md_help/html/topo_rugged_index.htm (Accessed: 16 September 2019).

Urama, K. C. and Ozor, N. (2010) 'IMPACTS OF CLIMATE CHANGE ON WATER RESOURCES IN AFRICA : the Role of Adaptation', *Network*, (December), pp. 1–29.

USDA_NRCS (2014) 'Inherent Factors Affecting Soil Infiltration', (May), pp. 1–6.

USGS (2016) 'Tracking Change Over Time : Understanding Remote Sensing', (March), pp. 2–5. Available at: https://pubs.usgs.gov/gip/133/pdf/RemSens-Student_web.pdf.

USGS (2017) *Mapping, Remote Sensing and Geospatial Data*. Available at: https://www.usgs.gov/faqs/what-are-band-designations-landsat-satellites?qt-news_science_products=0#qt-news_science_products (Accessed: 9 June 2019).

Utah State University (no date) *Tree Fruit Production Guide- Soil Water Content*. Available at: <https://intermountainfruit.org/orchard-irrigation/swc> (Accessed: 2 March 2020).

Vaghefi, S. A., Abbaspour, N. and Kamali, B. (2017) 'Climate Change Toolkit (CCT) User Guide', pp. 181–198.

Vasel, L. *et al.* (2015) 'Modelling Blue and Green Water Resources Availability in an Iranian Data Scarce Watershed Using SWAT', *Journal of Water Management Modelling* C391. doi: 10.14796/JWMM.C391.

de Villiers, S. and Mkwelo, S. T. (2009) 'Has monitoring failed the Olifants River, Mpumalanga?', *Water SA*, 35(5), pp. 671–676. doi: 10.4314/wsa.v35i5.49193.

Voctor, D. G. *et al.* (2014) *IPCC fifth Assessment Report*.

Voepel, H. *et al.* (2011) 'Quantifying the role of climate and landscape characteristics on hydrologic partitioning and vegetation response', *Water Resources Research*, 47(8). doi: 10.1029/2010WR009944.

Wai-Keung LAM, K. and Lau, W.-L. (2000) *THE EFFECTS ON IMAGE CLASSIFICATION USING IMAGE COMPRESSION TECHNIQUE*. Available at: <https://pdfs.semanticscholar.org/4437/8d8528a334da1e738b8a9ccee8fce664b950.pdf> (Accessed: 1 August 2019).

Wang, C. *et al.* (2018) 'Integrated effects of land use and topography on streamflow response to precipitation in an agriculture-forest dominated northern watershed', *Water (Switzerland)*, 10(5). doi: 10.3390/w10050633.

- Wang, F. *et al.* (2017) 'Impacts of land-use and land-cover changes on river runoff in Yellow River basin for period of 1956–2012', *Chinese Geographical Science*, 27(1), pp. 13–24. doi: 10.1007/s11769-017-0843-3.
- Wayne, P. G. (2013) 'The Beginner's Guide to Representative Concentration Pathways'. Available at: <https://skepticalscience.com/rcp.php> (Accessed: 10 November 2019).
- Williams, J. R. (1975) 'HYMO flood routing', *Journal of Hydrology*, 26(1–2), pp. 17–27. doi: 10.1016/0022-1694(75)90122-5.
- Willmott, C. J. (1981) 'On the validation of models', *Physical Geography*, 2(2), pp. 184–194. doi: 10.1080/02723646.1981.10642213.
- WWF (2016) *AGRICULTURE: FACTS & TRENDS South Africa*. Available at: http://awsassets.wwf.org.za/downloads/facts_brochure_mockup_04_b.pdf (Accessed: 15 May 2019).
- Yang, J. *et al.* (2008) 'Comparing uncertainty analysis techniques for a SWAT application to the Chaohe Basin in China', *Journal of Hydrology*, 358(1–2), pp. 1–23. doi: 10.1016/j.jhydrol.2008.05.012.
- Zhang, L. *et al.* (2016) 'Hydrological impacts of land use change and climate variability in the headwater region of the Heihe River Basin, northwest China', *PLoS ONE*, 11(6), pp. 1–25. doi: 10.1371/journal.pone.0158394.
- Zhu, C. and Li, Y. (2014) 'Long-Term Hydrological Impacts of Land Use/Land Cover Change From 1984 to 2010 in the Little River Watershed, Tennessee', *International Soil and Water Conservation Research*. Elsevier Masson SAS, 2(2), pp. 11–21. doi: 10.1016/S2095-6339(15)30002-2.
- Zhu, L. *et al.* (2018) 'A Review: Remote Sensing Sensors', in *Multi-purposeful Application of Geospatial Data*. InTech. doi: 10.5772/intechopen.71049.

8 APPENDICES

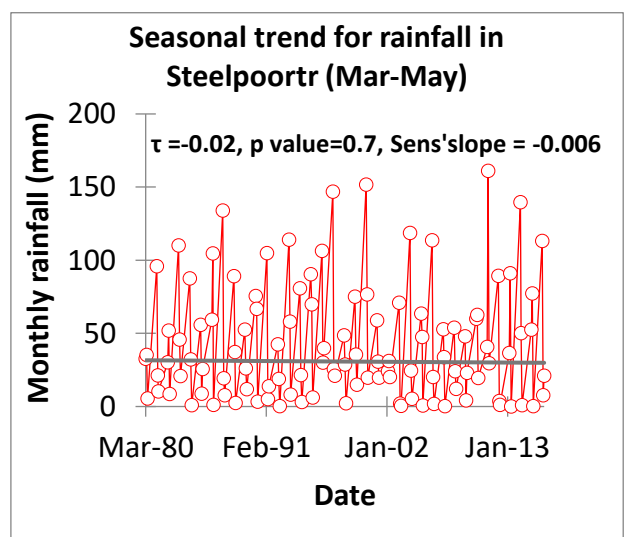
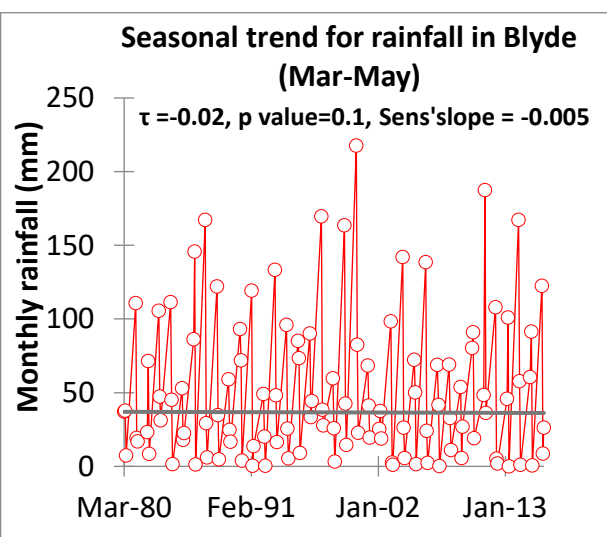
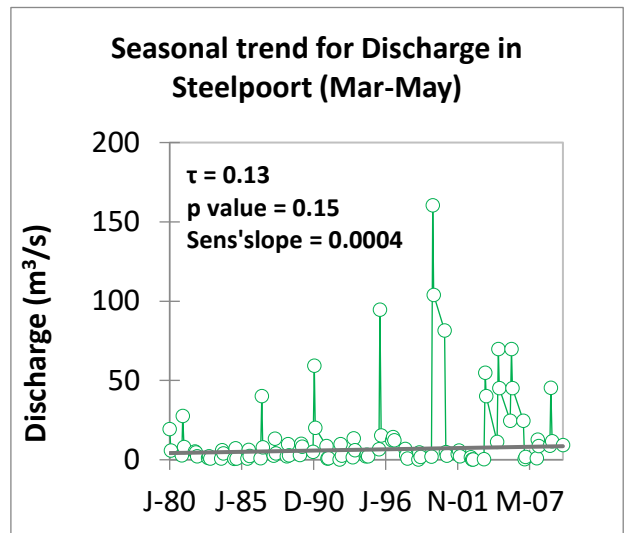
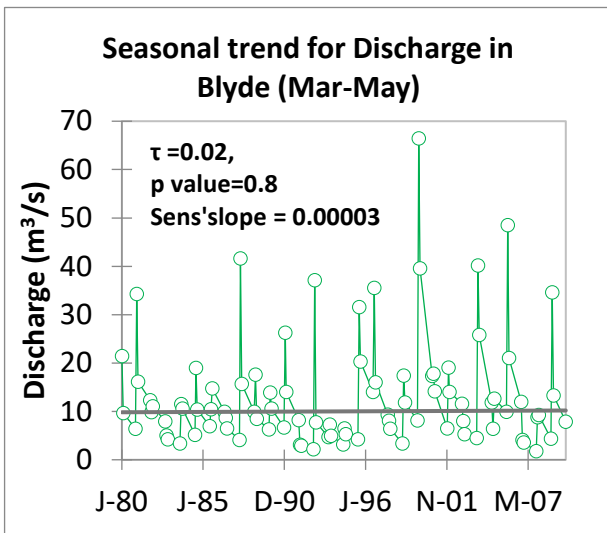
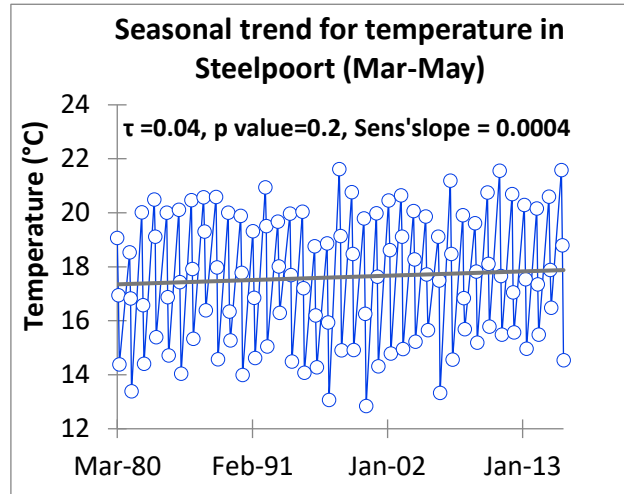
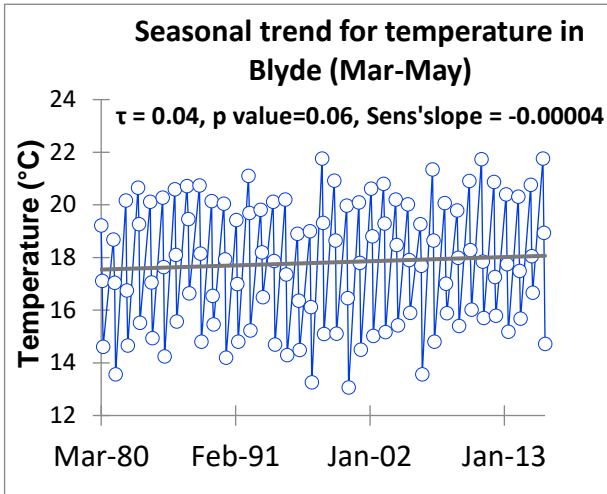
APPENDIX I. is related to Chapter 2 of this thesis. It contains graphical representation of various seasonal trends of temperature, rainfall, and discharge are in Blyde and Steelpoort River Basins

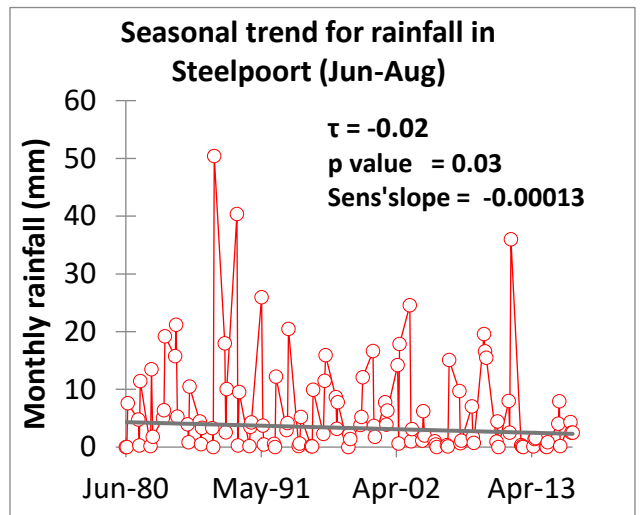
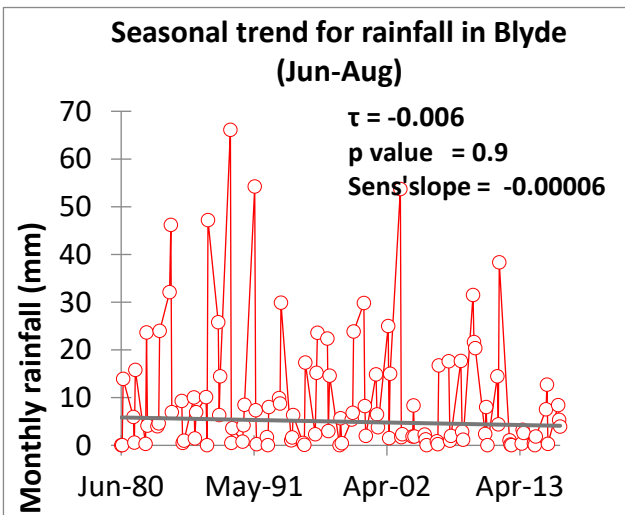
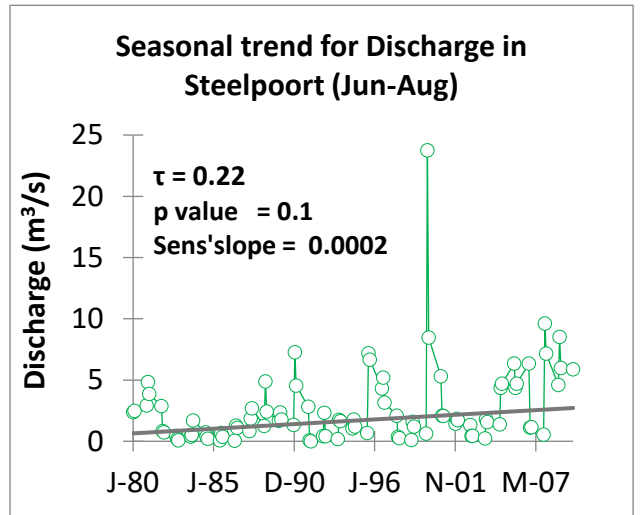
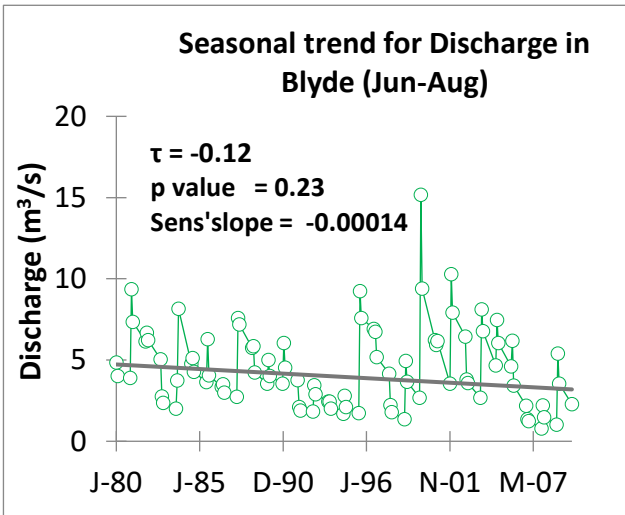
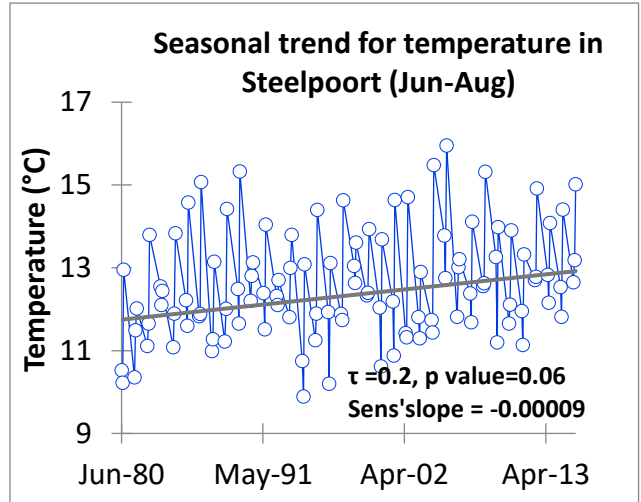
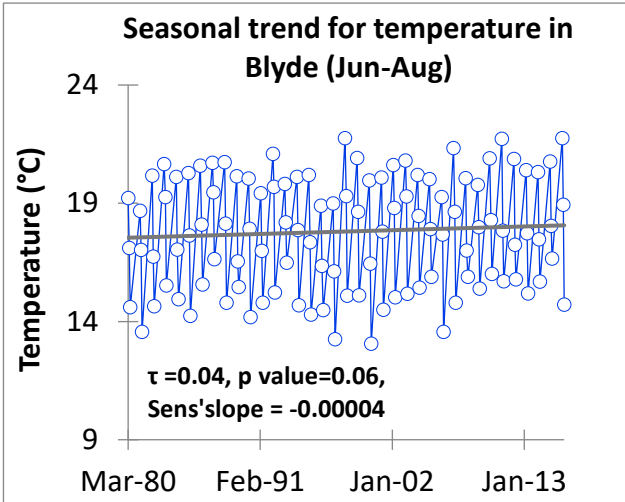
APPENDIX II is related to Chapter 3 of this thesis and it contains calibrated parameter values for the sub-basins within the Blyde and Steelpoort River Basins.

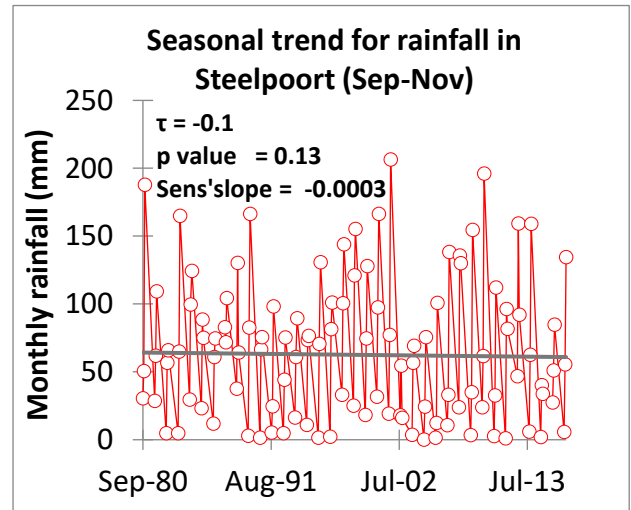
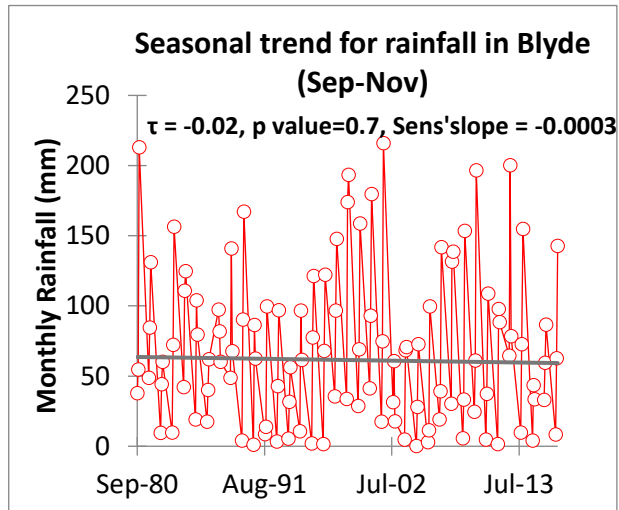
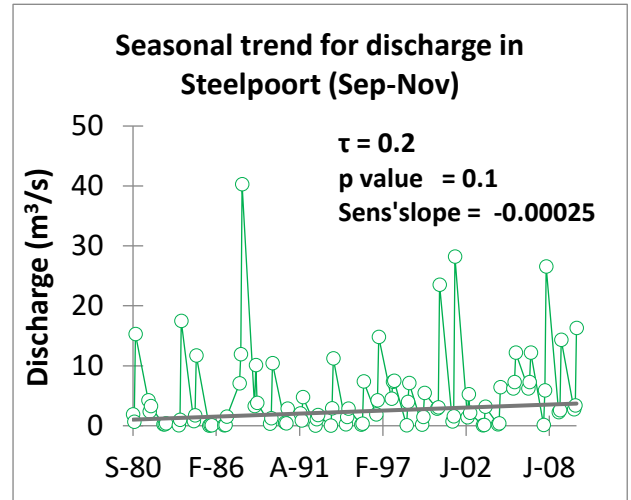
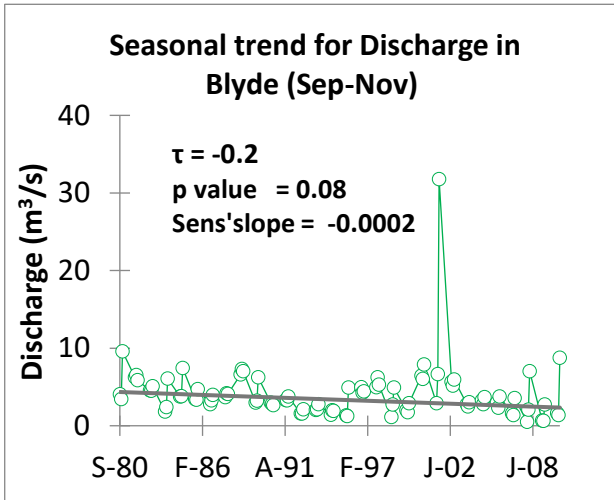
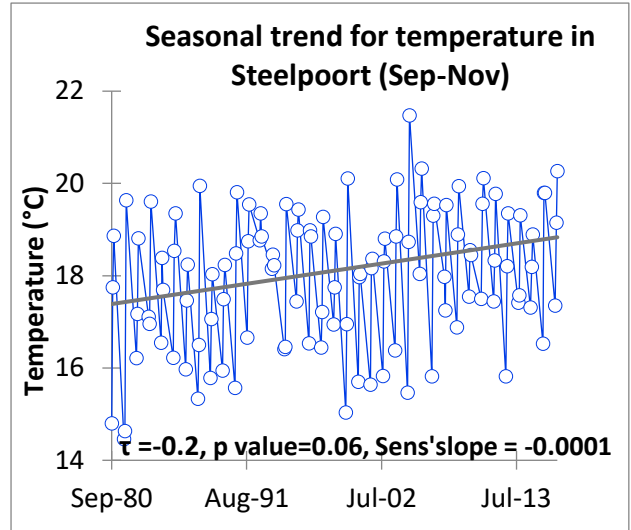
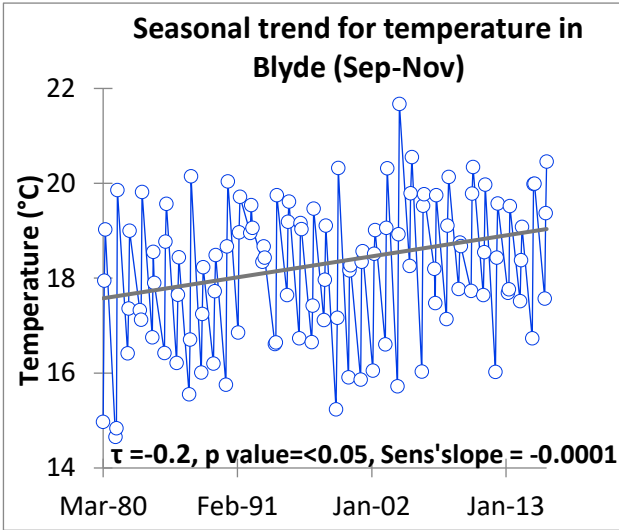
APPENDIX III is related to Chapter 4 of this thesis and it shows scatterplots for selected morphological parameters and various hydrological indices

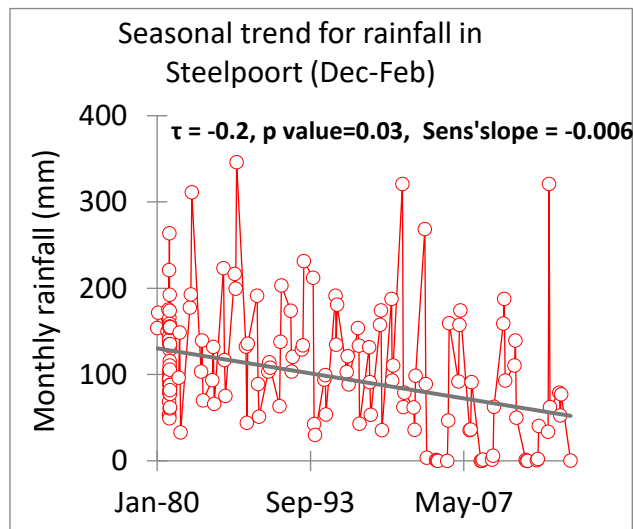
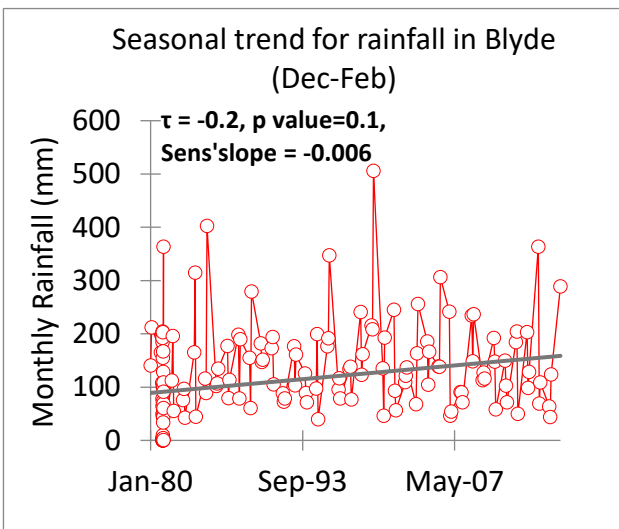
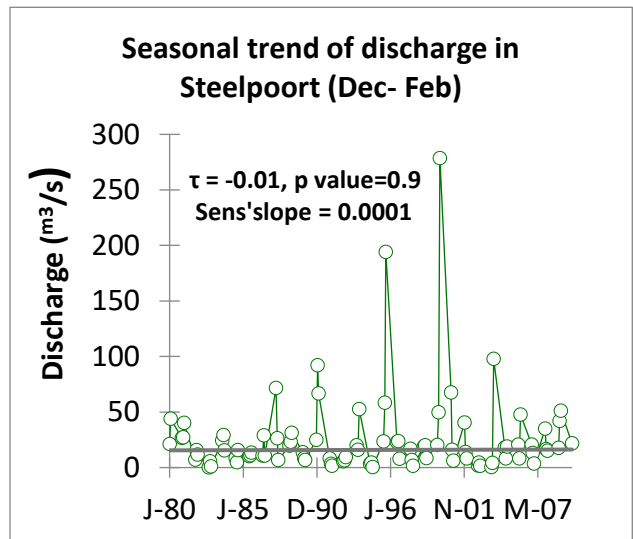
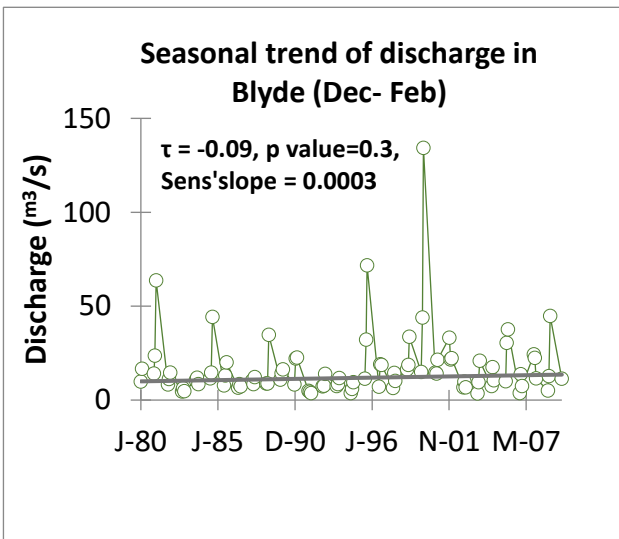
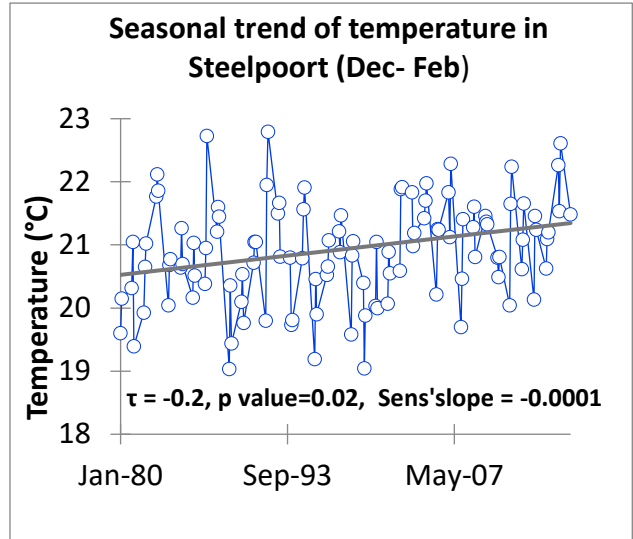
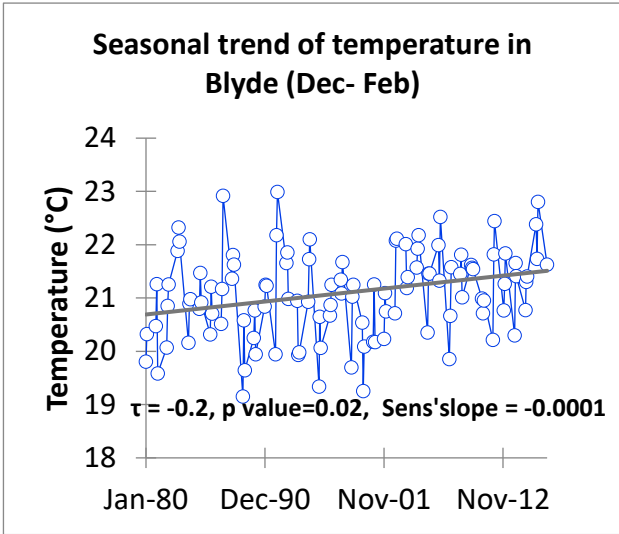
APPENDIX IV is related to Chapter 2 and Chapter 3 of this thesis. It shows the R-code used to extract data from NetCDF files to time-series in csv format: data extraction is based on point location coordinates.

APPENDIX I









APPENDICES

Calibrated parameters for sub-basins 1 - 12

Parameters	Sub-basin ID											
	BSN_1	BSN_2	BSN_3	BSN_4	BSN_5	BSN_6	BSN_7	BSN_8	BSN_9	BSN_10	BSN_11	BSN_12
CN2	83.02	73.26	56.30	68.53	53.24	79.97	53.53	57.25	78.83	58.17	50.00	59.72
SOL_AWC	0.30	0.32	0.29	0.13	0.28	0.11	0.29	0.15	0.28	0.15	0.20	0.34
SOL_Z	711.2	174.3	174.3	300.0	610.3	576.0	174.3	324.8	646.4	324.8	535.3	170.3
ALPHA_BF	1.00	0.29	0.29	0.29	0.11	0.77	0.29	0.76	0.06	0.76	0.28	0.60
GWQMN	764.2	2683	2683	2683	4125	2530	2683	801	550	801	3121	3912
ESCO	0.31	0.62	0.62	0.62	0.15	0.47	0.62	0.01	0.14	0.01	0.11	0.68
EPCO	0.32	0.28	0.30	0.31	0.27	0.32	0.23	0.26	0.26	0.28	0.30	0.32
SOL_K	11.50	20.27	30.55	9.71	40.08	6.48	26.71	16.64	13.85	18.01	13.04	34.77
CH_N2	0.10	0.13	0.13	0.13	0.05	0.22	0.13	0.06	0.29	0.06	0.29	0.20
OV_N	0.08	0.93	0.86	0.53	0.36	0.44	0.76	0.50	0.41	0.50	0.16	0.60
GWHT	3.89	6.58	6.58	6.58	14.29	9.45	6.58	19.38	13.18	19.38	16.61	7.31
HRU_SLP	0.15	0.15	0.13	0.16	0.14	0.23	0.12	0.15	0.13	0.15	0.11	0.13
GW_SPYLD	0.02	0.39	0.39	0.39	0.29	0.12	0.39	0.19	0.11	0.19	0.01	0.32
SURLAG	2.65	2.59	2.59	2.59	0.65	1.05	2.59	0.86	2.03	0.86	3.49	2.49
GW_DELAY	89.71	385.3	385.3	385.3	32.50	329.00	385.33	67.52	301.1	67.52	20.57	161.25
REVAPMN	284.2	550.0	550.0	550.0	81.7	614.00	550.0	430.4	47.14	430.44	935.71	27.50
GW_REVAP	0.05	0.12	0.12	0.12	0.08	0.03	0.12	0.03	0.06	0.03	0.11	0.13
CH_K2	7.14	122.0	122.0	122.0	180.33	120.40	122.00	0.13	36.29	0.13	17.43	363.75
SLSUBBSN	67.89	58.82	60.14	52.32	55.06	47.81	65.08	44.56	54.53	43.92	62.28	60.85

APPENDICES

Calibrated parameters for sub-basins 13 - 24

Parameters	Sub-basin ID										
	BSN_13	BSN_14	BSN_15	BSN_16	BSN_17	BSN_18	BSN_19	BSN_20	BSN_21	BSN_22	BSN_23
CN2	50.08	69.37	83.33	39.00	68.14	59.82	51.23	50.19	70.71	51.10	53.65
SOL_AWC	0.10	0.15	0.13	0.30	0.28	0.16	0.20	0.20	0.17	0.11	0.28
SOL_Z	459.82	156.08	653.82	607.65	190.50	324.79	535.33	535.33	156.08	459.82	610.35
ALPHA_BF	0.09	0.26	0.36	0.40	0.13	0.76	0.28	0.28	0.26	0.09	0.11
GWQMN	1862.5	162.50	450.00	4025.0	3492.8	801.6	3121.4	3121.4	162.50	1862.5	4125.0
ESCO	0.37	0.55	0.67	0.16	0.31	0.01	0.11	0.11	0.55	0.37	0.15
EPCO	0.29	0.29	0.26	0.29	0.29	0.27	0.30	0.27	0.27	0.30	0.32
SOL_K	18.24	11.63	18.62	51.84	5.19	3.51	12.87	17.49	12.74	17.22	29.67
CH_N2	0.16	0.27	0.20	0.08	0.28	0.06	0.29	0.29	0.27	0.16	0.05
OV_N	0.85	0.44	0.69	0.40	0.65	0.48	0.15	0.14	0.39	0.85	0.42
GWHT	17.94	7.81	24.25	1.63	24.46	19.38	16.61	16.61	7.81	17.94	14.29
HRU_SLP	0.17	0.19	0.16	0.17	0.13	0.16	0.13	0.14	0.19	0.16	0.14
GW_SPYLD	0.10	0.30	0.26	0.23	0.30	0.19	0.01	0.01	0.30	0.10	0.29
SURLAG	1.17	2.45	2.89	3.07	2.59	0.86	3.49	3.49	2.45	1.17	0.65
GW_DELAY	213.75	101.25	40.80	302.50	358.29	67.52	20.57	20.57	101.25	213.75	32.50
REVAPMN	372.50	552.50	766.00	65.00	958.57	430.44	935.71	935.71	552.50	372.50	81.67
GW_REVAP	0.06	0.11	0.14	0.13	0.07	0.03	0.11	0.11	0.11	0.06	0.08
CH_K2	46.50	32.50	100.40	362.50	116.86	0.13	17.43	17.43	32.50	46.50	180.33
SLSUBBSN	47.26	65.17	60.66	59.85	40.00	44.75	59.91	58.36	64.66	47.90	55.88

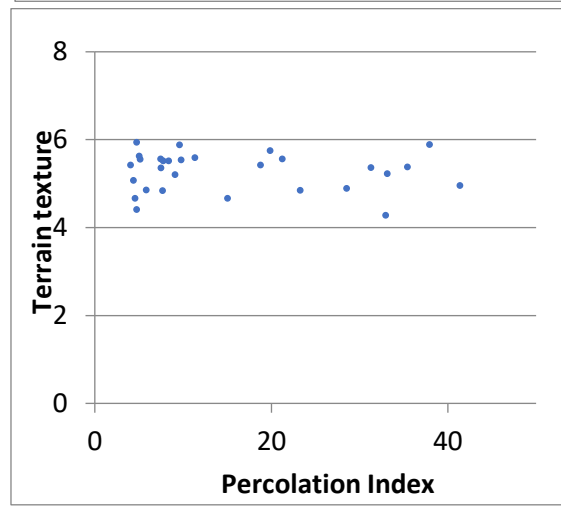
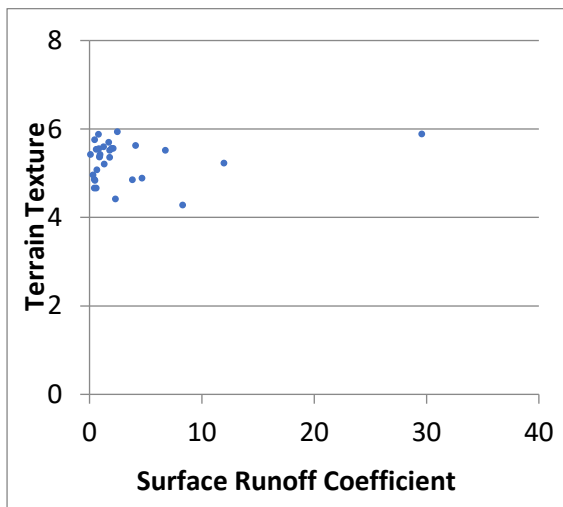
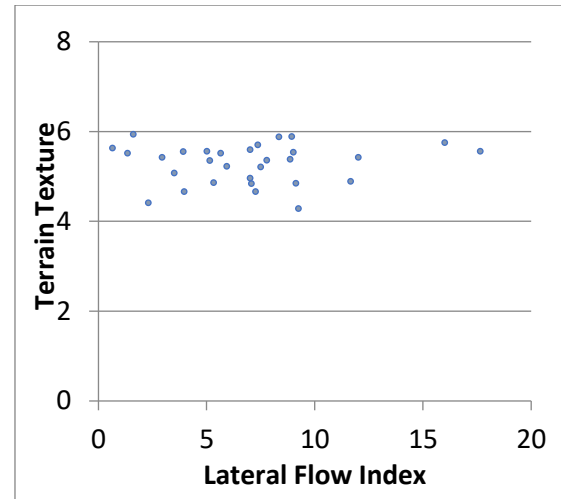
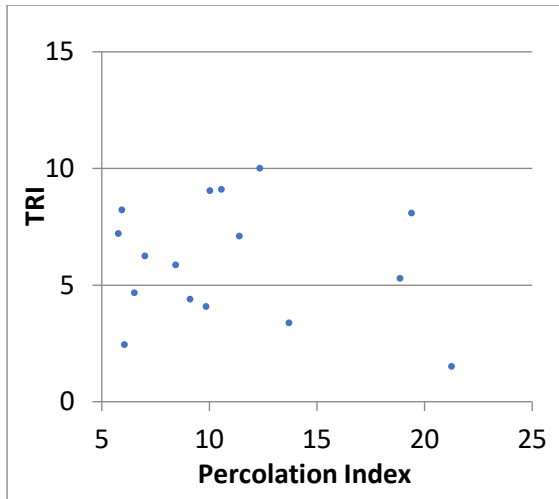
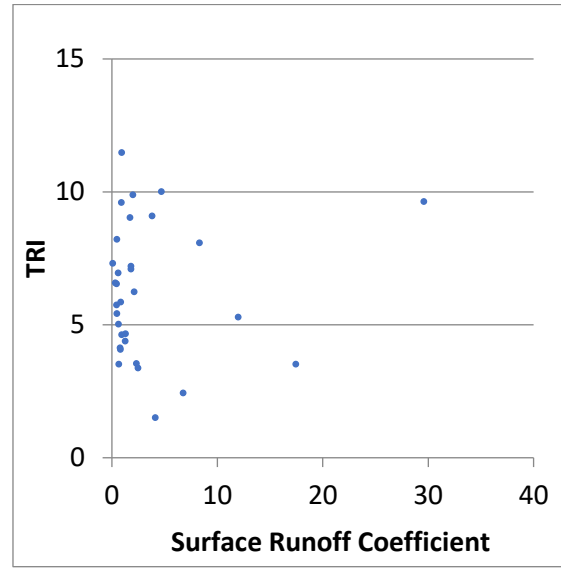
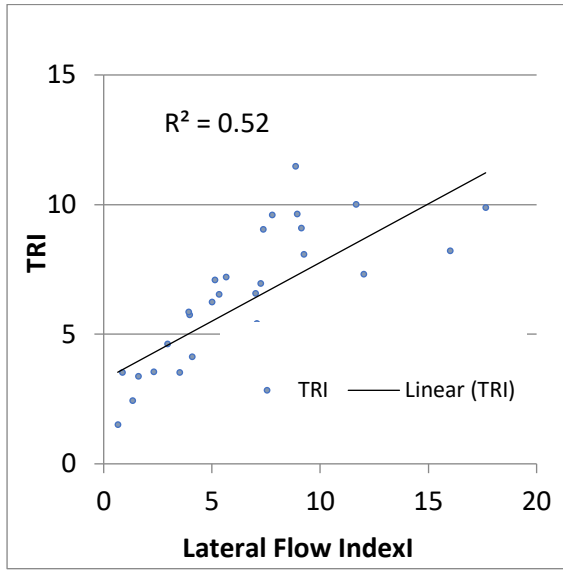
APPENDICES

Calibrated parameters for sub-basins 25 - 32

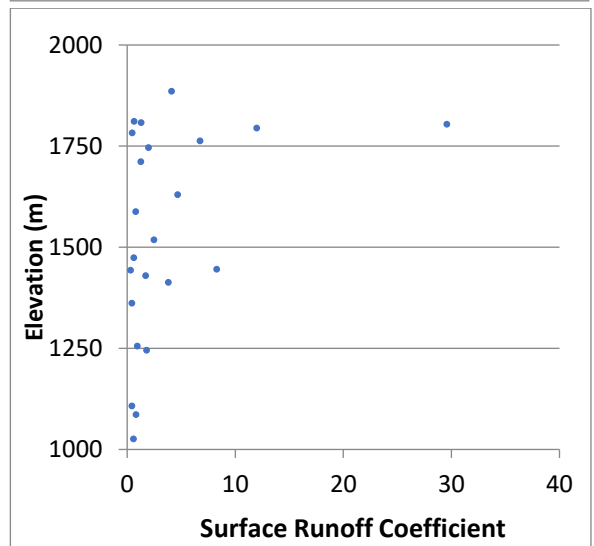
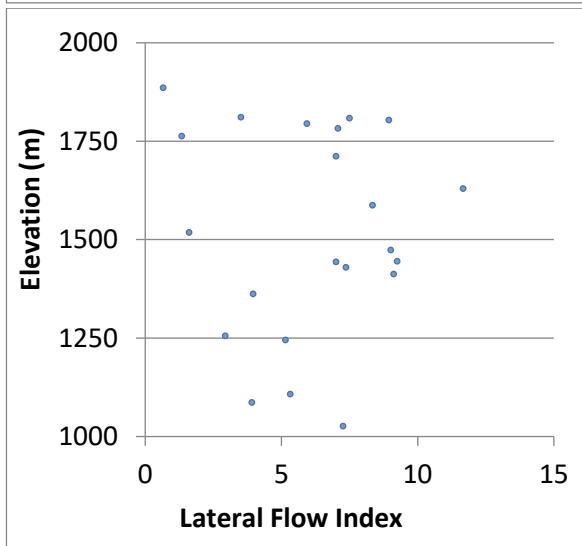
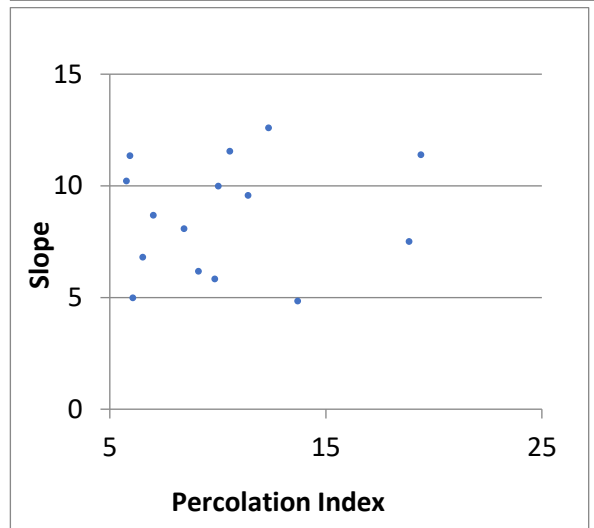
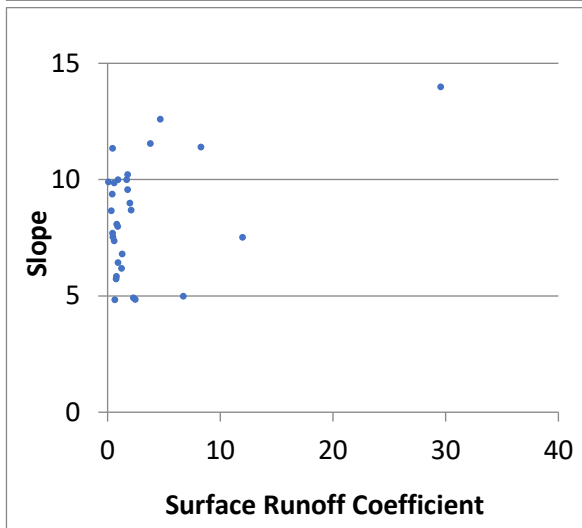
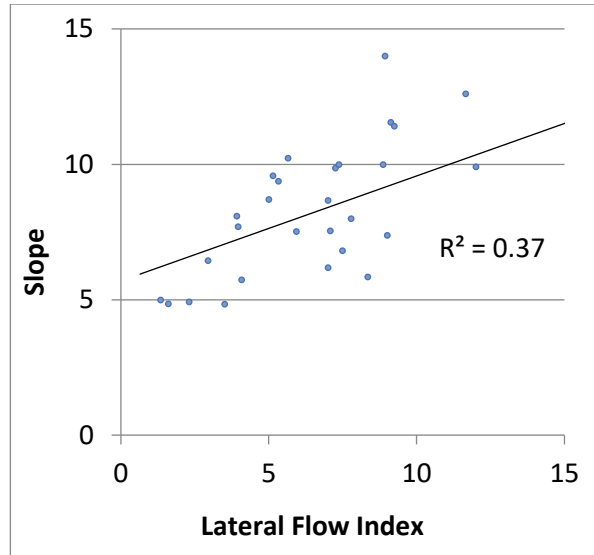
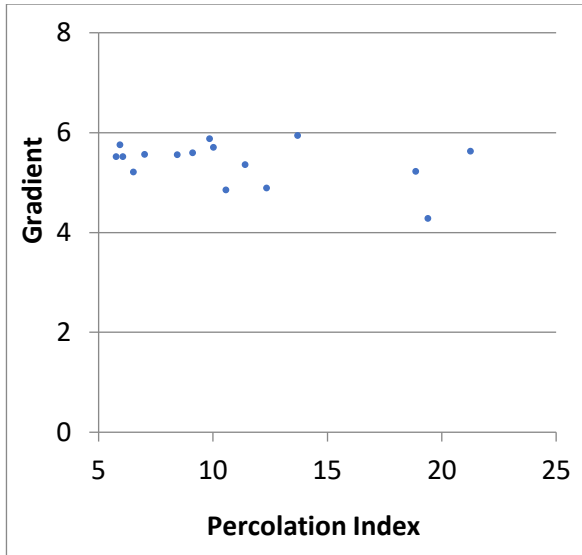
Parameters	Sub-basin ID								
	BSN_24	BSN_25	BSN_26	BSN_27	BSN_28	BSN_29	BSN_30	BSN_31	BSN_32
CN2	64.61	50.85	46.97	89.86	62.39	49.76	52.17	67.54	51.13
SOL_AWC	0.24	0.10	0.08	0.11	0.19	0.20	0.30	0.13	0.28
SOL_Z	387.21	459.82	912.56	459.82	861.64	535.33	646.41	300.00	646.41
ALPHA_BF	0.00	0.09	0.18	0.09	0.52	0.28	0.06	0.06	0.06
GWQMN	117.14	1862.50	735.71	1862.50	4550.00	3121.43	550.00	550.00	550.00
ESCO	0.68	0.37	0.34	0.37	0.51	0.11	0.14	0.14	0.14
EPCO	0.27	0.29	0.26	0.27	0.29	0.28	0.29	0.29	0.27
SOL_K	22.25	17.08	14.10	12.27	12.67	17.49	9.57	15.02	13.85
CH_N2	0.01	0.16	0.19	0.16	0.13	0.29	0.29	0.29	0.29
OV_N	0.55	0.84	0.67	0.81	0.43	0.15	0.43	0.50	0.38
GWHT	10.46	17.94	16.32	17.94	16.89	16.61	13.18	13.18	13.18
HRU_SLP	0.18	0.17	0.13	0.20	0.15	0.12	0.11	0.17	0.12
GW_SPYLD	0.21	0.10	0.32	0.10	0.32	0.01	0.11	0.11	0.11
SURLAG	2.31	1.17	1.41	1.17	2.09	3.49	2.03	2.03	2.03
GW_DELAY	219.29	213.75	265.71	213.75	48.57	20.57	301.14	301.14	301.14
REVAPMN	615.71	372.50	710.00	372.50	998.57	935.71	47.14	47.14	47.14
GW_REVAP	0.15	0.06	0.07	0.06	0.09	0.11	0.06	0.06	0.06
CH_K2	176.29	46.50	50.00	46.50	196.29	17.43	36.29	36.29	36.29
SLSUBBSN	63.95	48.26	60.87	46.32	47.45	58.77	60.97	52.55	57.32

APPENDIX III

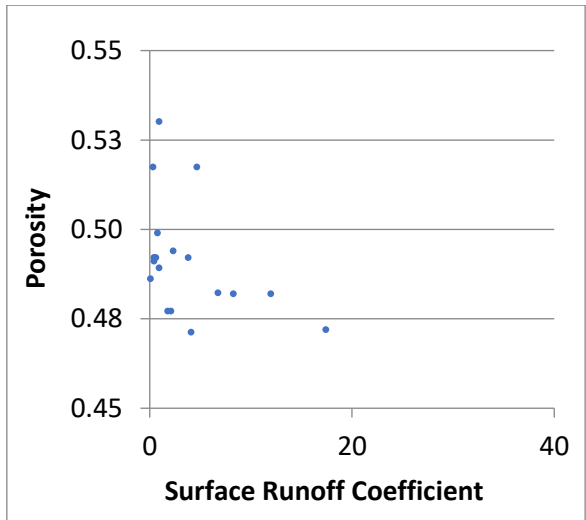
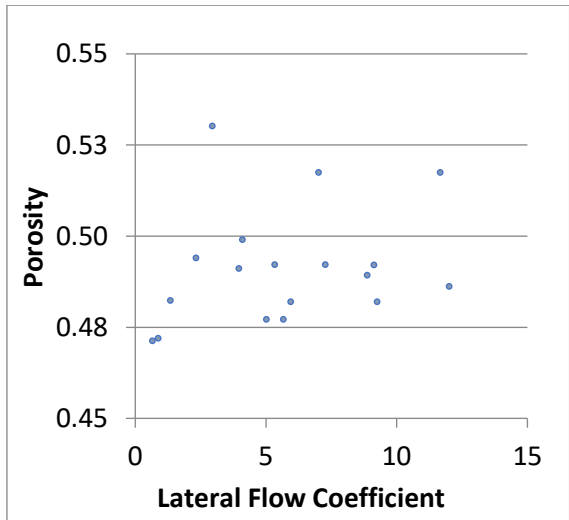
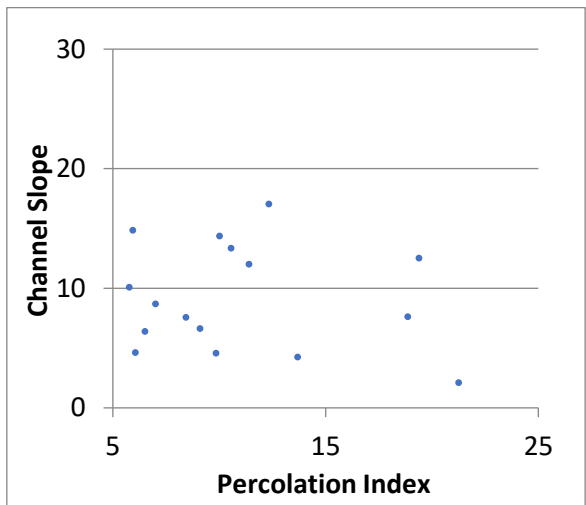
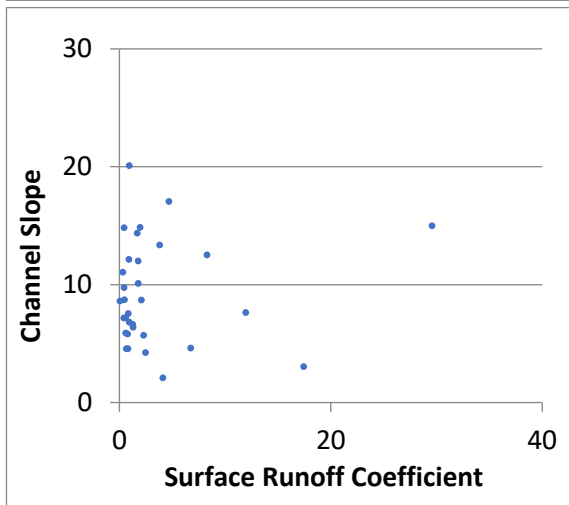
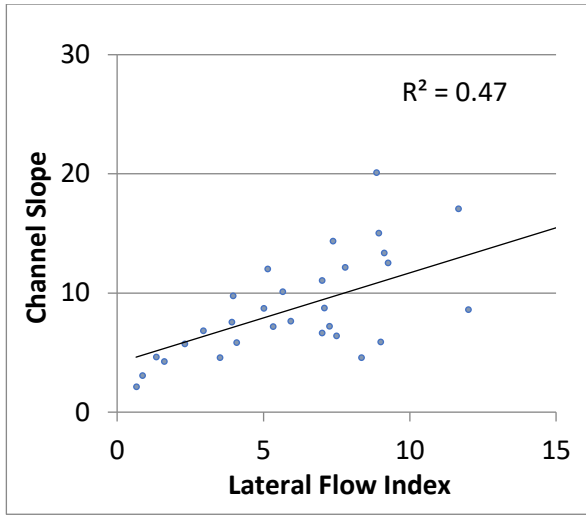
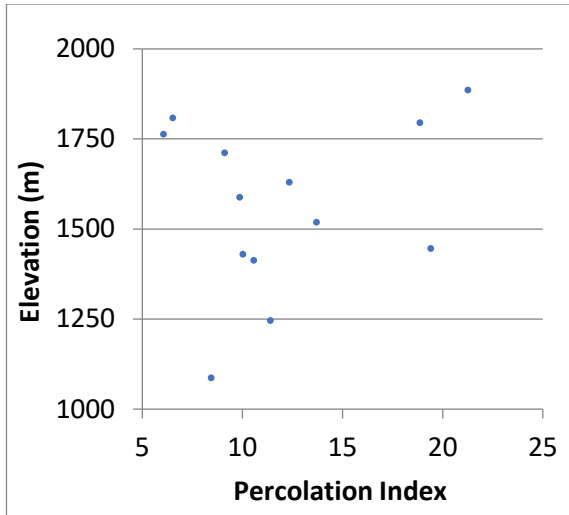
Correlation and scatter plots of morphological parameters and hydrological components



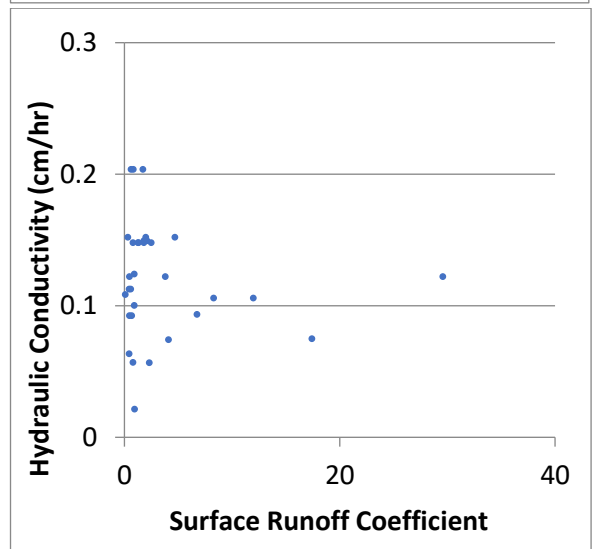
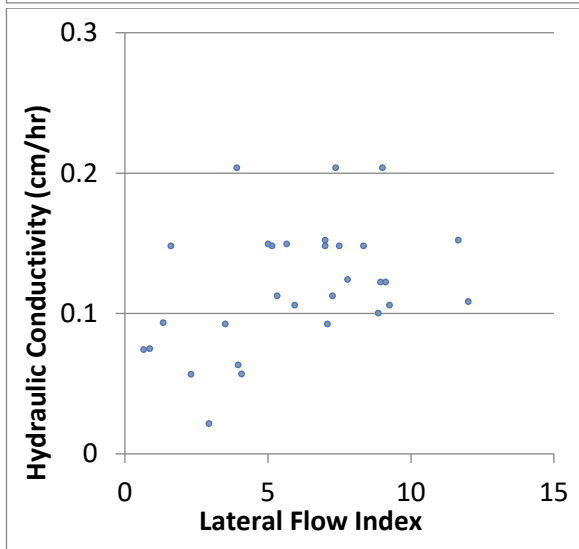
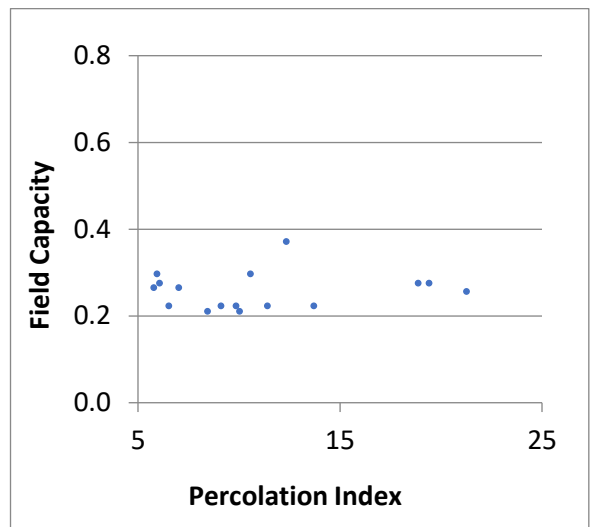
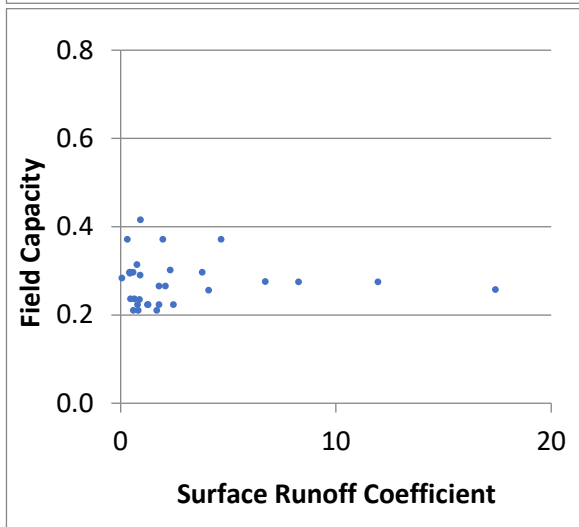
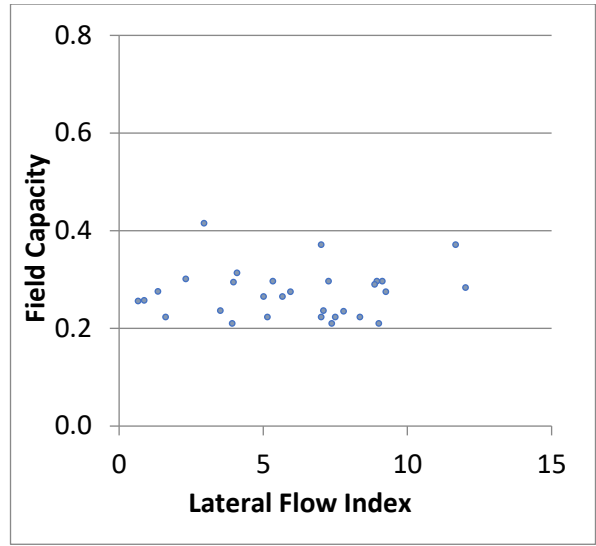
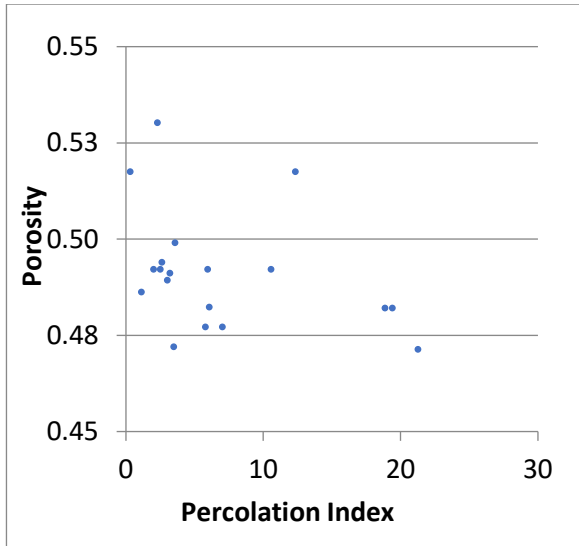
APPENDICES



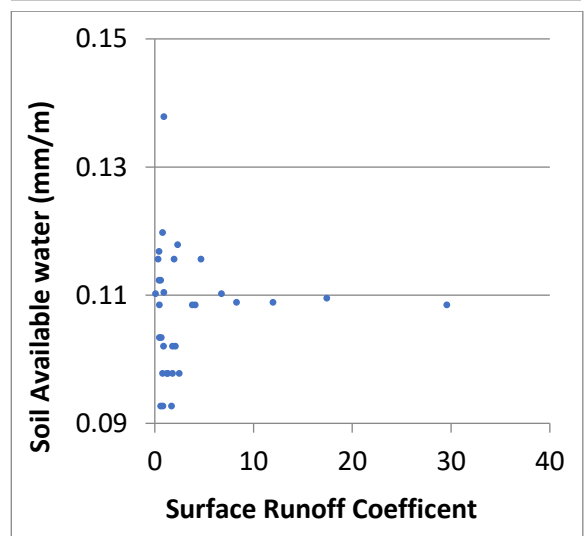
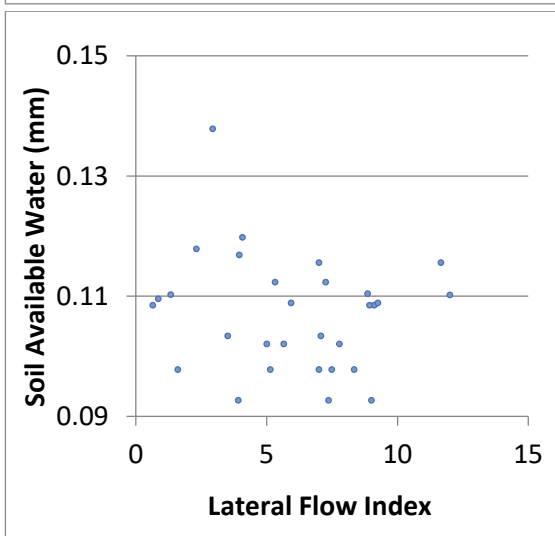
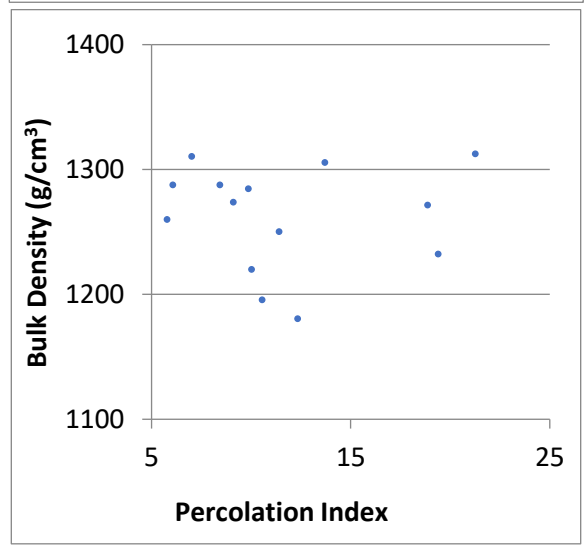
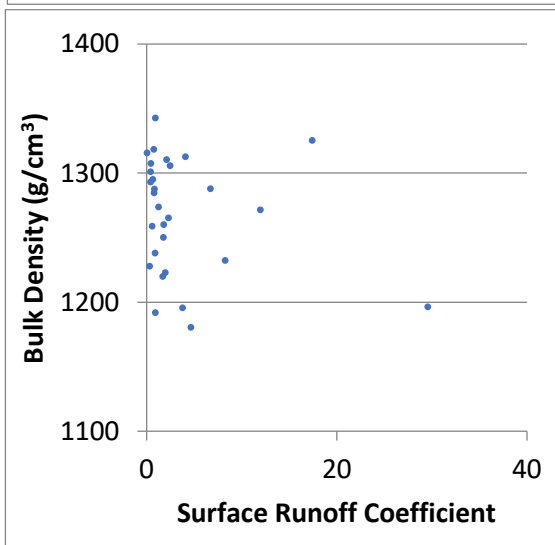
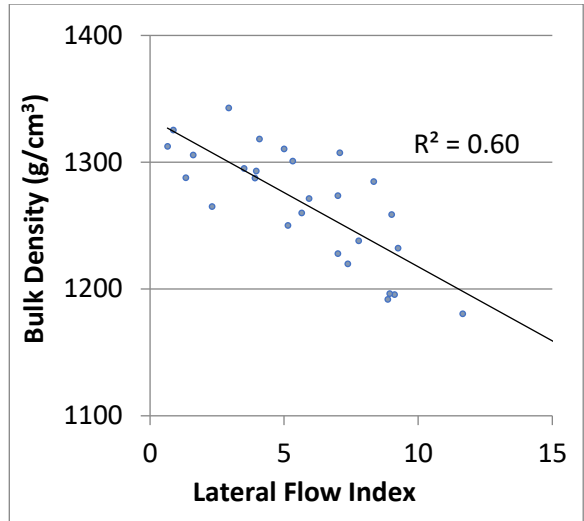
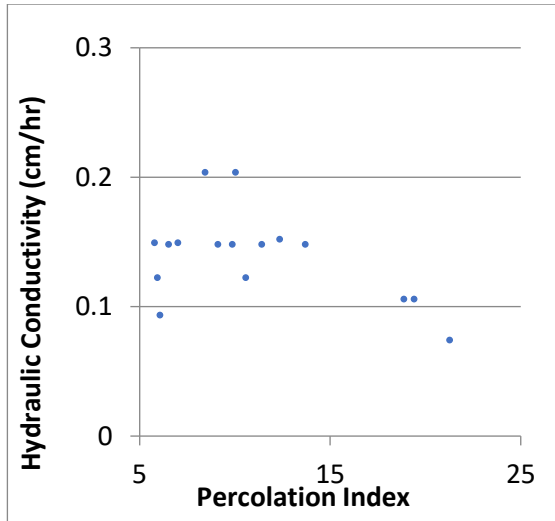
APPENDICES

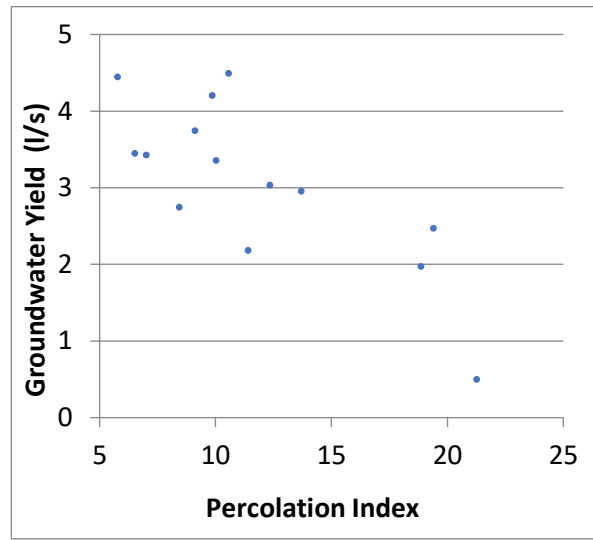
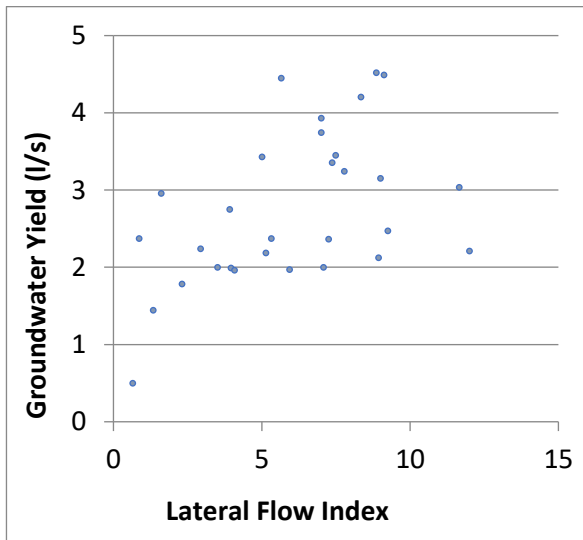
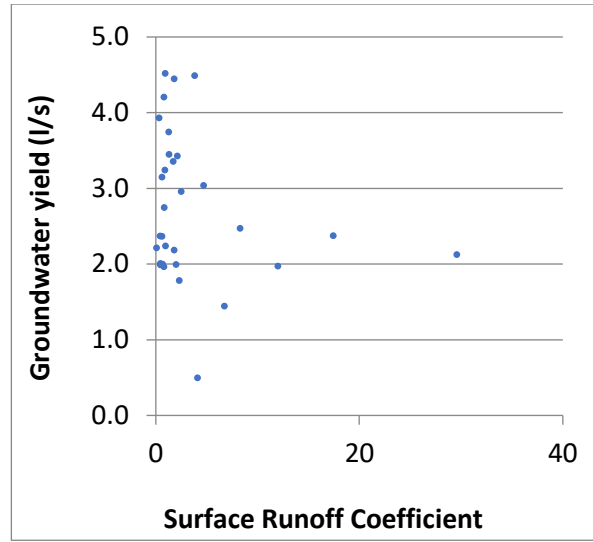
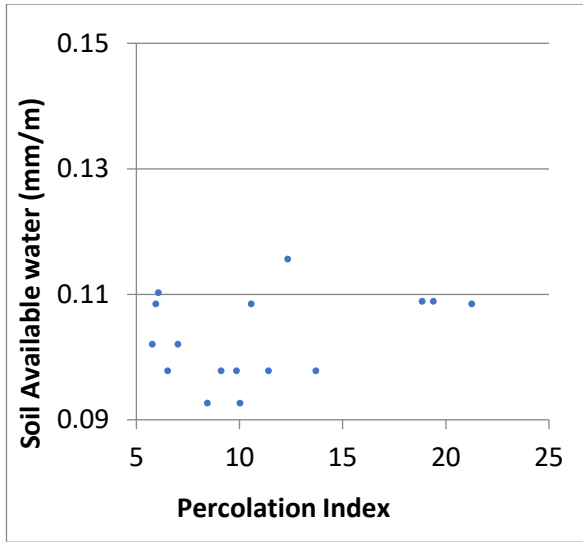


APPENDICES



APPENDICES





APPENDIX IV

The following is a sample R code use to extract temperature data at specific point locations:

```
# Definition of working directory and the packages required
setwd("D:/KIT/ACAD/CRU")
library(raster)
library(ncdf4)

# Read all layers in the NetCDF file (cru_ts4.01.1901.2016.tmn.dat.nc) by
# specifying the path to the file and the variable name
# Assign the layer list the ID "br"
br <- brick("D:/KIT/ACAD/CRU/cru_ts4.01.1901.2016.tmn.dat.nc", varname = "tmn")

# read and load the index of each layer of the NetCDF file
# Assign the date indices of the layers the ID "i"
i <- getZ(br)

# Load file (coords.csv) containing coordinates of point locations where data
# will be extracted
# Assign the coordinate list list the ID "coords"
coords <- read.table("D:/KIT/ACAD/CRU/coord.csv", header=T, sep=",")

# Extract values for all the time steps and write them to a dataframe with
# corresponding coordinates
# Assign the extracted values the ID "values"
values <- extract(br, coords, df=T)

# Merge dates and values and fix data frame names
df <- data.frame(i, t(vals)[-1,])
rownames(df) <- NULL
names(df) <- c('date', 'value')

#write results to a csv file
write.table(df, file="cru_tmn.csv")
```